coatings

Special Issue Reprint

Current Research in Cement and Building Materials

Edited by
Peng Liu, Lingkun Chen and Ying Chen

mdpi.com/journal/coatings

MDPI

Current Research in Cement and Building Materials

Current Research in Cement and Building Materials

Editors

Peng Liu
Lingkun Chen
Ying Chen

MDPI

Basel • Beijing • Wuhan • Barcelona • Belgrade • Novi Sad • Cluj • Manchester

Editors

Peng Liu Central South University Changsha China	Lingkun Chen Yangzhou University Yangzhou China	Ying Chen Central South University of Forestry and Technology Changsha China

Editorial Office
MDPI
St. Alban-Anlage 66
4052 Basel, Switzerland

This is a reprint of articles from the Special Issue published online in the open access journal *Coatings* (ISSN 2079-6412) (available at: https://www.mdpi.com/journal/coatings/special_issues/cement_building).

For citation purposes, cite each article independently as indicated on the article page online and as indicated below:

Lastname, A.A.; Lastname, B.B. Article Title. *Journal Name* **Year**, *Volume Number*, Page Range.

ISBN 978-3-7258-0277-7 (Hbk)
ISBN 978-3-7258-0278-4 (PDF)
doi.org/10.3390/books978-3-7258-0278-4

Contents

About the Editors

Peng Liu

Peng Liu is a professor and doctoral supervisor of the school of civil engineering in Central South University. He is engaged in research into concrete structure durability, concrete material and damage identification, ballastless track mechanical properties, prefabricated construction, and other topics, and he is credited with a series of innovative achievements. He has published more than 200 academic papers, 62 of which are included in SCI source journals, and 25 of which are included in EI. The applicant is in charge of two National Natural Science Youth Funds, one natural science fund in Hunan Province, one research innovation project for postgraduate students in Hunan Province, and one open sharing fund for valuable instruments and equipment in Central South University. He has participated in eight projects of the National Natural Science Foundation and China Railway. He served as a Chief Editor and Editorial Board Member for both domestic and foreign journals.

Lingkun Chen

Lingkun Chen received a Ph.D. in structural engineering from Central South University's School of Civil Engineering in 201206, studying high-speed rail bridge dynamics. Dr. Chen is a Postdoctoral Fellow at Edinburgh University School of Engineering, a Visiting Associate Professor at UCLA's Department of Civil and Environmental Engineering, and a Visiting Scholar at SUNY Buffalo's MCEER Lab. He is also a visiting scholar at the MCEER Laboratory at SUNY Buffalo, and a Specially Appointed Associate Professor (Faculty) at Yangzhou University. His research includes computational mechanics for seismic and wind resistance and dynamic bridge and tunnel models. He has studied advanced train–bridge–tunnel engineering system vibration and intelligent transportation theory, numerical modeling, and experimental dynamic testing.

Ying Chen

Ying Chen is a professor of the school of civil engineering in Central South University of Forestry and Technology. She is engaged in research into concrete structures and chemical materials and has published more than 30 academic papers. She was supported by the National Natural Science Youth Fund.

coatings

MDPI

Article

Experimental Analysis of Bearing Capacity of Basalt Fiber Reinforced Concrete Short Columns under Axial Compression

Xinzhong Wang [1,2], Yiming Yang [1,*], Rihua Yang [1] and Peng Liu [3,*]

[1] School of Civil Engineering, Hunan City University, Yiyang 413000, China; zhong811@126.com (X.W.); yrhzjh@163.com (R.Y.)
[2] Hunan Engineering Research Center of Structural Safety and Disaster Prevention for Urban Underground Infrastructure, Hunan City University, Yiyang 413000, China
[3] School of Civil Engineering, Central South University, Changsha 410013, China
[*] Correspondence: yangyiming@hncu.edu.cn (Y.Y.); 2015038@csu.edu.cn (P.L.); Tel.: +86-18173116706 (Y.Y.); +86-15116277646 (P.L.)

Abstract: Adding basalt fiber to concrete can improve the mechanical properties of concrete, and it is also one of the best ways to enhance the ultimate bearing capacity of concrete structure. In this paper, the construction performance and the compressive strength of basalt-fiber-reinforced concrete (BFRC) with five kinds of fiber lengths and eight kinds of fiber volume content subjected to an axial load are systematically investigated. The optimum fiber length and fiber volume content are obtained by comprehensively considering the construction performance and compressive strength. Moreover, the prediction model and finite element analysis method of the ultimate bearing capacity of basalt-fiber-reinforced concrete are developed. The results show that the optimum fiber length is about 12–24 mm and the fiber volume content is 0.15%. Adding an appropriate amount of basalt fiber can effectively improve the ultimate bearing capacity of concrete short columns, with maximum and average increases of 28% and 24%, respectively. In addition, the comparison with the experimental results shows that both the proposed prediction method and the finite element modeling method have good applicability, and they can be used to predict the ultimate bearing capacity of the BRFC short columns in practical engineering.

Keywords: basalt-fiber-reinforced concrete; concrete compressive strength; construction performance; ultimate bearing capacity; finite element analysis

Citation: Wang, X.; Yang, Y.; Yang, R.; Liu, P. Experimental Analysis of Bearing Capacity of Basalt Fiber Reinforced Concrete Short Columns under Axial Compression. *Coatings* **2022**, *12*, 654. https://doi.org/10.3390/coatings12050654

Academic Editor: Paolo Castaldo

Received: 15 April 2022
Accepted: 9 May 2022
Published: 11 May 2022

1. Introduction

Reinforced concrete (RC) short columns are some of the most basic components in structural engineering and are widely used in bridge piers, building frames, workshop columns, and other concrete structures. Their bearing capacity and durability are crucial to the safety, applicability, and economy of the entire structure. At present, they are effective at improving the mechanical properties of concrete by adding chopped fibers, such as steel fibers [1], glass fibers [2], synthetic fibers [3,4], basalt fibers [5], carbon fibers [6,7], etc. This is mainly because the appropriate fiber length and fiber volume contents can effectively combine with the weak matrix in concrete, so as to better control the development of internal cracks in concrete and finally improve the mechanical properties of concrete [8]. However, different types of fiber-reinforced concrete have different mechanical properties or application characteristics. For example, adding steel fiber to concrete can improve the toughness and tensile strength of concrete, but the processability and corrosion resistance of steel fiber are not good. Adding glass fiber into concrete can enhance the toughness of concrete, but its long-term strength will be reduced. Although carbon fiber has the characteristics of hardness and high strength, its use cost is high [9]. In view of the above problems, basalt fiber, which has the advantages of high tensile strength, high elastic modulus, corrosion resistance, good chemical stability, environmental protection, no pollution, and low cost, is gradually being studied [10–13]. Therefore, it is urgent to study the mechanical properties of the basalt-fiber-reinforced concret (BRFC) and its corresponding concrete members.

To date, researchers have mainly studied the reinforcement effect of basalt fiber and the mechanical properties of corresponding concrete. For example, both Ayub et al. [14] and Wang et al. [15] found that adding basalt fiber to concrete can improve its strength, and the maximum increase in compressive strength of basalt fiber concrete is 47.5%. According to previous research by Monaldo et al. [16], the tensile strength of concrete can be increased by 22.9% after 28 d by using 0.6% basalt fiber. A few scholars have determined the optimum content of basalt fiber based on the mechanical properties of concrete after adding basalt fiber. Based on the strength test of concrete with two kinds of fiber lengths and five kinds of fiber volume contents, Sun et al. [17] found that BFRC with 2% fiber volume content and 6 mm fiber length achieve the maximum strength. Tumadhir [18] believed that the optimum fiber volume content is about 0.3%, from the perspective of obtaining maximum compressive strength. However, most of the above studies obtain the optimal fiber length or fiber volume content based on the mechanical properties of specimens corresponding to a few fiber lengths and do not consider the construction performance of concrete. Therefore, it is urgent to carry out the mechanical property test of concrete under various fiber lengths and fiber volume contents and comprehensively determine the reasonable fiber parameters in combination with the construction performance.

Other than BFRC specimens, some scholars have studied the mechanical properties of basalt fiber concrete members, but most of them have focused on basalt fiber concrete beams. Based on the experimental research on BFRC beams, both Zhang [19] and Wang et al. [20] found the addition of basalt fiber can effectively prevent the development of cracks in reinforced concrete flexural members. Alnahhal and Aljidda [21] studied the flexural behavior and ultimate capacity of the BFRC beams experimentally and analytically based on the test results of 16 BFRC beams. At present, although a few scholars have conducted preliminary research on the performance of the BRFC short columns, such as Zhu [22], the research results on the ultimate bearing capacity of the BRFC short columns are highly deficient, and the relevant bearing capacity prediction methods have not been proposed. Therefore, it is necessary to further study the variation law of the bearing capacity of the BRFC short columns and propose corresponding prediction methods.

The objective of this study is to analyze the bearing capacity of the BRFC short columns under axial compression. First, the optimum fiber length and fiber volume content are obtained based on the construction performance and the concrete compressive strength. Then, the results of the axial compression test of the BRFC short columns are analyzed in depth. Finally, the theoretical and finite element calculation method of the ultimate bearing capacity of the BFRC short column are proposed, and their effectiveness is verified based on the test results. Among them, determining the optimum characteristic parameters of basalt fiber by comprehensively considering the construction and mechanical properties of concrete and proposing the assessment method of the ultimate bearing capacity of the BRFC short columns are the novelties of this paper.

2. Materials

The ordinary portland cement with the type of P.O 42.5 was selected. The crushed stone adopted two kinds of crushed stone of 5–10 mm and 10–25 mm, at a ratio of 2:3, to form a continuous secondary distribution. The corresponding crush value was 10.5, the sand fineness modulus was 2.85, and tap water was used. No water reducer was used during construction. The mix proportion data are shown in Table 1. The short cut basalt fiber produced by Zhejiang Hengdian Shijin Basalt Fiber Co., Ltd. Jinhua, China is adopted. Five lengths of basalt fibers are shown in Figure 1. The physical and mechanical properties of basalt fiber include the fiber diameter of 17 μm; the fiber density of 2650 kg/m^3; the tensile strength of 3000 MPa; the elastic modulus of 90 GPa; and fiber lengths of 12 mm, 18 mm, 24 mm, 30 mm, and 36 mm, respectively, as shown in Table 2.

Table 1. The mixed proportion of the concrete.

Target Intensity	Water Cement Ratio	Sand Ratio/%	Cement (kg/m^3)	Water (kg/m^3)	Sand (kg/m^3)	Crushed Stone (kg/m^3)
C30	0.55	34	355	195	703	1147

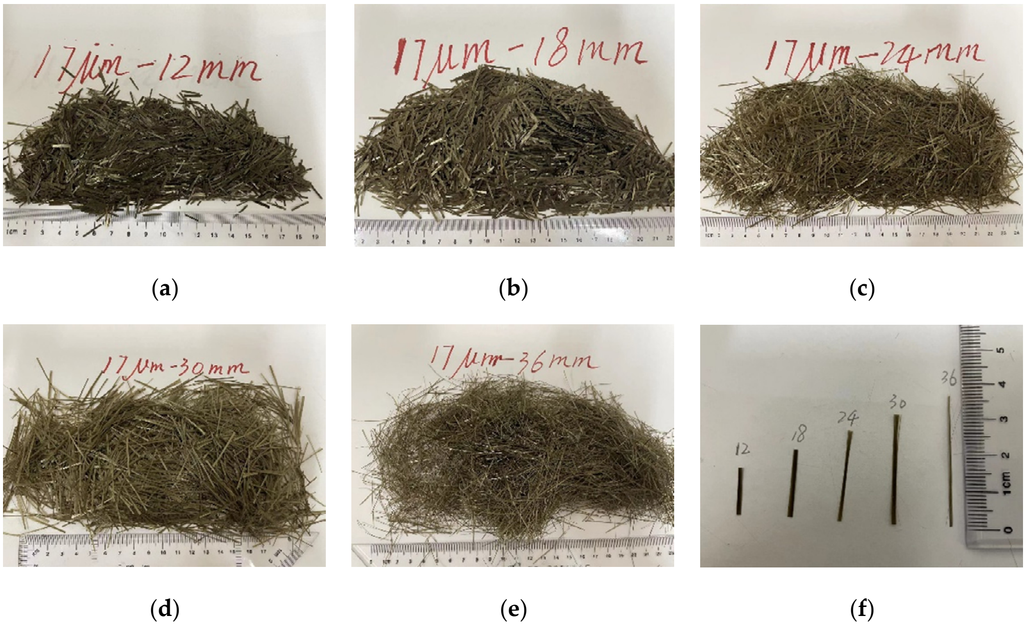

(**a**) (**b**) (**c**)

(**d**) (**e**) (**f**)

Figure 1. The five lengths of basalt fiber: (**a**) *L* = 12 mm; (**b**) *L* = 18 mm; (**c**) *L* = 24 mm; (**d**) *L* = 30 mm; and (**e**) *L* = 36 mm; and (**f**) a schematic diagram of the different fiber lengths.

Table 2. The physical and mechanical properties of the basalt fiber.

Index	Diameter (µm)	Length (mm)	Density (kg/m^3)	Tensile Strength (MPa)	Modulus of Elasticity (GPa)
Parameter	0.55	12/18/24/30/36	2650	3000	703

3. Construction Performance and Optimal Parameters of the BRFC

3.1. Construction Performance Test of the BRFC

The slump and expansion are selected here to analyze the construction performance of the BRFC, and the detailed test methods and procedures can be found in the Chinese specification of GB/T 50080-2016 [23]. A total of 13 groups of cube concrete specimens numbered ST1–ST13 are designed, and each group contains three parallel specimens. The STI, without adding fiber, is used as the reference specimen. Specimens ST2–ST6 are constructed using five kinds of basalt fibers with a fiber volume content of 0.15% and fiber lengths of 12 mm, 18 mm, 24 mm, 30 mm, and 36 mm. Five groups of the BRFC specimens with different fiber lengths are obtained to test the slump and expansion, and the average test results of each group of specimens are shown in Table 3. Specimens ST7–ST13 are constructed using seven kinds of basalt fibers with a fiber length of 12 mm and fiber volume contents of 0.075%, 0.10%, 0.15%, 0.20%, 0.25%, 0.30%, and 0.40%. The average test results of slump and expansion of ST7–ST13 are shown in Table 4. In order to better compare the difference between the slump and expansion of the BRFC and the ordinary concrete, the relative values of slump and relative expansion are calculated.

Table 3. The slump test results of the BRFC with different fiber lengths.

Group of Specimen	Fiber Length (mm)	Slump (mm)	Expansion (mm)	Relative Value of Slump (%)	Relative Value of Expansion (%)
ST1	0	30.4	61.5	100.0	100.0
ST2	12	27.8	53.4	91.4	86.8
ST3	18	25.7	48.6	84.5	79.0
ST4	24	23.2	43.2	76.3	70.2
ST5	30	24.7	47.1	81.2	76.6
ST6	36	26.8	49.4	85.1	80.3

Note: the relative value is the ratio of the measured value of the BRFC to that of the ordinary concrete.

Table 4. The slump test results of the BRFC with different fiber volume contents.

Group of Specimen	Fiber Volume Content (%)	Slump (mm)	Expansion (mm)	Relative Value of Slump (%)	Relative Value of Expansion (%)
ST1	0	30.4	61.5	100.0	100.0
ST7	0.075	28.2	56.3	92.8	91.5
ST8	0.10	27.8	54.2	91.4	88.1
ST9	0.15	25.4	52.1	83.6	84.7
ST10	0.20	23.1	43.4	76.0	70.6
ST11	0.25	20.2	38.3	66.4	62.3
ST12	0.30	18.3	32.4	60.2	52.7
ST13	0.40	15.8	30.1	52.0	48.9

As shown in Tables 3 and 4, the slump of the BRFC is lower than that of ordinary concrete. As the length of the added basalt fiber increases, the slump and expansion of the concrete first decreases and then increases. The slump and expansion of the BRFC is inversely correlated with the volume content of basalt fiber. This is due to the chaotic effect of basalt fibers, where a greater confinement effect on the concrete occurs with longer fiber and larger dosage and thus reduces the flow performance of the concrete. When the dosage is constant, the longer the fiber, the fewer the number of fibers, and thus the less restrictive the effect on the concrete.

3.2. Optimal Fiber Length and Fiber Volume Content

To further study the effect of fiber volume content on concrete compressive strength under different fiber lengths, we added BFRC specimens with a fiber length of 24 and fiber volume contents of 0, 0.075%, 0.10%, 0.15%, 0.20%, 0.25%, 0.30%, and 0.40% on the basis of ST1–ST13. Each case also contains three specimens. Then, based on the standard for the test methods of the mechanical properties of ordinary concrete (GB/T 50081-2002) [24], the 28 d compressive strength test is carried out on the cube concrete specimens with different fiber lengths and fiber volume contents, respectively. From the compressive failure modes of all specimens, the concrete specimens made an obvious cracking sound when they were damaged. The integrity of the BRFC specimen shows good resistance to damage regarding the rare cracking phenomenon. For the BFRC specimen that fails, the failure mode is brittle failure, although the characteristics of ductility are seen. The failure morphology of the BFRC specimens does not vary significantly with different fiber volume contents.

The compressive strength test results are presented in Figures 2 and 3. As indicated, with the increase of fiber length and fiber volume content, the concrete compressive strength basically conforms to the law of first increasing and then decreasing. This is mainly because under the action of short fiber length and small fiber volume content, the fiber distribution is more uniform, which can effectively prevent the generation of micro cracks in concrete, so as to improve the concrete compressive strength. For longer fiber length and larger fiber volume content, when they exceed a certain value, the fiber is easy to wind or agglomerate, which leads to the weakening of the connection effect between the fiber and the concrete matrix, thus leading to a failure to exert its reinforcing effect. It is worth noting that the average test strength of this group of concrete specimens with a fiber length of 36 mm does not comply with the above law, which may be caused by the good dispersion of fibers in the concrete. In addition, it can also be seen from Figures 2 and 3 that the concrete compressive strength is relatively high when the fiber length is about 12–24 mm and the fiber volume content is 0.15%. It is worth noting that although the construction performance cannot reach the optimal state under the effect of the above fiber length and content, it is sufficient to meet the normal construction needs. Thus, this paper focuses on the performance index of concrete compressive strength, and then obtains the optimal fiber length and fiber volume based on the analysis results.

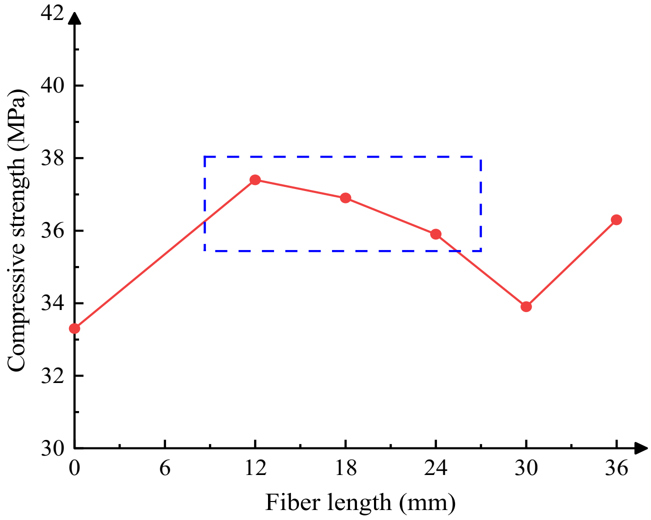

Figure 2. The 28 d compressive strength of the BRFC with different fiber lengths.

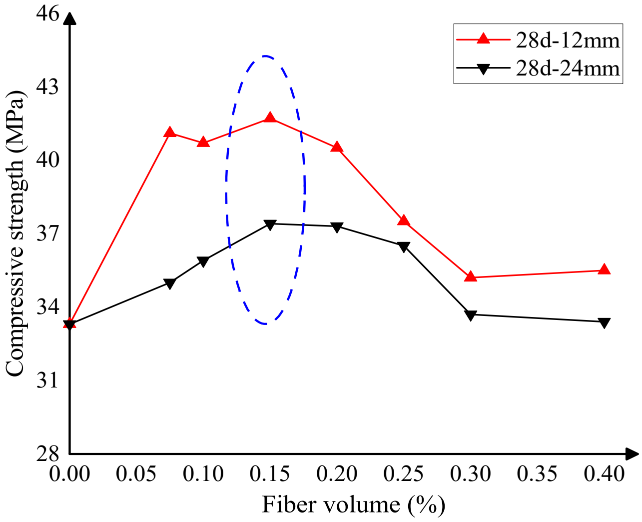

Figure 3. The compressive strength of the BRFC with different fiber volume contents.

4. Axial Compression Test of the BRFC Short Columns

4.1. Specimen Design

The analysis results of optimal design parameters in the previous section show that the optimal fiber length is 12–24 mm and the fiber volume content is 0.15%. As a result, in the subsequent experiments, only two fiber lengths of 12 mm and 18 mm, as well as fiber volume of 0.15%, are selected for the short column design. Here, a total of nine reinforced concrete short columns numbered S1–S9 are designed. Among them, the samples numbered S1–S3 are ordinary reinforced concrete short columns, and the samples numbered S4–S6 and S7–S9 are the BRFC short columns with fiber length of 12 mm and 18 mm, respectively. For all the BRFC short columns, the fiber volume content is selected as 0.15%, as previously described. The short column is featured with a cross-section size of width × height = 150 mm × 150 mm, and a slenderness ratio of 3.67 (length/width = 550/150 = 3.67), which is less than 8. The concrete cover is 10 mm. All short columns are arranged with four HRB400 threaded bars with a diameter of 12 mm as longitudinal reinforcement, and the stirrups are made of HRB335 plain round bars with a diameter of 6 mm and a spacing of 110 mm. The reinforcement configuration is provided in Figures 4 and 5. As required by GT/B 288.1-2010 [25], the yield and tensile strength of the two kinds of reinforcement are 486 MPa versus 360.1 MPa, and 590 MPa versus 570.4 MPa, respectively. Preloading is required before formal loading. Each short column is preloaded with 100 kN for 5 min to observe the reliability of the loading system and each measuring point. The formal loading is performed by the grading loading system. The loading of each stage is 50 kN, which is maintained for 2 min. When cracks or bulges appear, the loading is increased to 10 kN until the short column is damaged.

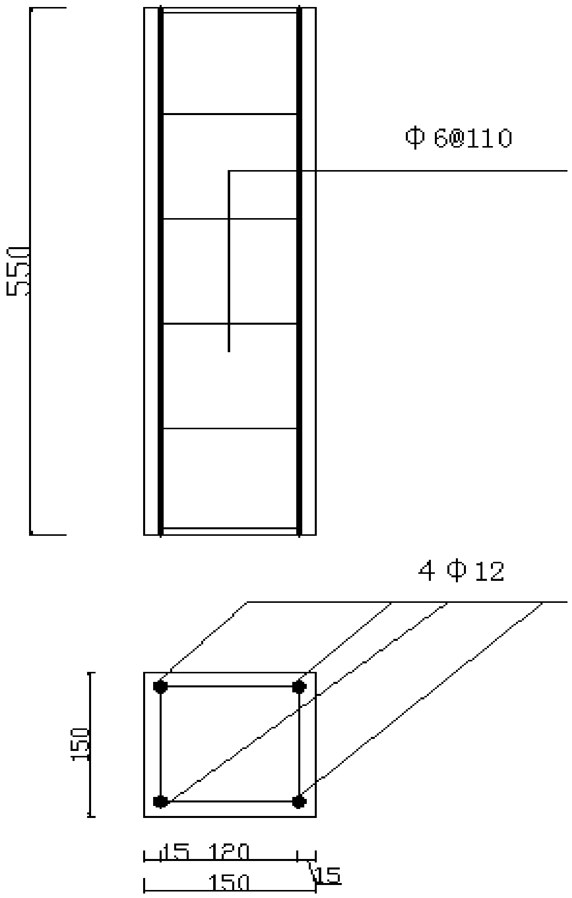

Figure 4. The structural dimension of the short column.

4.2. Experimental Phenomenon

During the loading process of all test short columns, no transverse cracks are found, while vertical cracks occur before failure. With the increase of load, the cracks develop gradually, the steel bars yield gradually, and the concrete is crushed and damaged. However, the stirrups remain intact when the short columns are damaged. The results reveal that the cracking of the BRFC short columns is significantly later than the ordinary RC short columns, which is also true for the failure load. The failure modes of the test specimens are shown in Figure 6.

Figure 5. The reinforcement of the short column.

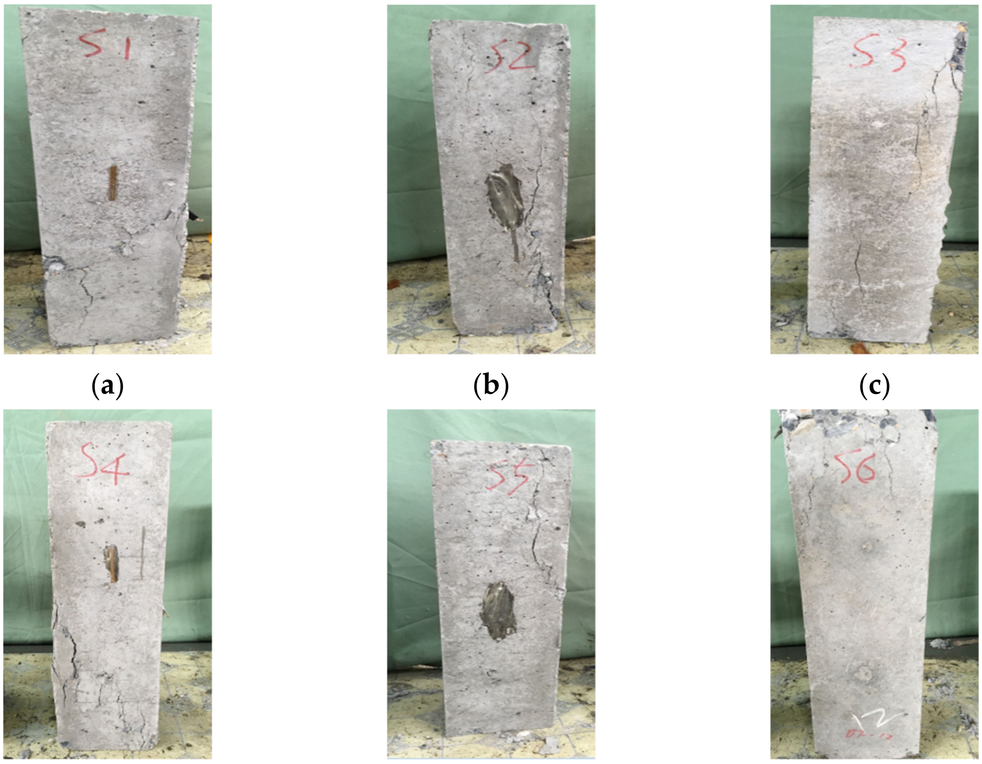

(**a**) (**b**) (**c**)

(**d**) (**e**) (**f**)

Figure 6. *Cont.*

(**g**) (**h**) (**i**)

Figure 6. The failure mode of the short columns: (**a**) S1; (**b**) S2; (**c**) S3; (**d**) S4; (**e**) S5; (**f**) S6; (**g**) S7; (**h**) S8; and (**i**) S9.

4.3. Results and Discussion

4.3.1. Ultimate Bearing Capacity

It can be seen in Table 5 that the ultimate bearing capacity (N_u) of the BRFCthe BRFC short columns is significantly higher than ordinary RC short columns. In particular, the maximum increase rate of axial compression ultimate bearing capacity is 28% for the BRFC short columns with fiber length of 12 mm and is 20% for the BRFC short columns with a fiber length of 18 mm. The average increase is 24%. The results highlight that basalt fiber is beneficial to the ultimate bearing capacity of reinforced concrete short columns. In addition, the average value of the ultimate bearing capacity of the BRFC short columns with a fiber length of 12 mm is 636.7 kN, which is 6.7% higher than the corresponding value (596.7 kN) with a fiber length of 18 mm. This conclusion matches the conclusion in Section 3.2 and other types of fibers reported in [26,27]. That is, when the fiber length exceeds a certain value, the reinforcement effect of the fibers will weaken.

Table 5. The axial compression test results of the BRFC short columns.

Specimen Number	Fiber Volume Content (%)	Fiber Length (mm)	N_u (kN)
S1	0	/	500
S2	0	/	500
S3	0	/	490
S4	0.15	12	640
S5	0.15	12	640
S6	0.15	12	630
S7	0.15	18	600
S8	0.15	18	590
S9	0.15	18	600

4.3.2. Load Strain Curve

The average value of the measured strain of the concrete and steel bar at the midpoint of each column is plotted in Figures 7 and 8. As indicated, the short columns are basically in the elastic stage at the beginning of loading and then enter the elastic–plastic stage with the increase of load. The concrete strain of the S1–S3 short columns reaches its peak around 0.0019, compared to a peak of around 0.0021 for the S4–S6 short columns. For the S7–S9 short columns, the peak value is about 0.0023. In addition to a slightly larger steel strain at peak value, the slope of the N-ε curve of the BRFC short columns in the elastic stage is also greater than that of the reinforced concrete short column.

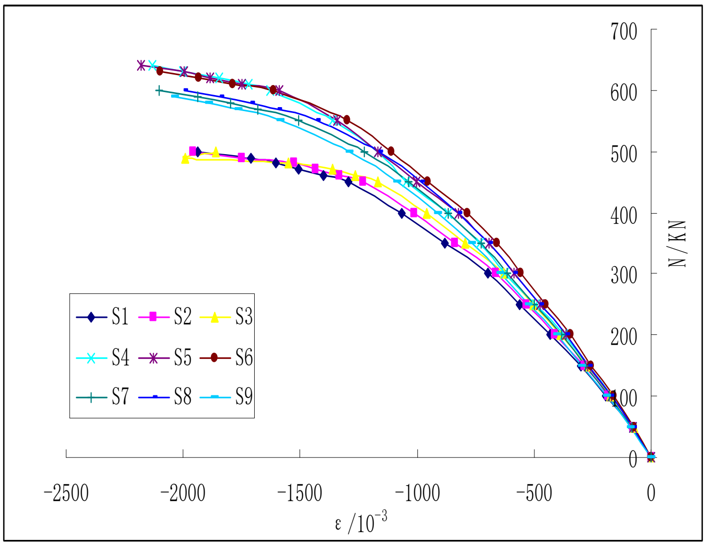

Figure 7. The average strain curve of the steel bars.

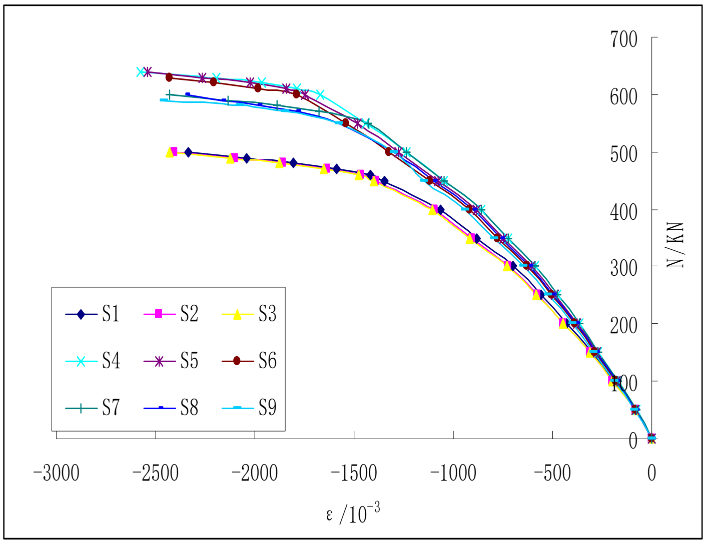

Figure 8. The average strain curve of the concrete.

Figure 9 shows the variation law of the vertical displacement at the top of each test short column. As indicated, the vertical displacement of the short column exhibits an obvious plastic stage with the increase of the load. The vertical displacement of the BRFC short columns is significantly greater than that of the ordinary RC short columns. More specifically, the vertical displacement of S4–S6 is the largest, followed by S7–S9, and is the smallest in S1–S3. Due to the restraint of fiber, the BFRC short column has greater displacement when the load reaches the peak value. From the elastic stage to elastic–plastic stage, the load displacement curve of the BRFC short columns is smoother and the plastic characteristics are obvious.

4.3.3. Influence Mechanism of Basalt Fiber

The chopped continuous basalt fiber is a hydrophilic material, which can be well combined with the cement-based material and form a spatial network structure between the concrete coarse aggregates. The structure encases the coarse aggregate and acts as a hindrance to aggregate movement during compression. Due to its high tensile strength, basalt fiber can provide circumferential restraint to resist transverse expansion when the specimen is compressed. As a result, its existence hinders the generation of a large number of microcracks or crosses countless microcracks. This makes the generation and development of cracks in the compression process require more energy. Thus, compared with the RC short columns, the ultimate bearing capacity of the BRFC short columns is significantly improved, and the initial crack time is also delayed. At the same time, when the basalt fiber concrete is equipped with an appropriate amount of stirrup and protective layer thickness, the anchorage ductility of the BRFC can be significantly increased. For the above reasons, the BFRC short column has higher ultimate bearing capacity and stronger deformation capacity.

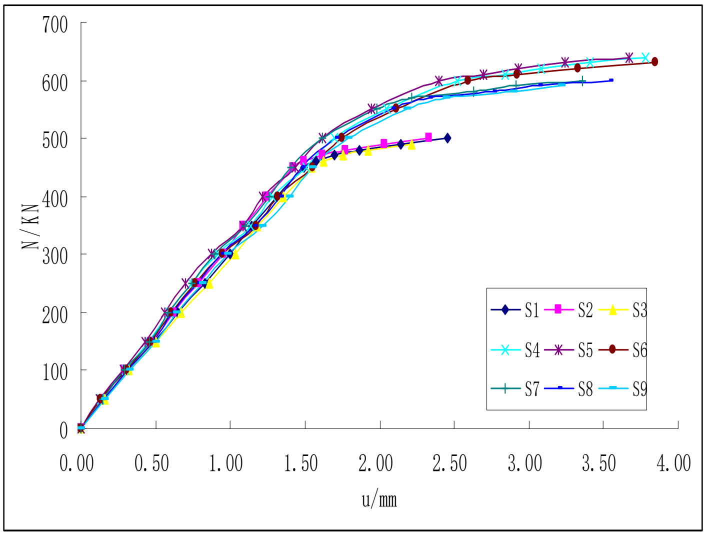

Figure 9. The load and the vertical displacement.

5. Calculation Method of Ultimate Bearing Capacity of BRFC Short Column

(1) Calculation method based on Standard approximate formula

In the specifications for the design of highway reinforced concrete and prestressed concrete bridges and culverts [28], the effect of the slenderness ratio is considered by solving the given calculation formula based on the sum of the maximum bearing capacity of concrete and steel bar. For the short columns with a rectangular cross-section, the calculation formula is as follows [28]:

$$N_u = 0.9\varphi(f_{cd}A + f'_{sd}A'_s) \tag{1}$$

where f_{cd} is the design value of the compressive strength of concrete, f'_{sd} is the design value of the yield strength of longitudinal reinforcement, A is the gross area of the cross section of a column, and A'_s is the area of longitudinal reinforcement. φ is the stability coefficient. The values or calculation methods of previous variables can be found in [28].

For the calculation of ultimate bearing capacity of the BRFC short column, the design value of concrete axial compressive strength in Equation (1) is replaced by the measured value of the compressive strength of the BRFC, and the other parameters remain unchanged. The calculation results are listed in Table 6.

(2) Finite element analysis method

The concrete constitutive model provided in [29] is adopted to calculate the ultimate bearing capacity of the BRFC short column, in which the peak strain, rising, and falling curves are modified by the measured strength of the BRFC. Moreover, considering the structural damage under the concrete stress, the elastic stiffness matrix is reduced and the correlation hardening is introduced into the constitutive model for the damage model of the ABAQUS software (version: 6.14.2), so as to better simulate the elastic–plastic behavior of the concrete in the loading. The C3D8R solid element and the T3D2 truss element are used for model concrete and reinforcement, respectively. The reference points are connected with the upper and lower surfaces by coupling. One end reference point is utilized to apply loads (with only one translational degree of freedom in the longitudinal direction of the column reserved), and another end reference point is used for boundary conditions (rigid junction). The reinforced concrete is connected by an embedded region and subject to load by a reference point according to the displacement. The point set is arranged at the loading point to facilitate reading the load in post-processing. A set of points is arranged at the core concrete to observe the relationship between the stress, the strain, and the load of the core concrete. The finite element model of the short column is illustrated in Figure 10, and the calculation results based on the finite element method are also shown in Table 6.

Table 6. The calculation value of the ultimate bearing capacity of the BRFC short column.

Specimen Number	Test Value (kN)	Calculation Value Based on Equation (1) (kN)	Calculation Value Based on Finite Element Analysis Method (kN)	η_1	η_2
S1	500	502	497	1.00	1.01
S2	500	502	497	1.00	1.01
S3	490	502	497	0.98	0.99
S4	640	630	637	1.02	1.00
S5	640	630	637	1.02	1.00
S6	630	630	637	1.00	0.99
S7	600	598	597	1.00	1.01
S8	590	598	597	0.99	0.99
S9	600	598	597	1.00	1.01

Note: η_1 = the ratio of the test value to the calculation value based on Equation (1); η_2 = the ratio of the test value to calculation value by the finite element analysis method.

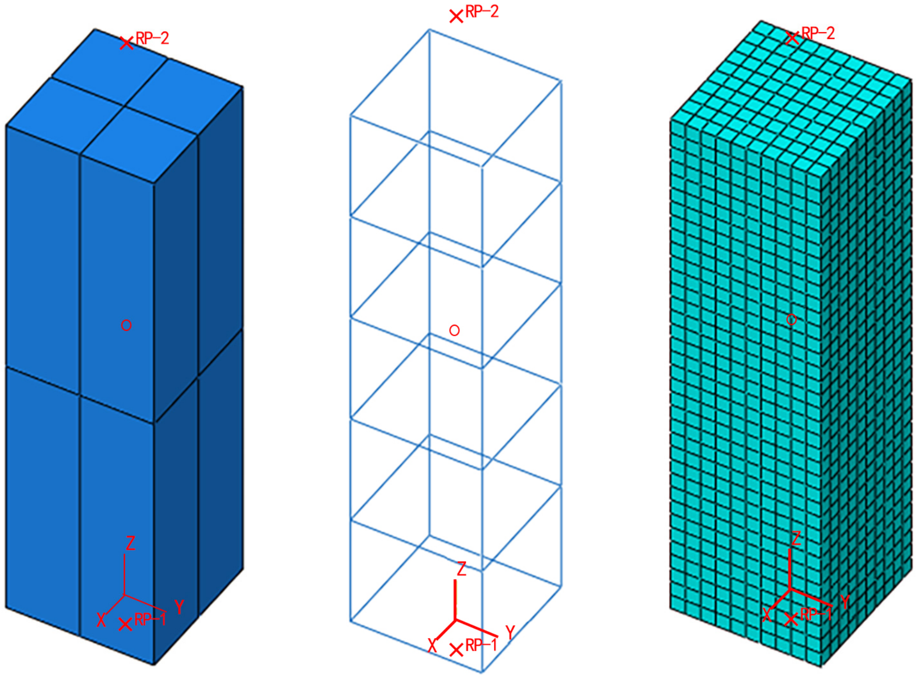

(**a**) (**b**) (**c**)

Figure 10. The finite element model of the short column: (**a**) the entity model; (**b**) the reinforcing element; and (**c**) the concrete unit.

As shown in Table 6, no matter which of the theoretical calculation methods based on the specification (i.e., Equation (1)) and the finite element simulation method is adopted, its calculation results are very consistent with the test results. More specifically, for the theoretical calculation method based on the specification, the calculated results of bearing capacity of the BRFC short columns are slightly lower than the measured values, while the corresponding results of the ordinary concrete short columns are slightly higher than the measured values. For the finite element simulation method, the calculation results of the BRFC and ordinary concrete short columns are mostly lower than the measured values. Although there is a certain deviation between the calculated results and the measured values, the maximum deviation is no more than 5%. This also verifies the feasibility of the bearing capacity prediction method of the BRFC short columns obtained by bringing the stress–strain relationship obtained from the test into the specification formula and the proposed finite element method. It is worth noting that due to the loading method of increasing 10 kN each time during the bearing capacity test of the concrete short columns (as described in Section 4.1), there is a certain deviation between the measured bearing capacity from the test and the actual bearing capacity of the concrete short columns. However, the deviation caused by this loading method is estimated to be between 1.5% and 2%. Therefore, it will not have a substantial impact on the effectiveness of the previous prediction methods.

6. Conclusions

In this paper, we obtained the optimum fiber length and fiber volume content based on the construction performance and the concrete compressive strength. The experimental phenomenon, the ultimate bearing capacity, the load strain curve, and the influence mechanism of basalt fiber are analyzed based on the results of the axial compression test of the BRFC short columns. In addition, the theoretical and finite element calculation method of the ultimate bearing capacity of the BRFC short column is proposed. The conclusions are summarized as follows:

(1) The optimum fiber length is about 12–24 mm, and the fiber volume content is 0.15%. In this case, the concrete has better slump and expansion properties and higher compressive strength.

(2) Adding appropriate basalt fiber can effectively improve the ultimate bearing capacity of the concrete short columns, and the maximum and average increases are 28% and 24%, respectively.

(3) No matter which of the theoretical calculation methods and the finite element simulation methods is adopted, its calculation results are very consistent with the test results. Even considering the deviation caused by the loading mode, the maximum deviation between the calculated results and the measured values is no more than 5%.

The limitation of this study is that only one diameter of basalt fiber is considered. In future research, the effect of the fiber diameter on the construction and mechanical properties of concrete needs to be further studied. Moreover, obtaining more measured data on the ultimate bearing capacity of the BRFC short columns to verify the effectiveness of the prediction method is also the focus of future research.

Author Contributions: Conceptualization, X.W.; methodology, X.W., R.Y. and P.L.; software, X.W.; validation, X.W. and Y.Y.; writing—original draft preparation, X.W. and Y.Y.; writing—review and editing, X.W., Y.Y., R.Y. and P.L.; supervision, R.Y. and P.L.; and funding acquisition, X.W., Y.Y. and R.Y. All authors have read and agreed to the published version of the manuscript.

Funding: This research was funded by the Hunan Provincial Natural Science Foundation of China (Grant Nos. 2021JJ50153, 2022JJ40024, and 2021JJ50156) and the Research Foundation of Education Bureau of Hunan Province (Grant Nos. 18A401, 21B0723, and 19C0343).

Institutional Review Board Statement: Not applicable.

Informed Consent Statement: Not applicable.

Data Availability Statement: Not applicable.

Acknowledgments: We would like to thank the anonymous reviewers and the editor for their valuable comments and remarks, which helped us to improve the original manuscript.

Conflicts of Interest: The authors declare that they have no known competing financial interests or personal relationships that could have influenced the work reported in this paper.

References

1. Iqbal, S.; Ali, A.; Holschemacher, K.; Bier, T.A. Mechanical properties of steel fiber reinforced high strength lightweight self-compacting concrete (SHLSCC). *Constr. Build. Mater.* **2015**, *98*, 325–333. [CrossRef]
2. Xin, H.; Liu, Y.; Mosallam, A.S.; He, J.; Du, A. Evaluation on material behaviors of pultruded glass fiber reinforced polymer (GFRP) laminates. *Compos. Struct.* **2017**, *182*, 283–300. [CrossRef]
3. Shaikh, F.U.A. Review of mechanical properties of short fibre reinforced geopolymer composites. *Constr. Build. Mater.* **2013**, *43*, 37–49. [CrossRef]
4. Hannawi, K.; Bian, H.; Prince-Agbodjan, W.; Raghavan, B. Effect of different types of fibers on the microstructure and the mechanical behavior of ultra-high performance fiber reinforced concretes. *Compos. Part B Eng.* **2016**, *86*, 214–220. [CrossRef]
5. Santarelli, M.L.; Sbardella, F.; Zuena, M.; Tirillo, J.; Sarasini, F. Basalt fiber reinforced natural hydraulic lime mortars: A potential bio-based material for restoration. *Mater. Des.* **2014**, *63*, 398–406. [CrossRef]
6. Bai, Y.; Nguyen, T.C.; Zhao, X.L.; Al-Mahaidi, R. Environment-assisted degradation of the bond between steel and carbon-fiber-reinforced polymer. *J. Mater. Civ. Eng.* **2014**, *26*, 04014054. [CrossRef]
7. Alabduljabbar, H.; Alyousef, R.; Mohammadhosseini, H.; Topper, T. Bond behavior of cleaned corroded lap spliced beams repaired with carbon fiber reinforced polymer sheets and partial depth repairs. *Crystals* **2020**, *10*, 1014. [CrossRef]
8. Meyyappan, P.L.; Carmichael, M.J. Studies on strength properties of basalt fiber reinforced concrete. *Mater. Today Proc.* **2021**, *43*, 2105–2108. [CrossRef]
9. Ramesh, B.; Eswari, S. Mechanical behaviour of basalt fibre reinforced concrete: An experimental study. *Mater. Today Proc.* **2021**, *43*, 2317–2322. [CrossRef]
10. Alaskar, A.; Albidah, A.; Alqarni, A.S.; Alyousef, R.; Mohammadhosseini, H. Performance evaluation of high-strength concrete reinforced with basalt fibers exposed to elevated temperatures. *J. Build. Eng.* **2021**, *35*, 102108. [CrossRef]
11. Branston, J.; Das, S.; Kenno, S.Y.; Taylor, C. Mechanical behaviour of basalt fibre reinforced concrete. *Constr. Build. Mater.* **2016**, *124*, 878–886. [CrossRef]
12. Wang, X.Z.; He, J.; Mosallam, A.S.; Li, C.; Xin, H. Effects of fiber length and volume on material properties and crack resistance of basalt fiber reinforced concrete (BFRC). *Adv. Mater. Sci. Eng.* **2019**, *4*, 7520549. [CrossRef]
13. Li, J.J.; Niu, J.G.; Wan, C.J.; Ling, X.Q.; Jin, Z.Y. Comparison of flexural property between high performance polypropylene fiber reinforced lightweight aggregate concrete and steel fiber reinforced lightweight aggregate concrete. *Constr. Build. Mater.* **2017**, *157*, 729–736. [CrossRef]
14. Ayub, T.; Shafifiq, N.; Khan, S.U. Compressive stress-strain behavior of HSFRC reinforced with basalt fibers. *J. Mater. Civ. Eng.* **2015**, *28*, 06015014. [CrossRef]
15. Wang, H.L.; Yuan, L.; Song, H. Experimental study on mechanical property of chopped basalt fiber reinforced concrete. *Build. Struct.* **2013**, *43*, 562–564.
16. Monaldo, E.; Nerilli, F.; Vairo, G. Basalt-based fiber-reinforced materials and structural applications in civil engineering. *Compos. Struct.* **2019**, *214*, 246–263. [CrossRef]
17. Sun, X.J.; Gao, Z.; Cao, P.; Zhou, C.J. Mechanical properties tests and multiscale numerical simulations for basalt fiber reinforced concrete. *Constr. Build. Mater.* **2019**, *202*, 58–72. [CrossRef]
18. Tumadhir, M. Thermal and mechanical properties of basalt fibre reinforced concrete. *Int. J. Civ. Environ. Eng.* **2013**, *7*, 334–337.
19. Zhang, Y. *Research on Basic Mechanical Properties of Chopped Basalt Fiber Reinforced Concrete*; Northeast Forestry University: Harbin, China, 2011.
20. Wang, J.; Luan, Y.; Ye, H.J. Experimental research on crack and deformation of basalt fiber reinforced concrete beams. *J. Archit. Civ. Eng.* **2016**, *33*, 76–81.
21. Alnahhal, W.; Aljidda, O. Flexural behavior of basalt fiber reinforced concrete beams with recycled concrete coarse aggregates. *Constr. Build. Mater.* **2018**, *169*, 165–178. [CrossRef]
22. Zhu, C.R. *Experimental Study on Fatigue of Basalt Fiber Reinforced Concrete Beams*; Inner Mongolia University of Technology: Hohhot, China, 2013.
23. *GB/T 50080-2016*; Standard for Test Method of Performance on Ordinary Fresh Concrete. MOHURD: Beijing, China, 2016.
24. *GB/T 50081-2002*; Standard for Test Method of Mechanical Properties on Ordinary Concrete. MOHURD: Beijing, China, 2002.
25. *GT/B288.1-2010*; Metallic Materials-Tensile Testing—Part 1, Method of Test at Room Temperature. National Technical Committee for Steel Standardization: Beijing, China, 2010.
26. Abirami, R.; Sangeetha, S.P. Study on fiber reinforced concrete beam-column connection—A review. *Mater. Today Proc.* **2020**, *33*, 415–419. [CrossRef]
27. Yoo, D.Y.; Banthia, N. Mechanical properties of ultra-high-performance fiber-reinforced concrete: A review. *Cem. Concr. Comp.* **2016**, *73*, 267–280. [CrossRef]
28. *JTG 3362-2018*; Specifications for Design of Highway Reinforced Concrete and Prestressed Concrete Bridges and Culverts. MOT: Beijing, China, 2018.
29. Shao, X.D.; Fan, W.; Huang, Z.Y. Application of ultra-high-performance concrete in engineering structures. *China Civ. Eng, J.* **2021**, *54*, 1–13.

coatings

Article

Long-Term Performance of Recycled Asphalt Pavement with Recycled Engine Oil Bottom Based on Accelerated Loading Test

Jin Li [1], Li Zhu [1,*], Miaozhang Yu [1], Shen Zuo [1], Xinzhuang Cui [1,2] and Peng Liu [3]

[1] School of Transportation Civil Engineering, Shandong Jiaotong University, Jinan 250357, China; sdzblijin@163.com (J.L.); 204153@sdjtu.edu.cn (M.Y.); zuoshen2006@163.com (S.Z.); cuixz@sdu.edu.cn (X.C.)
[2] School of Civil Engineering, Shandong University, Jinan 250061, China
[3] School of Civil Engineering, Central South University, Changsha 410083, China; liupeng868@csu.edu.cn
* Correspondence: 19011059@stu.sdjtu.edu.cn

Abstract: The practical performance of recycled asphalt obtained from recycled engine oil bottom (REOB) was evaluated by paving a test road of base asphalt and REOB-recycled asphalt mixture in a laboratory, where accelerated loading tests with 700,000 cycles were conducted. During accelerated loading, pavement temperature, layer bottom strain, pavement skid resistance, and rutting were monitored. The performance of pavement core material was tested after loading to analyze the index change of binder and the compaction degree of the mixture. The results show that the long-term anti-rutting ability of REOB-recycled asphalt pavement is approximately 10% higher than that of the base asphalt pavement, although the long-term anti-sliding force and anti-fatigue performance are poor. A developed model of rut with loading time can better predict the development trends of these parameters with loading cycles. The performance test of the pavement material after loading shows that 700,000 cycles can only degrade the performance of the test pavement, not damage it. The recycled asphalt pavement with 7% REOB has basically the same performance as the base asphalt under 700,000 cycles, indicating that REOB-recycled asphalt pavement can ensure basic road performance, while providing economic and environmental advantages. These results provide a reference for the application and form optimization of REOB-recycled asphalt pavement.

Keywords: recycled engine oil bottom; accelerated loading test; long-term performance; secondary aging

Citation: Li, J.; Zhu, L.; Yu, M.; Zuo, S.; Cui, X.; Liu, P. Long-Term Performance of Recycled Asphalt Pavement with Recycled Engine Oil Bottom Based on Accelerated Loading Test. *Coatings* **2022**, *12*, 522. https://doi.org/10.3390/coatings12040522

Academic Editor: Joaquim Carneiro

Received: 12 March 2022
Accepted: 8 April 2022
Published: 12 April 2022

1. Introduction

As a secondary by-product of engine oil, recycled engine oil bottom (REOB) presents a similar homology and compatibility with asphalt in production. The feasibility of using REOB as an asphalt modifier has previously been effectively verified [1–3]. Moreover, its product features, such as those related to economy and environmental protection, excellent performance, and waste treatment, have attracted global attention.

Golalipour et al. [4] studied ten types of oil-modified asphalt, including two kinds of recycled asphalt with REOB, and they found that both REOB blends that they tested were the least susceptible to aging among all of the oil blends they used. In addition, compared with the other eight kinds of oil, REOB most effectively improved the low-temperature performance of the binder. As early as 1998, Herrington et al. [5] paved a test road with a hot-recycled asphalt mixture produced by waste oil disintegration bottoms (WODB). After 57 months of testing, they found that all parts performed well, and the surface did not deteriorate, crack, or rut. Rostyslav et al. [6] used REOB-regenerated aging asphalt from different sources, before designing a mixture. They found that the permanent deformation and dynamic modulus of the REOB-modified asphalt mixture and the base asphalt mixture were similar when the performance grade (PG) of the mixture was consistent. Cooper et al. [7] designed five 12.5 mm asphalt mixtures for high-, medium-, and low-temperature performance tests using two base asphalts and three different REOB contents for recycled asphalt, and they established that the use of REOB can increase the temperature performance of the mixture.

REOB can effectively restore the performance of old asphalt, but during use, the low-temperature performance is often poor. Li et al. [8] tested the turning point temperature, freezing fracture temperature, and failure strength of asphalt mixtures mixed with 0%, 2.5%, 6.0%, and 15% REOB using the thermal stress restrained specimen test, and found that a high REOB content can have adverse effects on the low-temperature crack resistance of the asphalt mixture. Zaumanis et al. [9] studied aged REOB-recycled asphalt and discovered that its penetration index usually increases, which indicates that it is a more structural and brittle material and hence is easier to crack.

Related research has been conducted by means of basic indoor tests of materials. However, to date, no studies have been performed on the operation of REOB-recycled asphalt pavements owing to the long on-site test period required and high costs. In recent years, the simulated accelerated loading test method has received significant attention and is considered to be an important method for designing pavement based on service performance. This method is closest to simulating an actual traffic load in current research on road engineering.

In the history of pavement structural design, the AASHO full-scale pavement accelerated loading test is the most representative test method. By establishing the relationship between the service performance of a pavement structure and the cumulative number of axle loads in traffic, the AASHO test verified the mechanical design of pavement structure. This method also opened up new ways to study asphalt pavement. Sirin et al. [10] conducted tests on five test sections using a heavy vehicle simulator to predict pavement rutting in Florida. The five test sections adopted different running directions and different combinations of loading wheels. The results showed that when evaluating the rutting resistance of pavement under the traffic and climate conditions in Florida, driving the loading wheels in one direction is more effective than two-way driving. Choubane et al. [11] used accelerated loading test equipment to evaluate the long-term performance of high-performance asphalt pavement with either coarse or fine aggregate gradation. They found that fine aggregate asphalt pavement provides superior rutting resistance than coarse aggregate material. Theys et al. [12] proposed a semi-empirical–semi-mechanical subgrade design model using subgrade deflection as a road design standard instead of the generally accepted vertical stress by conducting a large number of heavy-duty simulator (HVS) tests in California, USA. Hugo [13], a researcher in South Africa, developed the fourth generation of the previous pavement accelerated loading simulation systems of MLS and MMLS and successfully applied it to evaluate pavement fatigue performance. Accelerated loading tests were carried out on cement- and lime-stabilized sandy soil base in Mozambique. During the test, indexes such as surface cracks, grooves, pits, dynamic deflection, pavement flatness, and rutting were examined. At the same time, the long-term performance of asphalt pavement was investigated by testing the mechanical properties of materials using indoor tests, and the fatigue performance laws of the asphalt mixtures were obtained. Clearly, accelerated loading tests can provide many useful conclusions to guide the design of pavement structures and materials.

In this study, pavement performance is compared and analyzed on the basis of the material and structural form by paving base asphalt and REOB-recycled asphalt roads. Accelerated loading equipment was used to quickly accumulate load on the test section to simulate the real service environment of pavement. Pavement performance in the loading process was monitored, which provides the basis for the research and application development of REOB-recycled asphalt pavement.

2. Materials and Methods

2.1. REOB Regenerant

The Recycled Engine Oil Bottom (REOB) selected in this test comes from a qualified recycled oil treatment plant in Zibo, Shandong Province. Its main treatment process is: filter waste oil—membrane distillation—uronic refining—clay process.

The United States of America state the requirements for REOB quality control in the "Standard specification for refined engine oil bottoms/vacuum tower asphalt extender (VTAE)" promulgated in 2017 [14]. Based on this specification, as well as the similarity between REOB and asphalt compatibility, the related physical indicators and components of REOB were tested, and the results are shown in Table 1.

Table 1. Basic technical properties of REOB.

Physical Properties	**Ash Content/%**	**Relative Density**	**60 °C Viscosity/Cst**	**Flash Point/°C**	**Thin Film Oven Test**	
					Viscosity Ratio	**Quality Change/%**
	3.7	0.911	484	247	1.69	−1.284
Four-component analysis		**Asphaltene/%**	**Colloid/%**	**Aromatics/%**	**Saturation/%**	
		0.2	17.7	81.2	0.9	

In this study, a representative REOB from factory machinery was selected. According to the results of testing the performance of this REOB shown in Table 1, it meets the following functions and characteristics of a regenerant:

(1) Security. The flash point index reflects its construction safety. If this value is too low, it is a fire hazard under high-temperature operation. After testing, the flash point value of REOB is 247 °C, and the flash point value as asphalt regeneration agent meets the requirements of construction safety standards shall not be less than 220 °C.

(2) Components. Aromatic components mainly play the role of dissolving and dispersing asphaltene in aged asphalt; thus, regenerants require a large amount of aromatic components. The four-component analysis revealed that the aromatic content of the REOB regenerant is high at 81.2%, which can supplement the aromatic content missing in the asphalt aging process, while the saturated content also meets the specification requirements of $\leq$30% regenerant.

(3) Anti-aging properties. The viscosity ratio and mass change reflect the increase in viscosity and the decrease in mass after the film is heated, respectively. The smaller these two values, the better the anti-aging properties of the material. Owing to the high content of light components in REOB, it easily volatilizes at high temperature. Certain amounts of mass loss and viscosity increase are inevitable, but they are within the specification and controllable ranges, namely, a viscosity ratio $\leq$3 and a mass loss from −4% to 4%.

2.2. Asphalt

This test design required two kinds of asphalt: base asphalt and recycled asphalt. The conventional base binder was A-grade 70# petroleum asphalt with a performance classification of PG64-28. Recycled asphalt was prepared by adding the REOB regenerant to the aged asphalt. The aged asphalt was prepared as follows: The base asphalt was weighed to 600 g and poured into a 40 cm × 30 cm × 4.8 cm iron plate. The iron plate with the base asphalt was transferred into a 163 °C oven and stirred every 2 h to ensure even heating and aging of the asphalt. The aging time was prolonged to 48 h. In this way, one oven could perform the aging test of at least 3.6 kg asphalt, thereby significantly improving the efficiency of aging asphalt preparation [15]. The results of our previous research showed that the ideal regeneration effect was obtained when the REOB content was approximately 7% [16]. The specific preparation method of recycled asphalt is as follows: 7% REOB was added to the aged base asphalt at 160 °C for mixing, followed by shearing at 3000 r/min at 165 ± 5 °C for 30 min. Thereafter, it was placed in an oven at 160 °C for 1 h. The performance of the different types of asphalt used in the test is shown in Table 2.

Table 2. Asphalt test parameters.

Test Index		Unit	Base Asphalt	Aged Asphalt	7% REOB-Recycled Asphalt
			Test Parameters		
Penetration (25 °C)		0.1 mm	72.7	29	71
Softening point		°C	49.7	68	51.9
Ductility (10 °C, 5 cm/min)		cm	56.4	0.6	50.0
Relative density (25 °C)		/	1.024	1.036	1.022
Viscosity (135 °C)		Cst	338.2	1651.5	391
RTFOT (163 °C, 5 h)	Mass loss	%	−0.17	−0.09	−0.18
	Residual Penetration ratio	%	79.1	67.0	80.2
	Residual ductility (10 °C)	cm	21.2	0	16.2

Taking the three index values of base asphalt as a reference, the penetration, softening point, and ductility of the aged asphalt could be restored to 97.7%, 104.4%, and 88.7%, respectively, after adding 7% REOB, which could achieve the complete regeneration of the aged asphalt.

2.3. Asphalt Mixture

The AC-13 and AC-20 asphalt mixtures were used for the upper and lower layers of the test road, respectively, and the use of the binder is shown in Figure 1. The new coarse and fine aggregates used in the mixture were all obtained from the Zhang Qiu limestone quarry in Jinan. Among the components, the recycled asphalt surface is made of REOB-recycled asphalt and new asphalt as the binder, which was then mixed with the new and old aggregate to yield a mixture. The Reclaimed Asphalt Pavement (RAP) in the recycled pavement was taken from the asphalt concrete surface course of an expressway in Shandong, in which the content of RAP was 40%. Calculations using the Marshall design method indicated that the oil–stone ratio was 5.0%, and the gradation designs are shown in Figures 1 and 2.

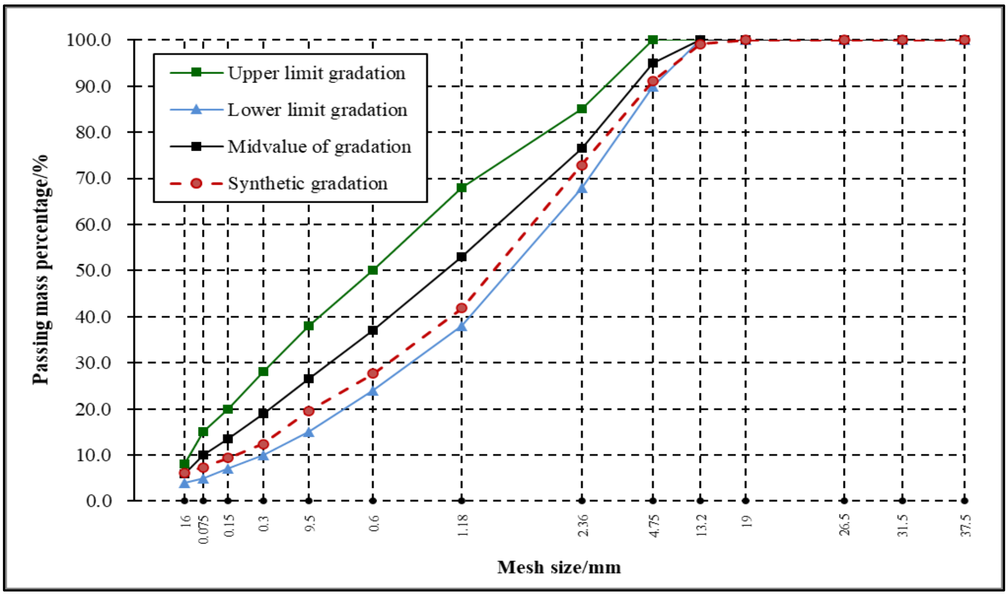

Figure 1. AC-13 aggregate gradation curve.

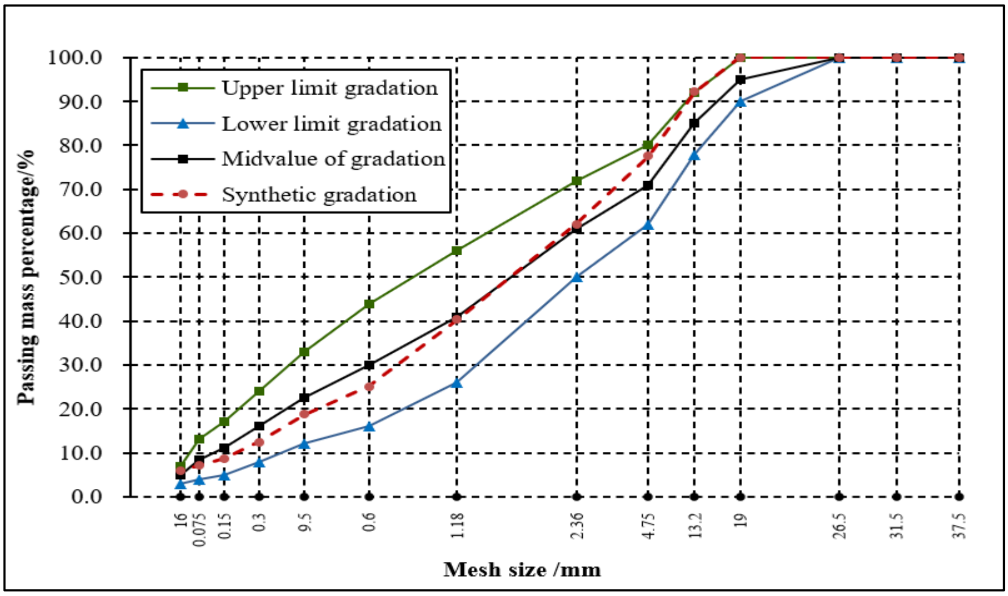

Figure 2. AC-20 aggregate gradation curve.

2.4. Test Plan

An accelerated loading test of the three pavement structures was conducted to compare the performance of different combinations of pavement. Five mixing pots of Shandong Provincial Key Laboratory of Asphalt Pavement Structure were used for mixing the mixture, and each mixing pot mixed 20 kg asphalt mixture each time. After research, it was decided that the temperature of the mixture that gets mixed from the completion to the paving stage be maintained by a large tray oven containing 1000 kg hot material in the Key laboratory of Asphalt Pavement structure in Shandong Province for hot material insulation process. The insulation temperature was uniformly set to 150 °C, which is conducive to the paving work of the test section.

This study was carried out according to the following flow chart, as shown in Figure 3. It involved two parts: (1) testing the pavement performance under loading and (2) extracting asphalt materials from the pavement after loading to examine changes in the properties of REOB-recycled asphalt.

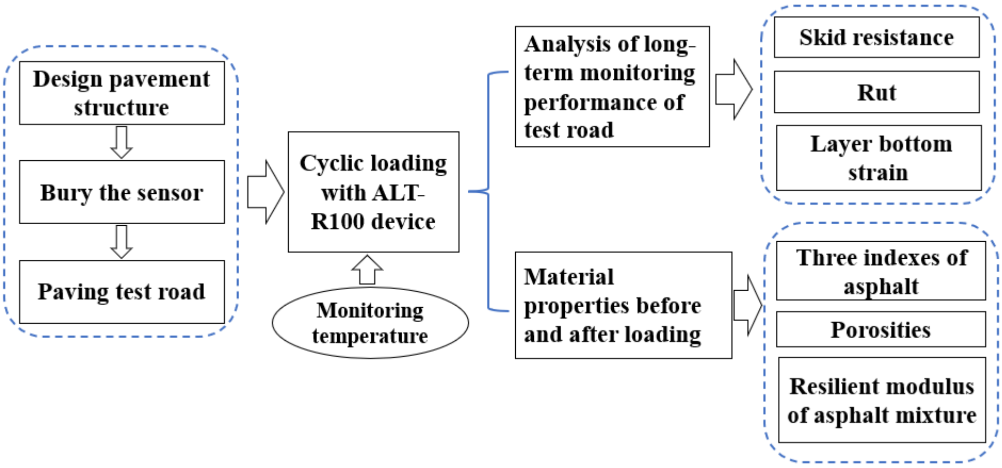

Figure 3. Flow chart of the accelerated loading test.

As shown in the paving plan in Figure 4, the upper and lower layers of the test pavement were made of dense-graded asphalt concrete. Fine-grained AC-13 gradation was selected for the upper layer, and medium-grained AC-20 gradation selected for the lower layer. The base layer cement stabilized the macadam base. The width and length of the pavement were designed to be 100 and 400 cm, respectively. To accelerate the destruction of the test road, the upper and lower layers were designed to be 4 and 6 cm thick, respectively. The lower layers of Pavements I and II were both an AC-20 base asphalt mixture However, the asphalt binders in their respective upper layers were different, namely, base asphalt and REOB-recycled asphalt, respectively. Using these materials in the upper layer enabled studying the performance difference between the REOB-recycled asphalt mixture and ordinary base asphalt concrete pavement. Meanwhile, Pavements II and III used base asphalt and REOB-recycled asphalt in the lower layer, respectively, which allowed investigating the long-term performance of pavement with REOB-recycled asphalt mixture in the underlying layer.

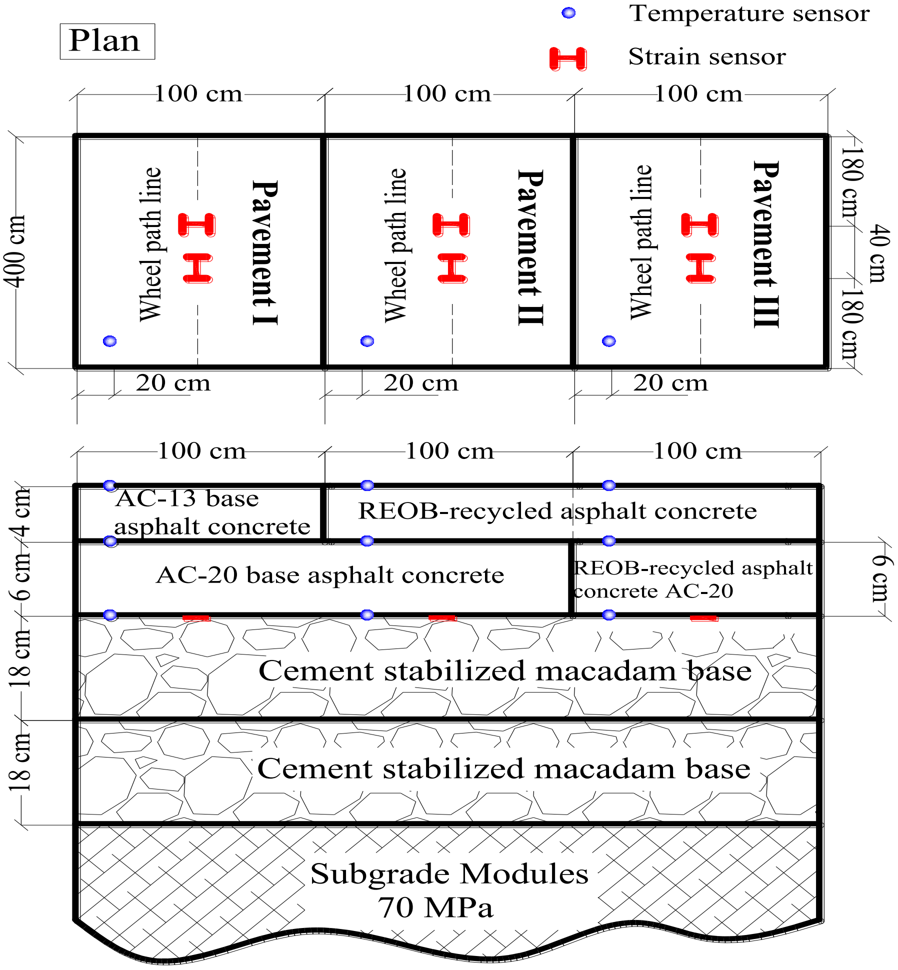

Figure 4. Road structure and sensor location map.

The equipment used in this model test was a small rotary road acceleration loading system (ALT-R100) independently developed by Shandong Jiaotong University. The equipment could be used in a three-wheel unidirectional cycle loading method, and the maximum loading speed reached 35 km/h (15,000 cycles/h). This approach was convenient to use and could quickly simulate the actual traffic load and environmental damage to the road surface in a short time. The reasonable structure and damage mechanism in the life cycle of a road could be effectively and accurately analyzed by monitoring the road conditions and test parameters during the loading process.

To accelerate the destruction speed of the test road, the upper and lower layers were designed to be 4 and 6 cm thick, respectively. The full-scale asphalt test pavement structure was paved with a 100 KN cyclic loading mode with a driving speed of 22 km/h, and the effective loading length of the equipment was 100 cm. To reduce the impact of environmental factors during the loading process, a reciprocating cyclic loading method was adopted: Pavement I was loaded for 50,000 cycles, translated to the loading area of Pavement II and loaded for 50,000 cycles, and then translated to the loading area of Pavement III and loaded for 50,000 cycles. This was the reciprocating cycle loading method. During the loading process, the pavement temperature, layer bottom strain, pavement friction coefficient, and rut depth were monitored regularly and at fixed points.

(1) Pavement temperature: Temperature monitoring was conducted using an embedded thermocouple temperature sensor with a measurement range able to reach −200–500 °C, while the accuracy reached 0.002 °C. A temperature sensor was embedded at the top of the upper layer, the bottom of the upper layer (the top of the lower layer), and the bottom of the lower layer of the three pavements of the test road in the form of pre-burying, which recorded temperature values every 1 h. The layout position is shown in Figure 4. Meanwhile, the indoor temperature of the corresponding time was recorded using a mercury thermometer.

(2) Layer bottom strain: After comparison, the layer bottom strain monitor was used to select the KM-100HAS "I"-shaped resistance strain gauge produced by Japan's TML company, which provided superior comprehensive performance. The three-dimensional position where the strain sensor was buried was located between the top of the cement-stabilized gravel layer and the bottom of the lower layer along the direction of the wheel track belt, and between the bottom of the upper layer and the top of the lower layer. The strain response data were collected every 10,000 cycles with a 100 Hz acquisition frequency, and the acquisition time was approximately 2 min/12 loading cycles. The strain data acquisition system included a DC-004P dynamic strain gauge that was made by Tokyo Measuring Instruments Lab in Japan, and visual log DC-7004P control software to collect and analyze the strain data.

(3) Anti-sliding performance: Each wheel of the loading equipment was rolled for 5000 cycles, and the friction coefficient data were collected once by a pendulum friction meter, which was the British Pendulum Number (BPN) condition value, representing the anti-sliding ability of the pavement. The friction coefficient of the asphalt pavement was monitored by setting three detection points along the wheel trace direction, as shown in Figure 5a.

(4) Anti-rutting performance: A laser car that was independently developed by Shandong Jiaotong University was used for the rutting test at points A and B in Figure 5. The test range of the laser car was 1 m^2. The rutting data were collected after every 5000 loading cycles, and the rutting of a cross-section was tested every 0.2 m, as shown in Figure 5b.

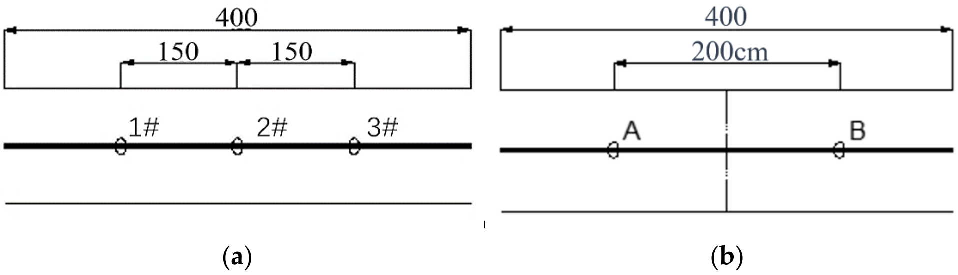

(**a**) (**b**)

Figure 5. Layout of monitoring points. (**a**) Layout of friction coefficient monitoring points; (**b**) Layout of track monitoring points.

3. Results and Discussion

3.1. Analysis of Long-Term Monitoring Performance of Test Road

3.1.1. Temperature

The relationship curve between the loading cycles and temperature of the three types of pavements is shown in Figure 6, with 20,000 loading cycles as a statistical unit. Owing to the reciprocating loading mode of the three pavements, the difference in pavement temperature among the pavements was relatively small. However, owing to the large time span from summer to autumn, the overall temperature showed a downward trend with decreasing room temperature (15–35 °C), and the temperature dropped sharply after loading for 420,000 cycles. Therefore, the experiment was divided into two stages based on the temperature gradient.

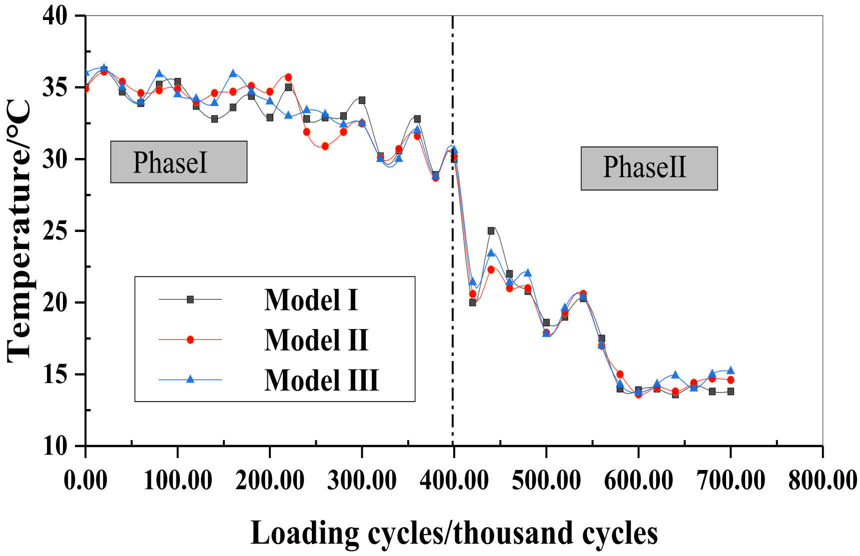

Figure 6. Temperature curve during loading.

Stage I: The average temperature of asphalt pavement was 33.3 °C, and the total number of loading cycles was 400,000.

Stage II: The average temperature of asphalt pavement was 17.4 °C, and the total loading number of loading cycles was 300,000.

3.1.2. Skid Resistance

The measured BPN values were all obtained for conventional dry road, and the thickness of the upper layer of the test road was 4 cm; thus, the measured values did not require temperature correction. The decay law of the friction coefficient of the three types of asphalt pavement structures under accelerated loading was obtained using a statistical method, as shown in Figure 7.

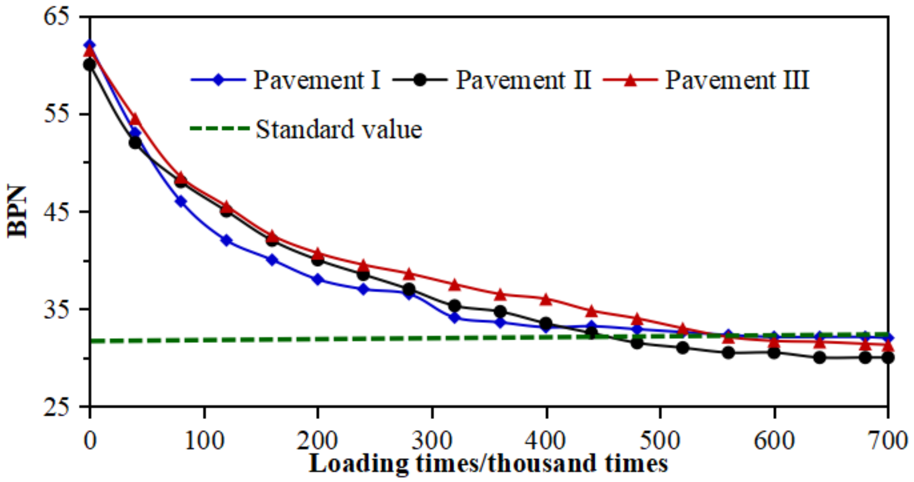

Figure 7. Variation law of pavement friction coefficient.

The initial friction coefficients of the three accelerated loading test sections were all above 60. The friction coefficient decreased gradually with increasing loading cycles and decreased rapidly in the early stage of loading. After loading for 400,000 cycles, the pendulum value dropped below 40, which is below 60% of the initial value, and Pavement I exhibited the fastest rate of decrease, falling to approximately 55% of the initial value. The difference in the skid-resistance performance of the three types of pavement was small, which indicates that REOB-recycled asphalt will not reduce the skid-resistance performance of asphalt pavement, which is mainly controlled by the characteristics of the aggregate and gradation. The pendulum value decreased slowly and tended to gradually stabilize after 400,000 loading cycles until the end of the test. The skid-resistance performance of Pavements II and III decayed rapidly. Their BPN values were lower than those of Pavement I at 440,000 and 560,000 loading cycles, respectively, and lower than the required value of 32 for class 2. Further, these were below highway maintenance specifications at 600,000 and 480,000 loading cycles, respectively.

Therefore, the skid-resistance performance of conventional asphalt mixture pavement is inferior to that of REOB-recycled asphalt mixture pavement in the short term because of the high viscosity of recycled asphalt, which will also cause a more serious degree of rutting in Pavement I compared to other pavements. With the increasing number of loading cycles, from the perspective of long-term pavement service, the anti-sliding performance of conventional asphalt mixture pavement is better than that of REOB-recycled asphalt mixture pavement.

3.1.3. Rut

The rut formed on the test road is typically unstable (flow type), owing to the reciprocating rolling action of the ALT-R100 system. Deformation curve of wheel rut section after 700,000 times of loading is shown in Figure 8a. Figure 8b shows the overall evolution of the road ruts of the three different pavement structures under the action of loading and rolling at room temperature.

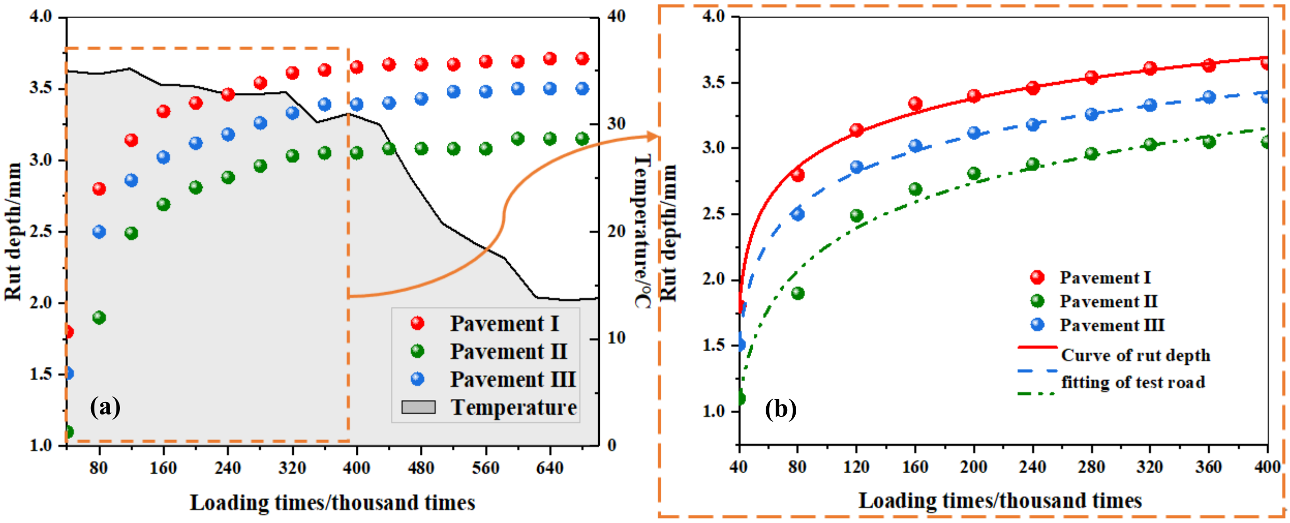

Figure 8. Variation law of pavement rutting. (**a**) Deformation curve of wheel rut section after 700,000 times of loading; (**b**) The overall evolution of the road ruts of the three different pavement structures under the action of loading and rolling at room temperature.

The tests reveal several results:

(1) The overall rutting shapes of the three pavement structures are similar after cycle loading, as shown in Figure 9. The rutting depths of the three types of pavement structures developed rapidly before 220,000 loading cycles with the acceleration loading system; at 160,000 loading cycles, the first inflection point appears in the

rutting development, and the second inflection point appears at 220,000 loading cycles. However, after 220,000 loading cycles, the rutting depth tended to increase at a slower rate and remained almost unchanged after 400,000 loading cycles. Because the compaction of the aggregate and the discharge of air were relatively fast, the pavement could be in the stage of aggregate compaction before 220,000 loading cycles.

(2) The gray area shown in Figure 8 is the change in room temperature; hence, higher room temperature and road temperature also played a certain role in promoting the generation of rutting, causing a greater change in the early rutting depth. At the end of 700,000 loading tests, the rutting depths of the first, second, and third structural pavements were 3.7, 3.2, and 3.5 mm, respectively.

(3) Compared with structural Pavements I and II, which had the same form of their lower layer, the anti-rutting ability of recycled Pavement II was approximately 13% better than that of conventional pavement "Pavement I," when the upper layer of asphalt mixture is comprised of 4 cm of base asphalt AC-13 and REOB-recycled asphalt AC-13, respectively. The upper and lower layers of Pavement III contained the recycled mixture, whereas Pavement II only contained the recycled mixture in the upper layer and showed better anti-rutting performance than Pavement III. Comprehensive analysis shows that the REOB-recycled asphalt mixture has good anti-rutting performance when used in the upper layer.

(4) At high temperature conditions, above 30 °C, damage is related to rutting but not fatigue. At intermediate temperature conditions, below 20 °C, damage is related to fatigue, and the ruts change slightly and gradually flatten out. According to the above test data results and relevant research data, the rutting changes with the loading cycles in a logarithmic form [17], and the regression curve above 30 °C (the first 400,000 loads) is shown in Figure 8b. The fitting model is shown in Table 3. The correlation coefficient R^2 of the fitted logarithmic curve is over 0.98, indicating that the fitted function is reliable.

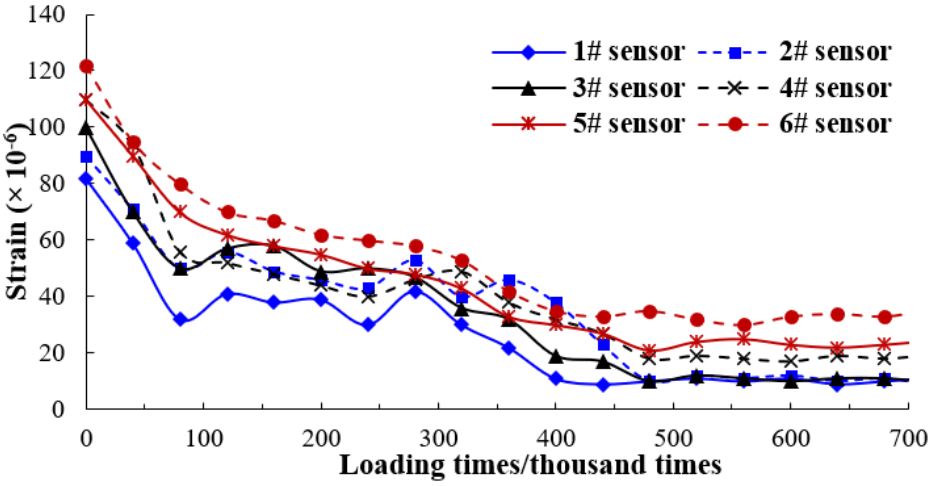

Figure 9. Relationship between layer bottom strain of each sensor and loading cycles.

Table 3. Rutting prediction Pavements of three pavement structures.

Pavement Structure Model	Rutting Prediction Model	R^2
Structural Pavement I	rut = 0.38959 ln(N − 3.71988) + 2.9481	0.99598
Structural Pavement II	rut = 0.41277 ln(N − 3.65412) + 1.94652	0.99743
Structural Pavement III	rut = 0.52695 ln(N − 3.27094) + 1.25467	0.98152

Where: rut is rutting depth, N is the number of loading cycles.

3.1.4. Layer Bottom Strain

An effective method to study the stress and fatigue of asphalt pavement is to analyze the layer bottom strain, as many problems with pavement are closely related to the layer bottom strain [18].

During the accelerated loading test, sensors No. 1, No. 3, and No. 5 were transverse strain sensors of Pavements I, II, and III, respectively, and sensors No. 2, No. 4, and No. 6 were longitudinal strain sensors. According to the monitoring results, the relationship between the layer bottom strain and loading time is shown in Figure 9.

(1) As seen in Figure 9, the change trends of the transverse and longitudinal sensors of each pavement structure are consistent, whereas the numerical values differ. The initial strain values of Pavements I, II, and III are above 80×10^{-6}, 100×10^{-6}, and 110×10^{-6}, respectively. After 80,000 loads, these values drop to approximately 40×10^{-6}, 50×10^{-6}, and 70×10^{-6}, respectively. At this time, the strain changes are related to the high temperature and compaction of the mixture. As there is only a limited number of load cycles for intermediate temperatures, fatigue does not occur yet, and thereafter, the strain is only related to the temperature conditions.

(2) The strain change during the entire loading process may be divided into three stages. In the initial stage of loading, the temperature is relatively high, in which the layer bottom strain is also high. In the middle stage of loading, the temperature drops sharply from 350,000 to 500,000 loading cycles. With the long-term effect of the load, the strain decreases gradually. Before the end of loading, from 500,000 to 700,000 loading cycles, the temperature drops, causing a halt in the change in strain value.

(3) In the later stage of loading (from 500,000 to 700,000 cycles), the strain values of Pavements I, II, and III are stable at $9\text{–}11 \times 10^{-6}$, $10\text{–}19 \times 10^{-6}$ and $21\text{–}33 \times 10^{-6}$, respectively. The strain at the bottom of the third layer of the pavement is at a relatively high level compared to other pavements. This result shows that the pavement using REOB-recycled asphalt mixture on both the upper and lower layers has less sufficient mechanical properties than the pavement using this asphalt mixture only in the upper layer and the conventional asphalt pavement in the lower one. Excessive strain could directly cause pavement damage, and the anti-fatigue performance of the third layer of the pavement is poor.

Studies have been conducted on the fatigue performance of asphalt mixtures in different ways, and different fatigue pavements of asphalt mixtures have been proposed.

The British Transport and Road Research Institute has proposed fatigue design standard Formulas (1) and (2) [19,20] for asphalt pavement, with a reliability of 85% and an equivalent temperature of 20 °C.

$$N_f = 1.66 \times 10^{-10} \times (\varepsilon_t)^{-4.32} (\mathrm{AC}) \tag{1}$$

and

$$N_f = 4.169 \times 10^{-10} \times (\varepsilon_t)^{-4.16}\ (\mathrm{AM}). \tag{2}$$

Elliot and Thomson established a relationship between the tensile strain and pavement fatigue life. For a typical Illinois dense graded I asphalt mixture, the following fatigue pavement Formula (3) can be adopted [21]:

$$N_t = 5 \times 10^{-6} \times (\varepsilon_t)^{-3.0}. \tag{3}$$

The fatigue test results of different asphalt mixtures show that the resilient modulus plays an important role in the fatigue performance of materials. Monismith et al. established the following general Formula (4) [22]:

$$N_f = K(\varepsilon_t)^{-n} (S_{min})^{-m}. \tag{4}$$

Wang Xudong et al. conducted constant stress bending fatigue tests, combined with load transverse distribution, load intermittent time, and adverse season days. They modified the indoor fatigue model as follows [23]:

$$N_e = N_f \times 7 \times 40 \times \frac{365}{60} \times 2 = 13.7 \times A_a A_g / A_C \sigma^{-4.17} \tag{5}$$

where N_f is the laboratory fatigue life, $N_f = 4025 A_a A_g / A_C \sigma^{-4.17}$; ε_t is the tensile strain; A_a is the coefficient of asphalt type; A_b is the gradation coefficient of asphalt mixture; A_c is the coefficient of highway grade coefficient; and σ is stress.

In the actual service process of pavement, its stress and strain are constantly changing and uncertain under vehicle loads. Most of the above fatigue models were obtained by testing under the stress control and strain control modes, which differ from the actual situation of real pavement. For an unstable variable stress, damage accumulation hypothesis should be used to estimate the fatigue failure life of the road. Cyclic loading is adopted in this test, and the loading times are sufficient. A comparative analysis of the transverse and longitudinal tensile strains is performed by the Wohler equation, and load action cycles of Pavement III are used as an example, by which the relationship between tensile strain and load action cycles is established, as shown in Figure 10.

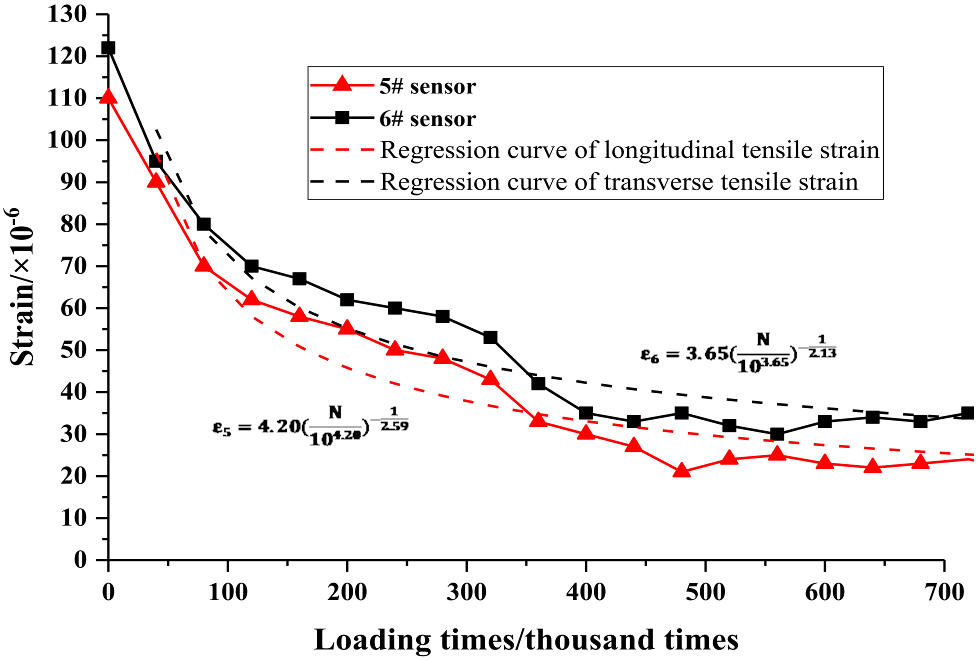

Figure 10. Relationship between strain and the number of loading cycles.

3.2. Material Properties before and after Loading

After 700,000 times of loading, cores were taken from the loading areas (including rutting pits and uplifts) and unloaded areas of the three pavements. Three index tests were performed on the extracted asphalt, and the mixture porosity test and resilience modulus test were performed on the core samples. Based on the original test data, the physical properties of the recovered binder and the porosity and modulus of the mixture of each group are shown in Figures 11 and 12 and Table 4.

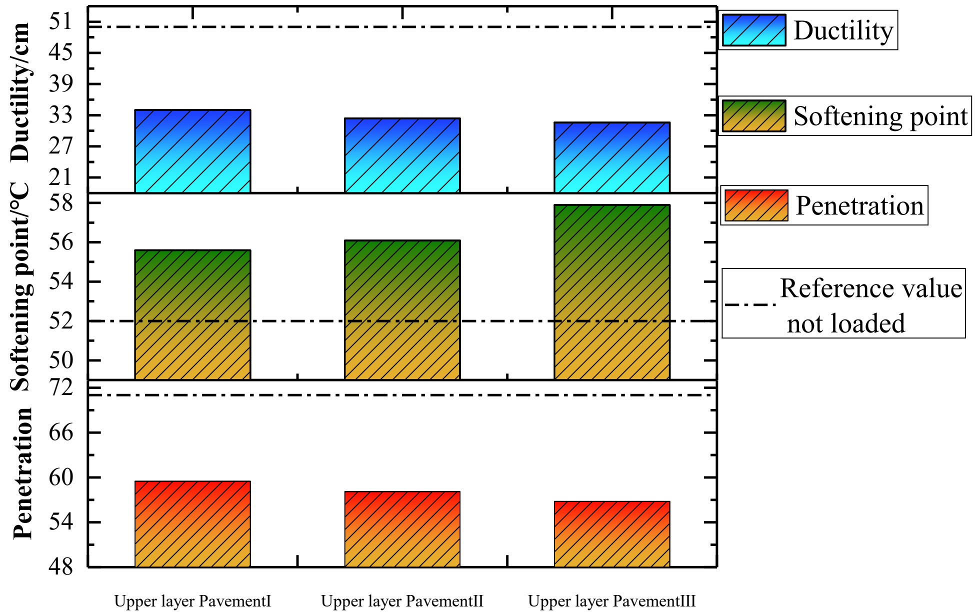

Figure 11. Three indexes of asphalt binder for each pavement.

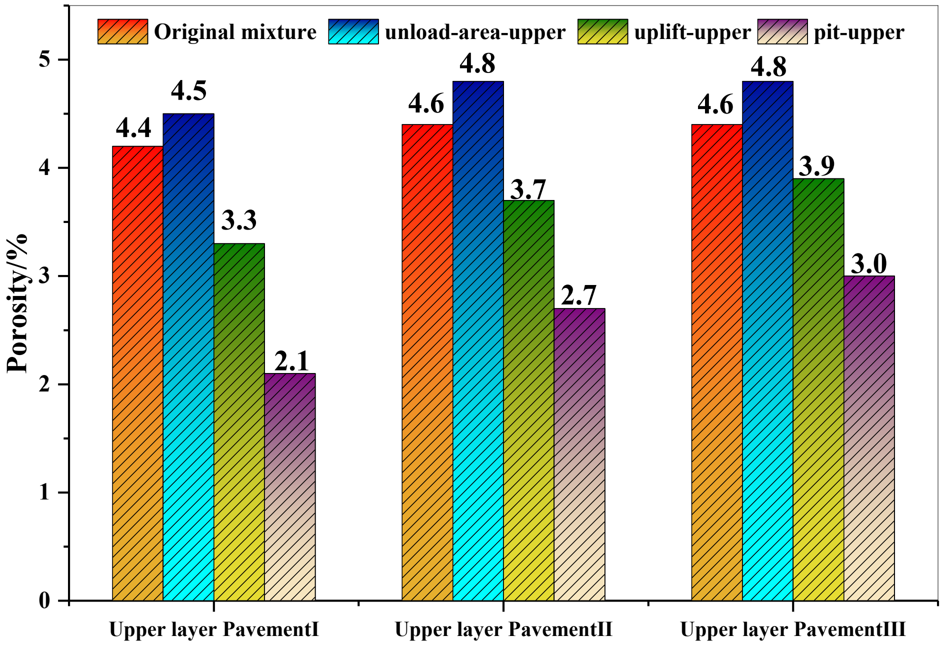

Figure 12. Porosities of cores taken from different pavements.

Table 4. Resilience modulus of cores taken from different pavements.

Coring Position	Resilience Modulus/MPa			
	Mixture	Unload-Area-Upper	Uplift-Upper	Pit-Upper
Upper layer Pavement I	673	666	785	826
Upper layer Pavement II	679	671	792	807
Upper layer Pavement III	679	670	788	801

The comparison of physical performance of the binder on the upper layer of each structural pavement after loading shows that among the three indexes, the degree of change in the softening point is the smallest, i.e., less than 6 °C, whereas the ductility changes to greatest degree, by more than 27 cm. Thus, the performance metrics of the asphalt binder decrease in varying degrees after mixing, paving, and wheel loading. The performance of the recycled asphalt of Pavement III decreases the most. The softening point of Pavement III is the most prominent; it is 6 °C and 1.2 °C higher than that of original asphalt and Pavement II with the same material, respectively. Pavement III has a penetration of 14.2 mm lower than original asphalt. In the rut fitting function $y = a - b \ln(x + c)$, b represents the slope of the curve. Model III has the largest b, and the rut develops the most rapidly, which verifies that the faster the asphalt performance declines, the faster the rutting resistance degrades.

Figure 12 shows the porosity comparison of materials at different positions in the upper layer of each pavement structure. Porosity index can reflect the compaction of pavement materials of each structure. The porosities of pavement II, III, and I are the highest, second highest, and lowest, respectively. The porosities of pit- and uplift-upper of pavement I are 53.3% and 26.7% lower than that of the unloaded area, respectively, whereas those corresponding to pavements II and III are 43.7% and 22.9% lower and 37.5% and 18.7% lower, respectively. The degree of wheel load compaction of pavement I is greater than that of other pavements. If the increase in porosity is attributed to the lateral flow of material, pavement I has more lateral material flow and is more affected by rutting. REOB-recycled asphalt is used as the mixture in the upper layer, which has obvious advantages over the base asphalt in terms of the rutting resistance of the whole asphalt layer. The porosity changes of Pavements II and III are basically equal, indicating that REOB-recycled asphalt can also provide satisfactory rutting resistance when used in the lower layer.

There is no significant difference in the modulus of compressive rebound between the new base asphalt Pavement I and the REOB-recycled asphalt Pavements II and III, as shown in Table 4. After 700,000 cycles, the modulus appreciations of uplift-upper of Pavements I, II, and III are 119 MPa, 121 MPa, and 118 MPa, respectively, and those of pit-upper are 160 MPa, 136 MPa, and 131 MPa, respectively. The moduli of Pavements II and III in the unload-area-upper and the uplift-upper remain large, and the possibility of damaging the pavement is greater under sufficient load. In addition, the moduli do not reach the attenuation stage, indicating that the pavement performance is only degraded under 700,000 cycles, but does not reach the damage stage. The performance of REOB-recycled asphalt pavement is basically equivalent to that of base asphalt surface under 700,000 loads.

To study the fatigue resistance of the material, loading times should be increased further.

4. Conclusions

In this study, REOB is used as an asphalt modifier in the field of aging asphalt recycling, which offers a certain amount of economic and environmental protection. To explore the practical long-term application performance of REOB-recycled asphalt pavement, the rotary accelerated loading test system (ALT-R100) independently developed by our university is used to carry out cyclic loading tests on three sections of REOB-recycled asphalt pavement, to simulate the long-term load behavior of service pavement in a short time. The following conclusions may be drawn:

(1) After using the ALT-R100 accelerated loading system to perform 700,000 loading cycles, the anti-skid performance and anti-rutting performance of concrete pavement with REOB-recycled asphalt and conventional asphalt are basically consistent, both meeting use requirements.

(2) The pavement with the REOB-recycled asphalt mixture in the upper and lower layers enters the compaction stage sooner; thus, it is prone to rutting damage earlier, and the asphalt binder is more prone to aging. This problem does not occur when REOB-recycled asphalt mixture is only used in the upper layer.

(3) A logarithmic model for predicting rutting and a Wohler-equation-based strain prediction model of the three-section test road under ALT-R100 accelerated loading were obtained, revealing the development laws for rutting and bottom strain within the applied loading times.
(4) The rutting depth, BPN value, and bottom strain of the pavement gradually stabilized after loading for 400,000 cycles. When ALT-R100 is used to evaluate the high-temperature rutting resistance and anti-skid performance of asphalt mixtures, the standard test can be performed for 400,000 to 500,000 loading cycles.

With sufficient time and funds, we can continue to conduct accelerated loading tests involving REOB-recycled asphalt pavement by constructing a field test road in the future to study the performance characteristics of base asphalts having different structures with REOB-recycled asphalt layers.

Author Contributions: Data curation, X.C.; Methodology, M.Y. and S.Z.; Project administration, P.L.; Writing—original draft, L.Z.; Writing—review & editing, J.L. All authors have read and agreed to the published version of the manuscript.

Funding: This research was funded by the project "Study on the Effect and Mechanism of Recycled Engine Oil Bottom on the Modification Performance of Asphalt" (ZR 2016EEM42) of Shandong Natural Science Foundation.

Institutional Review Board Statement: Not applicable.

Informed Consent Statement: Not applicable.

Data Availability Statement: The experimental data in this paper are from the pavement material laboratory of Shandong Jiaotong University, which is the provincial key laboratory.

Acknowledgments: The authors would like to acknowledge the assistance of staff at Shandong Natural Science Foundation and Shandong University Science and Technology Program of China, and thank Xiang Li, Jiabin Wang, Enzhou Di, and Zebin Guan for their help in the experiment.

Conflicts of Interest: The authors declare no conflict of interest.

References

1. Jia, X.; Huang, B.; Bowers, B.F.; Zhao, S. Infrared spectra and rheological properties of asphalt cement containing waste engine oil residues. *Constr. Build. Mater.* **2014**, *50*, 683–691. [CrossRef]
2. Hesp, S.A.; Shurvell, H.F. X-ray fluorescence detection of waste engine oil residue in asphalt and its effect on cracking in service. *Int. J. Pavement Eng.* **2010**, *11*, 541–553. [CrossRef]
3. Hesp, S.A.M.; Shurvell, H.F. Waste Engine oil Residue in Asphalt Cement. In Proceedings of the Seventh International Conference on Maintenance and Rehabilitation of Pavements and Technological Control, Thessaloniki, Greece, 12–17 June 2019.
4. Golalipour, A. Investigation of the Effect of Oil Modification on Critical Characteristics of Asphalt Binders. Ph.D Thesis, The University of Wisconsin—Madison, Madison, WI, USA, 2013.
5. Herrington, P.R.; Hamilton, P.G. *Recycling of Waste Oil Distillation Bottoms in Asphalt*; Transfund New Zealand Research Report; California Transit Association: Sacramento, CA, USA, 1998.
6. Bennert, T.; Ericson, C.; Pezeshki, D.; Haas, E.; Shamborovskyy, R.; Corun, R. Laboratory performance of refined engine oil bottoms (REOB) modified asphalt. *J. Assoc. Asph. Paving Technol.* **2016**, 163–207.
7. Cooper, S.B., Jr.; Mohammad, L.N.; Elseifi, M.A. Laboratory Performance of Asphalt Mixtures Containing Recycled Asphalt Shingles and Re-Refined Engine Oil Bottoms. *J. Mater. Civ. Eng.* **2017**, *29*, 04017106. [CrossRef]
8. Li, X.; Gibson, N.; Andriescu, A.; Arnold, T.S. Performance evaluation of REOB-modified asphalt binders and mixtures. *Road Mater. Pavement Des.* **2017**, *18*, 128–153. [CrossRef]
9. Zaumanis, M.; Mallick, R.B.; Frank, R. Evaluation of rejuvenator's effectiveness with conventional mix testing for 100% reclaimed asphalt pavement mixtures. *Transp. Res. Rec. J. Transp. Res. Board* **2013**, *2370*, 17–25. [CrossRef]
10. Sirin, O.; Tia, M.; Roque, R.; Choubane, B. Evaluation of performance characteristics of the heavy vehicle simulator in Florida. *Build. Environ.* **2007**, *42*, 1270–1277. [CrossRef]
11. Choubane, B.; Gokhale, S.; Sholar, G.; Moseley, H. Evaluation of coarse and fine graded superpave mixtures under accelerated pavement testing. *Transp. Res. Rec. J. Transp. Res. Board* **2006**, *1974*, 120–127. [CrossRef]
12. Theyse, H.L.; Hoover, T.P.; Harvey, J.T.; Monismith, C.L.; Coetzee, N.F. A mechanistic-empirical subgrade design model based on heavy vehicle simulator test results. *Pavement Mech. Perform.* **2006**, *154*, 195–202.

13. Hugo, F.; De Vos, E.R.; Tayob, H. Aspects of cement stabilized mozambique sand base material performance under MMLS3 and MLS10 APT trafficking. *SATC* **2007**. Available online: http://hdl.handle.net/10019.1/43003 (accessed on 6 April 2022).
14. *ASTM D8125-2017*; Standard Specification for re-Refined Engine Oil Bottoms (REOB)/Vacuum Tower Asphalt Extender (VTAE). American Society for Testing and Materials: West Conshohocken, PA, USA, 2017.
15. Yu, M.Z. Design and Road Performance Test of Recycled Asphalt Mixture with REOB. Ph.D. Thesis, Shandong Jiaotong University, Shandong, China, 2019. (In Chinese).
16. Li, J.; Yu, M.; Cui, X.; Wang, W. Properties and Components of Recycled Engine Oil Bottom Rejuvenated Asphalt and Its Grey Relationship Analysis. *Adv. Mater. Sci. Eng.* **2019**, *2019*, 1–11. [CrossRef]
17. Wang, P.C.; Hao, X.W.; Zhang, Y. Long term performance of warm mix asphalt mixture based on accelerated loading test. *J. Shenyang Jianzhu Univ.* **2020**, *36*, 860–869. (In Chinese)
18. Coutinho, R.P.; Babadopulos, L.F.A.L.; Freire, R.A.; Branco, V.T.F.C.; Soares, J.B. The use of stress sweep tests for asphalt mixtures nonlinear viscoelastic and fatigue damage responses identification. *Mater. Struct.* **2013**, *47*, 895–909. [CrossRef]
19. Luo, S.; Qian, Z.D.; Harvey, J. Fatigue decay characteristics test of epoxy asphalt mixture. *Chin. J. Highw.* **2013**, *26*, 20–25. (In Chinese)
20. Powell, W.D.; Potter, J.F.; Mayhew, H.C.; Nunn, M.E. The structural design of bituminous roads. *Transp. Road Res. Lab.* **1984**, *1132*, 1984.
21. Elliot, R.P.; Thompson, M.R. Mechanistic design concepts for conventional flexible pavement. *Transp. Eng. Ser. Urbana: Univ. Ill.* **1986**. Available online: https://www.researchgate.net/publication/269090247 (accessed on 6 April 2022).
22. Monismith, C.L.; Deacon, J.A. Fatigue of asphalt paving mixtures. *Transp. Eng. J.* **1969**, *95*, 122–131. [CrossRef]
23. Wang, X.D.; Sha, A.M.; Xu, Z.H. *Dynamic Characteristics and Dynamic Parameters of Asphalt Pavement Materials*; People's Communications Press: Beijing, China, 2002.

coatings

Article

Shear Behavior of Stud-PBL Composite Shear Connector for Steel–Ceramsite Concrete Composite Structure

Hongbing Zhu [1], Zhenghao Fu [1], Peng Liu [2,3,*], Yongcan Li [1] and Benlu Zhao [1]

[1] School of Urban Construction, Wuhan University of Science and Technology, Wuhan 430065, China; zhuhongbing@wust.edu.cn (H.Z.); whfzh1998@163.com (Z.F.); wslyc2007@126.com (Y.L.); 13628659252@163.com (B.Z.)
[2] School of Civil Engineering, Central South University, Changsha 410075, China
[3] National Engineering Laboratory for High Speed Railway Construction, Central South University, Changsha 410075, China
* Correspondence: 2015038@csu.edu.cn

Abstract: For steel–concrete composite structure, a new type of stud–PBL composite shear connector can improve the shear resistance of steel–concrete interface, and polypropylene fiber ceramsite concrete can reduce the self-weight. Therefore, investigating the shear behavior of stud–PBL composite shear connectors for steel–ceramsite concrete composite structures bears significance. In this study, static testing and numerical simulation of the composite shear connector push-out specimen of polypropylene fiber ceramsite concrete were first conducted. The influencing factors of the shear bearing capacity were then analyzed. The formula for determining the shear bearing capacity of the steel–ceramsite concrete composite structure stud–PBL composite shear connectors was ultimately established. The results indicated that the new composite shear connector exhibited excellent shear resistance and good deformation ability. In addition, increasing concrete's strength, stud's diameter, and perforated plate's thickness could significantly improve the shear bearing capacity of the composite shear connector. The calculated value of the shear bearing capacity of the composite shear connector was well correlated the measured value of the test. Overall, the stud–PBL composite shear connector could effectively improve the interfacial shear bearing performance of the steel–ceramsite concrete composite structure. Moreover, the established formula demonstrated broad applicability.

Keywords: bridge engineering; shear bearing capacity; push-out test; stud–PBL composite shear connector; finite element analysis; ceramsite concrete; composite structure

Citation: Zhu, H.; Fu, Z.; Liu, P.; Li, Y.; Zhao, B. Shear Behavior of Stud-PBL Composite Shear Connector for Steel–Ceramsite Concrete Composite Structure. *Coatings* **2022**, *12*, 583. https://doi.org/10.3390/coatings12050583

Academic Editor: Andrea Nobili

Received: 29 March 2022
Accepted: 21 April 2022
Published: 24 April 2022

1. Introduction

Steel–concrete composite structures are characterized by reasonable stress and have been widely used in recent years. Shear connectors are the pivotal elements that bond the steel beam to the concrete slab. Stud and Perfobond Leiste (PBL) shear connectors are mostly used in engineering thus far [1]. Stud shear connectors can resist longitudinal shear force through the stud rod, and a large part resists the lifting force of the concrete slab. To resist the longitudinal shear force and the interface separation force, a PBL shear connector mainly consists of three parts: a perforated steel plate, the concrete tenon, and the penetrating steel bars [2].

Comprehensive studies have been conducted on the combined structural performance of studs or solely PBL shear connectors, and these reports have been verified in various engineering practices [1–6]. To meet engineering requirements such as large shear and pull-out resistance for a composite structure interface, flexible stud shear connectors have been combined with rigid PBL shear connectors; this integration is aimed at forming composite shear connectors that can be used in steel–concrete composite structures. However, the process of combining stud shear connectors and PBL shear connectors in space remains inconclusive. Zhang [7] added two rows of studs to both sides of the perforated steel plate to improve the shear bearing capacity; this connector, which was composed of the perforated plate and the studs, was used in the Nakano Viaduct Project in Japan. For this method, push-out tests and finite element simulation analysis were performed by Deng [8] and Zheng [9]. Their study verified the superior shear resistance of the perforated plate + stud shear connector. Meanwhile, to strengthen the vertical shear resistance of the transition between the longitudinal steel box girder section and the concrete girder section in the hybrid box girder bridge, Jin [10] arranged the studs and PBL shear connectors alternately vertically in the web of a hybrid box girder bridge and studied the ratio of the shear force borne by the PBL shear connectors to the studs. Chen [11] proposed a composite shear connector in which studs were transversely welded to the perforated plate. The formula for the shear bearing capacity of the composite shear connector was derived by finite element simulation analysis of push-out tests. The aforementioned studies demonstrated that the combination of studs and PBL to form a composite shear connector can indeed improve shear resistance; however, existing composite shear connectors (mainly used in special stress parts of the structure) are not universal. The PBL shear connectors arranged lengthwise can divide the concrete slab into strips longitudinally, reducing the integrity of the concrete slab. Meanwhile, the PBL shear connectors arranged lengthwise may increase the amount of steel. Widely distributed welding residual stresses also exist in PBL shear connectors and steel beams. Therefore, it is of good engineering value to design a more reasonable stud–PBL composite shear connector, which can optimize the welding residual stresses, enhance the connection between concrete and steel beams, and improve the force performance of the steel–concrete interface.

In this study, PBL and stud were alternately arranged in the same plane to form a new composite shear connector. The intermittently arranged PBL shear connectors can reduce the amount of steel used and increase the integrity of the concrete slab. The bearing effect of the end concrete can also enhance the shear resistance of the shear connectors [12,13]. Meanwhile, the combination of rigid PBL shear connectors and flexible studs can complement the advantages of the two shear connectors, endowing the interface between the concrete slab and the steel beam with sufficient stiffness, good ductility, and toughness.

Shear bearing capacity is an important performance index of shear connectors. Therefore, it is very important for its popularization and application to accurately evaluate the shear resistance of shear connectors and obtain a reliable calculation formula of shear bearing capacity. In a previous study, Xue [14] proposed the load–slip curve formula for the sheared stud and the calculation formula for the shear bearing capacity, considering the length to diameter ratio of the stud by testing the stud push-out specimen. Using push-out testing, Lee [15] and Hu [16] presented formulas for calculating the shear bearing capacity of high-strength concrete stud shear connectors and ultra-high-performance concrete stud shear connectors, respectively. Huo [17] studied the shear bearing capacity of stud connectors under impact loading. Based on integrating some group studs push-out tests and theoretical analysis results [18–21], “Code for Design of Steel and Concrete Composite Bridges” (GB 50917-2013) also provided the formula for calculating the shear bearing capacity of ordinary concrete composite beams when the studs were damaged, and highlighted that the diameter of the stud is an important influencing factor. The effects of diameter [12,13,22–30], quantity [22] and strength [25,26] of penetrating steel bars, diameter of openings [12,13,22–27,29,30], concrete strength [12,13,22,23,25,26,28,29], number of openings [12,27], thickness of perforated plates [13,21–23,25,27,30], spacing of perforated plates [26], and concrete stress state [12] on the shear bearing capacity of PBL shear connectors have been evaluated in other reports. Moreover, formulas for calculating the shear bearing capacity of PBL shear connectors have been proposed. The influencing factors and function forms considered in each calculation formula are essentially identical, but vary in coefficients. No mature formulas are currently recognized in the industry. Therefore, the formula for the shear bearing capacity of stud shear connectors is highly mature. By contrast, the formula for the shear bearing capacity of the PBL shear connector has yet to be verified by more tests and engineering examples. After the stud and the PBL shear connector are integrated into a composite shear connector, adding both in the shear bearing capacity is evidently inappropriate. Therefore, the determination of the mutual influence of the stud and the PBL shear connector still needs to be clarified by experimental and analytical research.

The ceramsite concrete with an appropriate number of polypropylene fibers presents several advantages, including lightness, high strength, and good seismic performance [31]. However, the physical and mechanical properties of ceramsite concrete still differ from those of ordinary concrete. Thus, the performance of composite structures made from it needs to be further defined using experiments and theoretical analysis. Applying the stud–PBL composite shear connector in a composite structure consisting of steel–ceramsite concrete can form a structural system characterized by lightweight, dead weight, and high bearing capacity. Accordingly, studying its mechanical properties is highly crucial.

This study explores the following three aspects. (i) First, push-out tests of one stud shear connector (LT-S), one PBL shear connector (LT-P), and three stud-PBL composite shear connectors (LT-C) were performed to research the interfacial shear resistance of steel–ceramsite concrete composite structures with different shear connectors. The finite element software Abaqus was then used to simulate push-out tests with 5 samples. The test phenomenon, load–slip curve, shear bearing capacity, stress illustration, and damage illustration (among others) were compared and then verified among one another. Finally, the shear damage mechanism and the failure form of shear connectors were revealed from multiple angles. (ii) Nine groups of orthogonal test simulations with four factors and three levels were conducted for 49 finite element push-out samples. Subsequently, the influences of parameters such as the stud diameter, PBL perforated plate thickness, opening diameter, penetrating steel bar diameter, and concrete strength on the shear resistance of the composite shear connector were analyzed. (iii) Multivariate linear regression analysis was performed on the analysis results of 49 finite element models. Subsequently, the formula for the shear bearing capacity of the stud–PBL composite shear connector in the steel–polypropylene fiber ceramsite concrete composite structure was derived. The formula was then verified by the test results. The objectives of the study are to clarify the shear resistance of composite shear connectors, to obtain their influencing factors, and to establish reasonable calculation formulas. The significance of this paper is to provide a new and scientific reference for the design of steel–concrete composite structure interfaces.

2. Push-Out Experiment

2.1. Experimental Design

To study the shear resistance of the combined arrangement of studs and PBL, five push-out specimens were designed, with reference to Eurocode 4 (EN 1994-2: 2005, Eurocode 4) [32]. They were divided into three groups based on the type of the shear connector: the LT-S group (studs shear connector, one specimen), the LT-P group (PBL shear connector, one specimen), and the LT-C group (composite shear connector with the combined studs and PBL, three specimens).

The polypropylene fiber ceramsite concrete used in the test had a 28-d cube compressive strength of 52.3 MPa and a content of 0.9 kg/m^3 (the volume content was 0.1%). The model of the penetrating steel bar was HPB300 and its diameter was 12 mm. Its measured yield strength, ultimate tensile strength, and elastic modulus of the penetrating steel bar were 328, 480, and 209.2 GPa, respectively. Both H-beam and PBL perforated plates consisted of Q235 steel, and their thickness was 16 mm. They had the following measurements: yield strength, 330.9 MPa; ultimate tensile strength, 440 MPa; elastic modulus, 205.7 GPa. The material of the stud was ML15A1 and the diameter of the rod part of the stud was 16 mm. Its measurements were as follows: yield strength, 360 MPa; ultimate tensile strength, 400 MPa; elastic modulus, 205 GPa. The opening of the perforated plate was set to 40 mm.

The structural form of the LT-C (composite shear connector) specimen is presented in Figure 1. Each sample contained four PBL shear connectors and four stud shear connectors.

To ensure that the studs as flexible connectors could fully exert their shear resistance when the sample was under compression, the studs in the specimen were arranged in the lower part of the specimen. The PBL shear connectors on the upper layer of the LT-C specimen were replaced with studs, which comprised the LT-S specimen. Similarly, the studs on the lower layer of the LT-C specimen were replaced with PBL shear connectors, which comprised the LT-P specimen. (See Table 1).

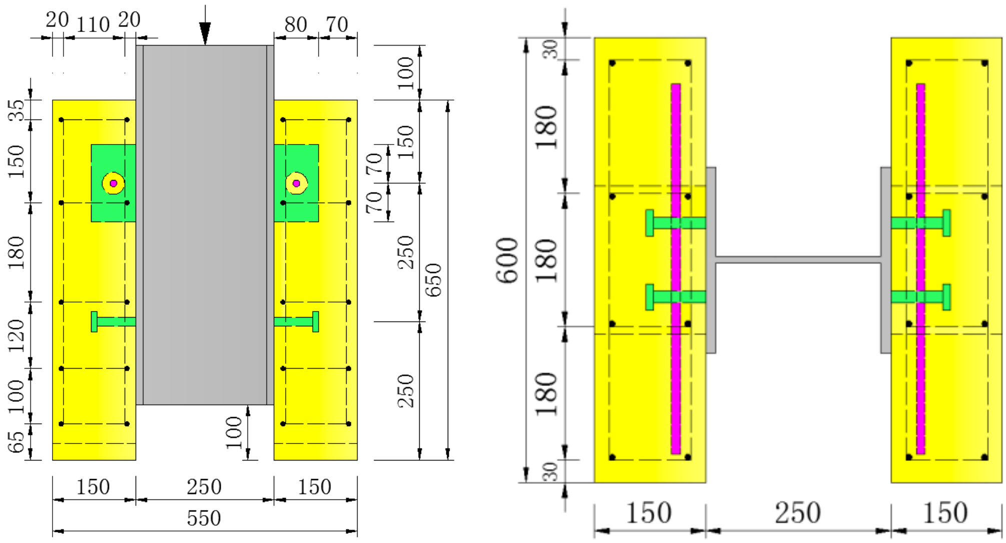

(**a**) (**b**)

Figure 1. Details of push-out specimen (LT-C) (Unit: mm): (**a**) Side view of LT-C; (**b**) Top view of LT-C.

Table 1. Parameters of push-out test specimen.

Group	Number of Studs in a Specimen	Number of PBL Shear Connectors and Openings in a Specimen	Number of Penetrating Steel Bars in a Specimen
LT-S	8	-	-
LT-P	-	8	4
LT-C	4	4	2

As displayed in Figure 2, a 2000 kN electrohydraulic servo pressure testing machine is used for loading. Three preloads were conducted before the official loading (the loading step was 20 kN. During preloading, after loading to 60 kN, it was unloaded to 0 kN, and the loading rate was 0.5 kN/s). After preloading, monotonic hierarchical loading was employed for the formal loading. First, the loading level distance was set to 1/10 of the limit load, which was calculated using the finite element method. Moreover, the sample was loaded to 80% of the calculated limit load value, step by step (loading rate was 1 kN/s) in accordance with this loading level distance. The loading level distance was then set to 20 kN (0.2 kN/s), and the sample was loaded to the measured value of the limit load. Finally, loading continued after this and the test was terminated when the load was reduced to 85% of the actual ultimate load, or the sample was unloaded after the appearance exhibited obvious damage. The data of dial indicators were recorded, and the development of cracks was observed after each level of loading was stable for 3 min.

Figure 2. Sketch of loading.

2.2. Experimental Phenomena

The test demonstrated that the three types of shear connector specimens included the three working stages: elasticity, plasticity, and failure. At the initial stage of loading, small relative displacement was present between the H-beam and the concrete slab. The load increased substantially and varied linearly with the relative slip value. Diagonal cracks in concrete slabs were small in width and short in length and developed slowly. After the elastic phase, the relative slip value of the specimen and the load increment exhibited a nonlinear behavior. Meanwhile, the width and length of the diagonal cracks continued to increase. The loading progressed gradually, but the relative slip value increased rapidly, and both again exhibited a linear change. In addition, vertical cracks appeared, and each crack developed rapidly to penetrate the entire specimen in the height direction until a loud "bang" was heard from the specimen. Concrete spalling, concrete slab and H-beam detachment, and specimen and loading equipment shaking then occurred. The three types of shear connector specimens ultimately demonstrated different damage phenomena.

Figure 3 presents in detail the failure of the push-out specimen. The studs on one side of the LT-S specimen were sheared from the root, and those on the other side exhibited plastic deformation. Moreover, the studs on both sides indicated large plastic deformation at the root in the H-beam direction. The concrete under the studs was compressed, leading to plastic deformation, and fine cracks were observed at the bottom of the concrete slab. When the LT-P specimen was damaged, no apparent deformation of the perforated plate occurred, and the concrete tenon in the hole was crushed. In addition, the penetrating steel bars between the PBL shear connectors were deformed and yielded in the H-beam direction, and grooves appeared in the corresponding part of the PBL. The bottom of the concrete slab was also crushed. The studs of the LT-C group were broken at the root or had major plastic deformation. The concrete around the studs had plastic deformation, and the concrete tenon was crushed. Similarly, the penetrating steel bars exhibited plastic deformation, and the bottom of the concrete slab was crushed.

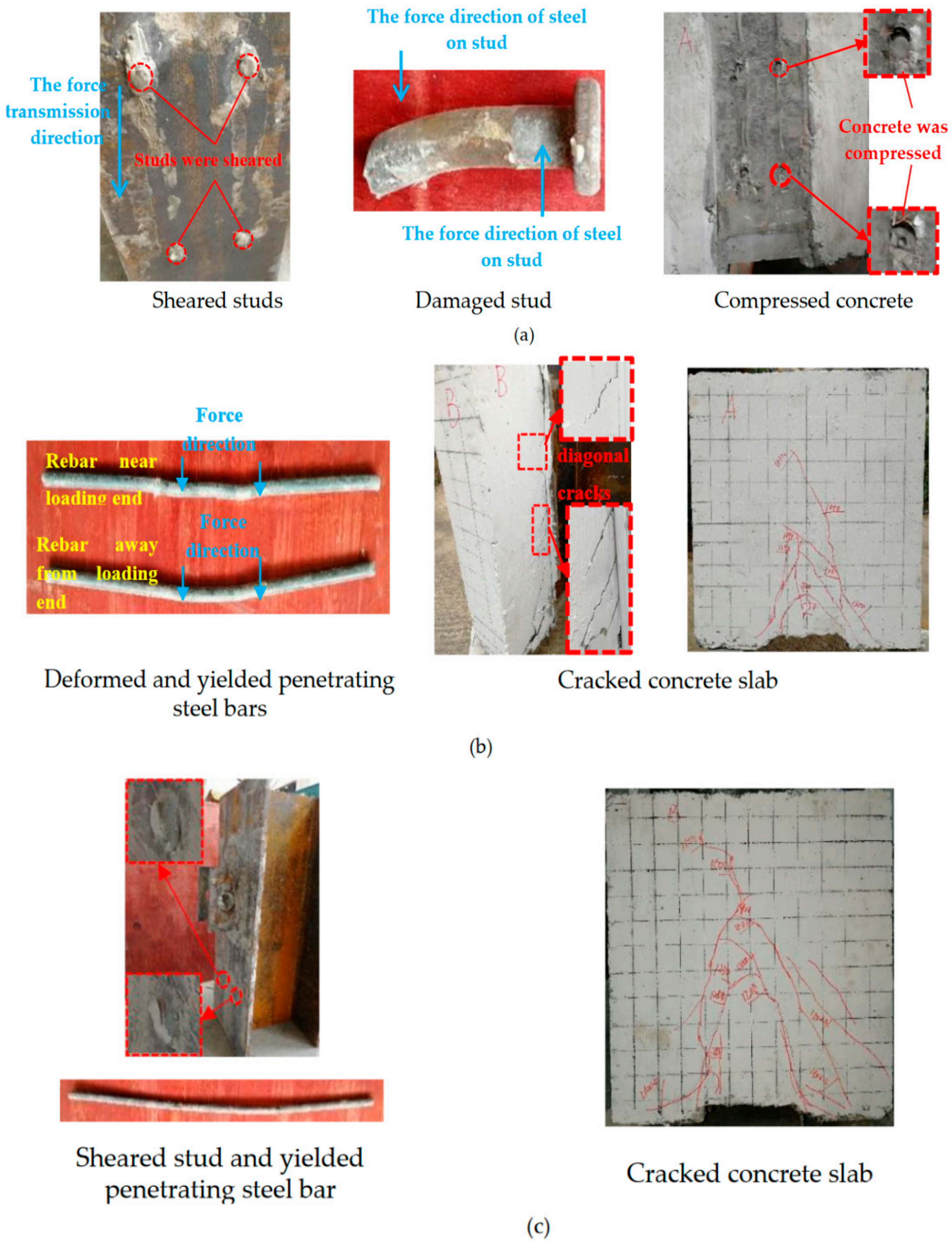

Figure 3. Typical failure model of push-out test specimens: (**a**) The failure details of LT-S specimen; (**b**) The failure details of LT-P specimen; (**c**) The failure details of LT-C specimen.

2.3. Experimental Results

Table 2 listed the shear bearing capacity of the specimens.

Table 2. Results of push-out test and finite element analysis (FEA).

Specimen Number	Test Value P_u/kN	Finite Element Calculation Value $P_{u,fea}$/kN	$P_{u,fea}/P_u$
LT-S	197.3	207.6	1.05
LT-P	325.0	334.0	1.03
LT-C-1	404.0	363.9	0.90
LT-C-2	375.1		0.97
LT-C-3	375.1		0.97
LT-C Average	384.7	363.9	0.95

Noted: P_u in the table was 1/4 of the shear bearing capacity of the test specimen. It meant the specimen LT-S contained 2 studs, the specimen LT-P contained 2 PBL, and the specimen LT-C contained 1 stud and 1 PBL.

As listed in Table 2, the measured shear bearing capacities of LT-S and LT-P are 197.3 and 325.0 kN, respectively. By superimposing the bearing capacity of a single stud and a single PBL, $(P_{u,\,LT\text{-}S} + P_{u,\,LT\text{-}P})/2 = 261.2$ kN (1 stud + 1 PBL)—that is less than the average shear capacity of LT-C (384.7 kN). This observation indicates the high shear resistance of the LT-C shear connector. The shear bearing capacity of LT-C was 18.4% higher than that of LT-P. The reason might be attributed to the high strength of the PBL shear connector. In addition, the concrete at the bottom of the perforated plate was in a state of concentrated stress, rendering it prone to cracking. Consequently, the effective bearing area of the concrete slab was reduced. Therefore, the shear bearing capacity of the specimen was decreased [9]. However, the flexible studs in LT-C could relieve the stress concentration of the rigid PBL to a certain extent to fully use the advantages of both the PBL and studs. This finding also suggests that the shear connector composed of studs and PBL could be better combined with the concrete slab and achieve the optimal performance of both the shear connector and the concrete slab.

Figure 4 illustrates the load–slip curve measured in the test. Only the load–slip curves of the samples in the elastic and plastic working stages were generated because of limitations to the equipment. The plastic stage of LT-S was the longest, followed by that of LT-C, and that of LT-P was the shortest. This reveals that under the condition of certain concrete strength, replacing the lower perforated plate with studs could improve the deformation performance of the push-out specimen. In the elastic stage, the stiffness of LT-S was significantly lower than that of LT-P, whereas the stiffness of the three LT-C specimens was similar to that of LT-P. It could be observed that the LT-C specimens were superior to the LT-P specimen in shear bearing capacity and ductility. However, they still had the same level of stiffness as that of LT-P.

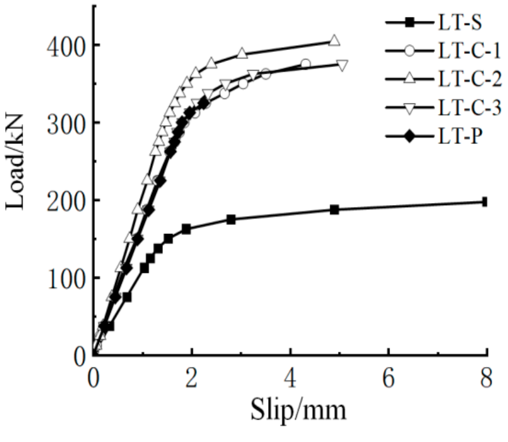

Figure 4. Load–slip curves of the push-out test.

After comprehensive analysis of the shear bearing capacity and deformation capacity of the three specimens, it was discovered that the composite shear connectors could improve the integrity of the concrete slab, and we also made full use of the flexibility of the stud and the rigidity of the PBL shear connector to improve the interface force performance. This made the LT-C specimen have the highest shear bearing capacity and stiffness while keeping an excellent deformation capacity.

3. Push-Out Experimental Finite Element Numerical Simulation

3.1. Overview of the Finite Element Model

As shown in Figure 5, a 1/4 model was established based on the actual size of the test sample, including H-beam, concrete slab, PBL shear connector, stud, penetrating steel bar, and rebar cages.

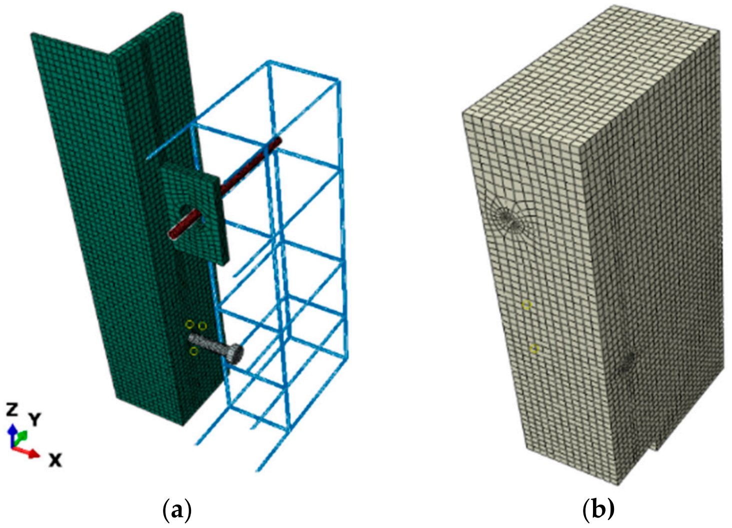

(**a**) (**b**)

Figure 5. 1/4 Finite element model (FEM) of push-out test for the composite shear connector: (**a**) The model of Steel member and steel bars; (**b**) Concrete slab model.

(1) Material constitutive model

The plastic damage model was selected as the concrete material model in the Abaqus finite element software. Polypropylene fibers have previously been proven to strongly influence the control parameters of the descending section of the concrete stress–strain curve section [33,34]. Therefore, the stress–strain relationship of the concrete used in the test adopted the formula suggested by Ding [35], and the Poisson's ratio was taken as 0.2. Moreover, the damage factor was obtained by referring to the calculation method previously studied [36].

The stress–strain relationship of H-beam, the PBL shear connector, the penetrating steel bar, and the rebar cage adopted the tri-polyline model, and that of the studs used the double-line model. In addition, the elastic modulus used the measured value in Section 2.1, and Poisson's ratio was calculated as 0.3. All of the above used the von Mises yield surface to define isotropic yielding.

(2) Element type and mesh division

The H-beam, PBL shear connector, stud, concrete slab, and penetrating steel bar were simulated using the 3D eight-node reduced-integration element (C3D8R). The rebar cage was simulated using the 3D two-node truss element (T3D2). The size of the seeds was 10 mm. The meshes in the contact areas of different components were refined and divided.

(3) Interaction and boundary conditions

Bond contacts were applied between the penetrating steel bar and the surrounding concrete. The rebar cage was placed inside the concrete slab. The H-shaped steel was combined with stud shear connectors and PBL shear connectors to form a component. General contact was also used to simulate contact with concrete. The contact property was normal "hard" contact, and tangential friction was simulated using the penalty function.

Two symmetric surfaces of the model were positive symmetric constraints. After the top surface of the H-shaped steel was fixed (the actual test was the upward loading force on the bottom platform of the sample, and the simulation was consistent with the test), an upward displacement load was applied on the bottom surface of the concrete.

3.2. Analysis of Finite Element Results

Figure 6 indicates the failure mode of the finite element simulation of the samples, including the von Mises stress diagram of the steel member and the damagec and damaget diagrams of the concrete when the specimen reached the shear bearing capacity. The von Mises stress illustration indicates the following: (i) Among the three types of shear connectors, the stud root had the largest stress, which was consistent with the stud in Figure 3. (ii) The stress level of PBL steel plate was small, and practically no significant deformation occurs. (iii) The penetrating steel bar located within the PBL opening indicated the largest stress, which was consistent with the larger yield bending deformation of the penetrating steel bar in the test. The illustrations of damagec (LT-S specimen) and damaget (LT-P and LT-C specimens of the concrete) indicate that the concrete around the studs has different degrees of compressive damage. However, the concrete at the bottom of PBL was mostly damaged by tension. These were consistent with the failure modes such as plastic deformation of the concrete near the studs due to compression, and cracking of the concrete slab in the test. The above demonstrated that the failure modes of the samples simulated by the finite element were consistent with the test results.

Figure 7 presents the load–slip curves of the five specimens in Table 2, which were generated by finite element simulation. The rising stage of the simulated curve roughly resembled the experimental curve. Moreover, the curve variation conditions of the descending section were obtained by the element simulation. After the peak load was reached, the LT-P sample immediately entered the descending stage. In this stage, with the increase of the slip value, the load value displayed a tendency of first accelerating down and then decelerating down. However, the LT-C specimen did not enter the decreasing phase immediately after reaching the peak load; it entered the holding stage first. In this stage, the load changed very slowly with the slip value, and the decreasing trend was not obvious. The decreasing stage of LT-C specimen was similar to that of LT-P.

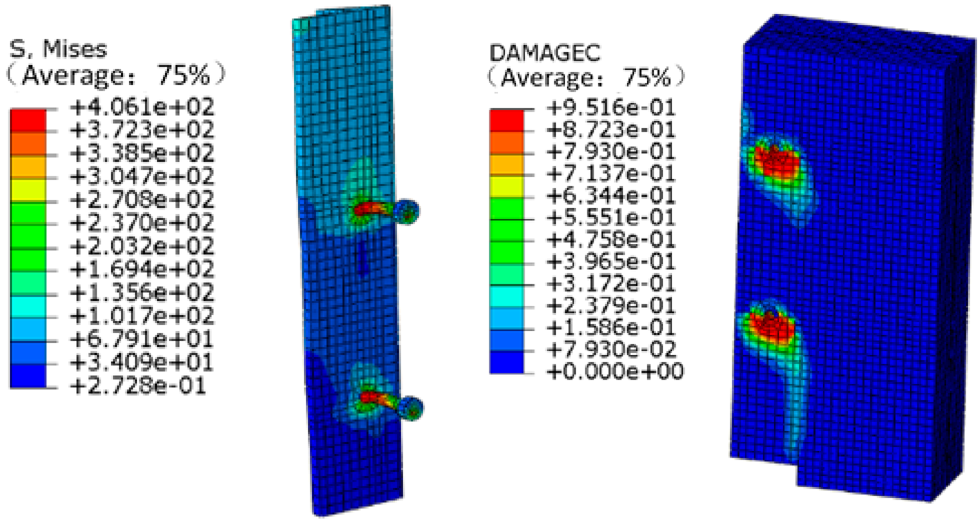

(a1) **(a2)**

Figure 6. *Cont.*

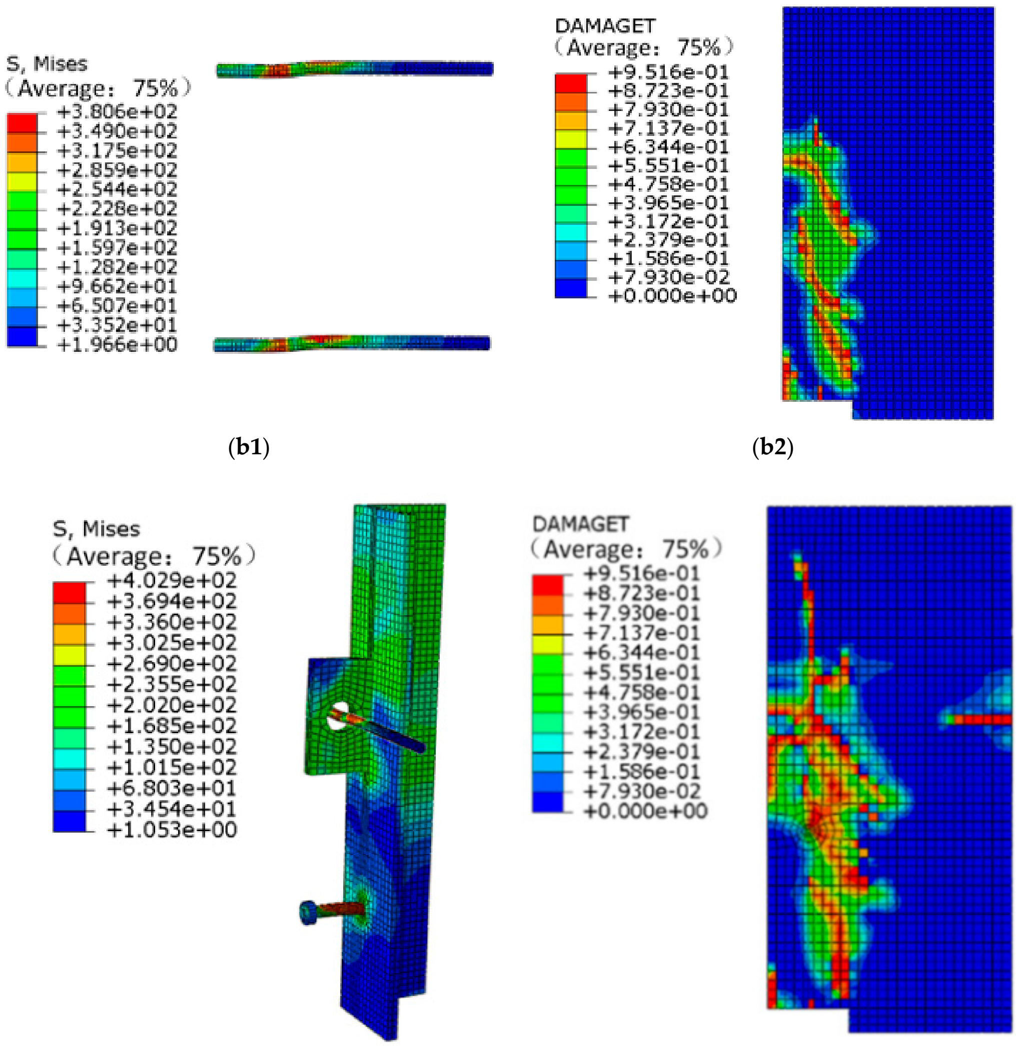

(**b1**) (**b2**)

(**c1**) (**c2**)

Figure 6. Von Mises stress and damage illustration of FEA models: (**a1**) The stress distribution of penetrating steel bars; (**a2**)The compressive damage to concrete; (**b1**) The stress distribution of penetrating steel bars; (**b2**) The Tensile damage to concrete slab; (**c1**) The Stress distribution of stud penetrating steel bar; (**c2**) The Tensile damage to concrete slab.

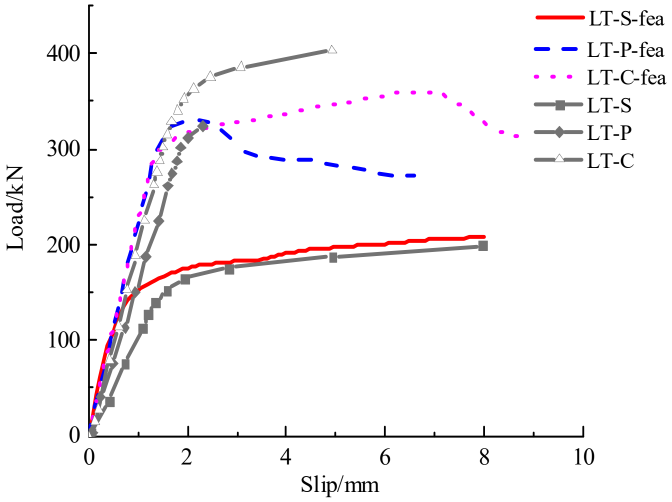

Figure 7. Load–slip curves of FEA models and push-out specimens.

The EC4 specification stipulates that the slip value corresponding to 0.9 Pu in the descending section of the load–slip curve of the shear connector is the slip characteristic value. The characteristic slip value of the composite shear connector exceeded 6 mm, as stated in the specification, which could be determined easily from Figure 7. Therefore, the composite shear connector had good deformation ability.

The shear bearing capacity results of the specimens obtained from the test and the finite element simulation (Table 2) illustrated that the composite shear connector possessed the highest shear bearing capacity, followed by the PBL shear connector and then by the stud shear connector. For the PBL shear connector specimen, the ratio of the finite element result to the test result was 1.03; for the stud shear connector specimen, the ratio was 1.05; and for the composite shear connector specimens, the ratio was 0.90–0.97. Therefore, the correlation between the simulated and measured values is excellent.

With the failure mode, load–slip curve, and shear bearing capacity of the specimen considered, the finite element simulation was consistent with the experimental phenomenon and results. Thus, finite element simulation was a feasible tool to reveal the force mechanism of the composite shear connector and conduct parametric analysis.

4. Finite Element Parameters Analysis

4.1. Parameters Design of Orthogonal Test Analysis Model

A total of 49 finite element models were established to evaluate the effects of different connector structures and different material parameters on the shear resistance of the specimens. According to existing research, the structural parameters set in this paper included the stud diameter, perforated plate opening diameter, perforated plate thickness, penetrating steel bar diameter, and concrete strength. Although the laws and mechanisms of the above parameters on the shear capacity of shear connectors have been revealed, they were for PBL shear connectors or stud shear connectors. For stud–PBL composite shear connectors, the above parameters were set in one member at the same time, and the effect on the shear resistance of the member would be variable and unclear, which was valuable to study. The first four factors were used to design nine groups of orthogonal experiments with four factors and three levels. In addition, the finite element analysis of changing a single parameter in the same finite element model (RP-C52.3) as the test sample construction was added. Table 3 lists the results of the finite element parametric analysis.

Table 3. FEA parametric analysis results of shear bearing capacity of composite shear connectors.

Group	Stud Diameter d_s/mm	Opening Diameter D/mm	Perforated plate Thickness t/mm	Penetrating Steel Bar Diameter d_r/mm	Concrete Cube Compressive Strength f_{cu}/MPa	FEA Shear Bearing Capacity Values $P_{u,fea}$/kN	Equation (6) Calculated Value of Shear Bearing Capacity $P_{u,c}$/kN	$P_{u,c}/P_{u,fea}$
1	13	30	16	12	40	287.4	229.31	0.80
					50	327.1	266.63	0.82
					60	355.0	303.37	0.85
2	13	40	20	16	40	326.2	289.21	0.89
					50	370.2	336.10	0.91
					60	388.0	382.27	0.99
3	13	50	24	20	40	345.1	356.92	1.03
					50	384.9	413.77	1.08
					60	401.0	469.73	1.17
4	16	30	20	20	40	349.9	324.60	0.93
					50	386.6	370.96	0.96
					60	408.3	416.58	1.02
5	16	40	24	12	40	339.1	341.59	1.01
					50	380.9	398.39	1.05
					60	417.2	454.24	1.09
6	16	50	16	16	40	325.2	307.75	0.95
					50	361.4	350.14	0.97
					60	391.7	391.41	1.00
7	19	30	24	16	40	349.4	380.04	1.09
					50	399.3	436.70	1.09
					60	437.2	492.34	1.13
8	19	40	16	20	40	335.7	345.87	1.03
					50	356.3	387.56	1.09
					60	378.6	428.11	1.13
9	19	50	20	12	40	339.2	366.93	1.08
					50	375.1	419.54	1.12
					60	401.9	470.75	1.17
RP	16	40	16	12	30	281.6	234.39	0.83
					40	327.9	276.38	0.84
					52.3	363.9	326.37	0.90
					60	388.7	356.43	0.92

Table 3. *Cont.*

Group	Stud Diameter d_s/mm	Opening Diameter D/mm	Perforated plate Thickness t/mm	Penetrating Steel Bar Diameter d_r/mm	Concrete Cube Compressive Strength f_{cu}/MPa	FEA Shear Bearing Capacity Values $P_{u,fea}$/kN	Equation (6) Calculated Value of Shear Bearing Capacity $P_{u,c}$/kN	$P_{u,c}/P_{u,fea}$
LT-d_s13	13	40	16	12	40	300.9	243.55	0.81
					52.3	355.9	291.61	0.82
					60	377.2	320.81	0.85
LT-d_s19	19	40	16	12	40	335.2	316.01	0.94
					52.3	372.9	368.31	0.99
					60	376.6	399.42	1.06
LT-D30	16	30	16	12	40	312.4	262.14	0.84
					52.3	360.8	310.08	0.86
					60	354.8	338.99	0.96
LT-D50	16	50	16	12	40	300.3	294.69	0.98
					52.3	351.8	347.30	0.99
					60	346.9	378.86	1.09
LT-t20	16	40	20	12	40	333.7	308.99	0.93
					52.3	375.7	369.00	0.98
					60	398.0	405.34	1.02
LT-t24	16	40	24	12	52.3	389.4	411.62	1.06
LT-d_r16	16	40	16	16	52.3	363.1	339.10	0.93
LT-d_r20	16	40	16	20	52.3	361.8	355.48	0.98

P_u in the table was 1/4 of the shear bearing capacity of the push-out specimen—that is, the specimen LT-C contained one stud and one PBL.

4.2. Analysis of the Orthogonal Test Simulation Results

With the C50 concrete grade as an example, the results in Table 3 were analyzed using the orthogonal test results of the experiment (4 factors, 3 levels).

As displayed in Table 4, K_{ij} is the sum of P_u corresponding to the level of factor i in column j, and $\kappa_{ij} = K_{ij}/3$. The optimal solution of each column of factors could be determined by analyzing the magnitude of κ_{ij}. Moreover, combining them yielded the optimal combination. Thus, the optimal structure of the composite shear connector was ds19-D50-t24-d16, which was obtained easily. Among them, the range R_j denotes the difference between the maximum value and the minimum value in the jth column factor, which can reflect the change in P_u when the level of the jth column factor changes. R_j in Table 4 indicates that the thickness of the perforated plate affects P_u the most, whereas the diameter of the opening influences P_u the least.

Table 4. Analysis of orthogonal test results.

Specimen Number	$j = 1$ Stud Diameter d_s/mm	$j = 2$ Opening Diameter D/mm	$j = 3$ Perforated Plate Thickness t/mm	$j = 4$ Penetrating Steel Bar Diameter d_r/mm	FEA Shear Bearing Capacity Values $P_{u,fea}$/kN
1-C50	13	30	16	12	327.1
2-C50	13	40	20	16	370.2
3-C50	13	50	24	20	384.9
4-C50	16	30	20	20	386.6
5-C50	16	40	24	12	380.9
6-C50	16	50	16	16	361.4
7-C50	19	30	24	16	399.3
8-C50	19	40	16	20	356.3
9-C50	19	50	20	12	375.1
K_{1j}	1082.2	1113	1044.8	1083.1	
K_{2j}	1128.9	1107.4	1131.9	1130.9	$\bar{P}_u = 371.3$
K_{3j}	1130.7	1121.4	1165.1	1127.8	
κ_{1j}	360.7	371	348.3	361.0	
κ_{2j}	376.3	369.1	377.3	377.0	
κ_{3j}	376.9	373.8	388.4	375.9	
R_j	16.2	4.7	40.1	15.9	
S_j	504.0	33.1	2573.4	476.9	$S_j = \sum_{i=1}^{3} (P_{ui} - \bar{P}_u)^2$
S_e	/	33.1	/	/	
F	15.2	/	77.7	14.4	$F = \frac{s_j}{f_j} / \frac{s_e}{f_e}$

P_u in the table is 1/4 of the shear bearing capacity of the push-out specimen—that is, the specimen LT-C contains 1 stud and 1 PBL.

The results of the variance analysis indicate that the test could be used to assess for significance. All columns of this orthogonal table contain factors; thus, the sum of the squared deviation S_j of the factors in the second column is regarded as the sum of the squared deviations of the errors S_e. f_j is the degree of freedom of the jth column factor, and f_j is equal to the number of levels of the j factor minus 1. The ratio F of the variance of each column factor could also be calculated. The factors could then be tested for significance $F \sim F_\alpha(f_j/f_e)$.

The results in Table 4 indicate that $F_3 > F_1 > F_4 > F_{0.10}$ (2,2) = 9.00, indicating that the thickness of the perforated plate, the diameter of the stud, and the diameter of the penetrating steel bar significantly affect shear capacity at $\alpha = 0.10$. Among the parameters, the thickness of the perforated plate has the greatest influence on the shear bearing capacity, followed by the diameter of the stud and then by the diameter of the penetrating steel bar.

4.3. Analysis of the Influencing Factors on the Shear Bearing Capacity of Composite Shear Connectors

By further parameter analysis of the model, the influencing factors of the shear bearing capacity of the composite shear connector were identified (Figure 8).

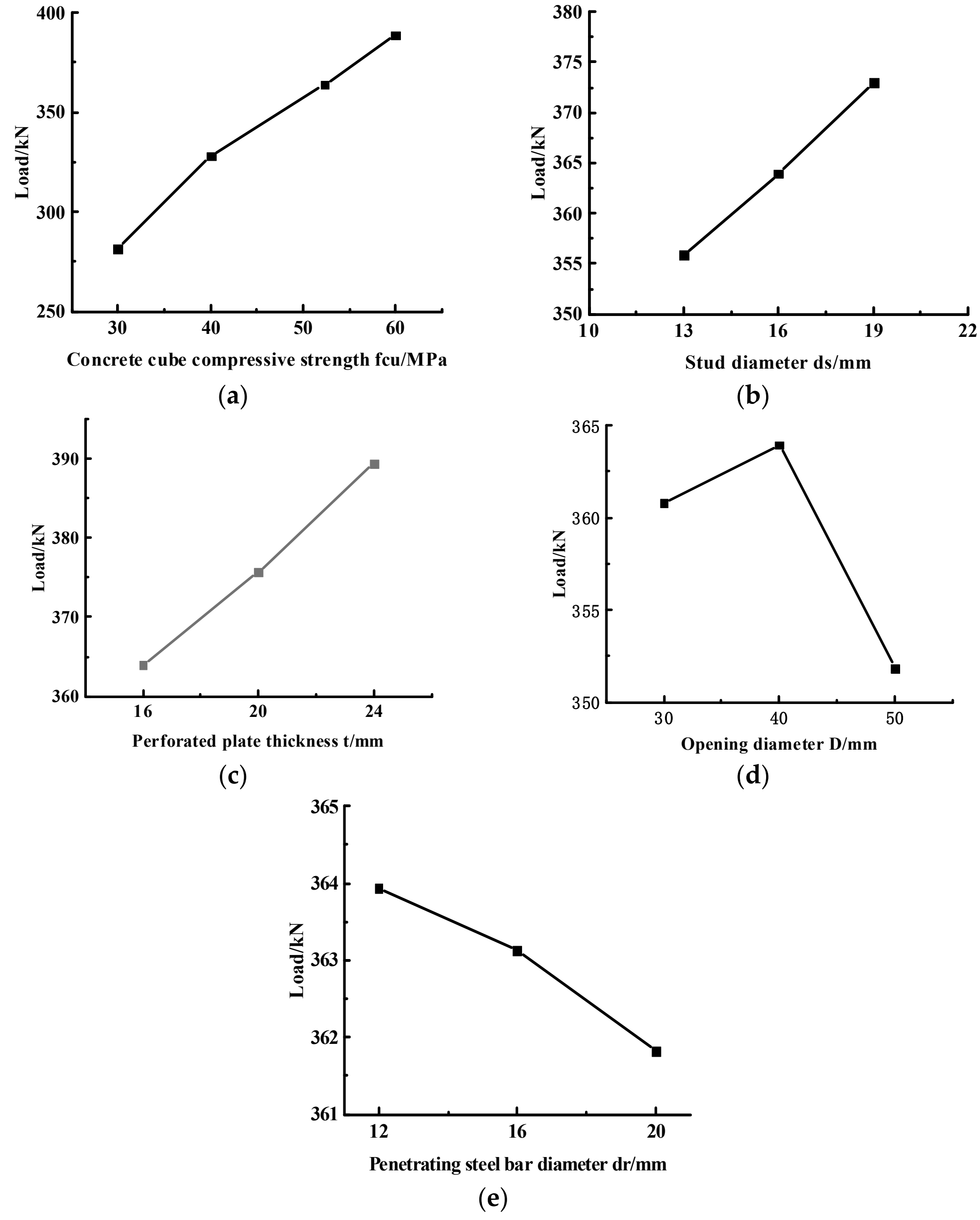

(**a**) (**b**) (**c**) (**d**) (**e**)

Figure 8. Results of FEM parametric analysis: (**a**) Influence of concrete cube compressive strength; (**b**) Influence of stud diameter; (**c**) Influence of perforated plate thickness; (**d**) Influence of opening diameter; (**e**) Influence of penetrating steel bar diameter.

(1) Influence of the strength of the concrete

The shear bearing capacities of the specimens RP-C30, RP-C40, RP-C52.3, and RP-C60 were 281.6, 327.93, 363.93, and 388.74 kN, respectively (Table 3 and Figure 8a). These results indicate that increasing the compressive strength of the concrete could improve the shear bearing capacity of the composite shear connector. When the concrete strength was increased from 30 to 52.3 MPa, the shear bearing capacity improved by about 29.2%.

(2) Influence of the diameter of the stud

The shear bearing capacities of the specimens LT-ds13-C52.3, RP-C52.3, and LT-ds19-C52.3 were 355.88, 363.93, and 372.94 kN, respectively (Table 3 and Figure 8b). These results indicate that increasing the diameter of the stud could improve the shear bearing capacity of the composite shear connector. When the diameter of the stud was increased from 13 mm to 19 mm, the shear bearing capacity improved by about 4.8%.

(3) Influence of the thickness of the perforated plate

The shear bearing capacities of the specimens RP-C52.3 and LT-t24-C52.3 were 363.93 and 389.41 kN, respectively (Table 3 and Figure 8c). These results reveal that increasing the thickness of the perforated plate could improve the shear bearing capacity of the composite shear connector. When the thickness of the perforated plate was increased from 16 mm to 24 mm, the shear bearing capacity improved by about 7%.

(4) Influence of the diameter of the opening

The bearing capacities of the specimens LT-D30-C52.3, RP-C52.3, and LT-D50-C52.3 were 360.78, 363.93, and 351.84 kN, respectively (Table 3 and Figure 8d). These results indicate that increasing the diameter of the opening could improve the shear bearing capacity, but an excessively large diameter could exert adverse effects. The reason was that increasing the diameter could enlarge the shear bearing area of the concrete tenon, thereby improving the shear bearing capacity. However, if the opening was too large, the strength of the perforated plate would decrease, reducing the shear bearing capacity.

(5) Influence of the diameter of the penetrating steel bar

The shear bearing capacities of the specimens RP-C52.3, LT-dr16, and LT-dr20 were 363.93, 363.12, and 361.82, respectively (Table 3 and Figure 8e). This demonstrated that increasing the diameter of the penetrating steel bar exerted no noticeable effect on the shear bearing capacity. The reason was that the shear bearing area of the concrete tenon in the hole would decrease with an increase in the diameter of the penetrating steel bar under the premise of a constant opening diameter; however, both the shear resistance of the concrete tenon and the flexural resistance of the penetrating steel bar could influence the shear bearing capacity of the specimen.

Based on the aforementioned analysis results, it can be observed that the concrete strength had the greatest influence on the shear bearing capacity, followed by the thickness of the perforated plate. When the concrete strength was constant in the actual project, it was the key to controlling the thickness of the perforated plate considering the structure of the composite shear connector.

5. Calculation Formula for Shear Resistance

The composite shear connector consists of studs and PBL shear connectors. The longitudinal shear resistance consists of the following parts: the dowel action of the concrete tenon in the hole of the perforated plate and the penetrating steel bar, the bearing effect of the bottom of the perforated plate, and the mechanical engagement of the stud. More research and theoretical analyses regarding these two shear connectors has been conducted by domestic and foreign scholars.

First, the "Code for Design of Steel-Concrete Composite Bridges" (GB 50917-2013) specified the formula for calculating the shear bearing capacity when the stud breaks:

$$P_{\mathrm{u}} = 1.19 A_{\mathrm{st}} \left(\frac{E_c}{E_s} \right)^{0.2} \left(\frac{f_{cu}}{f_{st}} \right)^{0.1} \tag{1}$$

where P_{u} is the shear bearing capacity (N) when the stud breaks; A_{st}, f_{st}, E_s are the cross-sectional area (mm^2), ultimate tensile strength (MPa), and elastic modulus (GPa) of the stud, respectively; f_{cu} and E_c are the cubic compressive strength (MPa) and elastic modulus (GPa) of concrete, respectively.

Moreover, Xue [13] produced the calculation formula of shear bearing capacity under the failure mode of stud rupture considering the length to diameter ratio of studs by push-the experimental study as follows:

$$\begin{gathered} P_{\mathrm{u}} = 3 A_{\mathrm{st}} \left(\frac{E_c}{E_s} \right)^{0.4} \left(\frac{f_{cu}}{f_{st}} \right)^{0.2} \\ \lambda = \begin{cases} 6 - \frac{H}{1.05 d_s} & (H/d \leq 5) \\ 1 & (5 < H/d < 7) \\ \frac{H}{d_s} - 6 & (H/d \geq 7) \end{cases} \end{gathered} \tag{2}$$

where *H/ds* is the aspect ratio of the stud, and the meanings of other symbols are the same as those of Equation (1).

Subsequently, Al-Darzi [37] performed a parametric analysis of PBL shear connectors by using the Ansys software. Based on the multiple linear regression analysis of the simulation results, the formula for calculating the shear bearing capacity of the PBL shear connectors with concrete end bearing effect is expressed as follows:

$$P_{\mathrm{u}} = 255.31 + 7.62 \times 10^{-4} h t f_c{}' - 7.59 \times 10^{-7} A_r f_{ry} + 2.53 \times 10^{-3} A_{sc} \sqrt{f_c{}'} \tag{3}$$

where P_{u} is the shear bearing capacity of PBL shear connector with concrete end bearing effect (kN); h and t are the height and thickness of the perforated plate (mm); A_{sc} and $f_c{}'$ are the area of the concrete tenon in the hole [2nπ(D2-dr2)/4, where n is the number of openings] (mm^2) and cylinder compressive strength of concrete (MPa); A_r and f_{ry} are the cross-sectional area (mm^2) and yield strength (MPa) of the penetrating steel bar, respectively.

In addition, Zhang [38] conducted a multiple linear regression analysis of the experimental and finite element simulation results and then proposed a formula for calculating the shear bearing capacity of the intermittently arranged PBL shear connectors as follows:

$$P_{\mathrm{u}} = 3.5 h t f_{cu,k} + 32 A_{sc} \sqrt{f_{cu,k}} + 5.2 A_r f_{ry} \tag{4}$$

where P_{u} is the shear bearing capacity of the intermittently arranged PBL shear connectors; $f_{cu,k}$ is the standard value of cubic compressive strength of concrete (MPa); the meanings of other symbols are the same as those of Equation (3).

Therefore, based on the aforementioned research results and the failure form of the test specimens, the formula for calculating the shear bearing capacity of the composite shear connector is proposed as follows:

$$P_{\mathrm{u}} = \beta_1 h t f_{cu} + \beta_2 A_r f_{ry} + \beta_3 A_{sc} {f_{cu}}^{0.5} + \beta_4 A_{st} \left(\frac{E_c}{E_s} \right)^{0.2} \left(\frac{f_{cu}}{f_{st}} \right)^{0.1} \tag{5}$$

where P_{u} is the shear bearing capacity of the combined shear key (N); h and t are the height and thickness of the perforated plate (mm); A_r and A_{st} are the cross-sectional area of the penetrating steel bar and the stud rod, respectively (mm^2); A_{sc} is the area of the concrete tenon in the hole [2nπ(D2-dr2)/4, where n is the number of openings] (mm^2); f_{cu} is the cubic compressive strength of concrete (MPa); f_{ry} is the yield strength (MPa) of the penetrating steel bar; f_{st} is the ultimate tensile strength of the stud (MPa); E_c and E_s are the elastic modulus (GPa) of concrete and stud, respectively; β_1, β_2, β_3, β_4 are undetermined coefficients.

The results of the 49-model analysis in Table 3 were subjected to multivariate linear regression on Equation (5), resulting in the formula for calculating the shear bearing capacity of the composite shear connectors as Equation (6). The Pearson correlation coefficient of the regression analysis was 0.87 (see Figure 9), which demonstrates that the calculated value is consistent with the value obtained using finite element analysis.

$$P_{\mathrm{u}} = 2.55htf_{cu} + 5.21 \times 10^{-1}A_r f_{ry} + 2.05A_{sc}{f_{cu}}^{0.5} + 2.34A_{sc}f_{st}\left(\frac{E_c}{E_s}\right)^{0.2}\left(\frac{f_{cu}}{f_{st}}\right)^{0.1} \quad (6)$$

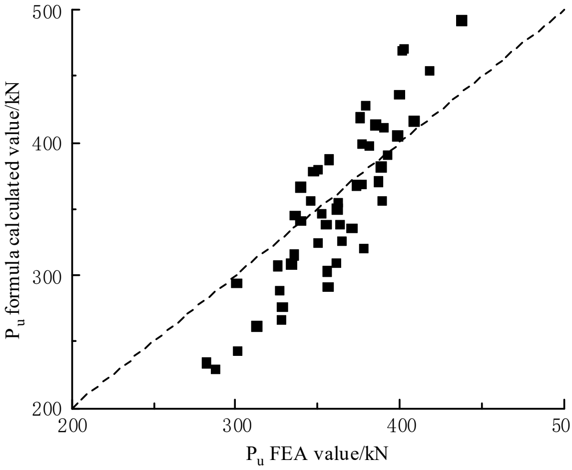

Figure 9. Results comparison of shear capacity Equation (6) and FEA.

Table 5 compares the measured shear bearing capacity of the specimens and the results calculated using Equation (6). The outcome indicates that the calculation results of Equation (6) are well correlated with the test results of the composite shear connector push-out specimens; however, the calculation results are conservative—about 0.85 times the measured value. With the safety factor considered, Equation (6) could be used to calculate the shear bearing capacity of the composite shear connector in practical engineering.

Table 5. Results comparison of Equation (6) and push-out test.

Specimen Number	The Test Measured Value of Shear Bearing Capacity P_u/kN	The Calculated Value of Equation (6) $P_{u,c}$/kN	$P_{u,c}/P_u$
LT-C-1	404.0	326.3	0.81
LT-C-2	375.1	326.3	0.87
LT-C-3	375.1	326.3	0.87
LT-C	384.7	326.3	0.85

P_u in the table is 1/4 of the shear bearing capacity of the push-out specimen—that is, the specimen LT-C contains one stud and one PBL.

6. Conclusions

Through the tests and numerical simulations of the shear bearing performance of the steel–polypropylene fiber ceramsite composite bonding interface, the following major conclusions are drawn:

(1) The push-out test on one stud shear connector (LT-S), one PBL shear connector (LT-P), and three stud–PBL composite shear connectors (LT-C) reveals the superior shear resistance of the composite shear connector. In addition, composite shear connectors have excellent plastic deformation properties.

(2) The finite element software Abaqus was used to simulate the push-out test with five specimens. The analysis results were in agreement with the experimental phenomenon, load–slip curve, and shear bearing capacity of the push-out test. In addition, the illustrations of stress and concrete damage can reveal the shear damage mechanism and failure form of the shear connector. It is feasible to use finite element simulation to reveal the force mechanism of the composite shear connector and perform parametric analysis.

(3) According to the results of the orthogonal test simulation analysis, increases in the stud diameter, perforated plate thickness, and concrete strength can improve the shear bearing capacity of the composite shear connector, among which the concrete strength has the most obvious effect. However, an increase in the diameter of the penetrating steel bar exerts no apparent effects on shear capacity. Regarding the opening diameter, the shear bearing capacity increases first and then decreases with its increase. When the diameter of the opening was nearly 40 mm, the shear bearing capacity was more favorable. The optimal construction combination for the composite shear connector is the stud with 19 mm diameter, the opening with 50 mm diameter, the perforated plate with 24 mm thickness, and the penetrating steel with 16 mm diameter. Moreover, when the concrete strength was constant in the actual project, it was the key to controlling the thickness of the perforated plate, considering the structure of the composite shear connector.

(4) By conducting multivariate linear regression analysis on the results of the finite element parameter analysis, the calculation formula of the shear bearing capacity of the composite shear connector was obtained. The calculated value is about 85% of the measured value, which displays a good correlation and verifies the feasibility of the calculation formula. The calculation results are conservative, and a formula can be used to calculate the shear bearing capacity of the composite shear connector in practical engineering with the safety factor considered.

(5) The experimental results, numerical simulation outcomes, and calculation formulas have a certain promoting effect on further reducing the self-weight of the composite structure and improving the shear resistance of the composite structure interface. However, the number of push-out test specimens is relatively small. In subsequent studies, experiments will be performed to further discuss the shear resistance of the stud–PBL composite shear connector and the method for calculating the shear bearing capacity.

Author Contributions: Conceptualization, H.Z. and Z.F.; methodology, H.Z.; software, P.L.; validation, Z.F. and B.Z.; formal analysis, Z.F.; investigation, Z.F.; resources, Y.L. and B.Z.; data curation, Z.F., Y.L. and B.Z.; writing—original draft preparation, Z.F. and Y.L.; writing—review and editing, H.Z. and Z.F.; visualization, Y.L.; supervision, H.Z.; project administration, H.Z.; funding acquisition, H.Z. All authors have read and agreed to the published version of the manuscript.

Funding: This study was funded by the National Natural Science Foundation of China (grant numbers 51778630, 52178182, and U1934217), China Railway Science and Technology Research and Development Plan Project (grant numbers 2020-Major project-02, 2021-Major project-02, 2021-Key projects-11).

Institutional Review Board Statement: Not applicable.

Informed Consent Statement: Not applicable.

Data Availability Statement: The data presented in this study are available on request from the corresponding author.

Conflicts of Interest: The authors declare no conflict of interest.

References

1. Liang, F.; Zhou, Z.X. New Shear Connectors Based on PBL Shear Connector for Composite Arch Members. *Struct. Eng. Int.* **2014**, *2*, 281–284.
2. Wu, F.; Liu, S.; Xue, C.; Yang, K.; Feng, Y.; Zhang, H. Experimental Study on the Mechanical Properties of Perfobond Rib Shear Connectors with Steel Fiber High Strength Concrete. *Materials* **2021**, *14*, 3345. [CrossRef] [PubMed]
3. Zhan, Y.L.; Yin, C.; Liu, F.; Song, R. Push out tests on headed studs and PBL shear connectors considering external pressure. *J. Bridge Eng.* **2020**, *25*, 04019125. [CrossRef]
4. Fang, Z.C.; Jiang, H.B.; Chen, G.F.; Dong, X.T.; Shao, T.F. Behavior of grouped stud shear connectors between precast high-strength concrete slabs and steel beams. *Steel Compos. Struct. Int. J.* **2020**, *34*, 837–851.
5. Kim, S.H.; Jung, C.Y.; Ann, J.H. Ultimate strength of composite structure with different degrees of shear connection. *Steel Compos. Struct. Int. J.* **2011**, *11*, 375–390. [CrossRef]
6. Ahn, J.H. Shear resistance of the perfobond-rib shear connector depending on concrete strength and rib arrangement. *J. Constr. Steel. Res.* **2010**, *66*, 1295–1307. [CrossRef]
7. Zhang, J.D.; Shoji, A.; Kobayashi, K. Design of a PC box girder bridge with corrugated steel webs in Hanshin expressway. In Proceedings of the First International Structural Engineering and Construction Conference, Honolulu, HI, USA, 24–27 January 2001; pp. 581–586.
8. Deng, W.Q.; Gu, J.C.; Liu, D.; Hu, J.; Zhang, J. Study of single perfobond rib with head stud shear connectors for a composite structure. *Mag. Concrete. Res.* **2019**, *71*, 920–934. [CrossRef]
9. Zheng, S.J.; Zhao, C.; Liu, Y.Q. Parametric push-out analysis on perfobond rib with headed stud mixed shear connector. *Adv. Civ. Eng.* **2019**, *2019*, 1–16. [CrossRef]
10. Jin, L.D. Analysis on spatial mechanical properties of steel-concrete segment with composite connectors. *Steel. Constr.* **2019**, *34*, 69–74.
11. Chen, H.; Guo, Z.X.; Liu, Y.; Guo, L.-T. Study on the shear resisting mechanism and strength for an innovative composite shear connector. *Eng. Mech.* **2019**, *36*, 159–168.
12. Gu, J.C.; Liu, D.; Deng, W.Q.; Zhang, J.D. Experimental study on the shear resistance of a comb-type perfobond rib shear connector. *J. Constr. Steel. Res.* **2019**, *158*, 279–289. [CrossRef]
13. Yang, Y.; Chen, Y. Experimental study on mechanical behavior of PBL shear connectors. *J. Bridge. Eng.* **2018**, *23*, 04018062. [CrossRef]
14. Xue, W.C.; Ding, M.; Wang, H.; Ziwen, L. Static behavior and theoretical model of stud shear connectors. *J. Bridge. Eng.* **2008**, *13*, 623–634. [CrossRef]
15. Young, H.L.; Min, S.K.; Heecheul, K.; Dae-Jin, K. Shear resistance of stud connectors in high strength concrete. *Struct. Eng. Mech.* **2014**, *52*, 647–661.
16. Hu, Y.; Yin, H.; Ding, X.; Li, S.; Wang, J.Q. Shear behavior of large stud shear connectors embedded in ultra-high-performance concrete. *Adv. Struct. Eng.* **2020**, *23*, 136943322093920. [CrossRef]
17. Huo, J.; Wang, H.; Zhu, Z.; Liu, Y. Experimental Study on Impact Behavior of Stud Shear Connectors between Concrete Slab and Steel Beam. *J. Struct. Eng.* **2018**, *144*, 04017203. [CrossRef]
18. Su, Q.T.; Yang, G.T.; Bradford, M.A. Static behaviour of multi-row stud shear connectors in high- strength concrete. *Steel Compos. Struct. Int. J.* **2014**, *17*, 967–980. [CrossRef]
19. Xu, C.; Sugiura, K.; Masuya, H.; Hashimoto, K. Experimental Study on the Biaxial Loading Effect on Group Stud Shear Connectors of Steel-Concrete Composite Bridges. *J. Bridge. Eng.* **2015**, *20*, 04014110. [CrossRef]
20. Xu, C.; Sugiura, K. FEM analysis on failure development of group studs shear connector under effects of concrete strength and stud dimension. *Eng. Fail. Anal.* **2013**, *35*, 343–354. [CrossRef]
21. Ding, J.; Zhu, J.; Kang, J.; Wang, X. Experimental study on grouped stud shear connectors in precast steel- UHPC composite bridge. *Eng. Struct.* **2021**, *242*, 112479. [CrossRef]
22. Zhang, Y.Z.; Li, Q.; Xia, S. Research on the Influence Factors to the Working Performance of PBL Shear Connectors. *Appl. Mech. Mater.* **2012**, *178–181*, 2192–2198. [CrossRef]
23. Xiao, L.; Qiang, S.Z.; Xu, X. Experimental Research on PBL Shear Connector for Steel-Concrete Composite Structures. *Adv. Mater. Res.* **2011**, *163–167*, 2137–2141. [CrossRef]
24. Zhang, Z.H.; Liu, P.; He, S.H.; Ji, T.G. Research on Influence Factors and Formulae for the Bearing Capacity of Twin-PBL Shear Connectors. *Appl. Mech. Mater.* **2013**, *253–256*, 3167–3171. [CrossRef]
25. Yu, B.C.; Zhang, Y.L. The Capacity Calculation and Finite Element Analysis to PBL Shear Key. *Appl. Mech. Mater.* **2014**, *501–504*, 722–726. [CrossRef]
26. Zhang, W.J.; Du, E.X.; Liu, B.Z.; Yang, S.C. Failure Mode Attribution Analysis of PBL Shear Connector. *Appl. Mech. Mater.* **2013**, *351–352*, 683–686. [CrossRef]
27. Zhao, C.; Li, Z.; Deng, K.; Wang, W. Experimental investigation on the bearing mechanism of Perfobond rib shear connectors. *Eng. Struct.* **2018**, *159*, 172–184. [CrossRef]
28. Li, Z.X.; Zhao, C.H.; Deng, K.L.; Wang, W. Load Sharing and Slip Distribution in Multiple Holes of a Perfobond Rib Shear Connector. *J. Struct. Eng.* **2018**, *144*, 264–276. [CrossRef]

29. Zhang, J.; Hu, X.; Kou, L.; Zhang, B.; Jiang, Y.; Yu, H. Experimental study of the short-term and long-term behavior of perfobond connectors. *J. Constr. Steel Res.* **2018**, *150*, 462–474. [CrossRef]
30. Wang, X.; Zhu, B.; Cui, S.; Lui, E.M. Experimental Research on PBL Connectors Considering the Effects of Concrete Stress State and Other Connection Parameters. *J. Bridge Eng.* **2018**, *23*, 04017125. [CrossRef]
31. Du, C.; Tian, W.L.; Wang, X.W.; Wang, D.J. Experimental Research on Ceramsite Concrete Beams. *Appl. Mech. Mater.* **2012**, *166–169*, 708–711. [CrossRef]
32. Eurocode 4: Design of Composite Steel and Concrete Structures – Part 2: General Rules and Rules for Bridges. European Standard: Brussels, Belgium, 2005; pp. 56–66.
33. Xu, L.H.; Li, B.; Ding, X.X.; Chi, Y.; Li, C.; Huang, B.; Shi, Y. Experimental Investigation on Damage Behavior of Polypropylene Fiber Reinforced Concrete under Compression. *Inter. J. Concr. Struct. Mater.* **2018**, *12*, 1–20. [CrossRef]
34. Cifuentes, H.; Garcia, F.; Maeso, O.; Medina, F. Influence of the properties of polypropylene fibres on the fracture behaviour of low-, normal- and high-strength FRC. *Constr. Build. Mater.* **2013**, *45*, 130–137. [CrossRef]
35. Ding, F.X.; Ying, X.Y.; Yu, Z.W. Unified calculation method of uniaxial mechanical properties of lightweight aggregate concrete. *J. Cent. South Univ. (Sci. Tec.).* **2010**, *41*, 1973–1979.
36. Qin, H.; Zhao, X.Z. Numerical analysis of composite columns with high steel ratio under cyclic loading. *Struct. Eng.* **2014**, *30*, 25–31.
37. Al-Darzi, S.Y.K.; Chen, A.R.; Liu, Y.Q. Finite element simulation and parametric studies of perfobond rib connector. *Am. J. Appl. Sci.* **2007**, *4*, 122–127. [CrossRef]
38. Zhang, J.D.; Gu, J.C.; Deng, W.Q.; Fu, H. Shear behavior of perfobond rib shear connectors for pre-fabricated composite bridges. *China J. Highw. Transp.* **2018**, *31*, 71–80.

coatings

Article

Research on Bending Performance of Concrete Sandwich Laminated Floor Slabs with Integrated Thermal and Sound Insulation

Peng Liu [1,2,3], Sisi Xie [1,*], Lei Liu [1,*], Ao Luo [1], Ning Zhang [4], Sasa He [4], Yingye Wu [5], Wen Xu [6], Ying Chen [2,7] and Zhiwu Yu [1,2]

[1] School of Civil Engineering, Central South University, 22 Shaoshan Road, Changsha 410075, China; liupeng868@csu.edu.cn (P.L.); ddt1205@163.com (A.L.); zhwyu0512@163.com (Z.Y.)
[2] National Engineering Laboratory for High Speed Railway Construction, Central South University, Changsha 410075, China; 2015038@csu.edu.cn
[3] Chenzhou Changxin Residence Technology Co., Ltd., 8 Huihuang Road, Chenzhou 423000, China
[4] Hunan Zhongda Design Institue Co., Ltd., 68 Shaoshan Road, Changsha 410075, China; l15116277646@163.com (N.Z.); szwang863@163.com (S.H.)
[5] Hunan Construction Project Investment Management Co., Ltd., 199 Xiangfu Road, Changsha 410007, China; llppp98@163.com
[6] Railway Group 5 Mechanization of Engineering Co., Ltd., 32 HongtangCong Road, Hengyang 421002, China; 216056@csu.edu.cn
[7] School of Civil Engineering, Central South University of Forestry and Technology, 498 Shaoshan Road, Changsha 410004, China
* Correspondence: xiesisicumtb@163.com (S.X.); llmysy@163.com (L.L.)

Abstract: In this study, a full-scale test on the bending performance of concrete sandwich laminated floor slabs with integrated thermal and sound insulation was carried out, and the effects of different reinforcement ratios on the bending performance of concrete sandwich laminated floor slabs were investigated as well as the variation law of the failure modes, characteristic loads, load-mid span deflection, load-rebar strain curves, and anti-slip performance. The results indicate that the concrete sandwich laminated floor slabs present typical bending failure characteristics. According to bending failure characteristics, the damage process can be divided into three stages, i.e., elasticity, cracking, and failure. The bearing capacity significantly increases with the increase in reinforcement ratio. The normal service, yield, and ultimate loads of bearing capacity of the floor slabs with a larger reinforcement ratio increase by 54.55%, 52.94%, and 46.46%, respectively. Moreover, the mid-span deflection decreases significantly with the increase in reinforcement ratio, and the cracking expansion is also delayed. Before cracking, the prefabricated layer and laminated layer can realize load bearing together, and the floor slab is in a state of complete interaction. When the floor slabs reach the ultimate state, the superimposed surface produces a sliding effect, and the floor slab is in a state of partial interaction. The finite element analysis software ABAQUS (with the version number of ABAQUS 2020, the chief creator of David Hibbitt, and the sourced location of the United States) was used to perform nonlinear numerical simulation. The test results accord well with the simulation results, which verifies the correctness of the finite element model. Based on finite element simulation, the influence of post-cast concrete strength on the ultimate load can be ignored.

Keywords: concrete sandwich laminated floor slab; bending properties; bond-slip; deflection

Citation: Liu, P.; Xie, S.; Liu, L.; Luo, A.; Zhang, N.; He, S.; Wu, Y.; Xu, W.; Chen, Y.; Yu, Z. Research on Bending Performance of Concrete Sandwich Laminated Floor Slabs with Integrated Thermal and Sound Insulation. *Coatings* **2022**, *12*, 1075. https://doi.org/10.3390/coatings12081075

Academic Editor: Paolo Castaldo

Received: 29 June 2022
Accepted: 28 July 2022
Published: 30 July 2022

1. Introduction

Laminated structures are widely used in architecture, aviation, train locomotives, and other fields. At present, extensive experimental research and theoretical analysis have been carried out [1–4]. Floor is an important inner envelope of the building to ensure safety, stability, and durability, which should be both heat insulation, sound insulation, waterproof, and moisture-proof at the same time. Laminated floor slab is a prefabricated concrete floor structure composed of prefabricated and laminated layers. It has good integrity and seismic resistance and has become an important horizontal bearing member of the prefabricated concrete structure [5,6]. However, its thermal and sound insulation effects fail to meet the code's requirements [7]. Therefore, it is necessary to study the structural system of thermal and acoustic bearing integrated floor slab that integrates energy saving, environmental protection, and green low-carbon [8,9]. The concrete sandwich laminated floor slab has the advantages of light weight, high strength, sound insulation, energy saving, fire resistance, good seismic performance, and convenient installation [10]. It is easy to realize product industrialization, standardization, and construction mechanization. Furthermore, it has become one of the most rapidly developing laminated floor structures.

Many studies regarding mechanical property tests and theoretical analysis of concrete sandwich laminated floor slabs have been conducted worldwide [11–14]. For example, Li et al. [15] derived a deflection calculation formula for the concrete sandwich plate in the ultimate limit state by experimental verification and numerical simulation technology. Chen et al. [16] investigated the factors that affect the bending performance of double reinforced concrete sandwich panels. Luo et al. [17] conducted bending tests of laminated slabs, and the results indicated that the prefabricated bottom plate construction form and core material significantly affect the bending performance of sandwich laminated floor slabs. Joseph et al. [18,19] analyzed the bending properties of prefabricated concrete sandwich panels under punching and bending loading conditions. Ahmad et al. [20] indicated that the cracks on the plate side were characterized by the combined effect of bending and shear stresses due to the sandwich layer. Tomlinson et al. [21] studied bending tests of laminated floor slabs with EPS as the core layer, and the results indicated that the floor slabs worked partially compositely when the shear connector failed. Currently, the expanded polystyrene (EPS) plate is mostly used as the core of concrete sandwich laminated floor slabs, which has advantages of light weight, low water absorption, good thermal insulation performance, etc. [22]. However, it has poor fire performance and is easy to burn, which can produce toxic smoke and has great safety hazards. Due to the less attention to the fire performance of insulation materials, fire accidents have been common in recent years [23]. Phenolic foam has low thermal conductivity, high fire safety coefficient, good thermal and sound insulation, etc. Therefore, when used in concrete sandwich laminated floor slabs, the thermal and sound insulation performance and the safety of the slab can be significantly improved.

The effective connection between the prefabricated and laminated layers is the basis that ensures the joint work of the laminated structure. According to research status worldwide, the primary method to solve this problem is the steel bar trusses in the laminated slabs. Wang et al. [24] investigated the bending performance of laminated slabs with trusses and stirrup reinforcement as the connections, respectively, and the results indicated that both structural forms could significantly improve the stiffness and shear resistance. Refs. [25–27] presented that truss webs can ensure the shear resistance of the laminated face. Huang et al. [28,29] investigated the bending performance of laminated slabs with different prefabricated bottom plates, and a design recommendation for structural measures was proposed. Thanoon et al. [30] regarded that truss reinforcement can provide good integrity to the laminated slab in all bending phases. Steel bar trusses can improve the shear capacity, limit the inter-story slip, and enhance the co-working property of the laminated floor slabs [31]. However, there are disadvantages such as numerous trusses, dense truss spacing, high cost, and complex vibration and compaction of post-cast layer concrete. Given the shortcomings of the steel bar truss connectors, the stirrup rebar is proposed to replace the steel bar trusses. Moreover, due to the advantages of low energy consumption, low cost, and saving the amount of steel reinforcement, the CRB600H high-strength steel bars are employed, which has remarkable economic and social benefits [32].

This paper proposed thermal and sound insulation integrated concrete sandwich laminated floor slab (Abbr. sandwich laminated floor slab). The sandwich laminated floor slab was combined with concrete layers on both sides and a phenolic core layer connected through the steel reinforcement grid. The phenolic foam board was the insulation layer, and the reinforcement grid consisted of stirrup rebars and upper and lower rebar mesh. The two-point bending tests of sandwich laminated floor slabs with different reinforcement ratios were carried out. The damage pattern, reinforcement strain, crack development distribution characteristics, and bending bearing capacity process were discussed. The influence law of reinforcement ratio on the characteristic load was also analyzed. Moreover, the slip resistance of sandwich laminated floor slabs in different stages was also studied. The force performance was numerically simulated by finite element analysis software ABAQUS. The results provided a scientific basis for the design and application of concrete sandwich laminated floor slabs with integrated thermal and sound insulation in practical projects.

2. Experimental Study

2.1. Design and Fabrication of Specimen

Two full-scale specimens were subjected to bending loads with the number of DBD01 and DBD02. Both the specimens were of the same size of 3600 mm × 2400 mm, and the thickness of the prefabricated and laminated layers was 90 mm and 70 mm, respectively. Figure 1 shows the schematic diagram of the interlayer structure.

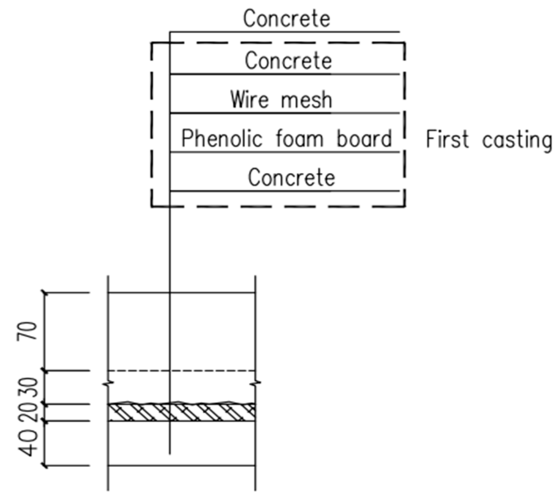

Figure 1. Schematic diagram of sandwich laminated floor slab interlayer structure.

Table 1 lists the principal design parameters of the specimens, Figure 2 shows the pouring process, and Figures 3–5 present the reinforcement diagram and the constructional detail.

The strength grade of concrete in the prefabricated and laminated layers of the specimen is C40. The type and diameter of reinforcement are the same, but their reinforcement ratios are different. The stirrup rebar is HPB300 with the design value of tensile strength f_y = 300 MPa. The longitudinal bearing and transverse distribution bars are CRB600H, with the design value of tensile strength f_y = 540 MPa. The diameters of longitudinal and distribution reinforcement are 8 mm and 6 mm, respectively. The surface reinforcement is HRB400 with a diameter of d = 8 mm, and the design value of tensile strength f_y = 400 MPa. Table 2 shows the mechanical property parameters of the steel bars.

Table 1. Detailed dimensions and reinforcement of sandwich laminated floor slabs.

Specimen Number	Size (mm)	Transverse Rebar	Longitudinal Rebar	Face Rebar	Stirrup Rebar	Rebar Ratio ρ/%
DBD01	3600 × 2400 × 160	$A^{RH}6@200$	$A^{RH}8@200$	C8@150	A6	0.26
DBD02			$A^{RH}8@100$			0.50

Figure 2. Pouring diagram of sandwich laminated floor slab.

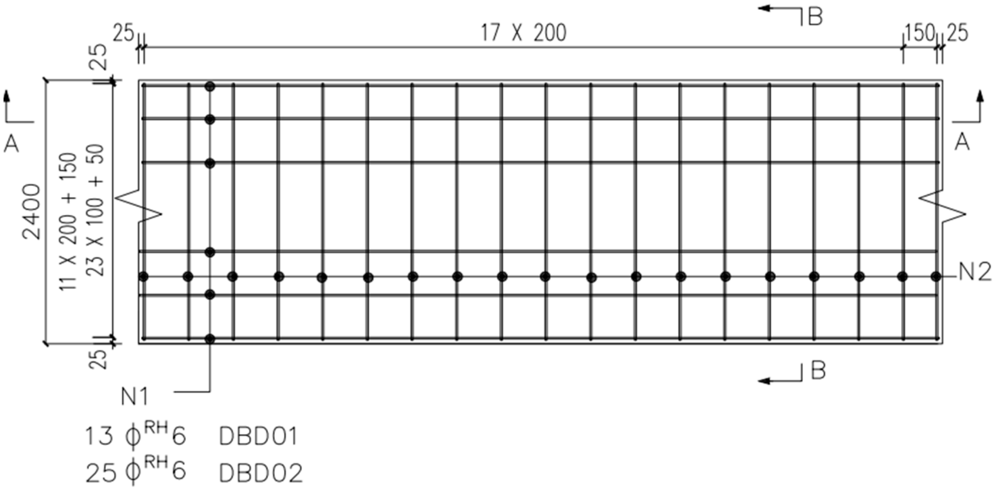

Figure 3. Reinforcement diagram of sandwich laminated floor slab (unit: mm).

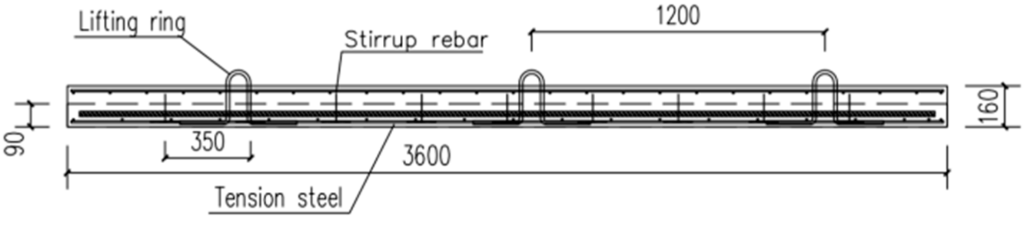

(**a**) A-A

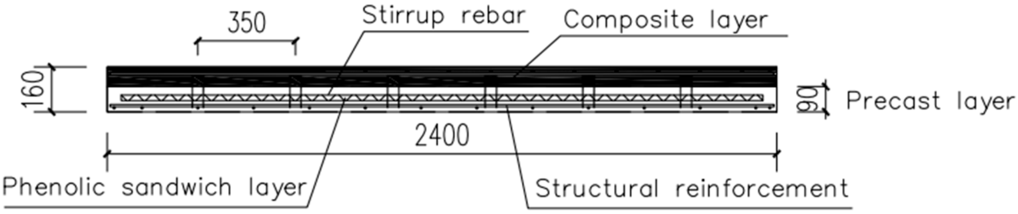

(**b**) B-B

Figure 4. Section diagram of sandwich laminated floor slab. (**a**) Section A-A of floor slab; (**b**) Section A-A of floor slab (unit: mm).

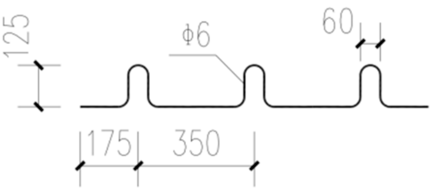

Figure 5. Schematic diagram of combined stirrup rebar (unit: mm).

Table 2. Mechanical properties parameters of steel bars.

Reinforcing Steel Type	f_{yk} (N/mm^2)	f_{stk} (N/mm^2)	E_s (N/mm^2)
CRB600H	540	600	190,000
HRB400	400	540	200,000
HPB300	300	420	210,000

The specimens were fabricated and cured according to GB/T50081-2019 [33] and were placed into a pool with the saturated solution of calcium hydroxide at (20 ± 2) °C for 28 d after demolding. There were two groups of pressure test blocks with the same batch of materials for the prefabricated and laminated layers. Moreover, three parallel specimens of each group were used to reduce the error caused by the randomness of the specimen. The loading equipment is a 100-ton electro-hydraulic servo material machine designed and produced by Shanghai New Sansi Measuring Manufacturing Co., Ltd. (Shanghai, China). Figure 6 shows the loading device and the failure mode under compression. Table 3 presents the mechanical performance parameters.

(**a**) Loading device (**b**) Loading process (**c**) Failure mode

Figure 6. Loading device and failure mode under compression.

Table 3. Mechanical properties of concrete materials.

Type	Measured Value of Compressive Strength of Prefabricated Layer (MPa)	Measured Value of Compressive Strength of Laminated Layer (MPa)	f_c (MPa)	E_c (MPa)
DB01	49.2	48.7	26.8	32,500
DB02	48.3	48.8		

2.2. Test Methods

According to GB 50010-2010 [34], instead of the equalized load, two-point centralized loading was used to load with the loading point at the trisection of the span. Sand was pre-laid at the loading point for leveling to prevent stress concentration. Figure 7 shows the schematic diagram of the test device and loading.

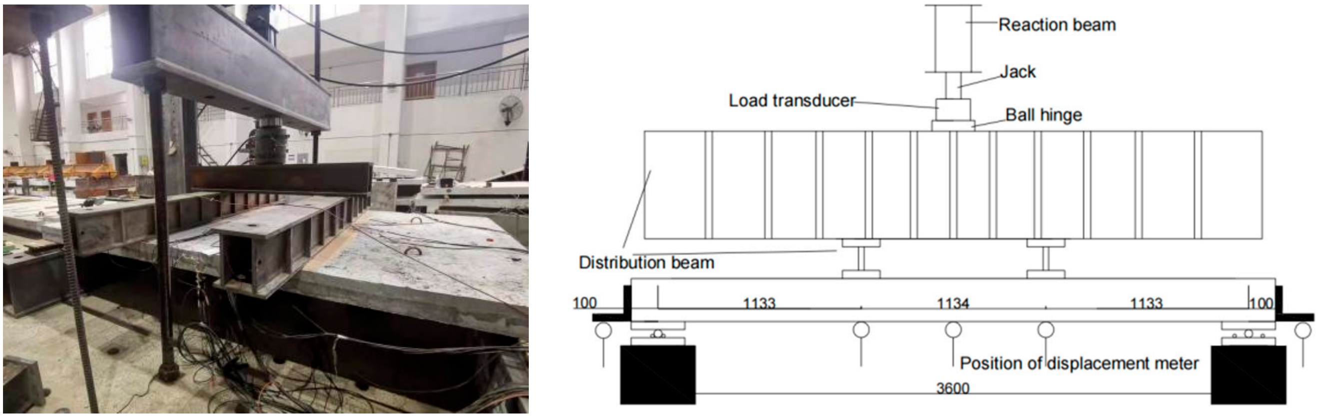

(**a**) Actual drawing of loading device (**b**) Schematic diagram of loading device

Figure 7. Schematic diagram of test device and loading (unit: mm).

The load-controlled loading system was used, including preloading and subsequent formal loading processes. The preloading process consisted of three levels, each taking 20% of the cracking load, then unloading after the preloading process and entering the formal loading stage. The formal loading process was divided into four stages. In the first stage, 20% of the cracking load was taken for each level and then entered the second stage after reaching 80% of the cracking load, and 5% of the cracking load value should be taken for each stage. Observing the strain change of the concrete at the bottom of the slab, the measured cracking load was determined when the strain deviated from the linear change significantly, and cracks appeared at the bottom of the slab. After the floor slab cracking, it entered the third stage, and 10% of the calculated value of the cracking load was taken for each level until the bearing capacity. Finally, it entered the fourth stage when reaching the ultimate state, and 5% of the limit load value was taken for each level until the specimen failed. The load holding time of each stage was 10 min. Figure 8 shows the loading system.

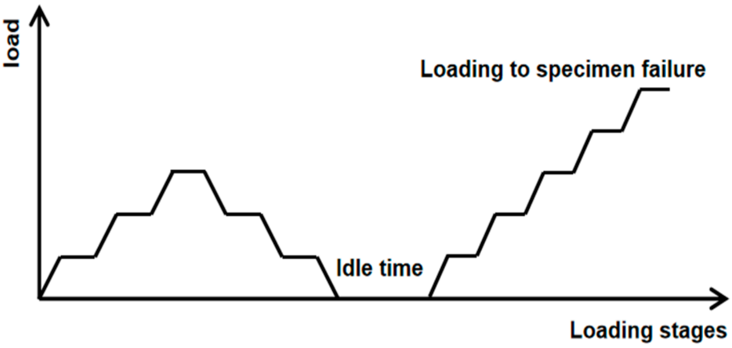

Figure 8. Loading mode diagram.

2.3. Measuring Point Layout

The reinforced strain gauges were arranged in the 1/2 and 1/3 of the bottom span and the middle of the top span, as shown in Figure 9. Concrete strain gauges were placed in the middle of both span bottom and side, as shown in Figure 10. The displacement gauges were placed at the 1/2 and 1/3 of the span and two-end supports to measure the corresponding deflection.

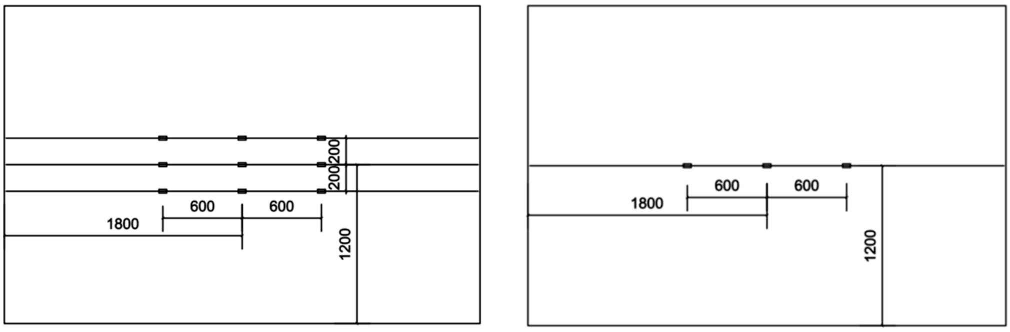

(**a**) Bottom of the floor slabs (**b**) Top of the floor slabs

Figure 9. Layout of measurement points for reinforcement strain gauges (unit: mm).

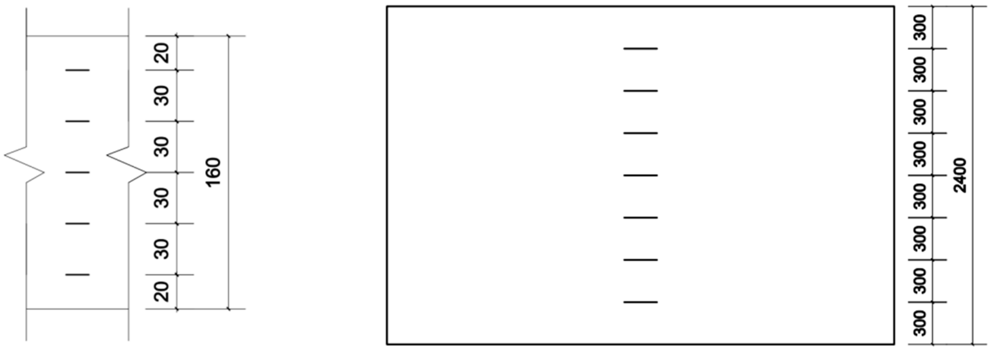

(**a**) Side of the floor slabs (**b**) Bottom of the floor slabs

Figure 10. Layout of measuring points of concrete strain gauge (unit: mm).

3. Results and Discussions

3.1. Failure Characteristics

The mid-span deflection, steel bar, and concrete strain increase slightly when the load is small. The first crack appears in the mid-span pure bending section with a load of 13 kN. At this time, the strain of steel bar, concrete, and the mid-span deflection increases slightly. Moreover, the cracks develop from the middle to both ends along the width with the load increases and mainly distributed symmetrically in the mid-span.

Firstly, the cracks on the side of the slab extend vertically upward in mid-span, and then the bending shear diagonal cracks successively appear within 1/3 of the span as the load increases. The interface between vertical and inclined cracks is a superposition surface, and the inclination angle of cracks decreases gradually. When the load is 66 kN, the deflection reaches 17.20 mm, corresponding to the width of 0.26 mm. According to GB 50010-2010, the deflection and crack width limit in the normal use stage is $L_0/200$ = 17 mm and 0.2 mm, respectively [34]. Based on the deflection and crack width control, the specimen reaches the normal use stage. When the load is 186 kN, the mid-span deflection instantly increases to 68.2 mm. According to GB 50010-2010, the deflection limit in the ultimate stage is $L_0/50$ = 68 mm [34], and the specimen reaches the ultimate state of the bearing capacity. The cracks at the bottom are mainly vertical to the axis of the short span and densely distributed within 1/3 of the span, as shown in Figure 11.

The first crack appears in the mid-span pure bending section when the load reaches 39 kN and then enters the limit stage of normal usage with the deflection of 17.10 mm when the load is 102 kN. The horizontal cracks appear at the superimposed surface when the load is 199 kN. According to GB50010-2010, the ultimate state of the bearing capacity is reached with a deflection of 17.20 mm and a width of more than 1.5 mm. Figure 12 shows the failure mode and crack distribution.

(**a**) Crack distribution at slab bottom (**b**) Crack distribution on slab side

Figure 11. Failure mode and crack distribution of DBD01.

(**a**) Crack distribution at slab bottom (**b**) Crack distribution at slab bottom

Figure 12. Failure mode and crack distribution of DBD02.

The cracking load is significantly higher, and the crack number and growth rate of DBD02 are apparently lower than that of DBD01, which indicates that the mid-span deflection of the specimen is reduced and the cracking expansion is delayed with the increase in reinforcement ratio. Table 4 shows the characteristic load of the sandwich laminated floor slab. P_{cr} is the cracking load, $P_{1/200}$ is the normal use load, P_{y} is the yield load, and P_{u} is the ultimate load. Both sandwich laminated floor slabs present typical bending failure characteristics with similar early failure characteristics and good ductility. The cracking load of DBD02 is three times of DBD01, and the normal use load, yield load, and ultimate load of bearing capacity increase by 54.55%, 52.94%, and 46.46%, respectively. This indicates that the ultimate bearing capacity is significantly improved with the increase in the reinforcement ratio, but the bonding performance of the superimposed surface should be considered as well.

Table 4. Characteristic load of sandwich laminated floor slab.

Type	P_{cr} (kN)	$P_{1/200}$ (kN)	P_{y} (kN)	P_{u} (kN)	$P_{\mathrm{cr}}/P_{\mathrm{u}}$	$P_{\mathrm{l/200}}/P_{\mathrm{u}}$	$P_{\mathrm{y}}/P_{\mathrm{u}}$
DBD01	13	66	102	127	10.24%	51.97%	80.31%
DBD02	39	102	156	186	20.97%	54.84%	83.87%

Note: The characteristic loads of the sandwich laminated floor slab include the weight of the distribution beam.

3.2. Bending Performance Analysis

3.2.1. Verification of Plane-Section Assumption

Figure 13 shows the average strain distribution of concrete along the section height in the mid-span, where ε_{c} is the concrete strain and h is the section height. Since the strain gauges are damaged after cracking, only the strain data without the cracking of floor slab side are plotted. As seen in Figure 13, the concrete average strain distribution along the height of the mid-span section is linear, which conforms to the assumption of the flat section. Strain hysteresis is not apparent between the prefabricated and laminated layers, so the flat section assumption can be taken as the basic assumption in the bearing capacity calculation analysis.

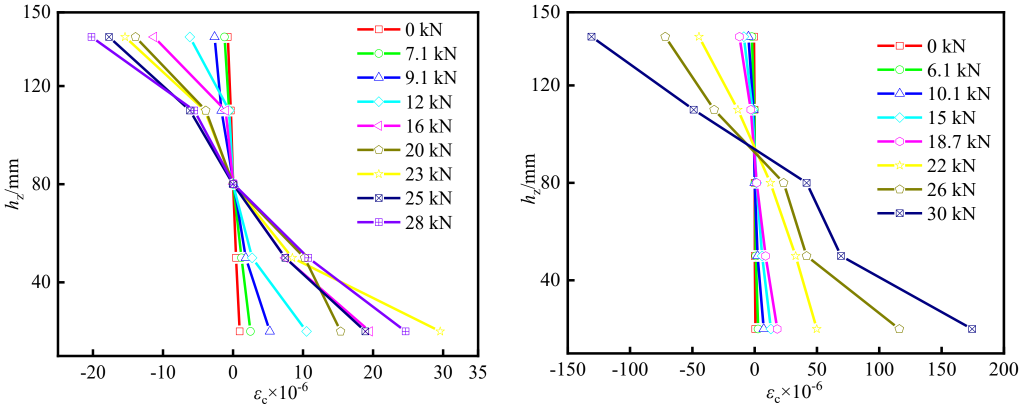

(**a**) DBD01 (**b**) DBD02

Figure 13. The concrete strain distribution along the section height in the mid-span.

3.2.2. Load-Mid Span Deflection Relationship

As shown in Figure 14, the load-mid span deflection curve is characterized by three straight lines, i.e., elasticity, cracking, and failure, indicating that the specimen has good ductility.

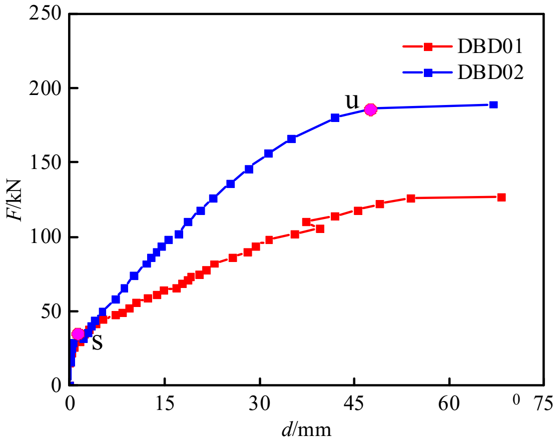

Figure 14. Load-mid span deflection curve.

a. Elastic stage (0~s). Before cracking, the specimen is in the elastic stage, and the load is proportional to the mid-span deflection. Due to the low tensile strength and high stiffness of concrete, the curve is short and steep. The cracking load of DBD02 is three times of DBD01 because the reinforcement ratio of DBD02 is twice of DBD01. The increase in reinforcement ratio can effectively delay the crack propagation.

b. Cracking stage (s~u). The slope of the curve and the bending stiffness decrease significantly after the crack appears. The load-mid span deflection curve nonlinearly increases as the floor slab enters the plastic stage. The cracking load, normal use load, and yield load of both specimens are 10%~20%, 50%~55%, and 80%~85% of the ultimate load, respectively. The curve slope of DBD02 is significantly larger than that of DBD01, and the deflection of DBD01 is lower than that of DBD01, which indicates that the increase in reinforcement ratio can effectively improve the late rigidity and reduce the mid-span deflection greatly.

c. Failure stage (u~). The curve slope sharply decreases, the load almost remains unchanged, and the deformation rapidly develops due to the low tensile strength of the phenolic foam board after the steel bars yield, which indicates that the sandwich layer significantly influences the latal rigidity and bearing capacity of specimens. The ultimate state of bearing capacity reaches when the concrete is crushed or deformed excessively, and the load-mid span deflection curve is almost horizontal.

3.3. Load-Reinforcement Strain Relationship

As shown in Figure 15, both sandwich laminated floor slabs have the same variation law. The curve development presents three-stage characteristics, i.e., elastic, elastoplastic, and failure. The curve develops linearly with a large curve slope when the load is small. When it reaches the cracking load, the reinforcement strain suddenly increases, and the slope of the curve decreases obviously. The variation trend is consistent with the load-mid span deflection curve. At this time, the concrete in the tensile zone fails, and the steel stress and strain instantly increase. The curve develops nonlinearly with the load increases, which indicates that the steel bar enters the plastic stage. Furthermore, the mid-span strain difference between the specimens increases with the increase in load, which demonstrates that the reinforcement stress is effectively retarded with the increase in reinforcement ratio.

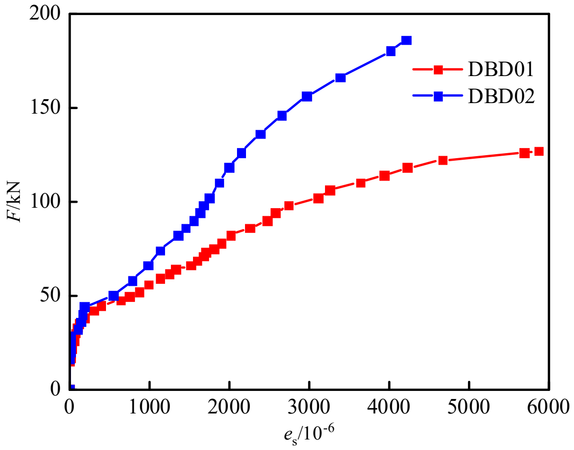

Figure 15. Load versus strain curve of reinforcement.

4. Analysis of the Slip Resistance of Sandwich Laminated Floor Slabs

4.1. Premise of Analysis

The concrete sandwich laminated floor slab is composed of reinforcement, concrete, and phenolic foam board with completely different physical and mechanical properties, which results in complex mechanical properties of the floor slab under load. The bonding performance of the laminated surface is the key to maintaining the integrity of the laminated floor slab, and the bending capacity will decrease rapidly when the laminated surface is damaged by the sliding [35], so the mechanical characteristics need to be studied before calculation.

The connection of the stirrup rebar is the key to the synergy of the upper and lower concrete slabs, whose bearing performance directly affects the overall mechanical properties of the structure. According to the stiffness of the connections, the forces of concrete sandwich laminated floor slabs can be divided into three types, i.e., non-composite, partially composite, and fully composite. For concrete sandwich laminated floor slabs of non-composite, there is no connection to transfer longitudinal shear force, and the upper and lower concrete layers are equivalent to two independent slabs with the same span and curvature. For concrete sandwich laminated floor slabs of partially composite, the magnitude of the transferred longitudinal shear force is related to the stiffness. The section strain effect also needs to be considered when performing equilibrium analysis. For concrete sandwich laminated floor slabs of fully composite, the stiffness of the connectors is large enough to avoid the slippage effect. The force pattern of the concrete sandwich plate is the same as that of the cast-in-place floor slab [36–38]. Figure 16 shows the distribution of shear and strain under bending moment.

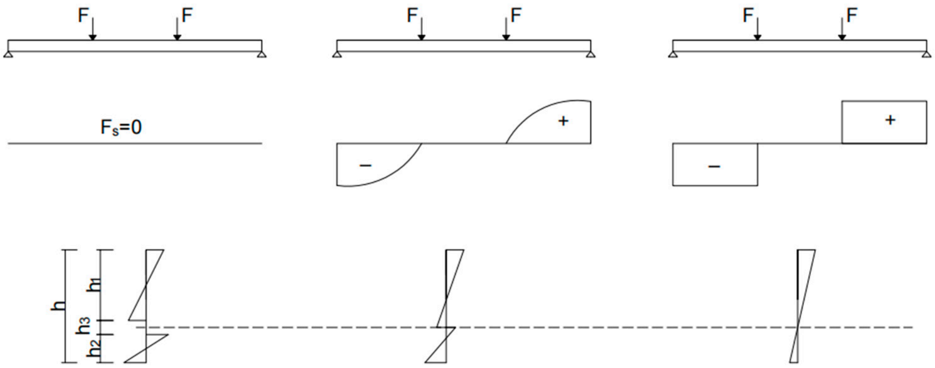

(**a**) Non-composite (**b**) Partially composite (**c**) Fully composite

Figure 16. Distribution of shear force and strain.

4.2. Anti-Slip Performance before Cracking

The overall performance of the floor slab is good before cracking, which conforms to the plane-section assumption. Therefore, the cracking load M_{cr} can be calculated according to the fully composite action. Moreover, the bending performance of the phenolic foam board is ignored while calculating the elastic moment due to the small bending stiffness. According to GB 50010-2010 [34], the formulas for calculating the cracking load are as follows:

$$M_{cr} = \gamma f_{tk} W_0 \quad (1)$$

$$\gamma = (0.7 + \frac{120}{h})\gamma_m \quad (2)$$

$$W_0 = \frac{I_0}{h - y_0} \quad (3)$$

where M_{cr} is the cracking load of the positive section of the concrete sandwich laminated floor slab, γ is the coefficient of plasticity influence of the resisting moment, γ_m is the base value of the plastic influence coefficient of the resisting moment of the cross-section, and W_0 is the elastic resisting moment of the tensile edge of the cross-section.

The cracking moment can be determined according to Equations (1)–(3), and the calculated values are compared and analyzed with the measured values, as shown in Table 5.

Table 5. Composite working performance of sandwich laminated floor slabs.

Specimen Number	Before Cracking			At Limit State			
	M_{cs} (kN·m)	M_{cr} (kN·m)	$\mid(M_{cs}-M_{cr})/M_{cs}\mid$	M_{ut} (kN·m)	M_{un} (kN·m)	M_{uf} (kN·m)	M_{ut}/M_{uf}
DBD01	7.3	6.9	6.1%	71.8	12.5	128.7	55.7%
DBD02	22.0	22.5	2.1%	105.1	15.5	169.5	62.0%

Noted: M_{cs} is the measured cracking moment, and M_{cr} is the calculated cracking moment.

4.3. Anti-Slip Performance in Limit State

The ultimate moment of the normal section at the state of non-composite and fully composite states are calculated, respectively [17], and then the composite working performance of both specimens is judged. The formulas for calculating the ultimate load of non-composite state are as follows:

$$\alpha_1 f_{ct} b x_t = f_{yt} A_{st} \quad (4)$$

$$\alpha_1 f_{cb} b x_b = f_{yb} A_{sb} \quad (5)$$

$$M_{un} = \alpha_1 f_{ct} b x_t (h_{0t} - \frac{x_t}{2}) + \alpha_1 f_{cb} b x_b (h_{0b} - \frac{x_b}{2}) \quad (6)$$

where M_{un} is the normal section ultimate bending moment, x_{t} and x_{b} are the calculated compression zone of laminated and prefabricated layers, respectively, $h_{0\mathrm{t}}$ and $h_{0\mathrm{b}}$ are the effective height of laminated and prefabricated layers, respectively, f_{yt} and f_{yb} are the strength of reinforcement tensile reinforcement in the laminated and prefabricated layers, respectively, A_{st} and A_{sb} are the area of tensile reinforcement in the laminated and prefabricated layers respectively, and f_{cb} and f_{ct} refer to the axial compressive strength of laminated and prefabricated concrete layers, respectively, which is calculated and determined according to $f_{\mathrm{c}} = 0.76 f_{\mathrm{cu,k}}$.

The formulas for calculating the ultimate load of a fully composite state are as follows:

$$\alpha_1 f_{\mathrm{ct}} b x = f_{\mathrm{yb}} A_{\mathrm{sb}} + f_{\mathrm{yt}} A_{\mathrm{st}} \tag{7}$$

$$M_{\mathrm{uf}} = \alpha_1 f_{\mathrm{ct}} b x (h_0 - \frac{x}{2}) + f_{\mathrm{yt}} A_{\mathrm{st}} (h_0 - a_{\mathrm{s}}) \tag{8}$$

where M_{uf} is the normal section ultimate bending moment, x is the height of the calculated compression zone, h_0 is the effective height of the section, and a_{s} is the distance from the resultant force point of the reinforcement in the compression area to the compression edge.

As shown in Table 5, the following conclusions can be drawn:

(1). Before cracking, the cracking moment error between the calculated and measured values is not larger than 7% under the fully composite state, and there is no relative slip, indicating good connection performance between the upper and lower concrete.

(2). When it reaches the ultimate state, the upper and lower concrete layers of the specimen are in a partially composite state. The reason is that the stirrup rebar is flexible and deforms under the transverse shear force, which results in the sliding effect and failure of co-working property.

(3). The slip resistance of DBD01 under the damage stage is less than that of DBD02, which indicates that the slip resistance at the later stage of loading can be enhanced with the increase in reinforcement rate.

5. Finite Element Analysis

The finite element calculation software ABAQUS is used to simulate the bending test. Except for the different reinforcement ratios, the other test conditions and loading methods of DBD01 and DBD02 are exactly the same. Therefore, only the finite element simulation analysis of DBD01 is carried out. The simulation is compared with the experimental results, and the finding can provide a theoretical basis for the structural mechanical analysis of the sandwich laminated floor slab.

The dimensions of the finite element model are the same as those of the actual specimen. The analysis includes the following steps: defining material properties and analysis types, defining loads and boundary conditions, defining interactions, meshing, and post-processing of results. The concrete damaged plasticity (CDP) model in the ABAQUS material library is selected to simulate concrete [39], and the constitutive relationship is calculated according to GB50010-2010 [34]. The bilinear model is used to simulate rebar, and the slope of the second section is 1/100 of the first section [40]. The three-dimensional solid element (C3D8R) with an eight-node reduced integral is used in concrete, and the two-node linear three-dimensional truss element (T3D2) is used in the steel bar. Establish four different material types, including a concrete material: C40, and three reinforcement types: CRB600H, HRB400 and HPB300. The constraint is applied at the bottom of the pad block to simulate the simply supported condition. Referring to the test value, the applied load value during finite element simulation is 140 kN. Assuming that the reinforcement and concrete are firmly bonded, they are coupled through embedded area constraint. The slip of the superimposed surface is ignored, and tie contact is used to simulate the bonding surfaces. The total number of elements is 91,163 and of nodes is 130,322. Figure 17 shows the constraints, loading, and mesh division of the model.

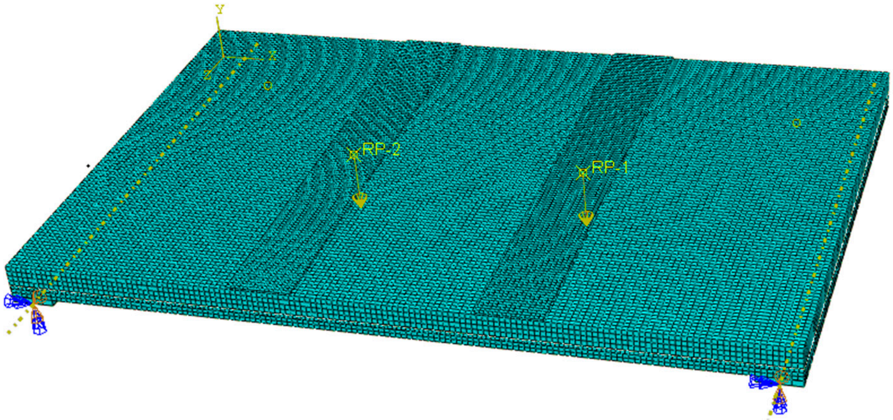

Figure 17. Finite element model of the specimen.

5.1. Damage Analysis of Sandwich Laminated Floor Slab

The damage and crack distribution of sandwich laminated floor slabs are closely related to the stress damage distribution, so it is necessary to carry out the stress damage analysis. As seen in Figure 18, the cracks at the bottom slab are mainly concentrated within the span of the loading point and are symmetrically distributed from the middle of the span to both ends. The crack direction is parallel to the short span of the sandwich laminated floor slabs. The cracks on the side of the slab gradually develop from the bottom to the top, with the inclination angle decreasing while passing through the sandwich layer. Moreover, the distribution of tensile damage at the bottom and side of the plate is roughly consistent with the crack location during the test. Therefore, the finite element simulation results can reflect the actual damage.

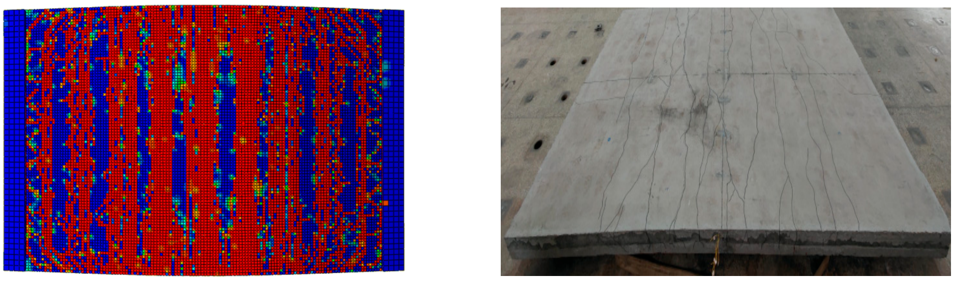

(**a**) Tensile damage nephogram of slab bottom (**b**) Test failure mode of slab bottom

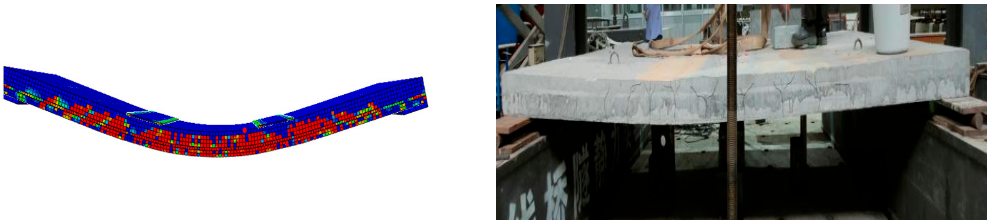

(**c**) Tensile damage nephogram of slab side (**d**) Test failure mode of slab side

Figure 18. Tensile damage nephogram and failure mode.

5.2. Comparative Analysis of Load-Deflection Curve, Load-Reinforcement Strain Curve, and Bearing Capacity

Figure 19 shows the comparison between the finite element simulation and the test curve, which indicates that the simulated results accord well with the measured results, so the finite element method can be used for deeper analysis. The experimental values of cracking load are slightly smaller than the simulated values, which is mainly due to incomplete constraints of combined interface and bond-slip between reinforcement and concrete. However, the influences of material difference, manufacturing error, and curing conditions are ignored during simulation calculation, which is assumed under the ideal conditions, and accordingly results in the deviation between the simulated and the measured values.

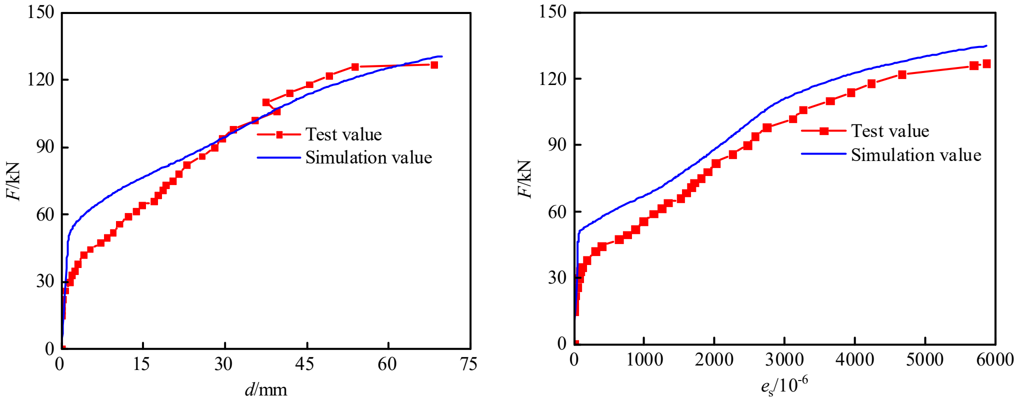

(a) Load-deflection curve

(b) Load-reinforcement strain curve

Figure 19. Load-deflection curve and load-reinforcement strain curve.

Table 6 shows the comparison of bearing capacity between the measured and the simulated value. The results show that the simulated values accord well with the measured values. The difference between the normal use load, yield load, and ultimate load of the specimen is 2%~16%. The root mean square error is 0.015, which indicates that the deviation between the simulated and the measured values between different characteristic loads is small. The deviation of cracking load is relatively large due to the discreteness of concrete properties and the deviation during manufacturing and loading. The simulation results reflect the test conditions well, especially the ultimate bearing capacity. Therefore, the finite element simulation method can be used to further analyze the mechanical performance of the sandwich composite floor.

Table 6. Comparison between simulated and measured values of specimen bearing capacity.

Specimen Number	Characteristic Load	Measured Value	Simulated Values	∣Simulated Values-Measured Value∣/Measured Value
DBD01	P_{cr} (kN)	13	24	0.46
	$P_{1/200}$ (kN)	66	79	0.16
	P_y (kN)	102	109	0.06
	P_u (kN)	127	130	0.02

5.3. Effect of Post-Cast Layer Concrete Strength

Concrete strength significantly influences the mechanical performance of the sandwich laminated floor slab. In order to further explore the influence of post-cast layer concrete strength on the normal use load and ultimate load of the specimen, the bearing performance under different post-cast concrete strength grades is compared and analyzed by numerical simulation. As shown in Figure 20, the load-deflection curves of the sandwich laminated floor slab with different concrete strength grades have the same variation trend, which shows an upward trend with the increase in concrete strength. The mid-span deflection of the same load decreases with the increase in concrete strength overall but is not significant. As the strength increases, the normal service load and ultimate load of the specimen gradually increase overall. When the concrete strength of the post-cast layer is C30, C35, and C40, the normal use load and ultimate load are the same at about 80 and 131 kN, respectively, and slightly increased to about 84 and 134 kN, respectively, when the concrete strength of the post-cast layer is C50 and C60. The tensile reinforcement firstly yields, and then the concrete is crushed, which is classified as an under-reinforced failure. The main reason is that during the period from the cracking to the ultimate bearing capacity, the post-cast layer concrete has not been damaged, and the load of the sandwich laminated floor slabs is borne by the tensile reinforcement at the bottom. The reinforcement ratio of the sandwich laminated floor slabs with different post-cast layer concrete strength is the same in the finite element simulation, so the difference in bearing capacity between the specimens is small. The effect of post-cast concrete strength can be ignored because of the small difference. Table 7 shows the effect of the concrete strength of the post-cast layer on the characteristic load.

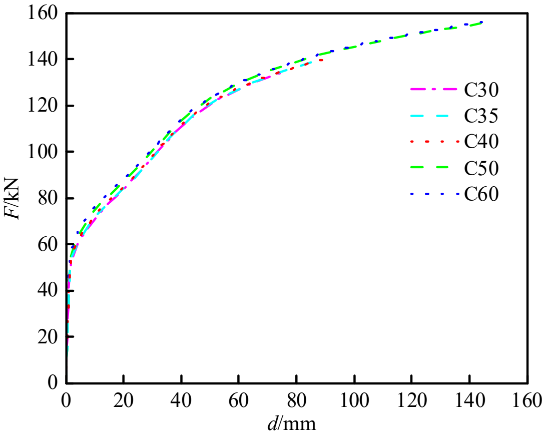

Figure 20. Load-deflection curve of specimens under different post-cast concrete strengths.

Table 7. Effect of concrete strength of post-cast layer on the characteristic load.

Concrete Strength of the Post-Cast Layer	C30	C35	C40	C50	C60
$P_{1/200}$ (kN)	80	80	80	83	85
P_{u} (kN)	131	131	132	134	134

6. Conclusions

The concrete sandwich laminated floor slabs with integrated thermal and sound insulation are proposed. The experimental research, theoretical analysis, and numerical simulation are carried out on two full-size specimens, and the major conclusions are as follows:

(1). The whole bending failure process of the sandwich laminated floor slab can be divided into three stages: elasticity, cracking, and failure. The demarcation points are concrete cracking and steel yielding, respectively. The bearing capacity of the sandwich laminated floor slab is significantly improved with the increase in reinforcement ratio. The normal use load, yield load, and the ultimate load with a larger reinforcement ratio are increased by 54.55%, 52.94%, and 46.46%, respectively. When the reinforcement ratio is increased, the late stiffness and the structural integrity are significantly improved. Moreover, the mid-span deflection decreases significantly with the increase in reinforcement ratio, and the cracking expansion is also delayed.

(2). The pure bending section of the sandwich laminated floor slab conforms to the plane-section assumption under the action of two-point symmetrical loads. The anti-sliding performance results show that the prefabricated and the laminated layer are fully composite before cracking, and the common bearing can be realized. The specimen is partially composite when reaching the ultimate state, with the slip effect on the superposition surface.

(3). The simulated and measured results accord well, which has the same variation of failure mode, load-deflection, and load-reinforcement strain. The difference between the simulated and the measured values of the ultimate load is less than 5%, which verifies the feasibility and effectiveness of the finite element analysis method. Further extending the analysis, the effect of the concrete strength of the post-cast layer on the normal use and ultimate load is not significant and can be neglected.

Author Contributions: Conceptualization, P.L. and S.X.; methodology, S.X. and L.L.; software, S.X. and A.L.; resources, N.Z.; data curation, S.H.; writing—original draft preparation, S.X.; writing—review and editing, P.L. and L.L.; visualization, Y.W.; supervision, W.X.; project administration, Y.C.; funding acquisition, Z.Y. All authors have read and agreed to the published version of the manuscript.

Funding: This study was funded by the National Natural Science Foundation of China (grant numbers 52178182, 52108262, and U1934217) and China Railway Science and technology research and development plan project (grant numbers 2020-Major project-02, 2021-Major project-02, 2021-Key projects-11). Authors also have received research grants from the Natural Science Foundation of Hunan Province of China (2020JJ5982), Science and Technology Innovation Program of Hunan Province (2020RC4049), Science and Technology Development Project of Chenzhou Municipal Science and Technology Bureau (ZDYF2020218), Hunan Innovative Province Construction Special Project (2020GK4058), and National Science Foundation for Distinguished Young Scholars of Hunan Province (Grant No. 2022JJ10075).

Institutional Review Board Statement: Not applicable.

Informed Consent Statement: Not applicable.

Data Availability Statement: Not applicable.

Conflicts of Interest: The authors declare no conflict of interest.

References

1. Huang, L.J.; An, Q.; Geng, L.; Wang, S.; Jiang, S.; Cui, X.P.; Zhang, R.; Sun, F.B.; Jiao, Y.; Chen, X.; et al. Titanium Matrix Composites: Multiscale Architecture and Superior High-Temperature Performance of Discontinuously Reinforced Titanium Matrix Composites. *Adv. Mater.* **2021**, *33*, 2170039. [CrossRef]
2. Kueh, A.B.H. Buckling of sandwich columns reinforced by triaxial weave fabric composite skin-sheets. *Int. J. Mech. Sci.* **2013**, *66*, 45–54. [CrossRef]
3. Soufeiani, L.; Ghadyani, G.; Kueh, A.B.H.; Nguyen, K.T.Q. The effect of laminate stacking sequence and fiber orientation on the dynamic response of FRP composite slabs. *J. Build. Eng.* **2017**, *13*, 41–52. [CrossRef]
4. Wang, S.; Huang, L.J.; An, Q.; Jiang, S.; Zhang, R.; Geng, L.; Qu, S.X.; Peng, H.X. Regulating crack propagation in laminated metal matrix composites through architectural control. *Compos. Part B Eng.* **2019**, *178*, 107503. [CrossRef]
5. Ding, K.W.; Zhang, Y. Study on Composite Slab Structure. *Appl. Mech. Mater.* **2012**, *214*, 311–314.
6. Wang, L.; Zhang, H.Y. Summary of Study on Composite Concrete Slabs. *Appl. Mech. Mater.* **2013**, *2544*, 695–698.
7. Wang, Q.J.; Huang, X. Configuration and construction technology of the heat preservation sound insulation mortar. *Concrete* **2012**, *5*, 108–110.
8. Joseph, J.D.R.; Prabakar, J.; Alagusundaramoorthy, P. Precast concrete sandwich one-way slabs under flexural loading. *Eng. Struct.* **2017**, *138*, 447–457. [CrossRef]
9. Sharkawi, N.; Baharun, A. Effect of Different Types of Paint to Residential Building. *J. Civ. Eng. Sci. Technol.* **2016**, *7*, 68–74. [CrossRef]
10. Bai, F.; Davidson, J.S. Analysis of partially composite foam insulated concrete sandwich structures. *Eng. Struct.* **2015**, *91*, 197–209. [CrossRef]
11. O'Hegarty, R.; Kinnane, O. Review of precast concrete sandwich panels and their innovations. *Constr. Build. Mater.* **2020**, *233*, 117145. [CrossRef]
12. Xu, D.F.; Chen, L.M.; Tao, S.N.; Cheng, S.C.; Xiao, F. The Study on Connector's Mechanical Performance of Energy-Saving Precast Concrete Sandwich Panel Structure. In Proceedings of the International Conference on Energy Development and Environmental Protection, Shenzhen, China, 17–18 September 2016; pp. 100–106.
13. Chen, Z.H.; Zhoum, T.; Lium, H.B.; Chen, Y.H.; Wang, X.D. Experimental and Theoretical Study on Structural Behavior of Fabric Reinforced Concrete Sandwich Panels. *Adv. Sci. Lett.* **2011**, *4*, 663–668. [CrossRef]
14. Zhu, M.C.; Liu, Z.R.; Chen, Z.H. Performance analysis of prestressed concrete sandwich composite slabs. *China Concr. Cem. Prod.* **2001**, *5*, 47–49.
15. Li, Y.B.; Du, Y.Y.; Men, D.H. Analysis on bending performance of concrete sandwich panels. *Build. Struct.* **2015**, *45*, 91–95.
16. Chen, H.Q.; Xie, J.; Zhu, L.M.; Dai, Z.Q. Experimental Research on Flexural Performance of Concrete Sandwich Two-Way Panels Reinforced by Bi-Steel. *J. Tianjin Univ.* **2009**, *42*, 35–40.
17. Luo, B.; Huang, W.; Ma, X.; Li, B.; Zhou, W.C.; Ren, S.S. Flexural behavior of sandwich composite panels with core material of expanded polystyrene thermal insulation motar. *J. Zhejiang Univ. Eng. Sci.* **2019**, *53*, 2185–2196.

18. Joseph, J.D.R.; Prabakar, J.; Alagusundaramoorthy, P. Flexural behavior of precast concrete sandwich panels under different loading conditions such as punching and bending. *Alex. Eng. J.* **2018**, *57*, 309–320. [CrossRef]
19. Joseph, J.D.R.; Prabakar, J.; Alagusundaramoorthy, P. Insulated precast concrete sandwich panels under punching and bending. *PCI J.* **2019**, *64*, 68–79. [CrossRef]
20. Ahmad, A.; Singh, Y. Flexural behavior of Expanded Polystyrene core Reinforced Concrete Sandwich Panels with different construction methods and end conditions. *Structures* **2021**, *34*, 2900–2911. [CrossRef]
21. Tomlinson, D.; Fam, A. Analytical approach to flexural response of partially composite insulated concrete sandwich walls used for cladding. *Eng. Struct.* **2016**, *122*, 251–266. [CrossRef]
22. Xu, M.G.; Wang, X.; Ding, Z.W. Development of Out-Wall External Thermal Insulation System Based on Rock-Wool. *Appl. Mech. Mater.* **2012**, *174–177*, 1589–1592.
23. Qi, B.; Zheng, C.; Lv, H.; Li, C.Z.; Le, B.L.; Zhang, F. Research and Application of Phenolic Resin in the External Thermal Insulation and Fire Resistance Composite System. *Eng. Plast. Appl.* **2012**, *40*, 28–30.
24. Wang, L.; Jin, L.Z.; Wang, D.W. Experimental study on flexural behavior of UHPC aminated plates with different superimposed surfaces. *J. Build. Struct.* **2018**, *39* (Suppl. S2), 43–51.
25. Zhang, X.Y. Experimental research on factors influencing the rigidity of concrete composite slab with steel bar truss. *J. Hefei Univ. Technol. Nat. Sci.* **2014**, *9*, 1122–1126.
26. De Seixas Leal, L.A.A.; de Miranda Batista, E. Composite floor system with CFS trussed beams, concrete slab and innovative shear connectors. *REM Int. Eng. J.* **2020**, *73*, 23–31. [CrossRef]
27. Cheng, J.Y.; Zhao, L.; Yang, J.J. Study on Short-Term Rigidity of Precast Composite Slab with Steel Truss and Concrete. *Adv. Mater. Res.* **2013**, *639–640*, 198–205.
28. Huang, W.; Luo, B.; Li, B.; Xu, X.K.; Su, Y.J. Experiment on Flexural Behavior of Green Concrete Composite Slab with Different Structural Forms. *J. Hunan Univ. Nat. Sci.* **2019**, *46*, 35–44.
29. Huang, H.L.; Wu, F.B.; Zhu, M.Q.; Zeng, C.J.; Lv, W.R. Influence of rib details on flexural behavior of concrete composite slab with precast prestressed ribbed panel. *J. Build. Struct.* **2015**, *36*, 66–72.
30. Thanoon, W.A.; Yardim, Y.; Jaafar, M.S.; Noorzaei, J. Development of interlocking mechanism for shear transfer in composite floor. *Constr. Build. Mater.* **2010**, *24*, 2604–2611. [CrossRef]
31. Chen, Z.H.; Wang, J.; Cui, X.T.; Jiang, J.Q.; Wang, Z.Y.; Qiu, H.F.; Huang, Z.Y. Field test study on bearing capacity of assembled concrete composite slab. *New Build. Mater.* **2020**, *47*, 49–52.
32. Hao, M.J.; Zheng, W.Z.; Chang, W. Evaluating Stress-Strain Properties of Reinforcing Steel for Reinforced Concrete. *Adv. Civ. Eng. Mater.* **2020**, *9*, 283–297. [CrossRef]
33. *GB/T 50081-2019*; Standard for Test Methods of Concrete Physical and Mechanical Properties. National Standard of the People's Republic of China: Beijing, China, 2019.
34. *GB 50010-2010*; Code for Design of Concrete Structures. National Standard of the People's Republic of China: Beijing, China, 2010.
35. Ma, X.; Huang, W.; Luo, B.; Zhang, J.R.; Xie, H.Q. Reviews of concrete composite slabs—Mechanical properties and design methods. *Concrete* **2020**, *364*, 129–133.
36. Huang, J.Q.; Xu, Y.Y.; Huang, H.; Dai, J.G. Structural behavior of FRP connector enabled precast geopolymer concrete sandwich panels subjected to one-side fire exposure. *Fire Saf. J.* **2022**, *128*, 103524. [CrossRef]
37. Lameiras, R.; Barros, J.A.O.; Valente, I.B.; Poletti, E.; Azevedo, M.; Azenha, M. Seismic behaviour of precast sandwich wall panels of steel fibre reinforced concrete layers and fibre reinforced polymer connectors. *Eng. Struct.* **2021**, *237*, 112149. [CrossRef]
38. Ma, S.; Hou, D.F.; Bao, P.; Wang, D.T. Influence of alkali-resistant glass fiber on seismic performance of precast ceramsite concrete sandwich wall panels. *Structures* **2022**, *38*, 94–107. [CrossRef]
39. Xu, G.L.; Xu, Q.; Wang, J.X.; Qi, H.; Bai, Y.S. Uniaxial elastic-plastic damage constitutive model and parameters of concrete. *J. Guangxi Univ. Nat. Sci.* **2016**, *41*, 332–338.
40. Dai, Y.; Nie, S.F.; Zhou, T.H. Finite element analysis of hysteretic behavior of square steel tube confined steel reinforced concrete column steel frame ring beam joint. *J. Jilin Univ. Eng. Technol. Ed.* **2018**, *48*, 1426–1435.

coatings

Article

Research and Experimental Application of New Slurry Proportioning for Slag Improvement of EPB Shield Crossing Sand and Gravel Layer

Yongshuai Sun [1,*] and Dongjie Zhao [2]

[1] College of Water Resources & Civil Engineering, China Agricultural University, Beijing 100083, China
[2] Zhongbing Survey and Design Research Institute Co., Ltd., Beijing 100053, China
* Correspondence: causys666@163.com

Abstract: Based on the construction practice of the Beijing Metro Line 10 shield tunneling project, this paper describes research on soil improvement technology for Beijing stratum characteristics (sandy gravel stratum) and covers similar engineering conditions. It also describes the development of a new type of mud improver. Based on the laboratory tests with bentonite as the base mud and different additives, the effects of guar gum, CMC, xanthan gum, and clay medium particles on mud performance are analyzed. Then, two kinds of mud were used to conduct indoor simulated muck improvement tests (mixing test, slump test, sliding plate test, and adhesion resistance test), and the improvement effects of new mud and ordinary mud applied in pebble/round gravel and sandy soil layers were compared. The results show that xanthan gum is the best material to improve the performance of slurry, using the contrast test of bentonite-based slurry and different additives. The optimum slurry preparation scheme is 4% bentonite, 0.2% xanthan gum, 0.04% soda ash, and 1% clay particles. Using indoor simulated muck improvement tests (mixing test, slump test, slide plate test, and adhesion resistance test), the improvement effects of applying new mud and ordinary mud in pebble/round gravel and sandy soil layers are compared, and the advantages of the new mud in the application of the above two formations are verified. Among them, the new slurry has great advantages for improving the two parameters of the soil adhesion resistance coefficient and slump during shield tunneling. When the improved soil mass reaches the flowing plastic state, the proportion of new mud added to different soil mass is different. The proportion of new mud added to improved pebble/pebble soil is 28%, and that of sand and clay is 32%. It can be seen that new mud is more suitable for improving pebble/pebble soil.

Keywords: EPB shield; fluid-plastic state; muck improvement; new mud; xanthan gum; sandy gravel stratum

Citation: Sun, Y.; Zhao, D. Research and Experimental Application of New Slurry Proportioning for Slag Improvement of EPB Shield Crossing Sand and Gravel Layer. *Coatings* **2022**, *12*, 1961. https://doi.org/10.3390/coatings12121961

Academic Editor: Valeria Vignali

Received: 4 November 2022
Accepted: 10 December 2022
Published: 14 December 2022

1. Introduction

With the rapid development of urban rail transit construction, subway shield construction has been widely used with its unique advantages [1]. The EPB shield tunneling in Beijing is often carried out in sandy gravel soil [2–4], and the excavated soil mass in the natural state cannot meet the requirements of plastic fluidization of soil mass [5–7]. Therefore, this can easily lead to the instability of the excavation surface [8–12], and cause the closure of the pressure chamber [13–15], the caking of the pressure chamber [16], gushing [17,18], and other technical problems often encountered in the construction of soil layers. To ensure the normal operation of shield tunneling, the soil must have good plasticity [19,20] and low permeability [21–23].

As one of the key technologies of EPB shield, muck improvement technology has been paid more and more attention in current shield research [13,24,25]. At present, the improvement additives mainly include foam agents, dispersant, clay minerals and flocculant. The clay minerals are predominantly bentonite and clay [26,27], which are mainly used to supplement the fine particles in order to reduce the internal friction angle of the soil mass in the pressure chamber [28]. Foam agent is composed of special foam agent and compressed air, which can be used to improve the fluidity [29,30] and impermeability [31,32] of the excavated soil mass. Flocculant is mainly applicable to water-rich consolidated clay, silt, sand and fine gravel formation, which can cause particles to agglomerate in the slag to improve the plastic flow behavior of the slag [33,34]. Dispersants can disperse substances in the water to form colloidal solutions, reducing the adhesion between particles [35,36]. At present, different scholars have conducted a great deal of research on the improvement effect of the selection and proportion of these soil improvers on the EPB shield construction, and these improvement evaluations are mostly seen in indoor tests.

Relying on a tunnel project in Fuzhou, Wang, S.M [37] carried out a study on the construction of an earth pressure shield machine in high permeability and high-pressure formation by using nano bentonite CMC as the muck improver, and they evaluated the effect of this soil improver through field tests. Zhu H. H and others [38–41] evaluated the stability of the earth pressure shield in the sandy gravel stratum by establishing the DEM model, and proposed measures to improve the fluidity and wear resistance. Zhao S. S. [36] discussed the effect of adding dispersant in mud on controlling clay cake, and verified the effectiveness of the dispersant in reducing viscosity through laboratory tests. Cheng Chihao and others [42,43] carried out laboratory soil improvement test research on the micro mechanism of soil improvement with different proportioning of foam and bentonite in the EPB shield construction, and evaluated the improvement effect of different schemes in combination with field tests. Jiang Houting and others [44–46] conducted relevant tests on foam improving round gravel formation during EPB shield construction and obtained the experimental law of foam's impact on plastic fluidity of round gravel formation and the optimal foam injection ratio suitable for EPB shield construction. Xiao Chao [47] studied the influence of modified bentonite grouting on the shield driving in the sand gravel layer by simulating the earth pressure balance shield system, and obtained the mixed proportion of modified bentonite slurry for the earth pressure shield driving in the sand gravel layer. Xu Q. W and others [48–51] injected different amounts of air bubbles into the soil with different water content to reflect the effect of air bubble mixed soil on torque reduction through the reduction rate of power consumption of the mixer. The results show that adding air bubbles to sandy pebble soil can reduce the power consumption of mixing by more than 50%.

In combination with the current research on the improvement of EPB shield tunneling, there is a lack of systematic theoretical evaluation standards and methods for the basic properties of the improver, the matching relationship between the improver and the improved soil, the improvement effect of the improver, and the relationship between the improver and the shield construction parameters, which leads to the blindness of the use of the improver in shield tunneling, and may cause problems such as large material consumption and environmental pollution. Therefore, based on the construction practice of Beijing Metro Line 10 shield tunneling project, this paper conducts research on soil improvement technology for Beijing stratum characteristics (sandy gravel stratum) and covers similar engineering conditions, as well as developing a new type of mud improver. Based on the laboratory tests with bentonite as the base mud and different additives, the effects of guar gum, CMC, xanthan gum, and clay medium particles on the mud performance are analyzed, and a new mud performance improvement material with the best performance is obtained. Then, two kinds of mud were used to conduct indoor simulated muck improvement tests (mixing test, slump test, sliding plate test, and adhesion resistance test), and the improvement effects of new mud and ordinary mud applied in pebble/round gravel and sandy soil layers were compared.

2. Study on Properties of New Mud Modifier

The soil state control in the pressure chamber is the key to EPB shield construction. The soil state in the pressure chamber is different in different strata. When most undisturbed soil enters the pressure chamber, it will cause construction difficulties, which are manifested in the increased torque of the cutterhead, the dumping efficiency of the screw conveyor, and the thrust of the shielding jack, which will lead to "blocking", "gushing", "caking" and other construction problems, and even lead to the instability of the excavation surface. To solve these problems, the ideal state of the soil mass in the pressure chamber, namely the "plastic flow state", is proposed. Its physical and mechanical indexes include the permeability coefficient, internal friction angle, slump, and compression coefficient. To effectively solve these problems in construction, it is necessary to add additives to the soil for soil improvement.

2.1. Site Mud Solution

The stability of the earth pressure balance shield excavation surface is achieved by the pressure of the sealed cabin. When the mud penetrates the soil, a layer of mud film with very low permeability is formed, and the mud pressure effectively acts on the excavation surface through the mud film, so it can prevent the deformation and collapse of the excavation surface and ensure the stability of the excavation surface. One of the key issues in earth pressure shield construction is to use of a muck modifier suitable for engineering geological conditions.

To compare the development of the mud, the mud configuration scheme adopted in the construction site was studied first. The mud used on the construction site is pure bentonite mud with a bentonite content of 9%, that is, 90~120 Kg of bentonite is added to one side of the water, and the performance parameters are shown in Table 1:

Table 1. Site mud performance parameters.

Mud Performance Index			
Density (g/cm^3)	1.04	pH	10
Marsh funnel viscosity (″)	40	Static filtration (mL/30 min)	21
Apparent viscosity η_A(MPa·s)	13.5	Plastic viscosity η_p(MPa·s)	3
Dynamic shear τ_d(Pa)	10.7	Dynamic to plastic ratio τ_d/η_p	3.6
Initial static shear force (Pa)	9.2	Final shear force (Pa)	10.7
Liquidity Index	0.17	Consistency coefficient (Pa·sn)	4.2
Colloid rate	90%		

It can be seen from the above parameters that the mud of this formula has a high consistency and does not flow easily. After standing, it is even more difficult for the mud in the test tube to flow out. Therefore, the comprehensive performance of the mud should be improved by adding other additives. At the same time, the cost can be reduced by reducing the amount of bentonite.

2.2. New Mud Solution

In this paper, a new type of soil amendment that combines mineral improvement materials and water-soluble polymer improvement materials is developed. Bentonite is the main raw material of mineral modifiers, and the mineral material used in the test is the red sodium bentonite produced by the Shamaying Sodium Clay Factory in Weifang City, Shandong Province, which is used in the construction site. The solution is prepared as follows: add water to the container, stir with a mixer at medium speed, and at the same time add the sodium bentonite and other materials evenly into the container and stir. If the solution is thick, stop the mixer every few minutes. Stir the bentonite attached to the bottom layer with your hands or with sticks to speed up the dissolution, then stir at medium speed for about ten minutes.

On the one hand, if only bentonite is used to prepare slurry, the amount of bentonite is large, which leads to high slurry cost. On the other hand, the performance of the slurry is difficult to guarantee, which cannot meet the requirements for slag improvement in the EPB shield. It is therefore necessary to optimize the mud performance by adding appropriate additives. Common additives mainly include: 1. tackifier: guar gum, sodium carboxymethyl cellulose (CMC), xanthan gum, polyacrylamide; 2. lubricant; 3. PH value regulator, mainly sodium carbonate; 4. other additives such as clay particles.

Soda ash has greatly improved the performance of mud. Therefore, a proper amount of soda ash is added to the subsequent formula to improve the PH value of mud. According to the mud configuration plan of the construction site, the bentonite dosage is 9%, but the thickness is too high and the viscosity is not high. The topic of this lesson is to reduce the bentonite dosage to reduce the cost and improve the mud performance to adapt to the earth pressure balance shield. Therefore, the bentonite dosage is preliminarily determined to be 3%~5%.

In this paper, four additives will be added to evaluate the mud improvement effect, and the research scheme of the mud improvement test with different additives is shown in Table 2.

Table 2. Test Design Scheme of Different Additives.

Drugs Scheme	Water (g)	Bentonite (g)	Sodium Carbonate (g)	Guar Gum (g)	Sodium Carboxymethylcellulose (g)	Xanthan Gum (g)	Polyacrylamide (g)
F1	1000	30 (4%)	0.5 (0.05%)	2 (0.2%)	/	/	/
F2	1000	40 (5%)	0.5 (0.05%)	2 (0.2%)	/	/	/
F3	1000	50 (3%)	0.5 (0.05%)	2 (0.2%)	/	/	/
F4	1000	30 (4%)	0.5 (0.05%)	/	2 (0.2%)	/	/
F5	1000	40 (3%)	0.5 (0.05%)	/	2 (0.2%)	/	/
F6	1000	50 (3%)	0.5 (0.05%)	/	2 (0.2%)	/	/
F7	1000	30 (3%)	0.5 (0.05%)	/	/	2 (0.2%)	/
F8	1000	40 (3%)	0.5 (0.05%)	/	/	2 (0.2%)	/
F9	1000	50 (3%)	0.5 (0.05%)	/	/	2 (0.2%)	/
F10	1000	30 (3%)	0.5 (0.05%)	/	/	/	2 (0.2%)
F11	1000	40 (3%)	0.5 (0.05%)	/	/	/	2 (0.2%)
F12	1000	50 (3%)	0.5 (0.05%)	/	/	/	2 (0.2%)

Where AV represents apparent viscosity, PV represents plastic viscosity, YP represents dynamic shear, Gelin represents initial shear, Gel10 represents final shear, FL represents filtration, K represents consistency index, n represents fluidity coefficient, and YP/PV represents a dynamic plastic ratio.

See Table 3 for data of mud properties with different additives.

Table 3. Mud Performance Test Data of Different Schemes.

Scheme	AV (Mpa·s)	PV (Mpa·s)	YP (Pa)	Gelin Pa	Gel10 (Pa)	FL (mL)	K (Pa.sn)	n	Marsh Funnel Viscosity S	Colloid Rate (%)	YP/PV
F0	13.5	3	10.7	9.2	10.7	21	4.2	0.17	40	90%	3.6
F1	9	7	2.04	1.53	2.04		1.48	0.21	35	80%	0.3
F2	15.5	10	5.6	2.6	3.6		0.33	0.56	38	80%	0.56
F3	18	13	8.2	3.1	4.1		0.71	0.47	40	82%	0.63
F4	9.5	8	1.53	1.53	2.04	19	0.04	0.79	36	99%	0.19
F5	14	11	3.07	2.04	2.56	18	0.10	0.72	41	99%	0.28
F6	18	13	5.11	3.57	4.09	17	0.20	0.65	54	99%	0.39
F7	14.5	7	7.67	4.09	6.13	21	0.93	0.40	47	99%	1.10
F8	21.5	10	11.8	7.67	9.20	19	1.58	0.38	61	99%	1.18
F9	26	9	17.4	8.69	9.20	17	2.82	0.33	94	100%	1.93

It can be seen from Table 3 that the overall viscosity of the slurry added with guar gum is low, and the colloid rate is about 80%, indicating that there is more water precipitation. After adding CMC, the mud performance is obviously improved, the viscosity is improved, and the filtration is within 20 mL/30 min, meeting the requirements of filtration. The colloid rate is also greatly improved. During the preparation of the three schemes F10-F12, a large number of insoluble matters were precipitated, most of which were white blocky colloids. During the API filtration test, the liquid continued to flow downwards, with a filtration loss of about 45 mL/30 min, which seriously exceeded the requirements. Therefore, the application of polyacrylamide in mud was extremely insoluble, and the viscosity increasing effect of the mud was not ideal, so it was abandoned in future tests.

2.3. Comparative Study on Mud Performance after Adding Different Additives

2.3.1. Viscosity Contrast

The plastic viscosity is the total reflection of the internal friction between solid particles, between solid particles and liquid phases, and between liquid molecules when the slurry flows. Apparent viscosity refers to the ratio of shear stress to the shear rate at a certain shear rate, which is the sum of plastic viscosity and structural viscosity.

The viscosity comparison of different mud schemes is shown in Figure 1.

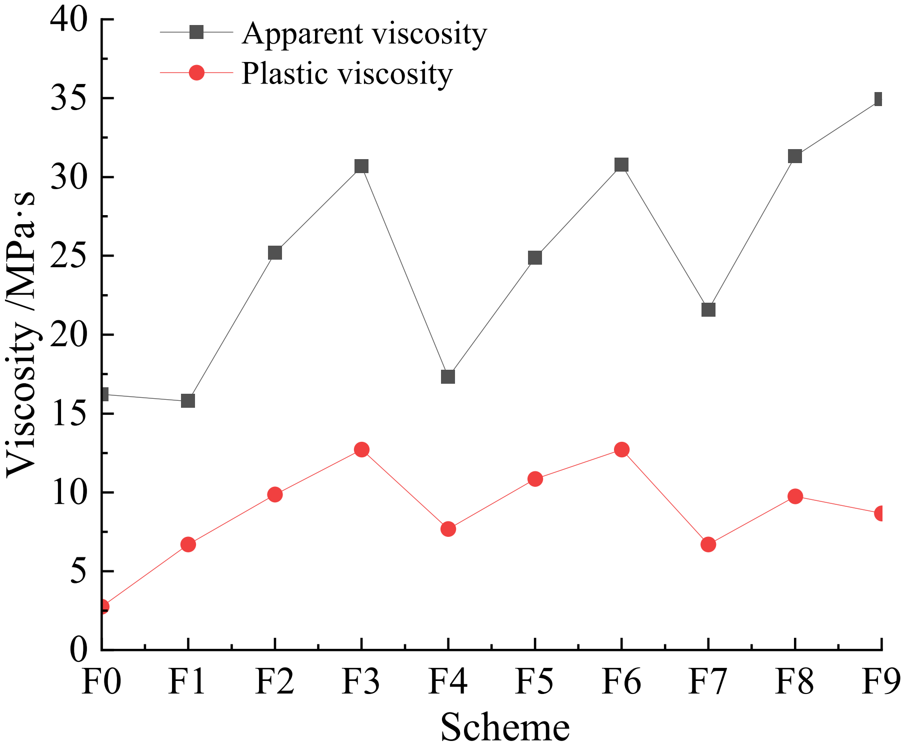

Figure 1. Viscosity Comparison of Different Mud Schemes.

It can be seen in Figure 1 above that the apparent viscosity of all schemes is higher than F0 except that the F1 and F4 schemes are lower than F0 of mud for a construction site. According to the requirements for the sand gravel layer of Beijing Metro Line 10, the slurry viscosity is high and favorable, so F1 and F4 schemes were abandoned. In the scheme of adding guar gum, CMC and xanthan gum, the formula with a bentonite dosage of 5% has the highest apparent viscosity value of mud, among which F9 is the highest, indicating that xanthan gum is superior to guar gum and CMC for improving the apparent viscosity of mud. In terms of plastic viscosity, the plastic viscosity of mud can be improved by adding a viscosity increaser, and the rule is roughly the same as the apparent viscosity. In comprehensive consideration, xanthan gum is higher than guar gum and CMC in improving mud viscosity.

2.3.2. Dynamic Shear Force Comparison

Microscopically, the dynamic shear force is the reaction of space grid structure force formed between clay particles when slurry flows, which can reflect the ability of slurry to carry sand and gravel to a certain extent. The dynamic shear force comparison of each scheme is shown in Figure 2.

As can be seen in Figure 2 above, among the schemes, only the F8 and F9 schemes have higher mud dynamic shear force values than the F0 scheme, indicating that only the addition of xanthan gum can effectively improve the mud dynamic shear force.

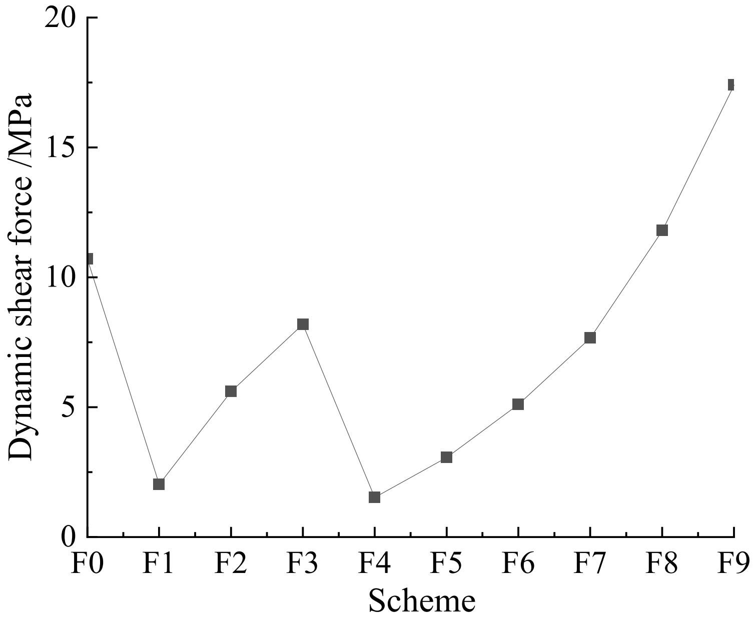

Figure 2. Dynamic shear force change diagram.

2.3.3. Static Shear Force Comparison

The static shear force comparison of each scheme is shown in Figure 3.

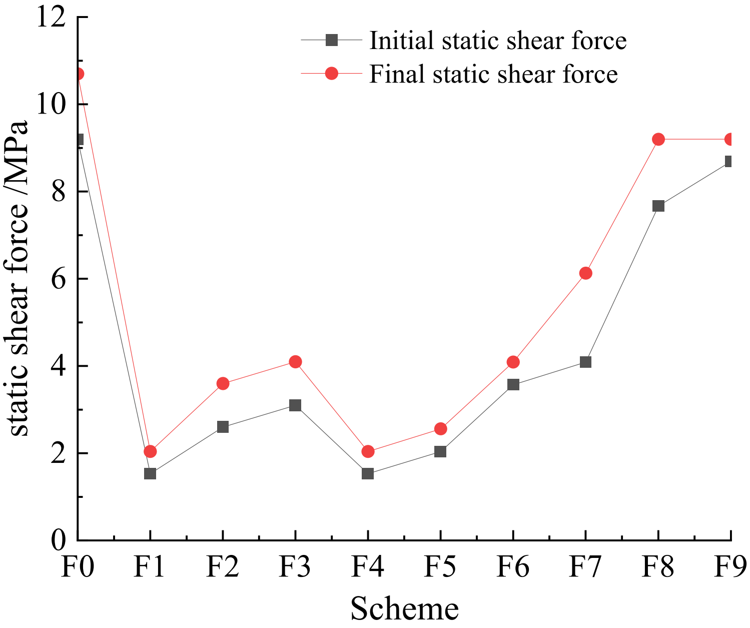

Figure 3. Variation diagram of static shear force of different muds.

The static shear force reflects the strength of the internal gel network structure when the drilling fluid is in a static state. A small initial shear force is conducive to reducing the starting power of the shield machine, so the initial shear force should be appropriately reduced; for larger sand and pebble formations, the large final shear force is conducive to the suspension and transportation of mud to the muck, so it should be appropriately increased. From the comparison of the above figures, it can be seen that except for schemes F8 and F9, the static shear forces of the other schemes are relatively small and unfavorable to the sandy cobble stratum. Only the plans F8 and F9 of adding xanthan gum are close to the construction site mud, and the initial shear force and final shear force of scheme F8 are more suitable.

2.3.4. Dynamic Plastic Ratio Comparison

The dynamic plastic ratio (τ_d/η_p) is an important indicator to measure the shear dilution characteristics of mud. Given the particularity of shield soil improvement materials, to prevent the excavated soil from settling and accumulating at the bottom of the earth ballast tank, the mud is required to have a greater rock-carrying capacity, and the dynamic-plastic ratio is recommended to be between 0.5–1.5 Pa/MPa·s in this test. The dynamic-plastic ratio comparison of each mud scheme is shown in Figure 4.

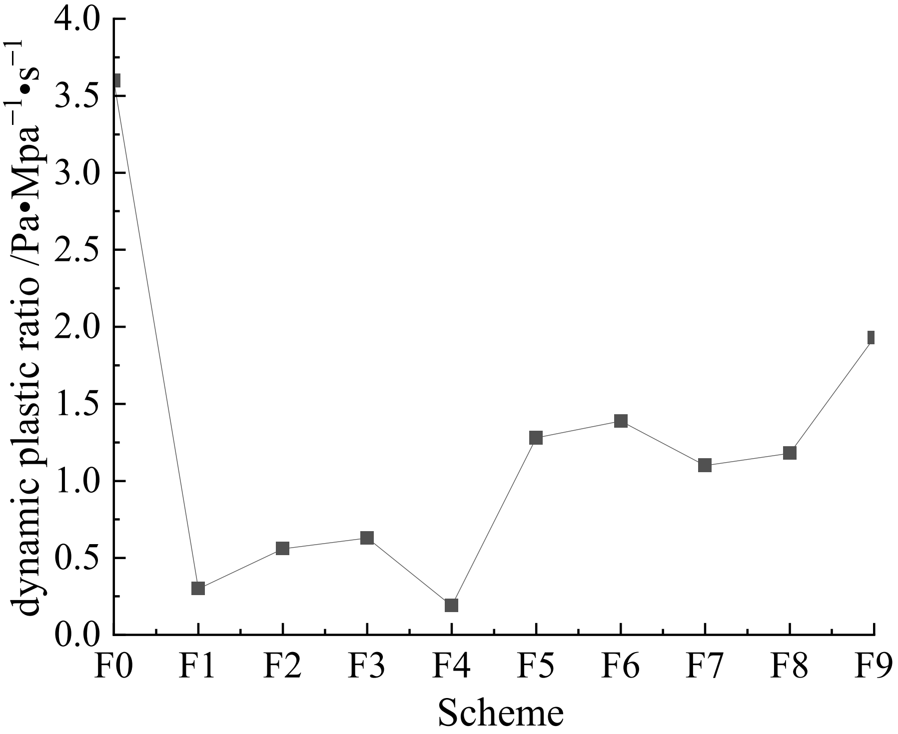

Figure 4. Changes in the dynamic-plastic ratio of different schemes.

An analysis of Figure 4 above shows that the F0 dynamic-plastic ratio of the mud scheme used on the construction site was too large, it is not conducive to the pumping of mud, and the dynamic-plastic ratio of the mud in the schemes F1~F6 was too small, which is not conducive to carrying cuttings. Scheme F8 is more suitable.

2.3.5. Flowability Index and Consistency Coefficient Comparison

The fluidity index n represents the non-Newtonian degree of the fluid within a certain flow velocity range, and the fluidity index is the representation of the fluidity of the mud. According to the knowledge of drilling fluids, the popularity index n is best around 0.5, and generally less than 1. The consistency coefficient k is the viscosity of the fluid under the 1 s^{-1} flow velocity gradient, and it is a reflection of the viscosity of the fluid; the larger the consistency coefficient, the more viscous the fluid. For the larger sand and pebble formation, the K value of the earth pressure balance shield should be 1.5~2. Figure 5 shows the fluidity index and consistency coefficient of the mud in each scheme.

An analysis of the Figure 5 above shows that the fluidity index of the mud F0 scheme used in the construction site is 0.17, which is too small; it will influence the effect of mud carrying gravel, and if the consistency coefficient is too large, the pumpability of the slurry will be poor. The consistency coefficients of schemes F2~F7 are all less than 1. It is more appropriate to comprehensively consider the fluidity index and consistency coefficient of scheme F8.

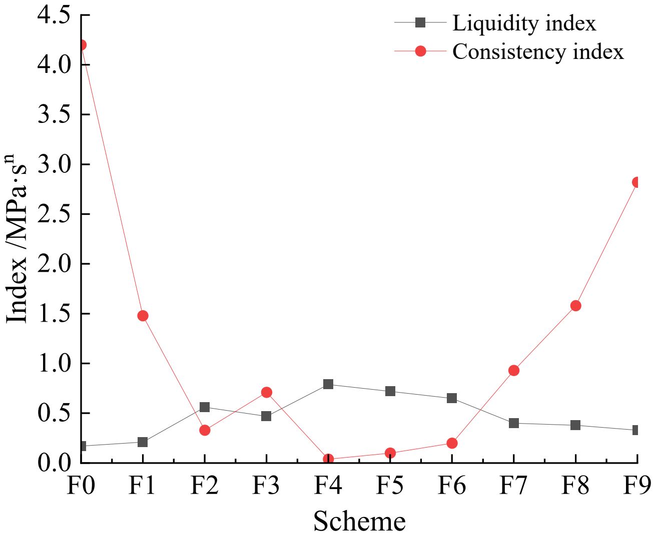

Figure 5. Changes of fluidity index and consistency coefficient for different schemes.

2.3.6. API Filtration Loss Comparison

Filtration loss is the degree of stability of the mud. The amount of water filtered by the mud is small, which can make the pore water pressure close to the excavation face rise less, ensuring that the effective mud-water pressure acting on the digging face remains unchanged after the mud film is formed, conducive to the stability of the excavation surface. To ensure mud performance, the smaller the water loss, the better. See Figure 6 for the comparison of mud filtration in each scheme.

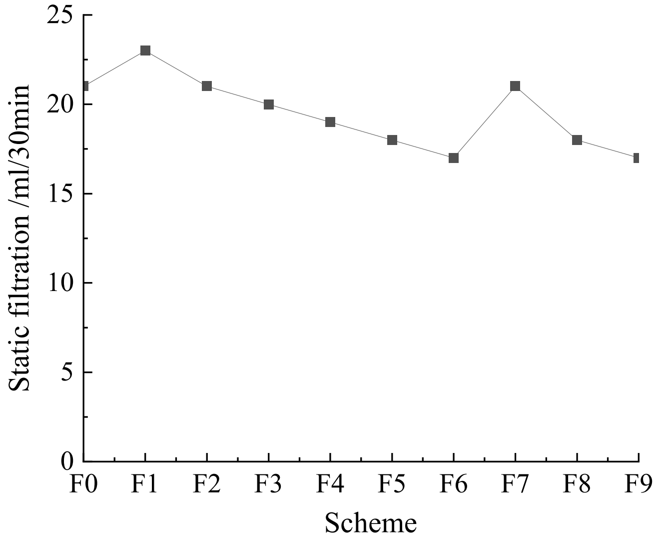

Figure 6. Variation diagram of filtration volume in different schemes.

For the earth pressure balance shield, the filtration loss is generally required to be less than 20 mL/30 min. Therefore, schemes F4, F5, F6, F8, and F9 can all meet the requirements.

2.4. Comprehensive Analysis of Mud Plan

Through the above comparative analysis of each index parameter of the mud of each scheme, it can be concluded that xanthan gum is superior to guar gum, CMC, and polyacrylamide in improving mud performance; in particular, the index parameters of scheme F8 are the most suitable, and follow-up programs were therefore carried out concerning the ratio of program F8.

2.5. Effect of Clay Particles on Mud Properties

When clay particles are added to the slurry, the particle surface dissolves, forming a layer of coating with viscous slurry. During shield construction, it will be filled in the space between sand and gravel, which plays a role in lubrication and drag reduction, increasing plasticity and reducing cutting power. To study the influence of clay particles on mud properties, the following experiments were conducted for scheme F8.

The additional amount of clay particles should not exceed 2%. The test plan is shown in Table 4.

Table 4. Test Scheme for Adding Clay Medium Particles.

Drugs Scheme	Water (g)	Bentonite (g)	Sodium Carbonate (g)	Xanthan Gum (g)	Clay Particles (g)
F13	1000	40 (4%)	0.5 (0.05%)	0.5 (0.05%)	5 (0.5%)
F14	1000	40 (4%)	0.5 (0.05%)	0.5 (0.05%)	10 (1%)
F15	1000	40 (4%)	0.5 (0.05%)	0.5 (0.05%)	15 (1.5%)

The data on mud properties are shown in Table 5.

Table 5. Test Data of Influence of Clay Particles on Mud Performance.

Scheme	AV (Mpa·s)	PV (Mpa·s)	YP (Pa)	Gelin (pa)	Gel10 (Pa)	FL (mL)	K (Pa.sn)	n	Marsh Funnel Viscosity S	Colloid Fraction(%)	YP/PV
F13	20.5	11	9.7	7.67	8.18	19	0.93	0.45	63	100%	0.88
F14	22.5	12	10.5	7.67	8.18	20	0.85	0.48	65	100%	0.88
F15	23	13	10	8.18	8.69	21	0.85	0.48	67	100%	0.77

See Figure 7 for a comparison of the parameters of each scheme.

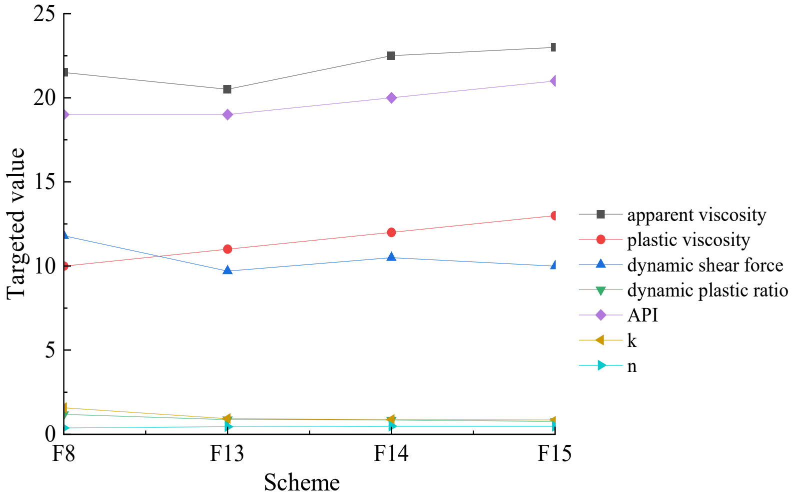

Figure 7. Comparison of clay particles' influence on mud.

It can be seen from the analysis of the above figure that the viscosity of medium particles has little impact on the overall performance of the mud. It is found in the test that the clay medium particles contain a small number of insoluble substances, and when the addition amount exceeds 1%, the insoluble substances in the mud will increase, which will have adverse effects on mud filtration and plastic viscosity. Therefore, the added amount will be controlled at 1% in the future.

3. Analysis of Indoor Muck Improvement Test

3.1. Soil Mixing Test Design

The soil mixing test mainly uses the mixing process of the mixer to simulate the soil mixing process in the pressure chamber of the earth pressure balance shield, to evaluate the improvement effect of the developed modifier on the simulated soil. The amount of soil amendment added can be controlled by changing the stirring power of the mixer. See Figure 8 for indoor mixer test. The steps of the soil stirring test are as follows:

(1) Use a plastic measuring cup to measure a certain volume of soil and pour it into the mixer, stir for 3 min, stop stirring after the reading of the power meter is stable, and record the stirring power when the reading is stable.

(2) Take out a certain amount of soil from the mixing tank and conduct the friction coefficient test, adhesion resistance test, and slump test in sequence.

(3) Pour the test soil back into the mixer, add a certain amount of soil amendment, stir the soil with a mixer for soil improvement, stir for 3 min and stop stirring after the reading of the power meter is stable. Record the stirring power when the reading is stable, and then remove the soil from the mixing drum for subsequent tests. The test cannot be terminated until the soil reaches the ideal plastic flow state. There were 3–5 groups in each experiment, and the results were averaged.

Figure 8. Indoor mixer test.

3.2. Friction Coefficient Test Design

The main purpose of the design of the friction coefficient test is to simulate the process of friction between the soil and the steel during the excavation process of the screw excavator. By measuring the external friction angle between the soil and the steel, the friction coefficient between the soil and the steel is obtained.

The specific test steps are as follows:

(1) Place the plastic ring on a stainless-steel plate, fill it with improved soil, and smooth the top of the plastic ring.

(2) Fix one end of the steel plate, and slowly lift the other end. When the ring with the improved soil starts to slide, stop and continue to lift.

(3) The angle at which the steel plate is tilted at this time is measured, which is the external friction angle φ between the improved soil and the steel plate.

(4) The friction coefficient between the improved soil and the steel plate can be obtained by the following formula. There were 3–5 groups in each experiment, and the results were averaged.

$$f = \tan\varphi$$

f—Improve the friction coefficient between soil and steel plate; φ—Improve the external friction angle between the soil and the steel plate.

3.3. Adhesion Resistance Test

The adhesion resistance test is to simulate the process of the soil adhesion to the steel surface during the excavation process of the screw excavator. By measuring the adhesion resistance of soil and steel, the adhesion resistance coefficient between soil and steel is obtained, which can be used to measure the fluidity of soil. The specific test steps are as follows:

(1) Place the iron cylinder on the iron box, fill it with the improved soil, and smooth the upper part of the improved soil.
(2) Lift the iron cylinder slowly, and stop lifting the iron cylinder when the iron cylinder is high enough.
(3) Measure the adhesion resistance F at this time, which is the adhesion resistance between the improved soil and the iron cylinder.
(4) After the adhesion resistance between the improved soil and the iron cylinder is measured, this does not provide the adhesion resistance between the reaction soil and the iron surface used, because this adhesion resistance only reflects the situation of this test. Therefore, this adhesion resistance should also be treated to a certain extent, obtaining the size of the adhesion resistance per unit area, to better reflect the change in the adhesion resistance between the soil and the iron cylinder. There were 3–5 groups in each experiment, and the results were averaged. The adhesion resistance coefficient k is obtained by the following formula. This adhesion resistance measuring device is shown in Figure 9.

Figure 9. Design of Adhesion Resistance Test Device.

Since the original adhesion resistance dimension measured in this test is a mass unit, to convert to weight units, first convert using the following formula:

$$F = M \times g$$

The surface area of the inner surface of the iron cylinder is:

$$S = \pi \times D \times h$$

The adhesion resistance coefficient between the improved soil and the iron cylinder is:

$$K = F/S = (M \times g)/(S = \pi \times D \times h)$$

M is the measured original lifting weight (kg); F is the adhesion resistance (N) between the improved soil and the iron cylinder; S is the surface area of the inner surface of the iron cylinder (m^2); D is the inner diameter of the iron cylinder (m); h is the height of the iron cylinder (m); K is the adhesion resistance coefficient between the improved soil and the iron cylinder (N/m^2).

3.4. Slump Test Design

The slump test uses standard test equipment, which is a standard slump tube. Its specifications are: the slump tube, the diameter of the upper mouth is 100 mm, the diameter of the lower mouth is 200 mm, and the height of the tube: 300 mm; Tamper, 16 mm diameter, 650 mm long, steel round bar with hemispherical ends. The slump test device is shown in Figure 10. Each experiment was conducted in 3-5 groups, and the average value of the data of each group was obtained.

Figure 10. Slump Test Device.

4. Results of Soil Improvement Test

The new mud formula is shown in Table 6.

Table 6. The new mud formula.

Raw Material	Bentonite	Xanthan Gum	Sodium Carbonate	Clay Particles
Increase the amount	4%	0.2%	0.04%	1%

4.1. Experimental Study on Improvement of Pebble/Gravel Soil

Through the qualitative analysis of the applicability of the new type of mud to pebble/gravel and sand, the improvement effect of the new mud soil amendment on the pebble/round gravel soil can be seen, and compared with the mud used in the construction site to determine the superiority of the new mud.

The test conditions are as follows: the amount of soil added is 7.5 L, after the initial test analysis, the amount of mud added was determined to be 18% of the soil volume (1350 mL), after each parameter measurement, the amount of mud added is 2% of the soil volume (150 mL) until the soil reaches the ideal plastic flow state.

4.1.1. Slump Test Design

The test soil is anhydrous round gravel soil, and the soil particle sieving is shown in Table 7.

Table 7. Particle size distribution of anhydrous round gravelly soil.

Particle Size(mm)	**60~20**	**20~5**	**5~2**	**2~0.5**	**0.5~0.25**	**0.25~0.075**	**0.075~0.005**
content(%)	30	20	15	15	10	5	5

The net power comparison curve is shown in Figure 11.

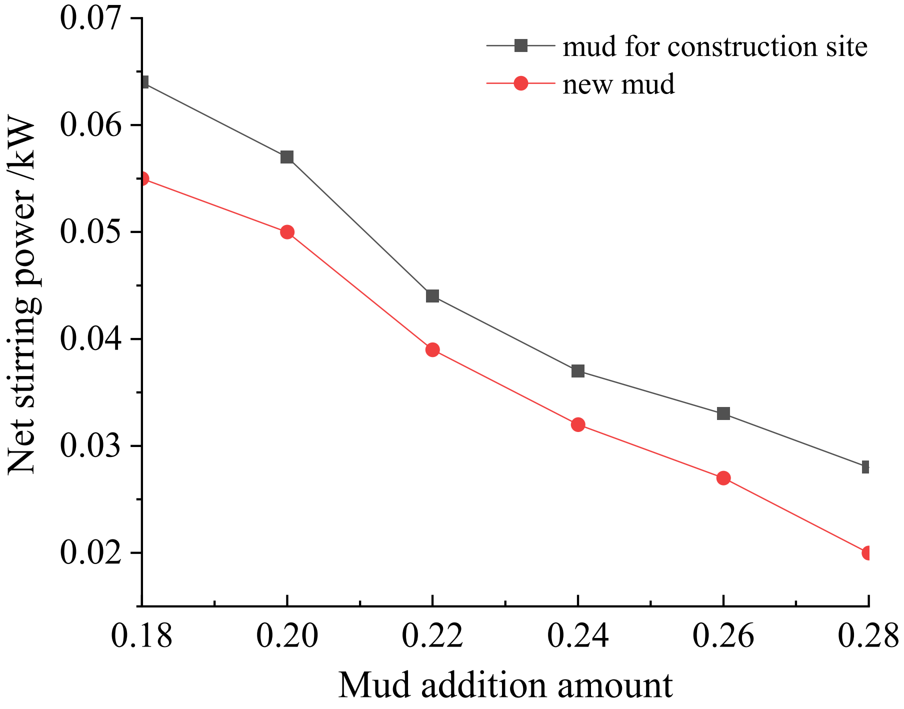

Figure 11. Comparison of net power of pebble/round gravel improved by two kinds of mud.

In Figure 11 above, it can be seen that the net stirring power of the soil is significantly reduced after adding the mud, and the influence of the two kinds of mud on the stirring power is roughly equal. It is found that when the net power is close to 0, the slag is in a better flow-plastic state. The net power of the new mud is smaller than that of the mud used on the construction site, therefore the effect of the new type of mud in reducing stirring power is better than that of the mud used in the construction site.

4.1.2. Friction Coefficient Test

The friction coefficient comparison curve is shown in Figure 12.

Through the comparison of friction coefficients, it can be seen that the friction coefficients tend to increase first and then decrease with the increase in mud addition; when the amount of mud used in the construction site is 26%, the friction coefficient has a maximum value of 0.6. The maximum value is 0.58 when the new mud addition is 22%. It was found in the test that when the friction angle was about 20°, the flow plasticity of the slag was better. When the amount of mud added was 28%, the friction coefficient of the new mud was smaller than that of the land-use mud, therefore, the performance of the new type of mud for improving the coefficient of friction of the muck is better than that of the mud used in the construction site.

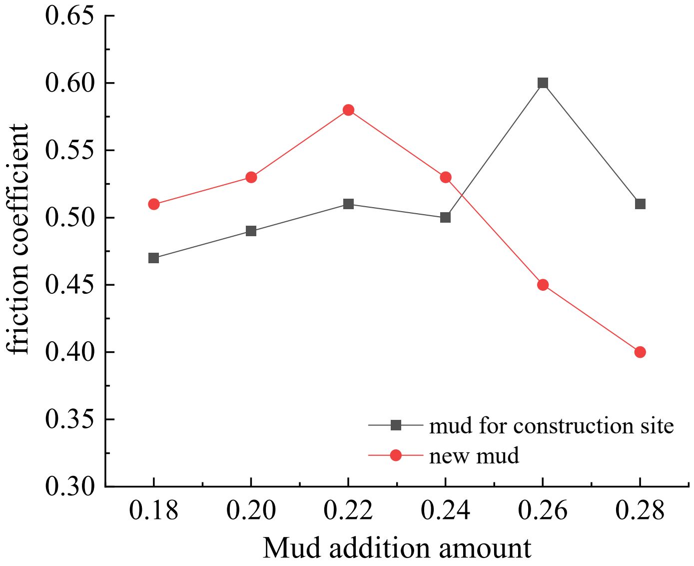

Figure 12. Comparison of friction coefficient of pebble/round gravel improved by two kinds of mud.

4.1.3. Adhesion Resistance Test

The adhesion resistance comparison curve is shown in Figure 13.

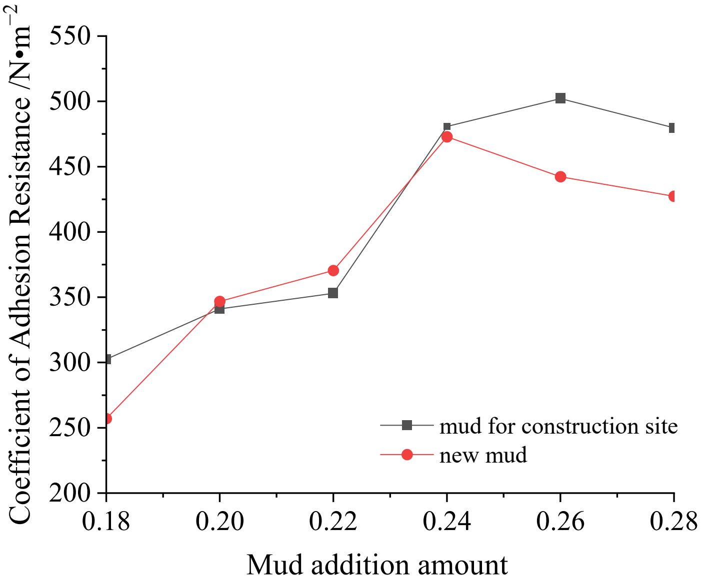

Figure 13. Comparison of adhesion resistance of pebble/round gravel improved by two kinds of mud.

It can be seen from the above curve that when the amount of mud added was less than 24%, the adhesion resistance of the slag increased with the increase in the amount of mud added. When the amount of mud added was about 28%, the adhesion resistance coefficient had a low, stable value, and the adhesion resistance coefficient of the new mud was smaller than that of the mud used on the construction site, therefore the new type of mud can better reduce the adhesion resistance coefficient of the muck, which is beneficial to the smooth discharge of the muck.

4.1.4. Slump Test

The slump comparison curve is shown in Figure 14.

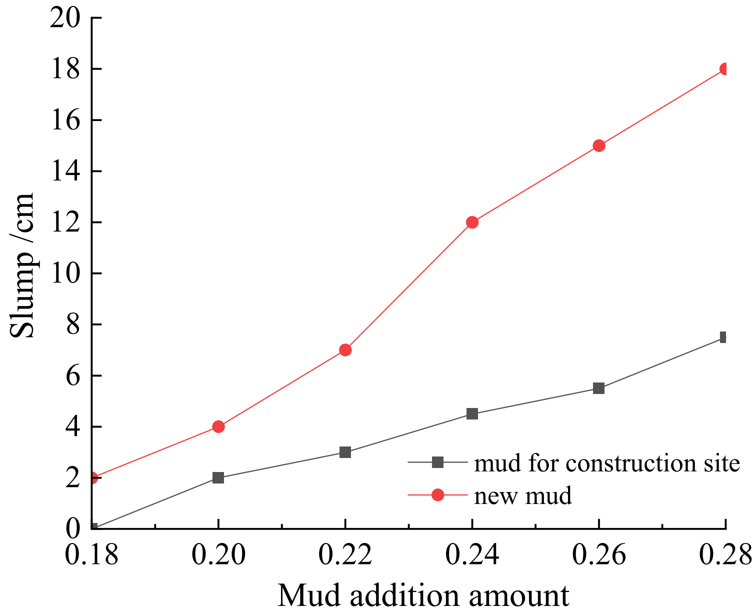

Figure 14. Comparison of the slump of pebble/round gravel improved by two kinds of mud.

It can be seen in Figure 14 above that with the increase of the amount of mud added, the slump of the muck increased significantly. When the amount of mud added was 28%, the slump of mud used on site was only 7.5 cm, and the soil slump requirement (12~20 cm) of the earth pressure balance shield was not met, while the slump of the new type of mud is 18 cm, which meets the requirement. Therefore, the new mud was better than the mud used on the construction site for improving the slump of the muck.

4.2. Experimental Study on Sandy Soil Improvement

Through qualitative analysis of the applicability of soil amendment and sandy soil, the applicability relationship between soil amendment and sandy soil was determined.

The soil volume used in the test analysis process was 7.5 L, and the amount of soil amendment added was determined according to the volume of the soil. The test soil was anhydrous sand, and the particle size distribution of the sand is shown in Table 8. After initial experimental analysis, the initial amount of mud added was determined to be 20% of the soil volume (1500 mL): After each parameter measurement, the amount of mud added was 4% of the soil volume (300 mL) until the soil reached the ideal plastic flow state. The following sub-soil improvement test categories were analyzed for the test results.

Table 8. Sand particle size distribution.

Particle Size (mm)	2~0.5	0.5~0.25	0.25~0.075	0.075~0.005
Content (%)	30	30	30	10

4.2.1. Sand Mixing Test

The net power comparison curve is shown in Figure 15.

When mud was added to the sand, the net stirring power was significantly reduced. When the mud addition amount was 32%, the net stirring power of the new mud was 0.002 KW, which means that the sandy soil is in a good fluid plastic state. The net stirring power of the mud used in the construction site was 0.009, significantly higher than the new type of mud, therefore the improved performance of the new mud on sandy soil was better than that of mud used on site.

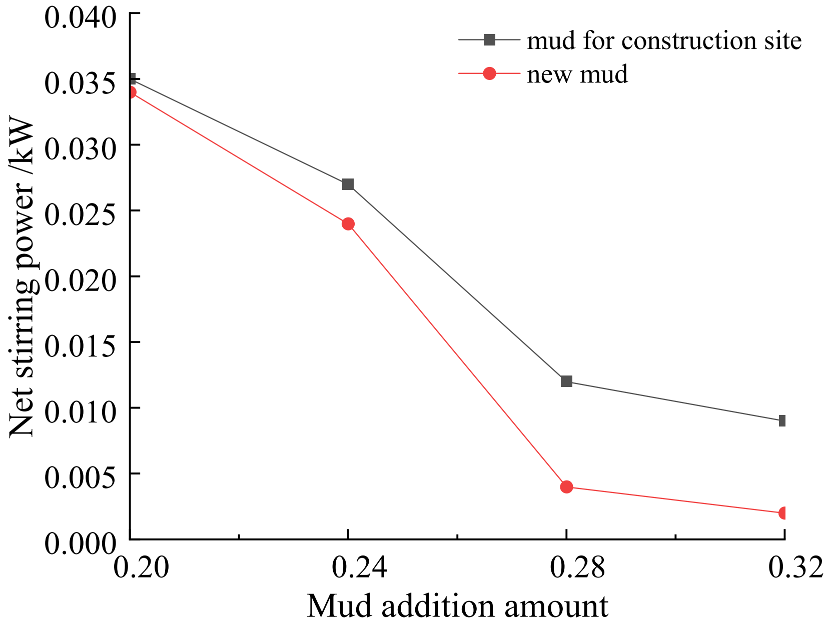

Figure 15. Comparison of net power of sand improved by two kinds of mud.

4.2.2. Sand Friction Coefficient Test

The friction coefficient comparison curve is shown in Figure 16.

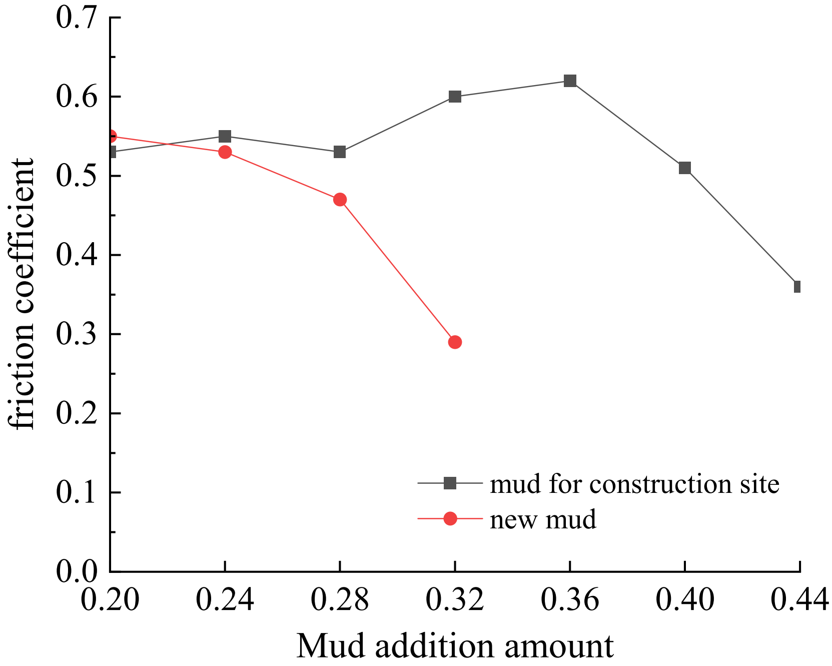

Figure 16. Comparison of friction coefficient of the sand improved by two kinds of mud.

As can be seen in Figure 16 above, when the mud addition amount was 32%, the friction coefficient of the new mud was 0.29, which meets the requirements of fluid plasticity. The construction site mud rose to a maximum value of 0.62, and then gradually decreased. When the amount of mud added to the construction site was 44%, the friction coefficient was reduced to 0.36, therefore the new type of mud was superior to the mud used on the construction site.

4.2.3. Sand Adhesion Resistance Test

The comparative analysis curve of adhesion resistance is shown in Figure 17.

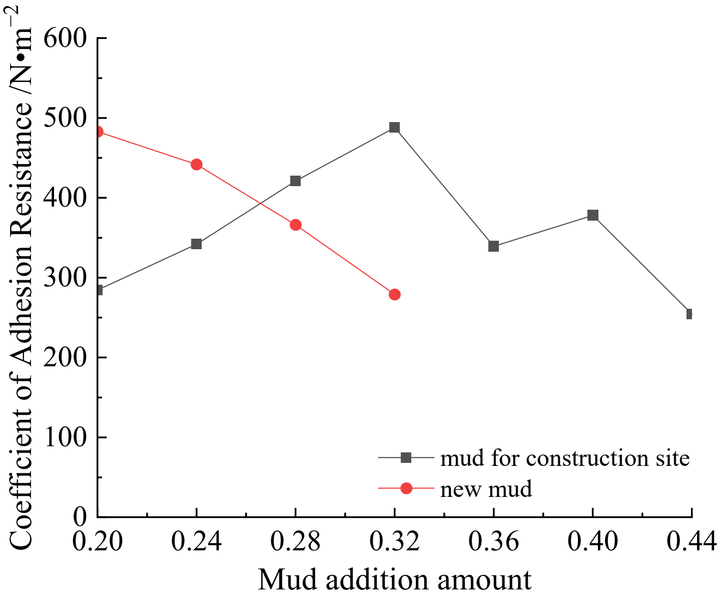

Figure 17. Comparison of adhesion resistance of sand improved by two kinds of mud.

It can be seen in the above figure that with the increase in the amount of mud added, the sandy soil increases, and the adhesion resistance coefficient first increases and then decreases. After adding the new mud to 20%, the adhesion resistance coefficient began to decrease. When the addition amount is 32%, the mud is in a fluid plastic state. The adhesion resistance reached the maximum value when the amount of mud used in the construction site was 32%; after that, it began to decrease. When the addition amount was 44%, the sand was in a fluid plastic state. Therefore, the improvement effect of the new mud was better than that of the mud used on the construction site.

4.2.4. Sand Slump Test

The slump comparison curve is shown in Figure 18.

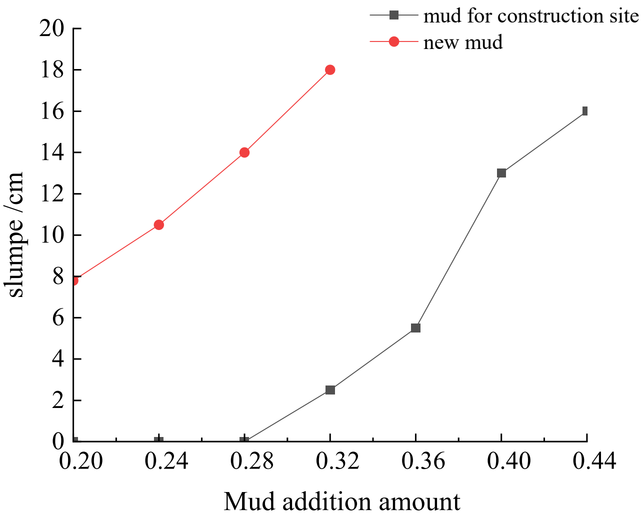

Figure 18. Comparison of the sand slump of pebble/round gravel improved by two kinds of mud.

From Figure 18 above, it can be seen that the sand slump gradually increased with the increase in the amount of mud. When the amount of new mud was 32%, the slump was 18 cm, which meets the requirements. The slump did not reach 16 cm until the amount of mud used on the construction site was 44%. Therefore, the new mud can effectively improve the sand slump.

5. Conclusions

(i) Through laboratory tests, the effects of guar gum, CMC, xanthan gum, and polyacrylamide, which are different additives, on the performance of the slurry are analyzed with bentonite as the base slurry. It was found that xanthan gum was the best material to improve the performance of the slurry. The best slurry preparation scheme is 4% bentonite, 0.2% xanthan gum, 0.04% soda ash, and 1% clay particles.
(ii) Through indoor simulated muck improvement tests (mixing test, slump test, slide plate test, and adhesion resistance test), the improvement effects of applying new mud and ordinary mud in pebble/round gravel and sandy soil layers were compared to verify the superiority of the new mud in the application of the above two kinds of formations.
(iii) In the soil improvement test, the effect of the new mud was similar to that of ordinary mud. However, it had greater advantages in improving the two parameters of the soil adhesion resistance coefficient and slumps during shield tunneling.
(iv) When used to improve pebble/round gravel soil, the test showed that when the net power was close to 0, the slag soil was in a good flow plastic state, and the net power of the new mud was less than that of the mud used in the construction site. When the friction angle was about 20°, the flow plasticity of slag was better. When the mud dosage was 28%, the friction coefficient of the new mud was smaller than that of the land mud. When the amount of mud was about 28%, the adhesion resistance coefficient had a low, stable value, and the adhesion resistance coefficient of the new mud was smaller than that of the mud used in the construction site. When the amount of mud added was 28%, the slump of the mud used at the construction site was only 7.5 cm, which cannot meet the requirements of the earth pressure balance shield on the slump of the muck, while the slump of the new mud was 18 cm, which meets the requirements.
(v) When used to improve the sand, the test found that when the amount of mud added was 32%, the net mixing power of the new mud was 0.002 KW, indicating that the sand was in a good flow plastic state, while the net mixing power of the mud used at the construction site is 0.009, which is significantly greater than the new mud. When the amount of mud added was 32%, the friction coefficient of the new mud was 0.29, which meets the requirements of flow plasticity. The site mud rose to the maximum value of 0.62, and then the friction coefficient decreased to 0.36 as the amount of mud added reached 44%. When the new mud dosage was 32%, the mud was in the flow plastic state, while when the mud dosage was 32%, the adhesion resistance reached the maximum value, and when the mud dosage reached 44%, the sand was in the flow plastic state. When the dosage of new mud was 32%, the slump was 18 cm, meeting the requirements. When the amount of mud used at the construction site was 44%, the slump reached 16 cm.
(vi) The new mud addition ratio was 28% for improved pebble/round gravel soil, and 32% for improved sand and clay. By comparison, it can be seen that the new mud is more suitable for improved pebble/round gravel soil and meets the requirements for the improvement of sandy pebble stratum.

Author Contributions: Data curation, D.Z.; Writing—original draft, Y.S.; Writing—review and editing, Y.S.; Supervision, D.Z.; Project administration, D.Z. All authors have read and agreed to the published version of the manuscript.

Funding: This research received no external funding.

Institutional Review Board Statement: Not applicable.

Informed Consent Statement: Not applicable.

Data Availability Statement: All data that support the findings of this study are available from the corresponding author upon reasonable request.

Conflicts of Interest: The authors declare no conflict of interest.

References

1. He, C.; Feng, K.; Fang, Y. Review and prospects on constructing technologies of metro tunnels using shield tunnelling method. *J. Southwest Jiaotong Univ.* **2015**, *50*, 97–109.
2. Qingke, N.; Guang, S.; Siyuan, G.; Hongtao, L.; Lichao, Z.; Jianpeng, H. Disturbance Process of Sandy Gravel Stratum Caused by Shield Tunneling and Ground Settlement Analysis. *Front. Earth Sci.* **2021**, *9*, 994. [CrossRef]
3. Hasheminezhad, A.; Farzalizadeh, R.; Rahimi, H.; Bahadori, H. Seismic performance assessment of wall-type gravel and rubber drains in liquefaction mitigation of sands. *Bull. Earthq. Eng.* **2022**, *20*, 3699–3714. [CrossRef]
4. Zhao, J.S.; Jiang, Q.; Lu, J.F.; Chen, B.R.; Pei, S.F.; Wang, Z.L. Rock fracturing observation based on microseismic monitoring and borehole imaging: In situ investigation in a large underground cavern under high geostress. *Tunn. Undergr. Space Technol.* **2022**, *126*, 104549. [CrossRef]
5. Chen, Z.T.; Bezuijen, A.; Fang, Y.; Wang, K.; Deng, R.Y. Experimental study and field validation on soil clogging of EPB shields in completely decomposed granite. *Tunn. Undergr. Space Technol.* **2022**, *120*, 104300. [CrossRef]
6. Wang, H.B.; Wang, S.Y.; Zhong, J.Z.; Qu, T.M.; Liu, Z.R.; Xu, T.; Liu, P.F. Undrained compressibility characteristics and pore pressure calculation model of foam-conditioned sand. *Tunn. Undergr. Space Technol.* **2021**, *118*, 104161. [CrossRef]
7. Farzalizadeh, R.; Hasheminezhad, A.; Bahadori, H. Shaking table tests on wall-type gravel and rubber drains as a liquefaction countermeasure in silty sand. *Geotext. Geomembr.* **2021**, *49*, 1483–1494. [CrossRef]
8. Dai, C.Q.; Sui, H.T.; Ma, C. Study on the Ultimate Supporting Force of Shield Excavation Face Based on Anisotropic Strength Theory. *Appl. Sci.* **2020**, *10*, 5222. [CrossRef]
9. Hasheminezhad, A.; Bahadori, H. Seismic response of shallow foundations over liquefiable soils improved by deep soil mixing columns. *Comput. Geotech.* **2019**, *110*, 251–273. [CrossRef]
10. Zhao, J.S.; Chen, B.R.; Jiang, Q.; Lu, J.F.; Hao, X.J.; Pei, S.F.; Wang, F. Microseismic Monitoring of Rock Mass Fracture Response to Blasting Excavation of Large Underground Caverns Under High Geostress. *Rock Mech. Rock Eng.* **2022**, *55*, 733–750. [CrossRef]
11. Liang, X.; Ye, F.; Ouyang, A.H.; Han, X.; Qin, X.Z. Theoretical Analyses of the Stability of Excavation Face of Shield Tunnel in Lanzhou Metro Crossing beneath the Yellow River. *Int. J. Geomech.* **2020**, *20*, 04020200. [CrossRef]
12. Sui, H.T.; Ma, C.; Dai, C.Q.; Yang, T.Z. Study on Stability of Shield Tunnel Excavation Face in Soil-Rock Composite Stratum. *Math. Probl. Eng.* **2021**, *2021*, 5579103. [CrossRef]
13. Huang, X.; Li, L.F.; Zhang, C.F.; Liu, B.; Li, K.J.; Shi, H.B.; Jing, B.Y. Multi-Step Combined Control Technology for Karst and Fissure Water Inrush Disaster During Shield Tunneling in Spring Areas. *Front. Earth Sci.* **2021**, *9*, 795457. [CrossRef]
14. Liu, P.F.; Wang, S.Y.; Ge, L.; Thewes, M.; Yang, J.S.; Xia, Y.M. Changes of Atterberg limits and electrochemical behaviors of clays with dispersants as conditioning agents for EPB shield tunnelling. *Tunn. Undergr. Space Technol.* **2018**, *73*, 244–251. [CrossRef]
15. Liu, W.; Shi, P.X.; Yu, M.; Jia, P.J. Analysis of working face stability during obstruction removal from a box tunnel machine. *Acta Geotech.* **2022**, *17*, 4627–4639. [CrossRef]
16. Zizka, Z.; Schoesser, B.; Thewes, M. Investigations on the transient support pressure transfer at the tunnel face during slurry shield drive Part 2: Case B-Deep slurry penetration exceeds tool cutting depth. *Tunn. Undergr. Space Technol.* **2021**, *118*, 104169. [CrossRef]
17. Newton, R.C. A Geo-Experimental Diagram for Garnet Amphibolite and Its Bearing on the Origin of Continents. *J. Geol.* **2018**, *126*, 531–539. [CrossRef]
18. Tomiczek, T.; Prasetyo, A.; Mori, N.; Yasuda, T.; Kennedy, A. Physical modelling of tsunami onshore propagation, peak pressures, and shielding effects in an urban building array. *Coast. Eng.* **2016**, *117*, 97–112. [CrossRef]
19. Zhu, C.H.; Wang, S.H.; Peng, S.; Song, Y.L. Surface settlement in saturated loess stratum during shield construction: Numerical modeling and sensitivity analysis. *Tunn. Undergr. Space Technol.* **2022**, *119*, 104205. [CrossRef]
20. Yu, H.J.; Mooney, M.; Bezuijen, A. A simplified excavation chamber pressure model for EPBM tunneling. *Tunn. Undergr. Space Technol.* **2020**, *103*, 103457. [CrossRef]
21. Cui, G.; Cui, J.; Fang, Y.; Chen, Z.T.; Wang, H.W. Scaled model tests on segmental linings of shield tunnels under earth and water pressures. *Int. J. Phys. Model. Geotech.* **2020**, *20*, 338–354. [CrossRef]
22. Wang, S.Y.; Huang, S.; Zhong, J.Z.; Zhang, S.; Hu, Q.X.; Qu, T.M.; Ye, X.Y. Permeability stability calculation model of foam-conditioned soil based on the permeability constant. *Int. J. Numer. Anal. Methods Geomech.* **2021**, *45*, 540–559. [CrossRef]
23. Zhang, P.; Chen, R.P.; Wu, H.N.; Liu, Y. Ground settlement induced by tunneling crossing interface of water-bearing mixed ground: A lesson from Changsha, China. *Tunn. Undergr. Space Technol.* **2020**, *96*, 103224. [CrossRef]
24. Lee, H.; Kim, D.Y.; Shin, D.; Oh, J.; Choi, H. Effect of foam conditioning on performance of EPB shield tunnelling through laboratory excavation test. *Transp. Geotech.* **2022**, *32*, 100692. [CrossRef]
25. Qu, T.M.; Wang, S.Y.; Hu, Q.X. Coupled Discrete Element-Finite Difference Method for Analysing Effects of Cohesionless Soil Conditioning on Tunneling Behaviour of EPB Shield. *KSCE J. Civ. Eng.* **2019**, *23*, 4538–4552. [CrossRef]

26. Kou, L.; Zhao, J.J.; Miao, R.H.; Lian, F.L. Experimental Study on Dynamic Mechanical Characteristics of Mud Slurry Penetrating into Excavation Surface of Large Diameter Slurry Shield. *Arab. J. Sci. Eng.* **2022**, *47*, 13139–13150. [CrossRef]
27. Ling, F.L.; Wang, S.Y.; Hu, Q.X.; Huang, S.; Feng, Z.Y. Effect of bentonite slurry on the function of foam for changing the permeability characteristics of sand under high hydraulic gradients. *Can. Geotech. J.* **2022**, *59*, 1061–1070. [CrossRef]
28. Huang, Z.Q.; Wang, C.; Dong, J.Y.; Zhou, J.J.; Yang, J.H.; Li, Y.W. Conditioning experiment on sand and cobble soil for shield tunneling. *Tunn. Undergr. Space Technol.* **2019**, *87*, 187–194. [CrossRef]
29. Liang, Y.; Huang, X.M.; Gao, S.J.; Yin, Y.H. Study on the Floating of Large Diameter Underwater Shield Tunnel Caused by Synchronous Grouting. *Geofluids* **2022**, *2022*, 2041924. [CrossRef]
30. Qian, Y.J.; Min, F.L.; Mo, Z.Z.; Fan, X.H. Experimental Study of the Influence of Excavation Surface Stability and Sand Flowability Caused by Dense Slurry-Earth Pressure Balance Shield Tunneling in Silty Sand Stratum. *Adv. Civ. Eng.* **2020**, *2020*, 8883190. [CrossRef]
31. Shevtsov, A.N.; Zhamaletdinov, A.A. Temperature and Rheological Parameters of the Baltic Shield Lithosphere from Electromagnetic Sounding Results. *Izv. Atmos. Ocean. Phys.* **2021**, *57*, 712–728. [CrossRef]
32. Yang, Z.Y.; Yang, X.; Ding, Y.J.; Jiang, Y.S.; Shao, X.K.; Qi, W.Q.; Liu, N. Effect of Soil Conditioning on Saturated Sand Layers in EPB Shields: A Microstructural Analysis Based on CT Scanning and SEM. *Arab. J. Sci. Eng.* **2022**, *47*, 12387–12397. [CrossRef]
33. Zhen, Z.; Ge, X.S.; Zhang, J. Soil Conditioning Tests on Sandy and Cobbly Soil for Shield Tunneling. *KSCE J. Civ. Eng.* **2021**, *25*, 1229–1238. [CrossRef]
34. Milligan, G. *Lubrication and Soil Conditioning in Tunnelling, Pipe Jacking and Microtunnelling: A State-of-the-Art Review*; Geotechnical Consulting Group: London, UK, 2000.
35. Wang, S.Y.; Liu, P.F.; Hu, Q.X.; Zhong, J.Z. Effect of dispersant on the tangential adhesion strength between clay and metal for EPB shield tunnelling. *Tunn. Undergr. Space Technol.* **2020**, *95*, 103144. [CrossRef]
36. Zhao, S.S.; Li, S.C.; Wan, Z.; Wang, X.W.; Wang, M.L.; Yuan, C. Effects of anti-clay agents on bubble size distribution and stability of aqueous foam under pressure for earth pressure balance shield tunneling. *Colloid Interface Sci. Commun.* **2021**, *42*, 100424. [CrossRef]
37. Wang, S.M.; Lu, X.X.; Wang, X.M.; He, C.; Xia, X.; Ruan, L.; Jian, Y.Q. Soil Improvement of EPBS Construction in High Water Pressure and High Permeability Sand Stratum. *Adv. Civ. Eng.* **2019**, *2019*, 4503219. [CrossRef]
38. Zhu, H.H.; Cheng, P.P.; Zhuang, X.Y.; Li, Y.H.; Li, P.N. Assessment and and structural improvement on the performance of soil chamber system of EPB shield assisted with DEM modeling. *Tunn. Undergr. Space Technol.* **2020**, *96*, 103092. [CrossRef]
39. Lee, H.; Choi, H.; Choi, S.W.; Chang, S.H.; Kang, T.H.; Lee, C. Numerical Simulation of EPB Shield Tunnelling with TBM Operational Condition Control Using Coupled DEM-FDM. *Appl. Sci.* **2021**, *11*, 2551. [CrossRef]
40. Liu, B.; Li, T.; Han, Y.H.; Li, D.Y.; He, L.L.; Fu, C.Q.; Zhang, G. DEM-continuum mechanics coupling simulation of cutting reinforced concrete pile by shield machine. *Comput. Geotech.* **2022**, *152*, 105036. [CrossRef]
41. Wu, L.; Qu, F.Z. Discrete element simulation of mechanical characteristic of conditioned sands in earth pressure balance shield tunneling. *J. Cent. South Univ. Technol.* **2009**, *16*, 1028–1033. [CrossRef]
42. Cheng, C.; Liao, S.; Chen, L.; Fan, M.; Huo, X.; University, T. Experiments of Soil Conditioning for Shield Tunneling in Watery Quartz Sand-Gravel Ground. *J. Shanghai Jiaotong Univ.* **2018**, *52*, 1492.
43. Shu-chao, Z.; Shao-hui, H.; Zi-peng, Z.; Cheng-hui, L. Research on soil conditioning for earth pressure balance shield tunneling in Lanzhou sandy pebble strata with rich water. *Rock Soil Mech.* **2017**, *38*, 279–286.
44. Jiang, H.; Gong, Q.; Du, X. Experimental study on soil conditioning in cobble layer by use of earth pressure balanced machine. *Chin. J. Geotech. Eng.* **2013**, *35*, 284–292.
45. Lee, H.Y.B.; Kwak, J.; Choi, J.; Hwang, B.; Choi, H. A lab-scale experimental approach to evaluate rheological properties of foam-conditioned soil for EPB shield tunnelling. *Tunn. Undergr. Space Technol.* **2022**, *128*, 104667. [CrossRef]
46. Zhao, S.S.; Li, S.C.; Wan, Z.; Wang, M.L. Dispersant for Reducing Mud Cakes of Slurry Shield Tunnel Boring Machine in Sticky Ground. *Adv. Mater. Sci. Eng.* **2021**, *2021*, 5524489. [CrossRef]
47. Xiao, C.; Tan, L.; Chen, R.; Zhong, Z.; Yang, J. Dynamic coupling simulation of shield construction mechanics considering characteristics of soils. *Chin. J. Geotech. Eng.* **2019**, *41*, 1108–1115.
48. Xu, Q.W.; Zhang, L.Y.; Zhu, H.H.; Gong, Z.Y.; Liu, J.G.; Zhu, Y.H. Laboratory tests on conditioning the sandy cobble soil for EPB shield tunnelling and its field application. *Tunn. Undergr. Space Technol.* **2020**, *105*, 103512. [CrossRef]
49. Li, L.P.; Sun, S.Q.; Wang, J.; Yang, W.M.; Song, S.G.; Fang, Z.D. Experimental study of the precursor information of the water inrush in shield tunnels due to the proximity of a water-filled cave. *Int. J. Rock Mech. Min. Sci.* **2020**, *130*, 104320. [CrossRef]
50. Wang, L.; Zhu, W.; Qian, Y.J.; Xu, C.; Hu, J.N.; Xing, H.T. Phenomenon and Critical Conditions of Chamber Soil Sliming during EPB Shield Tunneling in Water-Rich Weathered Diorite: Case Study of Jinan Metro, China. *Adv. Civ. Eng.* **2020**, *2020*, 6530832. [CrossRef]
51. Wei, Y.J.; Zheng, X.; Su, F.; Li, M.M.; Li, F.; Yang, Y.Y. Evaluation of Cutting Tool Wear of Earth Pressure Balance Shield in Granular Soil Based on Laboratory Test. *J. Test. Eval.* **2019**, *47*, 927–941. [CrossRef]

coatings

MDPI

Article

The Effect of Multi-Walled Carbon Nanotubes on the Compressive Strength of Cement Mortars

Nelli G. Muradyan [1], Harutyun Gyulasaryan [2], Avetik A. Arzumanyan [1], Maria M. Badalyan [1], Marine A. Kalantaryan [1], Yeghiazar V. Vardanyan [1], David Laroze [3], Aram Manukyan [2] and Manuk G. Barseghyan [1,*]

[1] The Educational, Scientific and Experimental Laboratory on Building Materials and Items, National University of Architecture and Construction of Armenia, 105 Teryan Street, Yerevan 0009, Armenia
[2] Laboratory for Solid State Physics, Institute for Physical Research, NAS RA, Ashtarak 0204, Armenia
[3] Instituto de Alta Investigación, CEDENNA, Universidad de Tarapacá, Casilla 7D, Arica 1000000, Chile
* Correspondence: manuk.barseghyan@nuaca.am or manuk.g.barseghyan@gmail.com

Abstract: In this work, multi-walled carbon nanotubes (MWCNTs) have been synthesized using a modified method of solid-phase pyrolysis. The MWCNTs are effectively dispersed using a simple and facile method such as ultrasonic energy without and with surfactant for two different sonication times (15 min and 40 min). In the present study, the effect of MWCNT concentration (0.001, 0.01, 0.05, 0.1 wt.%) on the compressive strengths of cement mortars has been investigated. Compressive tests were carried out on an automatic pressure machine (C089) with a loading rate of 0.5 kN/s at the age of 7 days and 28 days. It is shown that the optimal value of the nanotubes' concentration does not exist in the case of 15 min of sonication time, whereas the optimal value for 40 min of sonication time without and with surfactant is 0.01%. Moreover, in the absence of surfactants, the strength of the specimen over 7 days of hardening increased by 13%, and by 19.5% in the presence of surfactants. The compressive strength for a curing period of 28 days increased by 6.3% and 13.8%, respectively.

Keywords: carbon nanotubes; sonication time; surfactant; compressive strength; cement mortar

Citation: Muradyan, N.G.; Gyulasaryan, H.; Arzumanyan, A.A.; Badalyan, M.M.; Kalantaryan, M.A.; Vardanyan, Y.V.; Laroze, D.; Manukyan, A.; Barseghyan, M.G. The Effect of Multi-Walled Carbon Nanotubes on the Compressive Strength of Cement Mortars. *Coatings* **2022**, *12*, 1933. https://doi.org/10.3390/coatings12121933

Academic Editor: Peng Liu

Received: 17 October 2022
Accepted: 9 November 2022
Published: 8 December 2022

1. Introduction

Due to the increasing demand for high-performance cement composites, the properties of cement composites, such as architectural versatility, excellent mechanical properties, and durability, have been undergoing continuous improvements [1].

To this end, in the literature, various agricultural wastes [2,3], industrial wastes [4,5], natural minerals [6], and synthetic materials [7] have been successfully incorporated. These binders exhibited enhancement in the fresh, mechanical, durability, shrinkage, and microstructural properties of construction products. One such material sparingly used in the literature is carbon nanotubes (CNTs).

CNTs can be considered as seamless cylinders formed of one or more graphene roll sheets and can be classified based on the number of graphene layers [8]. Based on the number of graphene layers, there are two types: single-walled carbon nanotubes (SWCNTs) and multi-walled carbon nanotubes (MWCNTs) [9]. MWCNTs comprise manifold-wrapped graphene sheets arranged in concentric hollow tubes with outside diameters ranging from 2 nm to 100 nm [10]. High modulus of elasticity ($\geq$1 TPa), outstanding tensile strength (65–93 GPa), excellent thermal conductivity (two times more than that of a diamond), high aspect ratio (100–2500), and excellent electrical conductivity are the physical and mechanical characteristics of MWCNTs [11].

The use of CNTs in Portland cement matrices applied in civil engineering has a significant potential to enhance the mechanical properties of composites [12–14]. MWCNTs are used more frequently than SWCNTs because of their lower manufacturing costs and improved reinforcement. According to Lai and Basem [15], adding 0.25 percent MWCNTs to cement mass increased the flexural and tensile strengths of cement-based mortars by 25%. Using small amounts of MWCNTs at 0.08%, the authors reported enhanced flexural strength of 25% [16]. According to Jeevanagoudar et.al [17], MWCNT-reinforced mortars exhibit improved engineering properties compared to ordinary mortars. In particular, it has been discovered that 0.4 percent is the optimum concentration of MWCNT concentration in order to get the highest compressive strength.

CNTs' optimal dispersion is one of the important factors for the preparation of enhanced cement-based composite materials. There are two main methods for dispersing nanotubes: mechanical and chemical [18,19]. In this work, the dispersion of nanotubes by mechanical, in particular ultrasonication, method has been carried out. It is worth noting that the ultrasonication efficiency for MWCNT dispersion depends on many factors, including duration, sonicator type, energy, temperature, and the properties of MWCNTs [20–23]. Due to their high surface energy, MWCNTs have a tendency towards agglomeration, which may lead to the creation of week zones in the final product. By using surfactants, the efficiency of sonication increases; as a result, a more uniform dispersion of MWCNTs in cementitious matrices can be seen [24].

The effect of the concentration of MWCNTs synthesized by different methods, the duration of sonication, and the use of surfactants on the mechanical properties of cement-based materials, particularly cement mortar, still requires further investigation.

In the present work, the effects of concentration of MWCNTs, duration of sonication, and the use of surfactants on the compressive strength of cement-based mortar were investigated.

2. Experiment

2.1. Materials

Ordinary Portland cement 52.5 (GOST 31108-2020, which is available in Araratcement Factory, Yerevan, Armenia) has been used as a binder in the mortars within the framework of this study. The short MWCNTs have been synthesized (Figure 1) using a modified method of solid-phase pyrolysis of cobalt phthalocyanine. The pyrolysis was carried out in a closed quartz ampoule at a temperature of 900 °C and a duration of 30 min using pyrolysis analogs of Ni and Fe phthalocyanines [25,26]. The physical properties and the chemical composition of the used cement [27] (GOST EN 196-1-2002, 196-2-2002, 196-3-2002) are shown in Table 1, while the physical properties of the used sand are shown in Table 2.

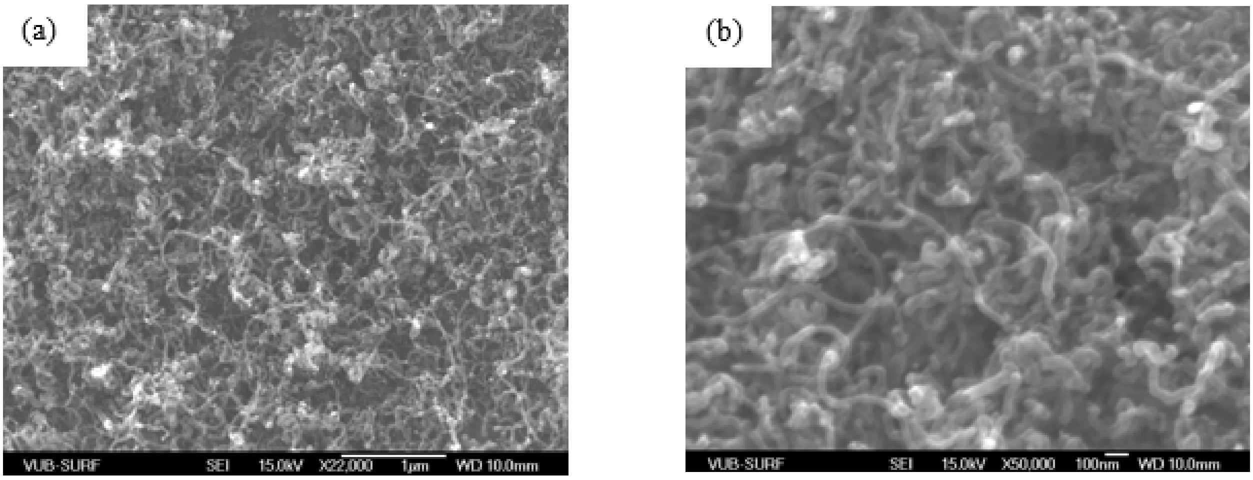

Figure 1. Scanning electron microscope (SEM) images (**a**) × 22,000 (**b**) × 50,000 of MWCNTs.

Table 1. Physical properties and chemical composition of cement.

<table>
<tr><th colspan="3">Characteristics</th><th colspan="3">Days</th><th colspan="3">Results Obtained</th></tr>
<tr><td colspan="3">Standard consistency (%)</td><td colspan="3">-</td><td colspan="3">31</td></tr>
<tr><td colspan="3">Specific gravity (g/sm^3)</td><td colspan="3">-</td><td colspan="3">3.1</td></tr>
<tr><td colspan="3">Blain's fineness (m^2/kg)</td><td colspan="3">-</td><td colspan="3">354.8</td></tr>
<tr><td colspan="3" rowspan="3">Compressive strength (MPa)
(EN 196-1)</td><td colspan="3">3 days</td><td colspan="3">23</td></tr>
<tr><td colspan="3">7 days</td><td colspan="3">38</td></tr>
<tr><td colspan="3">28 days</td><td colspan="3">52</td></tr>
<tr><td colspan="3" rowspan="2">Setting time (min)</td><td colspan="3">Initial</td><td colspan="3">60</td></tr>
<tr><td colspan="3">Final</td><td colspan="3">330</td></tr>
<tr><td colspan="9">Chemical composition of cement (wt.%)</td></tr>
<tr><td>Al$_2$O$_3$</td><td>SiO$_2$</td><td>Fe$_2$O$_3$</td><td>CaO</td><td>MgO</td><td>SO$_3$</td><td>Loss of Ignition</td><td>Insol. Resid.</td><td>Free CaO</td></tr>
<tr><td>3.21</td><td>23.2</td><td>1.25</td><td>57.5</td><td>5.1</td><td>2.9</td><td>3.7</td><td>2.1</td><td>1.13</td></tr>
</table>

Table 2. Physical properties of sand and MWCNTs.

Sand	**Fineness Modulus 2.43**	**Specific Gravity 2.17**	**Zone II**	**Bulk Density in Compact State (kg/m^3) 1829**	**Bulk Density in Loose State (kg/m^3) 1609**
MWCNTS	Outer diameter 40–50 nm	Length < 1 μm	Purity > 90%		

2.2. Dispersion of MWCNTs

Many researchers have reported MWCNT dispersion using various techniques. In this work, MWCNTs, in the required amount, were mixed with water and stirred continuously to ensure proper mixing. Two different sonication times were considered (15 min and 40 min). The sonication process is conducted at room temperature using the ultrasonic device UP400S. In the present investigation, DISPERBYK 199 was also used in order to increase the efficiency of the MWCNT dispersion process in the water. A similar procedure was followed for solutions containing different wt.% of MWCNT content (0.001, 0.01, 0.05, 0.1).

2.3. Mixing and Sample Preparation

The w/c ratio used in the present work was 0.47, and the cement to sand proportion used was 1:4. First, cement and sand were mixed (E095 Mortar mixer, Matest, Treviolo, Italy) for 2.0 min, then the MWCNTS/water mixture was added and mixed for 5 min. The size of the molds were 40 mm × 40 mm × 160 mm. The mortar was compacted through a vibration machine (C278 Vibrating table, Matest, Treviolo, Italy) for 30 s. Similarly, a series of mortars and the one without different MWCNT contents (0.001%, 0.01%, 0.05%, and 0.1% by weight of cement) were cast. The specimens were also prepared by adding in the MWCNTS/water surfactant DISPERBYK-199 (produced by company BYK, Wesel, Germany). The weights of the surfactants were 4.4, 44, 220, and 440 mg, respectively. After 24 h, the specimens were de-molded, and the mortar sample was immersed in water at 20 ± 0.2 °C temperature (Figure 2).

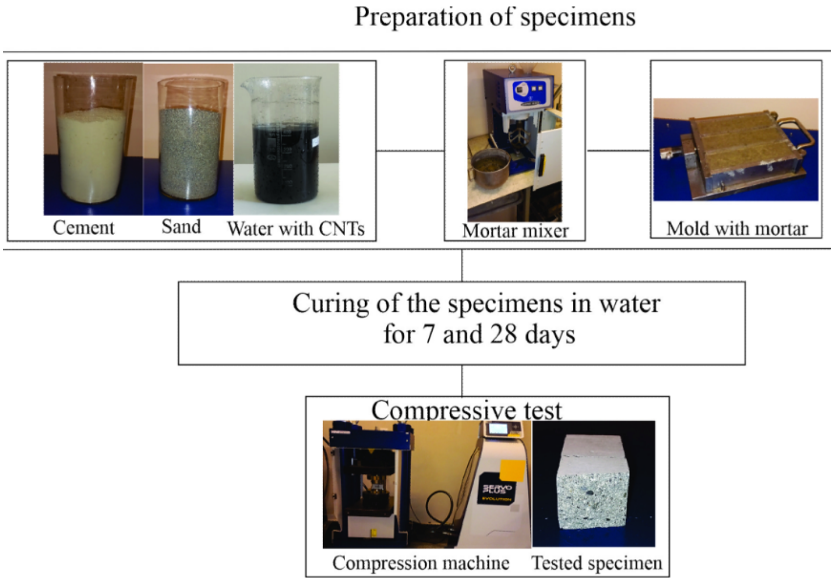

Figure 2. Diagram of the experimental procedure.

2.4. Compressive Strength Testing

Three cubes of each specimen were incidentally selected from each batch to test their average compressive strength according to the Concrete Compression Machine (Matest, Treviolo, Italy) 2000 kN automatic, Servo-Plus Progress (following the standard EN 196-1, and specimen sizes were 40 mm × 40 mm). Compressive tests were carried out on an automatic pressure machine (C089) (Matest, Treviolo, Italy) with a loading rate of 0.5 kN/s at the age of 7 days and 28 days.

3. Results and Discussions

First of all, the results obtained with 15 min sonication time and without surfactant are presented. Figure 3a,b show the compressive strength of the mortar with different wt.% of MWCNTs for 7 and 28 days, respectively. The results indicate that, for both cases of curing days of the cement mortar, the optimal value of MWCNT concentration does not exist. Furthermore, the compressive strength of the cement mortar in the presence of MWCNTs is lower than the compressive strength of the reference specimen. This can be explained due to the low-efficiency dispersion of the MWCNTs in the water, which will reduce the hydration degree. The results indicate that the compressive strength increases with increased curing period, which can be attributed to increased hydration with time.

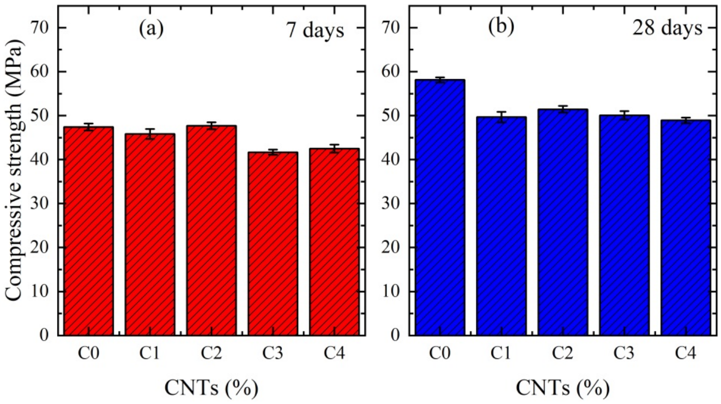

Figure 3. Compressive strength of cement mortars with different wt.% of MWCNTs. The results are for 15 min of sonication time without surfactant. (**a**) for 7 days, (**b**) for 28 days.

Figure 4a,b show the compressive strength of the mortar with different wt.% of MWCNTs for 7 and 28 days, respectively. C0, C1, C2, C3, and C4 correspond to the 0%, 0.001%, 0.01%, 0.05%, and 0.1% of MWCNTs, respectively. The results indicate that the compressive strength of each specimen increases as the curing period increases. This is associated with increased hydration over time. The addition of nanotubes with an appropriate concentration of MWCNTs leads to an increase in compressive strength. The compressive strength reaches the maximum value, then starts to decrease. In other words, the optimal value of the nanotube concentration at which the compressive strength for both cases of curing days reaches its maximum value was obtained. The indicated optimal value of nanotubes is 0.01 wt.%. This is due to the chosen composition of the mortar, as well as the physical and mechanical properties (structure and size) of nanotubes. It is known that in order to make the effect of nanotubes on the physical and mechanical properties of cement-based mortars or concretes effective, it is first necessary to ensure a homogeneous distribution of nanoparticles throughout the volume. For each case, with the increase of nanotube concentration, under the same conditions, the degree of homogeneous distribution decreases, as a result of which the compressive strength decreases. Elsewhere [17], the authors studied rather large values of nanotube concentration, and at 0.4 wt.% of MWCNTs the maximum compressive strength was found only for 28 days of curing (in this work for 7 curing days the optimal values of MWCNTs were not obtained). It can be seen from the figures that the strength of specimens with 7 curing days increased by 13%, and in the case of 28 curing days it increased by 6.3%.

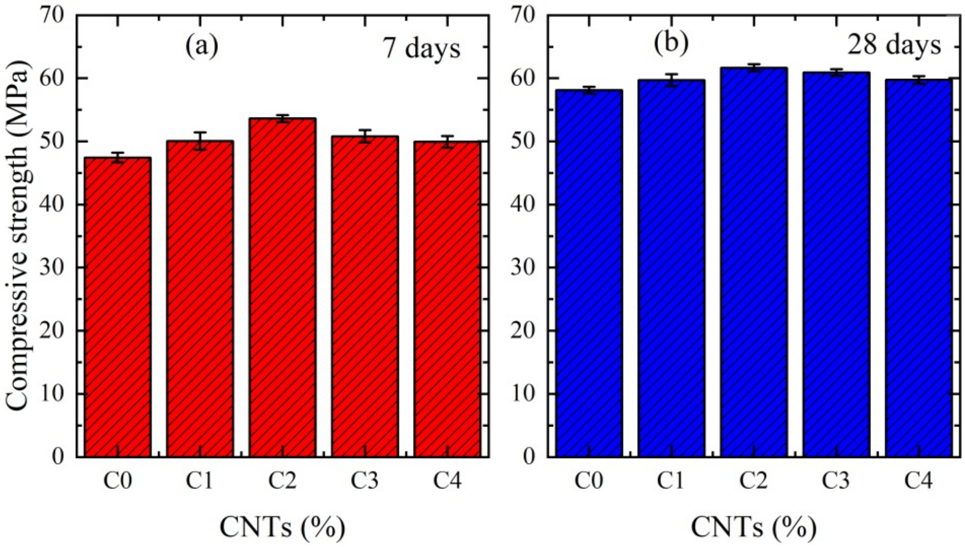

Figure 4. Compressive strength of cement mortars with different wt.% of MWCNTs. The results are for 40 min of ultrasonication time without surfactant. (**a**) for 7 days (**b**) for 28 days.

Figure 5a,b show the compressive strength of the mortar with different wt.% of MWCNTs for 7 and 28 days, respectively, when the surfactant in the MWCNT/water was added.

For both cases of curing days, the optimal values of the MWCNT concentration have been obtained at 0.01 wt.%. The improvement in the efficiency of the dispersion process of MWCNTs in the water brought an increase in the maximum value of the compressive strength. In particular, the strength of a sample with 7 curing days increased by 19.5%, and by 13.8% in the case of 28 curing days.

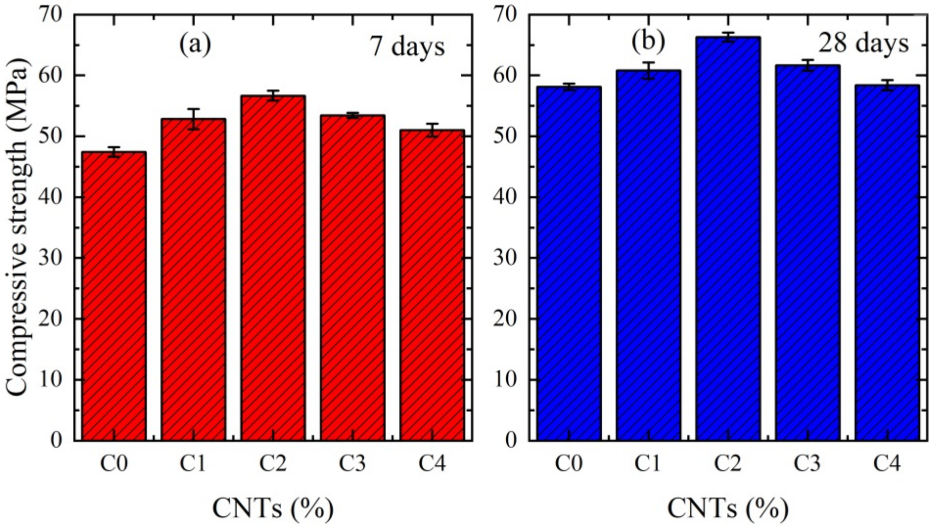

Figure 5. Compressive strength of cement mortars with different wt.% of MWCNTs. The results are for 40 min of ultrasonication time with surfactant. (**a**) for 7 days (**b**) for 28 days.

4. Conclusions

In the present research, the mechanical properties, such as compressive strength, of cement mortar with different concentrations of MWCNTs have been investigated. The sonication technique with and without surfactant, in particular DISPERBYK-199, was employed. For 15 min sonication time, the optimal values of MWCNT concentration to obtain maximum compressive strength do not exist, while in the case of 40 min of sonication it was found to be 0.01%, which is much less than the optimal value obtained in known works. In particular, in the absence of surfactants, the strength of the specimen over 7 days of hardening increased by 13%, and by 19.5% in the presence of surfactants. The compressive strength for a curing period of 28 days increased by 6.3% and 13.8%, respectively. Thus, the optimal mass of surfactants was found, and it was shown that when added to MWCNTs/water, the maximum value of compressive strength can increase by up to 7.5%.

Author Contributions: Conceptualization, M.M.B.; Data curation, N.G.M., H.G. and A.A.A.; Formal analysis, M.M.B., D.L., A.M. and M.G.B.; Funding acquisition, Y.V.V.; Investigation, N.G.M., H.G., A.A.A., M.M.B., M.A.K., A.M. and M.G.B.; Methodology, A.M.; Project administration, M.G.B.; Resources, M.A.K.; Supervision, Y.V.V.; Writing—original draft, A.A.A. and A.M.; Writing—review & editing, D.L. and M.G.B. All authors have read and agreed to the published version of the manuscript.

Funding: The authors would like to acknowledge the financial support by the Science Committee of the Republic of Armenia (Project no. 21AG-1C008). D.L. acknowledges partial financial support from the Centers of excellence with BASAL/ANID financing, Grant AFB180001, CEDENNA.

Institutional Review Board Statement: Not applicable.

Informed Consent Statement: Not applicable.

Data Availability Statement: Not applicable.

Conflicts of Interest: The authors declare no conflict of interest.

References

1. Xiao, J.; Han, N.; Li, Y.; Zhang, Z.H.; Shah, S.P. Review of recent developments in cement composites reinforced with fibers and nanomaterials. *Front. Struct. Civ. Eng.* **2021**, *15*, 1–19. [CrossRef]
2. Nasir, M.; Al-Kutti, W. Performance of Date Palm Ash as a Cementitious Material by Evaluating Strength, Durability, and Characterization. *Buildings* **2019**, *9*, 6. [CrossRef]
3. Nasir, M.; Al-Kutti, W.; Kayed, T.S.; Adesina, A.; Chernykh, T. Synthesis and SWOT analysis of date palm frond ash–Portland cement composites. *Environ. Sci. Pollut. Res.* **2021**, *28*, 45240–45252. [CrossRef]

4. Khan, M.U.; Nasir, M.; Baghabra Al-Amoudi, O.S.; Maslehuddin, M. Influence of in-situ casting temperature and curing regime on the properties of blended cement concretes under hot climatic conditions. *Constr. Build. Mater.* **2021**, *272*, 12186.
5. Nasir, M.; Johari, M.A.; Maslehuddin, M.; Yusuf, M. Sodium sulfate resistance of alkali/slag activated silicomanganese fume-based composites. *Struct. Concr.* **2020**, *79*, 1.
6. Ibrahim, M.; Salami, B.A.; Algaifi, H.A.; Rahman, M.K.; Nasir, M.; Ewebajo, A.O. Assessment of acid resistance of natural pozzolan-based alkali-activated concrete: Experimental and optimization modelling. *Constr. Build. Mater.* **2021**, *304*, 124657. [CrossRef]
7. Nasir, M.; Aziz, M.A.; Zubair, M.; Ashraf, N.; Hussein, T.N.; Allubli, M.K.; Manzar, M.S.; Al-Kutti, W.; Al-Harthi, M.A. Engineered cellulose nanocrystals-based cement mortar from office paper waste: Flow, strength, microstructure, and thermal properties. *J. Build. Eng.* **2022**, *51*, 104345.
8. Dresselhaus, M.S.; Dresselhaus, G.; Eklund, P.C.; Rao, A.M. Carbon nanotubes. In *The Physics of Fullerene-Based and Fullerene-Related Materials*; Andreoni, W., Ed.; Springer: Dordrecht, The Netherlands, 2000; Volume 23, pp. 331–374.
9. Tasis, D.; Tagmatarchis, N.; Bianco, A.; Prato, M. Chemistry of carbon nanotubes. *Chem. Rev.* **2006**, *106*, 1105–1136. [CrossRef] [PubMed]
10. US Research Nanomaterials, Inc. Layers of Multi Walled Carbon Nanotubes, MWNTs, MWCNTs, Short MWNTs, Short MWCNTs. Available online: https://www.us-nano.com/layers (accessed on 30 April 2020).
11. Makar, J.M.; Beaudoin, J.J. *Carbon Nanotubes and Their Application in the Construction Industry*; Royal Society of Chemistry: Cambridge, UK, 2004; pp. 331–341.
12. Silvestro, L.; Gleize, P.J.P. Effect of carbon nanotubes on compressive, flexural and tensile strengths of Portland cement-based materials: A systematic literature review. *Constr. Build. Mater.* **2020**, *264*, 120237. [CrossRef]
13. Han, B.; Yu, X.; Kwon, E.; Ou, J. Effects of CNT concentration level and water/cement ratio on the piezoresistivity of CNT/cement composites. *J. Compos. Mater.* **2012**, *46*, 19–25. [CrossRef]
14. Shi, T.; Li, Z.; Guo, J.; Gong, H.; Gu, C. Research progress on CNTs/CNFs-modified cement-based composites—A review. *Constr. Build. Mater.* **2019**, *202*, 290–307. [CrossRef]
15. Lai, Y.C.; Bassem, A. Finite element analysis of carbon nanotube/cement composite with degraded bond strength. *Comput. Mater. Sci.* **2010**, *47*, 994–1004.
16. Konsta-Gdoutos, M.S.; Metaxa, Z.S.; Shah, S.P. Highly dispersed carbon nanotube reinforced cement based materials. *Cem. Concr. Res.* **2010**, *40*, 1052–1059.
17. Jeevanagoudar, Y.V.; Krishna, R.H.; Gowda, R.; Preetham, R.; Prabhakara, R. Improved mechanical properties and piezoresistive sensitivity evaluation of MWCNTs reinforced cement mortars. *Constr. Build. Mater.* **2017**, *144*, 188–194. [CrossRef]
18. Assi, L.; Alsalman, A.; Bianco, D.; Ziehl, H.; El-Khatib, J.; Bayat, M.; Hussein, F.H. Multiwall Carbon Nanotubes (MWCNTs) Dispersion & Mechanical Effects in OPC Mortar & Paste: A review. *J. Build. Eng.* **2021**, *43*, 102512.
19. Hilding, J.; Grulke, E.A.; Zhang, Z.G.; Lockwood, F.J. Dispersion of Carbon Nanotubes in Liquids. *Dispers. Sci. Technol.* **2003**, *24*, 1–41.
20. Elkashef, M.; Wang, K.; Abou-Zeid, M.N. Acid-treated carbon nanotubes and their effects on mortar strength. *Front. Struct. Civ. Eng.* **2016**, *10*, 180–188. [CrossRef]
21. Alrekabi, S.; Cundy, A.; Lampropoulos, A.; Savina, I. Experimental investigation on the effect of ultrasonication on dispersion and mechanical performance of multi-wall carbon nanotube-cement mortar composites. *Int. J. Civil Environ. Struct. Constr. Archit. Eng.* **2016**, *111*, 268–274.
22. Metaxa, Z.S.; Boutsioukou, S.; Amenta, M.; Favvas, E.P.; Kourkoulis, S.K.; Alexopoulos, N.D. Dispersion of Multi-Walled Carbon Nanotubes into White Cement Mortars: The Effect of Concentration and Surfactants. *Nanomaterials* **2022**, *12*, 1031. [CrossRef]
23. Sobolkina, A.; Mechtcherine, V.; Khavrus, V.; Maier, D.; Mende, M.; Ritschel, M.; Leonhardt, A. Dispersion of carbon nanotubes and its influence on the mechanical properties of the cement matrix. *Cem. Concr. Compos.* **2012**, *34*, 1104–1113. [CrossRef]
24. Rashidi, Y.; Roudi, M.R.R.; Korayem, A.H.; Shamsaei, E. Investigation of ultrasonication energy effect on workability, mechanical properties and pore structure of halloysite nanotube reinforced cement mortars. *Constr. Build. Mater.* **2021**, *304*, 124610. [CrossRef]
25. Avakyan, L.; Manukyan, A.; Bogdan, A.; Gyulasaryan, H.; Coutinho, J.; Paramonova, E.; Sukharina, G.; Srabionyan, V.; Sharoyan, E.; Bugaev, L. Synthesis and structural characterization of iron-cementite nanoparticles encapsulated in carbon matrix. *J. Nanoparticle Res.* **2020**, *22*, 30. [CrossRef]
26. Manukyan, A.; Gyulasaryan, H.; Ginoyan, A.; Kaniukov, E.; Petrov, A.; Yakimchuk, D.; Shashov, S.; Nurijanyan, M.; Mirzakhanyan, A. Structural, morphological and magnetic properties of nickel-carbon nanocomposites prepared by solid-phase pyrolysis of Ni phthalocyanine. In *Fundamental and Applied Nano-Electromagnetics*; Maffucci, A., Maksimenko, S.A., Eds.; NATO Science for Peace and Security Series B: Physics and Biophysics; Springer: Dordrecht, The Netherlands, 2016; pp. 273–290.
27. Arzumanyan, A.A.; Tadevosyan, V.G.; Muradyan, N.G.; Navasardyan, H.V. Study of "Saralsk" Deposit for Practical Applications in Construction. *J. Arch. Eng. Res.* **2021**, *1*, 3–6. [CrossRef]

coatings

MDPI

Article

The Influence of Extractant Composition on the Asphaltenes Extracted from Asphalt

Dachuan Sun [1,2,*,†], Yang Song [2,*,†] and Feiyong Chen [2]

[1] School of Transportation Engineering, Shandong Jianzhu University, Jinan 250101, China
[2] Huzhou Nanxun District Jianda Ecological Environment Innovation Center, Shandong Jianzhu University, Jinan 250101, China
* Correspondence: sundc@iccas.ac.cn (D.S.); songyang20@sdjzu.edu.cn (Y.S.); Tel.: +86-199-5312-0288 (D.S.)
† These authors contributed equally to this work.

Abstract: The compositions of extractants containing xylene (G) and n-heptane (P) recovered and reused in the asphaltene extraction process were determined by densimetry and the extracted asphaltenes were analyzed to study the influence of extractant composition on their elemental, spectral and structural properties. With increasing the number of extraction, the G/P ratio in extractant increases, which dissolves more asphaltenes of higher aromaticity and causes a decrease of asphaltene yield, the polarity and aromaticity in molecular structure of the extracted asphaltenes. Asphaltenes extracted at a higher G/P ratio were found to have less fractions of N and O elements as well as higher fractions of H and S elements, a lower C/H atom ratio and molecular unsaturation. Moreover, they have a smaller fraction of aromatic rings and aromatic carbon ratio, a higher substitution rate on aromatic rings, a higher fraction of alkyl chain and free ends in their average molecular structure. Compared with the base asphalt, asphaltenes' infrared absorptions generally move towards smaller wave numbers owing to more aromaticity in their molecules and subsequent stronger conjugative and inductive effects. The asphaltenes extracted at a higher G/P ratio have a denser packing of alkyl chains and a looser packing of aromatic rings, according to their spectra of X-ray diffraction.

Keywords: densimetry method; extractant composition; n-heptane and xylene; asphaltene extraction; molecular structure

Citation: Sun, D.; Song, Y.; Chen, F. The Influence of Extractant Composition on the Asphaltenes Extracted from Asphalt. *Coatings* **2022**, *12*, 1600. https://doi.org/10.3390/coatings12101600

Academic Editor: Ajay Vikram Singh

Received: 21 September 2022
Accepted: 20 October 2022
Published: 21 October 2022

1. Introduction

Asphalt is one kind of coating materials widely used for roof waterproofing, interface bonding and surface layers of high-grade highways [1,2]. Asphalt has a complex chemical structure and composition [3–5]. According to the different solubility, it can be divided into four components: saturate, aromatic, resin and asphaltene [1,5,6]. In our previous work [7], using the solubility discrepancy of asphaltene in different solvents [8], a simple scheme for extracting asphaltenes from asphalt at room temperature was proposed and verified experimentally. The scheme firstly dissolves the asphalt in a good solvent (denoted as G) and then uses a poor solvent (denoted as P) to precipitate the asphaltenes out. As the scheme is carried out at room temperature without heating, it avoids the problems of high energy cost, expensive devices, and safety risks of flammable steam in traditional methods (JTG E20-2011 or IP 143) of asphaltene extraction [6,9]. After extraction, the good solvent was mixed with the poor solvent. To reduce costs, these waste (used) solvents need to be recovered and reused as new extractants. However, the yield decreased significantly when the recovered solvent was used, probably caused by the variance of extractant composition. To better study the effect of extractant composition on asphaltene yield, a method is needed to analyze the extractant concentration or G/P ratio, which is also helpful to optimize the separation condition and improve the separation efficiency of the waste extractants.

Alkanes and aromatics are volatile components in coating materials and widely used as extractants or eluents [3,10]. When extracting asphaltenes from asphalt, the good solvents are generally aromatic hydrocarbons, such as xylene and toluene while the poor solvents are n-alkanes, such as n-heptane and n-hexane [3,5,9]. Xylene is a C_8 aromatic mixture containing isomers and a small amount of ethylbenzene [11,12]. Both xylene and heptane are volatile and miscible with each other in any ratio. Heptane is a poor solvent or precipitant for asphaltenes, owing to the difference of molecular structures (thus higher enthalpy penalty) between heptane and asphaltenes as well as high molecular weight of asphaltene (thus less mixing entropy) [3,6]. Asphaltene is precipitated only when the G/P ratio is below a critical precipitation point [9,13,14]. The analysis of G/P ratio in extractant is helpful to judge whether the critical precipitation point is exceeded, and helpful to guide the industrial extraction of asphaltenes. Compared with the analytical methods such as high performance liquid chromatography (HPLC), nuclear magnetic resonance (NMR) and gas chromatography-mass spectrometry (GC-MS) [15,16], the densimetry method may be the simplest and cheapest without requiring expensive equipment [17].

The physical properties [2,18] and molecular structures [4,5] of the extracted asphaltenes may vary with extraction number or G/P ratio. Asphaltenes have been analyzed via elemental analysis (EA), NMR, Fourier transform infrared (FTIR) and X-ray diffraction (XRD) methods [19,20] to get average molecular structure [3] to compare with other bitumen components [6] or with asphaltenes precipitated from different alkanes [10,21]. There are few studies for the effect of G/P ratio on the properties of extracted asphaltene. Such a study is helpful to evaluate the property discrepancy and to judge whether these asphaltenes can be mixed and used together. In this paper, the compositions of recovered extractants were analyzed via densimetry, while the properties of asphaltenes extracted at different G/P compositions were studied. Mechanisms were discussed for the variance of asphaltene properties and for the decrease of asphaltene yield with extraction number or G/P ratio.

2. Materials and Methods

2.1. Materials and Devices

The asphalt used is Qilu No. 70 base asphalt from Qilu Petrochemical Company (Zibo, China). Potassium bromide (KBr, crystals, of 99% purity) with chemical abstracts service number (CAS No.) 7758-02-3 is purchased from Merck & Co., Ltd. (Beijing, China). Deuterated chloroform ($CDCl_3$, CAS No. 865-49-6, 99.8% purity) containing 0.03% v/v tetramethylsilane (TMS) is purchased from Cambridge Isotope Laboratories, Inc. (Beijing, China). Xylene (xylene isomer + ethylbenzene, CAS No. 1330-20-7) and n-heptane (CAS No. 142-82-5) of analytical reagent (AR) grade are purchased from Macklin Biochemical Technology Company (Shanghai, China).

The glasswares were purchased from Chongqing Synthware Glass Company (Chongqing, China). The HJ-6A thermostatic magnetic stirrer is purchased from Jiangsu Zhongda Technology Instrument Company (Nanjing, China). The PX224ZH/E electronic balance and STX portable balance are purchased from Ohaus International Trading (Shanghai) Company (Shanghai, China). The sand-core filter device with a filter bottle of 1000 mL volume and a filter cup of 300 mL volume is purchased from Jiangsu Feida Glass Products Company (Nanjing, China) and used to get the precipitated asphaltenes by suction filtration. The RE-52AA rotary evaporator and SHZIII circulating water vacuum pump are purchased from Shanghai Yarong Biochemical Instrument Factory (Shanghai, China) and used to recover extractant via vacuum distillation. The medium-speed setting filter paper is purchased from Hangzhou Fuyang Northwood Pulp Company (Hangzhou, China). The 0.45 μm filter membrane is purchased from Shanghai Xinya Purification Device Factory (Shanghai, China). The polypropylene dropper and other consumables are supplied by Shandong Laboratory Experimental Instrument Company (Jinan, China).

2.2. Experimental Procedures

2.2.1. Preparation of Standard Samples of Extractants

The subscripts P and G represent poor solvent (n-heptane) and good solvent (xylene), respectively, in Table 1 and in the following. All operations were carried out in a fume hood. The room temperature was maintained at 20 °C by an air conditioner.

Table 1. The volume fraction v and mass fraction w of each component for standard samples of extractants containing xylene (G) and n-heptane (P) at room temperature.

No.	P (mL)	G (mL)	Sum (mL)	v_P	v_G	w_P	w_G
0	0	20	20	0%	100%	0.00	1.00
1	2	18	20	10%	90%	0.08	0.92
2	4	16	20	20%	80%	0.17	0.83
3	6	14	20	30%	70%	0.25	0.75
4	8	12	20	40%	60%	0.35	0.65
5	10	10	20	50%	50%	0.44	0.56
6	12	8	20	60%	40%	0.54	0.46
7	14	6	20	70%	30%	0.65	0.35
8	16	4	20	80%	20%	0.76	0.24
9	18	2	20	90%	10%	0.88	0.12
10	20	0	20	100%	0%	1.00	0.00

The procedures for preparing standard samples are as follows:

1. 30 mL cylindrical bottles are cleaned, dried and put on the desk. The bottles and their caps are marked with numbers from 0 to 10 by an oil-based pen;
2. The n-heptane is pipetted into graduated cylinders until a target volume is reached;
3. The n-heptane is poured into a glass bottle. The bottle number and corresponding volume of n-heptane for each sample are listed in Table 1;
4. The xylene is pipetted into another graduated cylinders until its target volume is reached. Then it is poured into the glass bottle with the designated number. The bottle number and volume of xylene are shown in Table 1;
5. The bottles are sealed and shaken for 1 min to mix sufficiently.

The sum of volume is 20 mL for each sample, as shown in Table 1. To simplify the subsequent analysis, the volume fraction v and mass fraction w of each component are calculated and listed in Table 1, according to the quantities [11,12] in Table 2. The graduated cylinders were calibrated by weighing 10 mL of ultrapure water on the PX224ZH/E balance and the density ρ of water at 20 °C is 0.9982 g/mL.

Table 2. Basic physical quantities of n-heptane (P) and xylene (G) at room temperature.

Physical Quantity	P	G	Physical Meaning
ρ	0.68 g/mL	0.86 g/mL	Density
M_W	100.20 g/mol	106.17 g/mol	Molecular weight
T_b	98 °C	140 °C	Boiling point

2.2.2. Procedures to Get Extracted Asphaltene and Real Samples of Extractants

A detailed method of recovering solvents and extracting asphaltenes from bitumen was documented in a previous report [7]. A total of 3 consecutive extractions were performed and the main steps are as follows:

1. In the first extraction, a total of 5 g asphalt is dissolved in 50 mL xylene of AR purity and then poured into 500 mL n-heptane of AR grade to precipitate the asphaltenes. The solution is then filtered to get the filtrate and filter cake, respectively. The filter cake is dried to obtain asphaltenes (denoted as A1). The weight ratio of A1 to asphalt is defined as asphaltene yield;

2. The above filtrate is recovered via vacuum distillation and the vacuum is provided by connecting SHZIII vacuum pump. The continuously supplied tap water (around 15 °C) is used for condensation and different distillates are obtained by controlling the temperature of the water bath of the rotary distillation equipment. The temperature firstly rises from room temperature to 45 °C and is then held for 1 h, during which the dripping of condensed liquid from the condenser is observable from 30 °C and usually completed within 30 min. The collected fraction is sealed and denoted as P1. Then, the temperature is raised from 45 °C to 80 °C and held for 1.5 h. The dripping of condensed liquid starts from 60 °C and is usually finished within 45 min. The collected fraction is sealed in another bottle and denoted as G1;
3. In the second extraction, asphalt is dissolved in G1, and then poured into P1 to precipitate the asphaltenes (A2). The ratio of asphalt/G1/P1 is maintained at 5 g/50 mL/500 mL for consistency. Subsequent operations are the same as steps (1) and (2), except that the collected condensates at 45 °C (heptane-rich fraction) and 80 °C (xylene-rich fraction) are denoted as P2 and G2, respectively;
4. In the third extraction, asphalt is dissolved in G2, and then poured into P2 to precipitate the asphaltenes (A3). The ratio of asphalt/G2/P2 is maintained at 5 g/50 mL/500 mL for comparison. Subsequent operations are the same as steps (1) and (2). The collected fractions at 45 °C and 80 °C are denoted as P3 and G3, respectively.

The concentration of real samples obtained above (P1, P2, P3 and G1, G2, G3) was measured by densimetry. The elements, spectra and structures are analyzed for the extracted asphaltenes (A1, A2, and A3).

2.2.3. Procedures of the Densimetry Method

A fitting curve or equation is made based on the standard samples and then used to analyze real samples. The main steps are as follows:

1. From the standard samples prepared according to Table 1, a 10 mL liquid is transferred to the graduated cylinder with a pipette for each sample;
2. The graduated cylinder is weighed on the PX224ZH/E electronic balance to calculate the mass and density of the sample. Each sample is independently pipetted and measured four times, and the resulting densities are averaged as the final density;
3. A standard curve of densimetry is obtained by plotting the density versus the sample concentrations. The curve is fitted to obtain the standard equation via ORIGIN software (version: OriginPro 2018C 64-bit SR1 for Windows);
4. For the real samples recovered by rotary evaporation, their densities are measured according to the same procedures as the standard samples. The concentration is obtained by substituting the measured density into the equation.

As the blank signals (Y_B) are chosen as the starting points of standard curves, the limits of detections (LOD) are three standard deviations of the blank (s_B). Seven replicates are analyzed for blank samples at $v_G = 0$ to calculate the standard deviations and the LOD of the densimetry method.

2.3. Characterization Methods

For extracted asphaltenes (A1, A2, and A3), their elements, spectra and structures were analyzed via EA, NMR, FTIR and XRD methods. The same characterization was performed on the base bitumen for comparison.

EA was performed via the Elemantar Vario EL cube Elemental Analyzer for the C, H, N and S elements (CHNS mode) at 25 °C. Firstly, a standard sample of 2 mg of sulfanilamide was measured for three independent times to obtain its mass percentages of CHNS elements and then compared with its standard values to obtain the correction factor. The correction factor was updated every 20 measurements, and used for EA calibration during the measurement of real samples. Each real sample was measured four times independently to calculate the mean and deviation. A total of 2 mg was used for each measurement of real sample. The oxidation furnace temperature was 1150 °C and the reduction furnace temperature was 850 °C. The flow rate of carrier gas (helium) was 200 mL/min and the flow rate of combustion oxygen was 200 mL/min. The combustion time of oxygen addition was 90 s.

NMR measurements were performed on a Bruker BioSpin GmbH instrument at 25 °C. $CDCl_3$ was used as the deuterated solvent. A 50 mg sample was sufficiently mixed with 0.5 mL of $CDCl_3$ and transferred into a 5 mm NMR tube for one-dimensional (1D) liquid ^{1}H-NMR characterization. Pulse sequence was zg30 and pulse width was 9.27. Number of scans was 16 and receiver gain was 101. Relaxation delay was 20.0 s and acquisition time was 4.0894 s. Spectrometer frequency was 400 MHz and flip angle was 30°. Acquired size was 32,768 and spectral size was 65,536. The spectral width was 8012.8. The NMR spectra were analyzed via MestReNova software (version 6.1.0-6224 for Windows). The chemical shift of TMS was set as 0 ppm for reference. The n-heptane of AR purity was measured firstly to get the relative ratio of residual solvent (chloroform) signal in deuterated solvent to the TMS signal. The ratio was found to be 0.48 ± 0.04. Based on this ratio and TMS signal, the area for chloroform signal was subtracted and the rest areas integrated for the selected ranges in NMR spectrum were normalized to sum 1 for ease of comparison. Each real sample was measured 3 times independently to calculate the mean and deviation of integrated areas.

For FTIR analysis, the samples were uniformly ground with KBr in an agate mortar and then pressed into round flakes under a pressure of 10 MPa for 60 s. The samples were then measured in transmission mode (TR) on Bruker Tensor II FTIR spectrometry at 25 °C, with a scanning range of 400–4000 cm^{-1} and a resolution of 0.5 cm^{-1}. A round flake of pure KBr was scanned for baseline, which was automatically subtracted in each spectrum. Each sample was scanned 16 times and the averaged spectrum was recorded. The infrared (IR) spectrum was processed via the Omnic software (version 8.2.0.387 for Windows).

The XRD analysis was performed with a D8 Advance X-ray diffractometer produced by Bruker (Germany) at 25 °C. The Cu target source (0.15406 nm) was selected. The measurement angle (2θ) ranged from 5° to 60°, which was twice the angle of X-ray incidence (θ). The scan rate was 1°/min and the step size was 0.02°. The spot diameter was 1 mm with LynxEye XE array detector. Asphaltene was ground to fine powder in an agate mortar prior to analysis.

3. Results and Discussion

3.1. Extractant Compositions Determined via Densimetry

The extractant used in this paper is a binary mixture of xylene (G) and n-heptane (P) in different G/P ratio. For standard samples of extractants with compositions listed in Table 1, their densities ρ were measured and plotted versus the volume fraction v_G. ρ shows a linear relation with v_G in Figure 1 and the coefficient of determination (R^2) is 0.99967 for the fitting equation

$$\rho = 0.67783 + 0.18164\, v_G, \tag{1}$$

The densities ρ of recovered extractants (P1, P2 and G1, G2) were measured by densimetry and substituted into Equation (1) to get v_G. Xylene and heptane of AR purity were used for the 1st extraction of asphaltenes. G1 and P1 were used for the 2nd extraction while G2 and P2 were used for the 3rd extraction. For heptane-rich fractions P1 and P2, their volume fraction of n-heptane v_P ($v_P = 1 - v_G$) is 0.907 ± 0.026 and 0.832 ± 0.011, respectively. The xylene-rich fractions G1 and G2 have higher purity, whose v_G is 0.992 ± 0.014 and 0.966 ± 0.014, respectively, as shown in Figure 1. The negative pressure (vacuum) generated by the pump during vacuum distillation draws away a large amount of solvent and causes a solvent loss and air pollution issue. The average yield for distillate P1 was only 75%. Owing to volatility and good compatibility between xylene and n-heptane, a shorter time of vacuum distillation is preferred to improve the distillate yield and to avoid the xylene vapor dissolving into the heptane-rich fraction. Solvent separation conditions need further optimization, for example, under appropriate negative pressure and distillation time. To reduce the solvent loss in the recovery process, it may be necessary to connect a cold trap to the vacuum pump or use other separation methods instead of vacuum distillation [22,23]. For blank samples at $v_G = 0$, the s_B of calculated volume concentration is 1.2% and the LOD of v_G is 3.6% for the densimetry method.

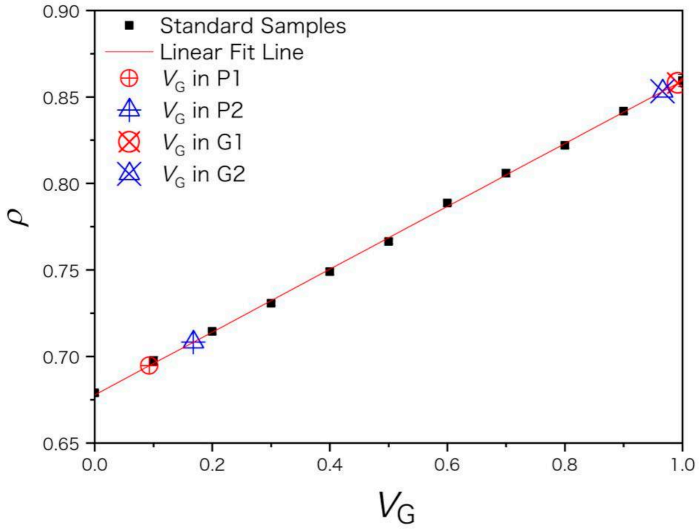

Figure 1. The red line is a linear fit of the volume fraction of xylene v_G and density ρ of standard samples (marked in black squares). The real samples of recovered extractants (P1, P2 and G1, G2) are marked by larger symbols along the fitted line. ρ is in unit of g/mL.

The asphaltene yield was 13.2 ± 0.4%, 10.8 ± 0.4% and 8.3 ± 0.4%, respectively, for the 1st, 2nd, and 3rd extractions. The asphaltene yield decreased with the extraction number but the mechanism was not known exactly [7]. To understand the scenarios of asphaltene precipitation more intuitively, the actual volumes of n-heptane and xylene in the solution for settling asphaltenes during the 1st, 2nd, and 3rd extractions were calculated according to their concentrations in Figure 1 and listed in Table 3, assuming 50 mL G and 500 mL P used in each extraction for ease of comparison. With increasing the extraction number, the heptane-rich fraction contains more and more xylenes, reducing the ability of n-heptane to sediment asphaltenes. Simultaneously, the concentration and total volume of xylene in the solution increase. Thus, more asphaltenes are dissolved while the sedimentation amount and final yield decrease. Even when the xylene-rich fraction is as low as $v_G = 96.6\%$, the asphalt can be completely dissolved, while the heptane-rich fraction is still capable to precipitate asphaltene as low as $v_P = 83.2\%$. Thus, the proposed extraction method [7] has good robustness and great prospects for industrialization, since asphaltenes can be efficiently extracted with solvents much lower than AR purity. Goual et al. found that the onset of asphaltene flocculation occurred near a toluene/heptane volume ratio of 70:30 [14]. The xylene/heptane volume ratio is 24:76 for the 3rd extraction in Table 3, well below the critical ratio of asphaltene precipitation. How the precipitation amount varies with the G/P ratio is an interesting question and may help address asphaltene deposits in oil pipelines [9,24].

Table 3. The actual volumes of n-heptane (P) and xylene (G) in extractant solution, calculated from the concentration of G and P. 50 mL G and 500 mL P were sequentially added for each extraction. Solvents G and P of AR purity were used for the 1st extraction. G1 and P1 were used for the 2nd extraction while G2 and P2 were used for the 3rd extraction.

Extraction No.	P (mL)	G (mL)	Total Volume (mL)	G/P Volume Ratio
1st	500	50	550	0.10
2nd	454	96	550	0.21
3rd	418	132	550	0.32

3.2. Properties of Asphaltenes Extracted at Room Temperature

Asphaltene is usually the most polar and cohesive component of asphalt, and forms the core of the asphalt colloid structure. In Table 4, with increasing the extraction number (from A1 to A3), the mass fractions of C, H and S elements increase while the fractions for element N and others (mainly oxygen) decrease. The fraction of N decreases sequentially from 1.50% in A1 to 1.38% in A3 then to 0.73% in asphalt. Because element N increases the molecular polarity [3], the polarity of asphaltenes from A1 to A3 may decrease with the extraction number and be larger than that of asphalt. C/H atomic ratio is defined as q, which decreases sequentially from 0.99 in A1 to 0.78 in asphalt. q reflects the degree of unsaturation of the molecule, usually in range of 0.5 to 1 for bitumen and its components [1,6,7]. q is larger than 1 for fused-ring molecules, and approaches to infinity for chars and graphites [25,26]. As asphaltenes and asphalt have apparently different q, their unsaturation discrepancy is much larger than the discrepancy between different asphaltenes [6]. Since the polarity and unsaturation increases from asphalt to A3 then to A1, the π-π conjugation and inter-molecular interactions increase, causing higher cohesion and hardness for asphaltenes than asphalt. Thus, asphaltenes extracted at larger G/P ratio have smaller unsaturation, polarity and inter-molecular interactions.

Table 4. Mass percentage of elements from EA (CHNS mode) and the calculated C/H atomic ratio (q) for extracted asphaltenes (A1, A2 and A3) and asphalt.

Fractions	N (%)	C (%)	H (%)	S (%)	Others (%)	q
A1	1.50 ± 0.03	82.46 ± 0.08	6.95 ± 0.04	5.97 ± 0.06	3.13 ± 0.15	0.99
A2	1.44 ± 0.02	82.62 ± 0.07	7.07 ± 0.06	6.09 ± 0.04	2.79 ± 0.10	0.97
A3	1.38 ± 0.03	83.31 ± 0.09	7.24 ± 0.06	6.20 ± 0.06	1.87 ± 0.18	0.96
Asphalt	0.73 ± 0.07	83.08 ± 0.12	8.84 ± 0.05	4.20 ± 0.06	3.15 ± 0.31	0.78

Asphaltenes with larger unsaturation are more easily dissolved in solvents with larger G/P ratio, allowing asphaltenes with smaller unsaturation to preferentially precipitate out. Thus, the averaged molecular structure of the extracted asphaltene may change with the extraction number. Owing to complex compositions and chemical structures of asphalt and asphaltenes [5], NMR is generally used to analyze their average molecular structure [1,27] rather than their content quantification [2,28]. As in Figure 2, the protons are divided into A, α, β, and γ categories [1,6,29], whose chemical shifts are, respectively, in ranges of 6.0–9.0 ppm, 2.0–4.0 ppm, 1.0–2.0 ppm and 0.5–1.0 ppm [1,6]. Their integrated areas are denoted as h_A, h_α, h_β, and h_Υ, respectively. Protons directly attached to the single (S) and fused (F) rings are in the range of 6.0–7.4 ppm and 7.4–9.0 ppm, respectively [30], whose integral areas are denoted by h_S and h_F in Table 5. From A1 to A3 then to asphalt, both h_S and h_F decrease, which has a consistent trend with q and indicates a decrease of aromatic ring fractions. The aromatic carbon ratio f_A [1] shows a decrease trend while the hydrogen substitution rate around aromatic rings σ [6] shows an increase trend. Thus, with increasing the G/P ratio in extractant or with increasing the extraction number, the aromatic rings of extracted asphaltenes have more branched chains and occupy less proportion. From A1 to A3 then to asphalt, h_A decreases while h_β and h_Υ increase. Therefore, the fraction of alkyl branches and (methyl) ends increases in extracted asphaltenes. In terms of averaged molecular structures, the extracted asphaltenes are significantly different from the base asphalt [29]. In terms of physical properties, the asphaltenes obtained from the 1st, 2nd and 3rd extractions are all brittle, hard and shiny, without apparent adhesion to glass, skin or plastics at room temperature, which are apparently different from the base asphalt. The remaining asphalt after asphaltene extraction is much softer and stickier than the original (base) asphalt, which can be used as a new coating material.

Table 5. Calculated values for the average molecular structure of the extracted asphaltenes (A1, A2 and A3) and the base asphalt according to their NMR spectra [1].

NMR Quantities	A1	A2	A3	Asphalt
h_F	0.08 ± 0.01	0.06 ± 0.01	0.04 ± 0.01	0.02 ± 0.01
h_S	0.11 ± 0.02	0.09 ± 0.01	0.08 ± 0.01	0.04 ± 0.01
f_A	0.59 ± 0.01	0.56 ± 0.01	0.54 ± 0.01	0.40 ± 0.02
σ	0.39 ± 0.02	0.43 ± 0.01	0.47 ± 0.02	0.52 ± 0.03
h_A	0.19 ± 0.02	0.15 ± 0.01	0.12 ± 0.01	0.06 ± 0.01
h_α	0.24 ± 0.03	0.23 ± 0.01	0.21 ± 0.01	0.12 ± 0.02
h_β	0.43 ± 0.03	0.47 ± 0.02	0.49 ± 0.02	0.62 ± 0.03
h_γ	0.13 ± 0.01	0.14 ± 0.01	0.17 ± 0.02	0.20 ± 0.01

[1] h_i is the normalized integral area (fraction) for protons of i category; f_A is the aromatic carbon ratio and calculated via $f_A = 1 - (h_\alpha + h_\beta + h_\gamma)/(2q)$; σ is substitution rate on aromatic rings and calculated via $\sigma = h_\alpha/(2h_A + h_\alpha)$.

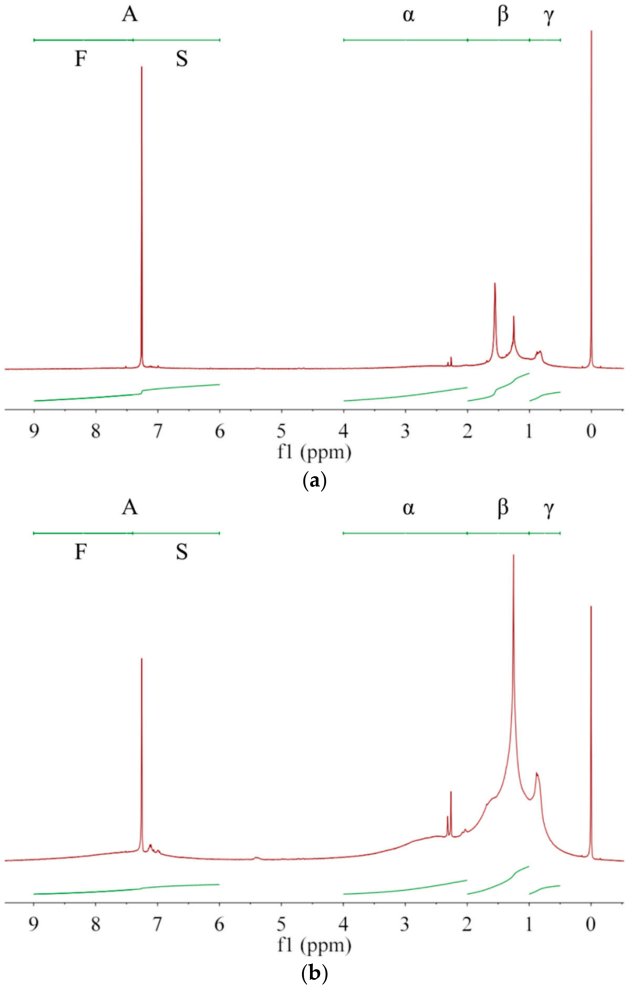

(**a**)

(**b**)

Figure 2. *Cont.*

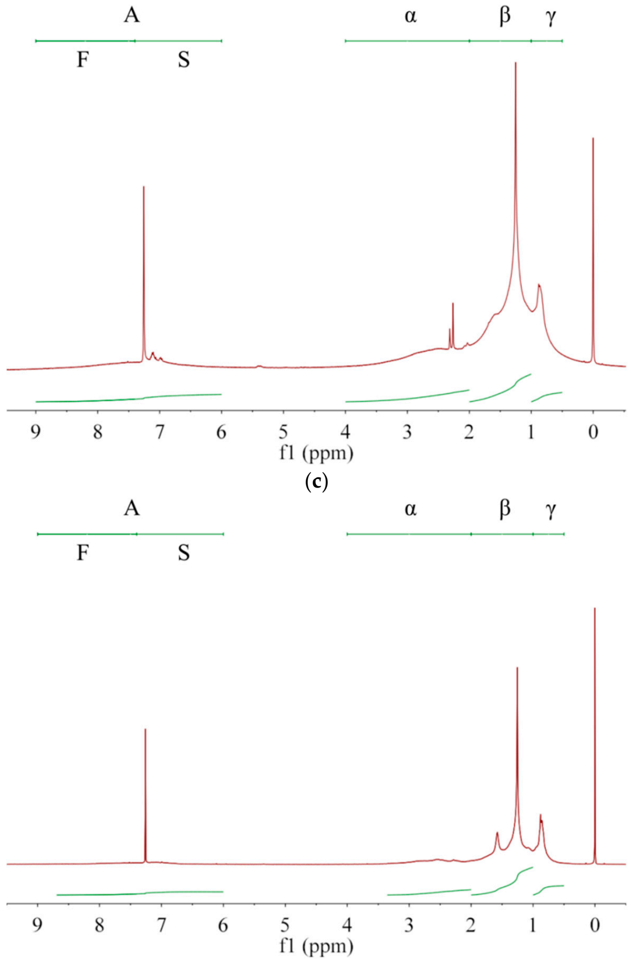

(**c**)

(**d**)

Figure 2. The ^{1}H-NMR spectra for (**a**) asphaltene A1, (**b**) asphaltene A2, (**c**) asphaltene A3 and (**d**) base asphalt. Protons are divided into A, α, β, and γ categories while the category A includes protons on single (S) and fused (F) aromatic rings.

In Figure 3, main absorption peaks are marked with purple letters on FTIR spectra and the wave numbers for these peaks are listed in Table 6 with peak assignments [6,31,32]. A general rule is that the peak of asphaltenes locates at smaller wave numbers than that of base asphalt. For example, the peak g arises from the skeleton stretching (C=C) of aromatic rings. It locates at 1592 cm^{-1} for A1 and locates at 1603 cm^{-1} for base asphalt. The shift of peak location towards higher wave number from A1 to asphalt arises from the decrease of molecular aromaticity. The aromatic ring makes the distribution of electron cloud density between single-bond and double-bond more uniform. This conjugative effect reduces the electron cloud density of double bond, and reduces its force constant and vibration frequency, so that the peak g moves towards smaller wave number in Figure 3 and Table 6. Moreover, aromatic rings have stronger electron absorption than saturated alkanes. This inductive effect reduces the electron cloud density and reduces the force constant and vibration frequency of the adjacent bond, thus its absorption peak moves towards lower wave number in Table 6. According to the previous EA and NMR results of Tables 4 and 5, from asphalt to A3 then to A1, the values of h_{S}, h_{F} and h_{A} increase while the unsaturation and aromaticity of the molecular structure increase. Such increase may improve the inductive and conjugation effects and shift the peak location towards lower wave number, which is consistent with results in Figure 3 and Table 6.

The aromatic rings can only influence a small proportion of chemical bonds adjacent to the rings while asphalt and asphaltene may have dramatically different proportion. In Table 6, the discrepancy between asphaltenes (A1, A2 and A3) is relatively smaller than that between asphaltenes and base asphalt. For example, the discrepancy of location for peak g is only 3 cm^{-1} between A1 and A3 while it is 11 cm^{-1} between A1 and asphalt, according to Table 6. The reason may be that the proportion of chemical bonds influenced by aromatic rings increases more dramatically (larger discrepancy) from asphalt to asphaltene A3 than it increases from asphaltenes A3 to A1. From asphalt to asphaltene A3, the asphaltene percentage increases from below 20% to nearly 100%. Such a shift of peak location was also observed for asphaltenes and even resins near 1603 and 1030 cm^{-1} in previous FTIR spectra [6]. Moreover, as asphalt was a complex mixture and its four components had significantly different spectra [6], the peak position and height may vary with the proportion of its components. Compared with asphaltenes, the saturates lacked peaks near 1030 cm^{-1} (peak d) and 1600 cm^{-1} (peak g) [6], owing to lacking S and O elements and double-bond in their molecules. The peak around 1377 cm^{-1} is used for the quantification of poly(styrene-*b*-butadiene-*b*-styrene) (AASHTO T302-15, JT/T 1329-2020) or other modifiers in asphalt [31,33,34]. According to Table 6, the position of this peak (e) moves towards a lower wave number from base asphalt to asphaltenes; thus, its specific position may vary with asphaltene proportion and should be checked carefully when calculating peak height or area integral for quantification.

Table 6. The wave number (in unit of cm^{-1}) for main peaks on IR spectra for the extracted asphaltenes (A1, A2 and A3) and the base asphalt [1].

IR Peak No.	A1	A2	A3	Asphalt
a	743	743	744	749
b	805	805	807	818
c	857	857	857	861
d	1027	1028	1028	1032
e	1372	1373	1374	1377
f	1452	1452	1452	1457
g	1592	1592	1595	1603
h	2849	2849	2849	2853
i	2919	2919	2919	2924
j	3053	3053	3054	3055

[1] Peaks a, b and c arise from the (C-H) aromatic ring substitution bands. The peak d may arise from the stretching vibration of sulfoxide (S=O) group. Peaks e and f arise from the bending vibration absorption of aromatic methyl (-CH_3) and methylene (CH_2) groups. The peak g is the skeleton stretching (C=C) of aromatic rings. The peak h arises from the symmetric stretching vibrations of aliphatic methyl (-CH_3) group. The peak i arises from the antisymmetric stretching vibrations of aliphatic methylene (CH_2) group. Peak j arises from the stretching vibration (=C-H) on the unsaturated bond or aromatic ring.

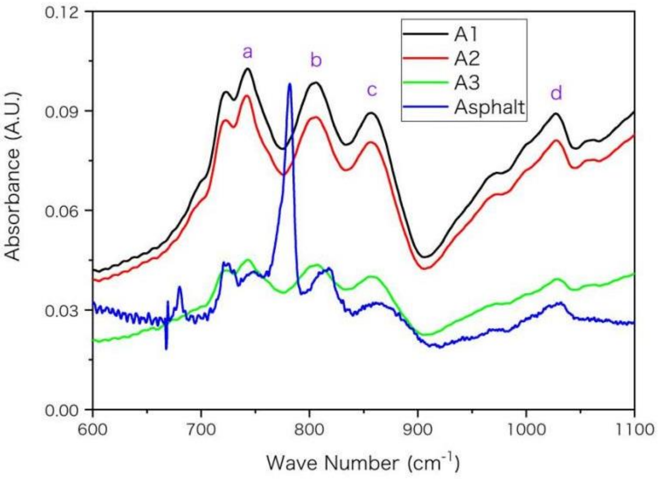

(**a**)

Figure 3. *Cont.*

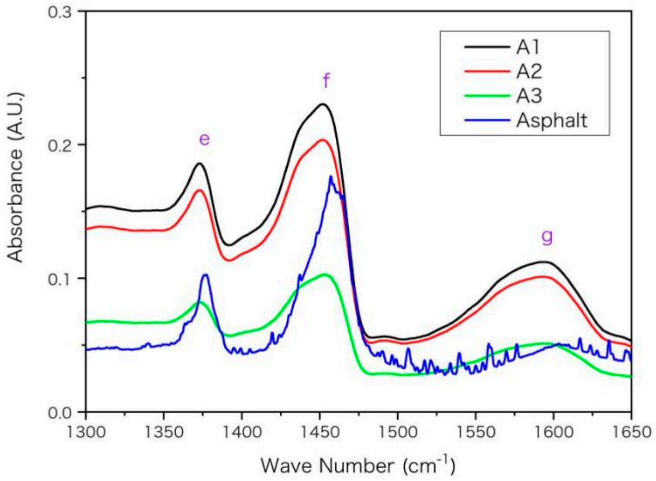

(**b**)

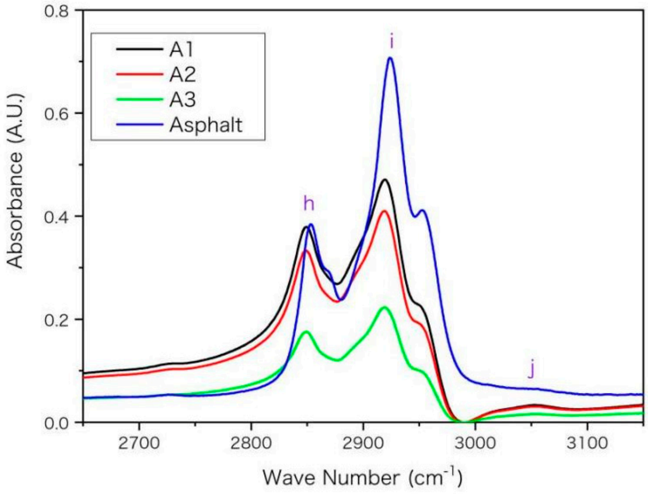

(**c**)

Figure 3. The FTIR spectra for the asphaltenes (A1, A2 and A3) and asphalt with wave number (in unit of cm^{-1}) in ranges of (**a**) 600–1100, (**b**) 1300–1650, (**c**) 2650–3150, respectively. The absorbance is in arbitrary unit (A.U.) and main peaks are marked in alphabetical order.

The XRD spectra of asphaltenes mainly have 3 characteristic peaks of γ, 002 and 10 band, which are labelled as γ, m and a, respectively, in Figure 4. The X-ray wavelength λ is 1.5406 angstrom (Å). According to their diffraction angles (2θ) listed in Table 7 and the Bragg equation $d = \lambda/(2\sin\theta)$ [35–37], the characteristic lengths d are calculated and listed in Table 7. The peaks γ and m reflect the packing structure of saturated alkyl chains and aromatic rings, respectively, while the peak a is related to the size of the aromatic sheet [35,37,38]. From A1 to A3 in Table 7, the decrease of average distance d_{Υ} indicates a denser packing of alkyl chains, while the increase of layer spacing d_{m} implies a looser packing of aromatic rings. According to previous EA, IR and NMR results, the unsaturation, polarity and aromaticity of asphaltenes decrease while the number of substituted branches and fraction of methyl groups increase from A1 to A3. Thus, the packing of aromatic rings becomes looser owing to more substituted branches on aromatic rings and smaller inter-molecular interactions, while the packing of alkyl chains becomes denser because of the increased fraction of free chain (methyl) end. The decreased ring fraction and molecular unsaturation is also helpful to decrease the molecular rigidity and beneficial to the packing of alkyl chains. Therefore, the variation trend of molecular structure of asphaltenes reflected by XRD spectra is consistent with the previous experimental results.

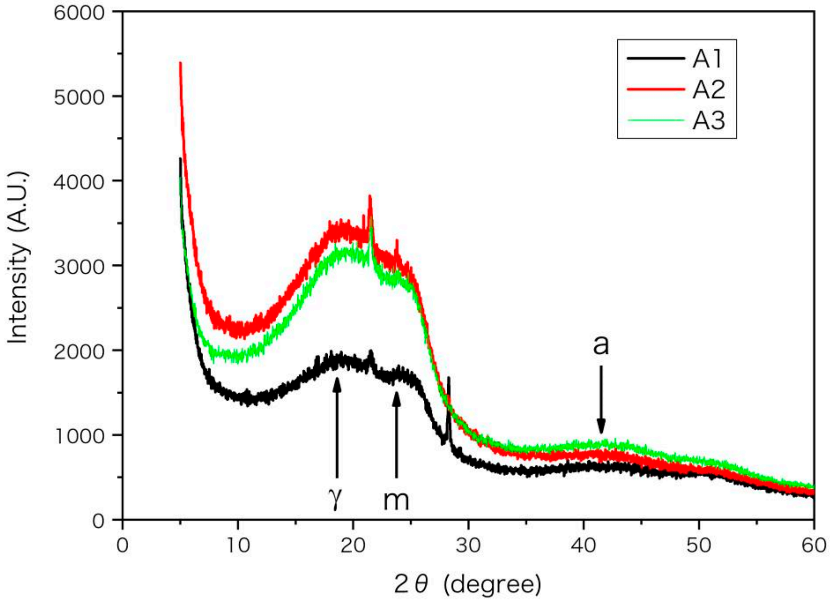

Figure 4. The XRD spectra for the asphaltenes (A1, A2 and A3). The diffraction intensity from position sensitive detector (PSD) is in arbitrary unit (A.U.) and plotted versus diffraction angle 2θ. The peaks of 002 and 10 band are labelled as m and a respectively.

Table 7. The packing length d (in unit of Å) calculated according to diffraction angles (2θ) from XRD spectra for the extracted asphaltenes (A1, A2 and A3). Subscripts m and a represent peaks of 002 and 10 band, respectively.

XRD Quantities	A1	A2	A3
$(2\theta)_{\mathrm{Y}}$	19.07°	19.21°	19.49°
$(2\theta)_{\mathrm{m}}$	23.90°	23.79°	23.76°
$(2\theta)_{\mathrm{a}}$	41.89°	40.34°	41.61°
$d_{\mathrm{Y}}/\text{Å}$	4.650	4.617	4.551
$d_{\mathrm{m}}/\text{Å}$	3.720	3.737	3.742

4. Conclusions

The linear equation between the density and concentration for standard samples of extractant containing xylene (G) and n-heptane (P) was fitted with $R^2 = 0.99967$ and used to analyze the real samples of extractant recovered and reused in asphaltene extraction process. With the increase of extraction number, the G/P ratio in extractant increases. The proportion of asphaltenes dissolved in solution rises and the proportion of precipitation from solution falls, resulting in a decrease of the asphaltene yield with the number of extractions. The results of EA, IR, NMR and XRD reached a consistent conclusion. For asphaltenes (A1, A2 and A3) sequentially extracted at room temperature, the fractions of substituted alkyl chains on aromatic rings and chain ends increase while the fractions of N and O elements as well as the C/H atom ratio (unsaturation) decrease, with increasing G/P ratio of extractant or with the extraction number. With increasing the G/P ratio of extractant, the extracted asphaltenes have smaller fractions of C and H of aromatic rings (aromaticity). The decrease of unsaturation and aromaticity from A1 to asphalt leads to reduced conjugative and inductive effects, which shift IR peaks towards higher wave numbers. Since asphaltenes extracted at higher G/P ratio have a smaller fraction of aromatic rings, more substitution rate on aromatic rings and bigger fraction of alkyl and methyl groups in molecular structure; they have smaller molecular rigidity and weaker inter-molecular conjugation. Thus, asphaltenes extracted at a higher G/P ratio have a denser packing of alkyl chains and a looser packing of aromatic rings.

Author Contributions: Conceptualization, D.S.; data curation, Y.S.; methodology, D.S.; visualization, Y.S.; writing—original draft, D.S. and Y.S.; writing—review and editing, D.S. and F.C. All authors have read and agreed to the published version of the manuscript.

Funding: This research received funding from the Nanxun Collaborative Innovation Center Key Research Project (SYS01001), the Open-ended Fund of Key Laboratory of Urban Pollutant Conversion, Chinese Academy of Sciences (KLUPCKF-2020-4), the Special Research Funds in Shandong Jianzhu University (X20087Z0101) and Doctoral Fund in Shandong Jianzhu University (X20078Z0101).

Institutional Review Board Statement: Not applicable.

Informed Consent Statement: Not applicable.

Data Availability Statement: The data presented in this study and the source codes are available on request from the corresponding author Dachuan Sun.

Acknowledgments: The author Dachuan Sun acknowledged Xianglong Zhao and Rui Feng for helpful discussions.

Conflicts of Interest: The authors declare no conflict of interest.

References

1. Gong, Y.; Xu, J.; Yan, E. Intrinsic temperature and moisture sensitive adhesion characters of asphalt-aggregate interface based on molecular dynamics simulations. *Constr. Build. Mater.* **2021**, *292*, 123462. [CrossRef]
2. Que, Y.; Wang, Y.; Xu, S.; Fan, Y. Quantitative detection of polymer content in styrene-butadiene-styrene modified asphalt after aging. *Polym. Eng. Sci.* **2022**, *62*, 2197–2206. [CrossRef]
3. Hassanzadeh, M.; Abdouss, M. A comprehensive review on the significant tools of asphaltene investigation. Analysis and characterization techniques and computational methods. *J. Pet. Sci. Eng.* **2022**, *208*, 109611. [CrossRef]
4. Lemarchand, C.A.; Greenfield, M.L.; Dyre, J.C.; Hansen, J.S. ROSE bitumen: Mesoscopic model of bitumen and bituminous mixtures. *J. Chem. Phys.* **2018**, *149*, 214901. [CrossRef] [PubMed]
5. Strausz, O.P.; Mojelsky, T.W.; Lown, E.M. The molecular structure of asphaltene: An unfolding story. *Fuel* **1992**, *71*, 1355–1362. [CrossRef]
6. Guo, M.; Liang, M.; Fu, Y.; Sreeram, A.; Bhasin, A. Average molecular structure models of unaged asphalt binder fractions. *Mater. Struct.* **2021**, *54*, 173. [CrossRef]
7. Sun, D. A Simple Scheme for Extraction of Asphaltenes from Asphalt at Room Temperature. *Coatings* **2022**, *12*, 407. [CrossRef]
8. Gray, M.R.; Yarranton, H.W.; Chacón-Patiño, M.L.; Rodgers, R.P.; Bouyssiere, B.; Giusti, P. Distributed properties of asphaltene nanoaggregates in crude oils: A review. *Energy Fuels* **2021**, *35*, 18078–18103. [CrossRef]
9. Ali, S.I.; Awan, Z.; Lalji, S.M. Laboratory evaluation experimental techniques of asphaltene precipitation and deposition controlling chemical additives. *Fuel* **2022**, *310*, 122194. [CrossRef]
10. Shao, R.; Li, D.; Pei, L.; Yuan, Y.; Liu, X.; Li, W. Effect of Deasphalting Solvent on Structure of Coal Tar Asphaltene. *Acta Pet. Sin. (Pet. Process. Sect.)* **2017**, *33*, 1209–1217.
11. Yang, Y.; Bai, P.; Guo, X. Separation of Xylene Isomers: A Review of Recent Advances in Materials. *Ind. Eng. Chem. Res.* **2017**, *56*, 14725–14753. [CrossRef]
12. Cui, X.; Niu, Z.; Shan, C.; Yang, L.; Hu, J.; Wang, Q.; Lan, P.; Li, Y.; Wojtas, L.; Ma, S.; et al. Efficient separation of xylene isomers by a guestresponsive metal–organic framework with rotational anionic sites. *Nat. Commun.* **2020**, *11*, 5456. [CrossRef] [PubMed]
13. Mousavi-Dehghani, S.A.; Riazi, M.R.; Vafaie-Sefti, M.; Mansoori, G.A. An analysis of methods for determination of onsets of asphaltene phase separations. *J. Pet. Sci. Eng.* **2004**, *42*, 145–156. [CrossRef]
14. Goual, L.; Sedghi, M.; Wang, X.; Zhu, Z. Asphaltene Aggregation and Impact of Alkylphenols. *Langmuir* **2014**, *30*, 5394–5403. [CrossRef]
15. Roy, M.M. HPLC analysis of aldehydes in automobile exhaust gas: Comparison of exhaust odor and irritation in different types of gasoline and diesel engines. *Energ. Convers. Manag.* **2008**, *49*, 1111–1118. [CrossRef]
16. Vempatapu, B.P.; Kanaujia, P.K. Monitoring petroleum fuel adulteration: A review of analytical methods. *TrAC-Trend. Anal. Chem.* **2017**, *92*, 1–11. [CrossRef]
17. Hale, C.S.; Bhakta, H.C.; Jonak, C.R.; Yonan, J.M.; Binder, D.K.; Grover, W.H.; Rodgers, V.G.J. Differential densimetry: A method for determining ultra-low fluid flux and tissue permeability. *AIP Adv.* **2019**, *9*, 095063. [CrossRef]
18. Zhang, M.; Hao, P.; Dong, S.; Li, Y.; Yuan, G. Asphalt binder micro-characterization and testing approaches: A review. *Measurement* **2020**, *151*, 107255. [CrossRef]
19. Ismail, M.; Yang, Y.; Chaisoontornyotin, W.; Ovalles, C.; Rogel, E.; Moir, M.E.; Hoepfner, M.P. Effect of chemical inhibitors on asphaltene precipitation and morphology using ultra-small-angle X-ray scattering. *Energy Fuels* **2019**, *33*, 3681–3693. [CrossRef]
20. Nguyen, M.T.; Nguyen, D.L.T.; Xia, C.; Nguyen, T.B.; Shokouhimehr, M.; Sana, S.S.; Grace, A.N.; Aghbashlo, M.; Tabatabaei, M.; Sonne, C.; et al. Recent advances in asphaltene transformation in heavy oil hydroprocessing: Progress, challenges, and future perspectives. *Fuel Process. Technol.* **2021**, *213*, 106681. [CrossRef]

21. Fan, M.; Zhao, S.; Sun, X.; Xu, Z. Comparison of properties of C_5 and C_7 asphaltenes from different heavy oils. *China Pet. Process. Petrochem. Technol.* **2019**, *50*, 96–102.
22. Liu, S.; Zhou, G.; Cheng, G.; Wang, X.; Liu, G.; Jin, W. Emerging membranes for separation of organic solvent mixtures by pervaporation or vapor permeation. *Sep. Purif. Technol.* **2022**, *299*, 121729. [CrossRef]
23. AlTuwaim, M.S.; Alkhaldi, K.H.A.E.; Al-Jimaz, A.S.; Alanezi, K.M. Separation of Alkylbenzenes from n-Heptane Using Binary Mixtures of Ionic Solvents. *J. Chem. Eng. Data* **2019**, *64*, 1187–1194. [CrossRef]
24. Cimino, R.; Correra, S.; Sacomani, P.A.; Carniani, C. Thermodynamic modelling for prediction of asphaltene deposition in live oils. In Proceedings of the SPE International Symposium on Oilfield Chemistry, San Antonio, TX, USA, 14–17 February 1995.
25. Kreuger, T.; Bos, A.N.R.; Kersten, S.R.A. Predicting gasification rates of pyrolytic graphite deposited from methane. *Chem. Eng. J.* **2022**, *440*, 135487. [CrossRef]
26. Wang, C.; Zhang, X.; Wang, W.; Sun, J.; Mao, Y.; Zhao, X.; Song, Z. A stepwise microwave synergistic pyrolysis approach to produce sludge-based biochars: Optimizing and mechanism of heavy metals immobilization. *Fuel* **2022**, *314*, 122770. [CrossRef]
27. León, A.Y.; Alexander, G.M.; Picón, H.; Dionisio, L.C.; Daniel, R.M.V. Reactivity of Vacuum Residues by Thermogravimetric Analysis and Nuclear Magnetic Resonance Spectroscopy. *Energy Fuels* **2021**, *34*, 9231–9242. [CrossRef]
28. Zhao, H.; Chai, X.; Wang, Y.; Shi, H.; Zhang, R.; Dong, Z.; Han, L. Analysis of styrene-butadiene-styrene (SBS) content in modified asphalt with ^{1}H NMR Spectroscopy. *Chin. J. Magn. Reson.* **2017**, *34*, 323–328.
29. Huang, J. Characterization of asphalt fractions by NMR spectroscopy. *Pet. Sci. Technol.* **2010**, *28*, 618–624. [CrossRef]
30. Mondal, S.; Yadav, A.; Kumar, R.; Bansal, V.; Das, S.K.; Christopher, J.; Kapur, G.S. Molecular Level Structural Insight into Clarified Oil by NMR Spectroscopy: Estimation of Hydrocarbon Types and Average Structural Parameters. *Energy Fuels* **2017**, *31*, 7682–7692. [CrossRef]
31. Hou, X.; Lv, S.; Chen, Z.; Xiao, F. Applications of Fourier Transform Infrared Spectroscopy Technologies on Asphalt Materials. *Measurement* **2018**, *121*, 304–316. [CrossRef]
32. Wang, K.; Yuan, J.; Gao, N. Determination of Styrene-Butadiene-Styrene Block Copolymer in Modified Asphalt by Dissolution Coating Infrared Spectroscopy. *PCTA (Part B Chem. Anal.)* **2015**, *51*, 357–359.
33. Xu, S.; Fan, Y.; Feng, Z.; Ke, Y.; Zhang, C.; Huang, H. Comparison of quantitative determination for SBS content in SBS modified asphalt. *Constr. Build. Mater.* **2021**, *282*, 122733. [CrossRef]
34. Luo, S.; Tian, J.; Liu, Z.; Lu, Q.; Zhong, K.; Yang, X. Rapid determination of styrene-butadiene-styrene (SBS) content in modified asphalt based on Fourier transform infrared (FTIR) spectrometer and linear regression analysis. *Measurement* **2020**, *151*, 107204. [CrossRef]
35. Jennings, J.; Growney, D.J.; Brice, H.; Mykhaylyk, O.O.; Armes, S.P. Application of scattering and diffraction techniques for the morphological characterization of asphaltenes. *Fuel* **2022**, *327*, 125042. [CrossRef]
36. AlHumaidan, F.S.; Hauser, A.; Rana, M.S.; Lababidi, H.M.S.; Behbehani, M. Changes in asphaltene structure during thermal cracking of residual oils: XRD study. *Fuel* **2015**, *150*, 558–564. [CrossRef]
37. Caputo, P.; Ventruti, G.; Calandra, P.; Porto, M.; Teltayev, B.; Angelico, R.; Rossi, C.O. Searching effective indicators of microstructural changes in bitumens during aging: A multi-technique approach. *Colloid Surface A* **2022**, *641*, 128529. [CrossRef]
38. AlHumaidan, F.S.; Rana, M.S.; Vinoba, M.; Rajasekaran, N.; AlHenyyan, H.Y.; Ali, A.A. Synthesizing few-layer carbon materials from asphaltene by thermal treatment. *Diam. Relat. Mater.* **2022**, *129*, 109316. [CrossRef]

coatings

Article

On Strain Gradient Theory and Its Application in Bending of Beam

Anqing Li ^{1,2,*}, Qing Wang ^{3}, Ming Song ^{1,2}, Jun Chen ^{1,2}, Weiguang Su ^{1,2}, Shasha Zhou ^{1,2} and Li Wang ^{1,2,*}

1 School of Mechanical Engineering, Qilu University of Technology (Shandong Academy of Sciences), Jinan 250353, China
2 Shandong Institute of Mechanical Design and Research, Jinan 250031, China
3 College of Mechanical and Electronic Engineering, Qingdao University, Qingdao 266071, China
* Correspondence: akin@qlu.edu.cn (A.L.); liwang@qlu.edu.cn (L.W.)

Abstract: The general strain gradient theory of Mindlin is re-visited on the basis of a new set of higher-order metrics, which includes dilatation gradient, deviatoric stretch gradient, symmetric rotation gradient and curvature. A strain gradient bending theory for plane-strain beams is proposed based on the present strain gradient theory. The stress resultants are re-defined and the corresponding equilibrium equations and boundary conditions are derived for beams. The semi-inverse solution for a pure bending beam is obtained and the influence of the Poisson's effect and strain gradient components on bending rigidity is investigated. As a contrast, the solution of the Bernoulli–Euler beam is also presented. The results demonstrate that when Poisson's effect is ignored, the result of the plane-strain beam is consistent with that of the Bernoulli–Euler beam in the couple stress theory. While for the strain gradient theory, the bending rigidity of a plane-strain beam ignoring the Poisson's effect is smaller than that of the Bernoulli–Euler beam due to the influence of the dilatation gradient and the deviatoric stretch gradient along the thickness direction of the beam. In addition, the influence of a strain gradient along the length direction on a bending rigidity is negligible.

Keywords: strain gradient theory; beam bending; size effect; plane-strain; couple stress theory

Citation: Li, A.; Wang, Q.; Song, M.; Chen, J.; Su, W.; Zhou, S.; Wang, L. On Strain Gradient Theory and Its Application in Bending of Beam. *Coatings* **2022**, *12*, 1304. https://doi.org/10.3390/coatings12091304

Academic Editor: Bohayra Mortazavi

Received: 12 August 2022
Accepted: 1 September 2022
Published: 5 September 2022

1. Introduction

A micro-beam is a typical component in micro-electro-mechanical systems (MEMSs). Accurate description of mechanical behavior of a beam is necessary for the design and performance prediction of MEMSs [1–3]. Although the traditional beam model has matured, the mechanical behavior of beams at the micro-scale is obviously different from that at the macro-scale, which cannot be captured by the traditional models [4–6]. Many experiments have reported that the mechanical properties of a micro-beam show obvious size effects [7–10]. McFarland and Colton observed that the bending stiffness of polypropylene cantilever beams with thicknesses of 15 and 30 μm is more than four times the value predicted by traditional theory [9]. Lam et al. found that the dimensionless bending stiffness of the epoxy polymeric beam with a thickness of 20 μm was approximately 2.3 times higher than that of 115 μm [7]. For the purpose of capturing the size-dependent mechanical properties, the strain gradient theory has been presented.

In strain gradient theory, the strain gradient is regarded as an additional (higher-order) deformation metric in addition to the traditional strain. Among the strain gradient theories, the couple stress theory is the earliest strain gradient theory that uses the rotation gradient as an additional deformation metric [11]. In fact, the stain gradient includes dilatation gradient, rotation gradient and deviatoric stretch gradient [12]. The rotation gradient is only the anti-symmetric part of the strain gradient. As with the development of strain gradient theory, the general strain gradient theory, including all strain gradient components, is proposed by Mindlin and Eshel by introducing five higher-order material constants [13]. Then, the general strain gradient theory of Mindlin has been re-formulated by Lam et al. on the basis of the equilibrium of moments of couples [7], and by Zhou et al. according to the independent strain gradient components [14], respectively. The two re-formulated strain gradient theories include three higher-order material constants. A simple strain gradient theory with only one higher-order material constant has been presented by Aifantis [15]. The general form of couple stress theory includes two higher-order material constants, which has been further simplified to include only one higher-order material constant by Yang et al. [16] and Hadjesfandiari and Dargush [17], respectively, by choosing only the symmetric or anti-symmetric parts as the higher-order deformation metrics. However, in our opinion, although these re-formulated strain gradient theories with three or fewer higher-order constants can also capture the size-effect phenomenon, these theories ignore the contribution of some strain gradient components and underestimate the stiffening effect of the strain gradient. In fact, Mindlin's strain gradient theory is a general strain gradient theory and should be used to develop micro-component models.

According to the strain gradient theory, many strain gradient beam models have been established to capture the size-dependent mechanical behaviors [18–23]. Based on Mindlin's strain gradient theory, a linear model of Bernoulli–Euler beams has been presented by Niiranen et al. [24], and a geometrically non-linear model was further developed by Tran and Niiranen [25] by adopting the von Kármán strain assumption. Based on the modified couple stress theory, Vo et al. presented the models of planar [26] and spatial [27] arbitrarily curved micro-beams and Li et al. investigated the bending and free vibration of bi-directional functionally graded graphene nano-platelets-reinforced composite micro-beams [28]. However, these existing models are contradictory [29]. The non-zero strain of Bernoulli–Euler beams is an axial strain, and its non-zero strain gradient includes the gradients of axial strain along the thickness direction and along the length direction. Currently, there are three main types of models available, depending on the stain gradient components used. The first category considers the strain gradient along the thickness direction and the length direction at the same time [30–33]. The second type considers only the strain gradient along the length direction and does not consider the strain gradient along the thickness direction [34]. The third type considers the strain gradient along the thickness direction rather than the length direction, since the strain gradient along the length direction can be neglected compared with that along the thickness direction for Euler beams [35]. The third type may be seen as an approximation of the first type. However, the second and third types are polar opposites, and one of them must be wrong. Thus, it is important to figure out which type is correct.

Lurie and Solyaev [29] checked the beam models of the first and second types and believed that only the second type (uniaxial stress state) could guarantee the satisfaction of boundary conditions on the top and bottom surfaces of the beams. However, in our opinion, the satisfaction of boundary conditions on the top and bottom surfaces of the beams depends on the definition of moment, which includes the higher-order stress. The first type can satisfy the boundary conditions on the top and bottom surfaces of the beams by defining a different moment from that of Lurie and Solyaev.

The purpose of this work is to establish a correct beam model and analyze the contribution of the strain gradient components to bending stiffness. This paper is organized as follows: Mindlin's general strain gradient elasticity theory is re-formulated by introducing a new set of strain gradient components so as to investigate the effects of each strain gradient component conveniently in Section 2. Then, the bending theory for plane-strain beams is presented in Section 3, and the semi-inverse solution for pure bending beams is developed in Section 4. Section 5 investigates the bending of Bernoulli–Euler beams and compares the results of plane-strain beams and Bernoulli–Euler beams. Finally, conclusions are summarized in Section 6.

2. Formulations of Strain Gradient Elasticity Theories

2.1. A Summary of Strain Gradient Theory

In strain gradient theory, not only the traditional strain ε_{ij} but also its gradients η_{ijk} are considered in the internal energy density U, written as:

$$U = U(\varepsilon_{ij}, \eta_{ijk}) \tag{1}$$

with

$$\varepsilon_{ij} = \frac{1}{2}(u_{i,j} + u_{j,i}),\ \eta_{ijk} = \varepsilon_{jk,i} \tag{2}$$

where u_i denotes the displacement vector and a comma represents the differentiation with respect to the coordinates. The work-conjugated Cauchy stress σ_{ij} and higher-order stress τ_{ijk} with respect to strain and strain gradient, respectively, are given by:

$$\sigma_{ij} = \frac{\partial U}{\partial \varepsilon_{ij}},\ \tau_{ijk} = \frac{\partial U}{\partial \eta_{ijk}} \tag{3}$$

Obviously, the stress tensor σ_{ij} is a symmetric tensor and the higher-order stress tensor τ_{ijk} is symmetric with respect to subscripts j and k.

For a solid of volume V with surface boundary S and sharp edge C, the virtual work principle of the strain gradient theory is given as [14]:

$$\int_V (\sigma_{ij}\delta\varepsilon_{ij} + \tau_{ijk}\delta\eta_{ijk})\mathrm{d}V = \int_V \bar{b}_k \delta u_k \mathrm{d}V + \int_S (\bar{t}_k \delta u_k + \bar{r}_k D\delta u_k)\mathrm{d}S + \oint_C \bar{f}_k \delta u_k \mathrm{d}C \tag{4}$$

Thus, the equilibrium equation can be obtained by applying the variation of internal energy, as shown in Appendix A in detail, given as:

$$\sigma_{ik,i} - \tau_{ijk,ij} + \bar{b}_k = 0 \tag{5}$$

and the boundary conditions on surface boundary S and sharp edge C are:

$$n_i(\sigma_{ik} - \tau_{jik,j}) + (D_p n_p) n_i n_j \tau_{ijk} - D_i(n_j \tau_{jik}) = \bar{t}_k \text{ or } u_k = \bar{u}_k \tag{6}$$

$$n_i n_j \tau_{ijk} = \bar{r}_k \text{ or } \overline{Du_k} = Du_k \tag{7}$$

and

$$[[k_j n_i \tau_{ijk}]] = \bar{f}_k \text{ or } u_k = \bar{u}_k \tag{8}$$

where $D = n_i \partial_i$ is the normal gradient operator with n_i representing a unit vector normal to the boundary surface S, $D_i = (\delta_{ik} - n_i n_k)\partial_k$ represents the surface gradient operator, the square brackets stands for the difference between the values of the enclosed quantity on the two sides of the edge and k_i denotes the outer co-normal vector.

For linear elastic isotropic materials, the internal energy density of Equation (1) is generally written as:

$$U = \frac{1}{2}k\varepsilon_{ii}\varepsilon_{jj} + \mu\varepsilon'_{ij}\varepsilon'_{ij} + g_1\eta_{iik}\eta_{kjj} + g_2\eta_{ijj}\eta_{ikk} + g_3\eta_{iik}\eta_{jjk} + g_4\eta_{ijk}\eta_{ijk} + g_5\eta_{ijk}\eta_{kji} \tag{9}$$

where $\varepsilon'_{ij} = \varepsilon_{ij} - \frac{1}{3}\delta_{ij}\varepsilon_{nn}$ denotes the deviatoric strain tensor. Then, the constitutive equations in terms of Equation (3) are given by:

$$\sigma_{ij} = k\delta_{ij}\varepsilon_{nn} + 2\mu\varepsilon'_{ij} \tag{10}$$

$$\begin{aligned}\tau_{ijk} = {} & \tfrac{1}{2}g_1(\delta_{ij}\eta_{knn} + \delta_{ik}\eta_{jnn} + 2\delta_{jk}\eta_{nni}) \\ & + 2g_2\delta_{jk}\eta_{inn} + g_3(\delta_{ij}\eta_{nnk} + \delta_{ik}\eta_{nnj}) + 2g_4\eta_{ijk} + g_5(\eta_{kji} + \eta_{jki})\end{aligned} \tag{11}$$

in which k and μ are the bulk and shear moduli, δ_{ij} denotes the Kronecker delta and g_i (i = 1, 2, 3, 4, 5) is the introduced higher-order constant.

2.2. Development of Strain Gradient Components, and Equilibrium and Boundary Conditions

Strain gradient has been decomposed into its orthogonal components to re-formulate the strain gradient theory [14]. In fact, strain gradient includes dilatation gradient γ_i, deviatoric stretch gradient $\eta_{ijk}^{(1)}$ and rotation gradient χ_{ij}. These strain gradient components are defined as:

$$\begin{aligned} &\gamma_i = \eta_{inn} \quad \chi_{ij} = e_{ilk}\eta_{ljk} \\ &\eta_{ijk}^{(1)} = \tfrac{1}{3}(\eta_{ijk} + \eta_{jki} + \eta_{kij}) \\ &\qquad -\tfrac{1}{15}[\delta_{ij}(2\eta_{nnk} + \eta_{knn}) + \delta_{jk}(2\eta_{nni} + \eta_{inn}) + \delta_{ki}(2\eta_{nnj} + \eta_{jnn})] \end{aligned} \tag{12}$$

with e_{ilk} denoting the alternating tensor. The rotation gradient can be further decomposed into its symmetric and anti-symmetric parts, given as:

$$\chi_{ij}^s = \frac{1}{2}(\chi_{ij} + \chi_{ji}), \chi_{ij}^a = \frac{1}{2}(\chi_{ij} - \chi_{ji}) \tag{13}$$

Additionally, the anti-symmetric rotation gradient tensor χ_{ij}^a can be represented by its dual vector κ_i which is called as the curvature vector [17], written as:

$$\kappa_i = \frac{1}{2}e_{ijk}\chi_{kj}^a \tag{14}$$

Then, the strain gradient can be finally expressed as the sum of dilatation gradient γ_i, deviatoric stretch gradient $\eta_{ijk}^{(1)}$, symmetric rotation gradient χ_{ij}^s and curvature κ_i, given as [12]:

$$\eta_{ijk} = A_{ijks}\gamma_s + \eta_{ijk}^{(1)} + B_{ijkpq}\chi_{pq}^s + D_{ijks}\kappa_s \tag{15}$$

with the coefficients being:

$$\begin{aligned} A_{ijks} &= \tfrac{1}{5}(\delta_{ij}\delta_{ks} + \delta_{jk}\delta_{is} + \delta_{ik}\delta_{js}) \\ B_{ijkpq} &= \tfrac{1}{3}(\delta_{kq}e_{ijp} + \delta_{jq}e_{ikp}) \\ D_{ijks} &= \tfrac{1}{5}(2\delta_{jk}\delta_{is} - 3\delta_{ij}\delta_{ks} - 3\delta_{ik}\delta_{js}) \end{aligned} \tag{16}$$

Thus, the internal energy density becomes a function of strain and strain gradient components, written as $U = U(\varepsilon_{ij}, \gamma_i, \eta_{ijk}^{(1)}, \chi_{ij}^s, \kappa_i)$. The corresponding work-conjugated higher-order stress components p_i, $\tau_{ijk}^{(1)}$, m_{ij}^s, μ_i with respect to strain gradient components γ_i, $\eta_{ijk}^{(1)}$, χ_{ij}^s, κ_i, respectively, are given by:

$$p_i = \frac{\partial U}{\partial \gamma_i},\ \tau_{ijk}^{(1)} = \frac{\partial U}{\partial \eta_{ijk}^{(1)}},\ m_{ij}^s = \frac{\partial U}{\partial \chi_{ij}^s},\ \mu_i = \frac{\partial U}{\partial \kappa_i} \tag{17}$$

The virtual work density can be rewritten in terms of the new strain metrics as:

$$\begin{aligned} \delta U &= \sigma_{ij}\delta\varepsilon_{ij} + p_i\delta\gamma_i + \tau_{ijk}^{(1)}\delta\eta_{ijk}^{(1)} + m_{ij}^s\delta\chi_{ij}^s + \mu_i\delta\kappa_i \\ &= \sigma_{ij}\delta\varepsilon_{ij} + (\delta_{jk}p_i + \tau_{ijk}^{(1)} + \tfrac{1}{2}m_{sj}^s e_{sik} + \tfrac{1}{2}m_{sk}^s e_{sij} + \tfrac{1}{2}\delta_{jk}\mu_i - \tfrac{1}{4}\delta_{ij}\mu_k - \tfrac{1}{4}\delta_{ik}\mu_j)\delta\eta_{ijk} \end{aligned} \tag{18}$$

From Equation (18), it can be concluded that the higher-order stress τ_{ijk} is associated with the higher-order stress components p_i, $\tau_{ijk}^{(1)}$, m_{ij}^s, μ_i by:

$$\tau_{ijk} = \delta_{jk}p_i + \tau_{ijk}^{(1)} + \frac{1}{2}m_{sj}^s e_{sik} + \frac{1}{2}m_{sk}^s e_{sij} + \frac{1}{2}\delta_{jk}\mu_i - \frac{1}{4}\delta_{ij}\mu_k - \frac{1}{4}\delta_{ik}\mu_j \tag{19}$$

Finally, applying the principle of virtual work yields the equilibrium equation in V as:

$$\sigma_{ik,i} - p_{i,ik} - \tau_{ijk,ij}^{(1)} - \frac{1}{2}e_{lik}m_{lj,ij}^s - \frac{1}{4}\mu_{i,ik} + \frac{1}{4}\mu_{k,ii} + \overline{b}_k = 0 \tag{20}$$

and the boundary conditions on S as:

$$\begin{array}{c} n_j(\sigma_{jk} - \delta_{jk}p_{i,i} - \tau_{ijk,i}^{(1)} - \frac{1}{2}e_{lik}m_{lj,i}^s - \frac{1}{2}e_{lij}m_{lk,i}^s - \frac{1}{2}\delta_{jk}\mu_{i,i} + \frac{1}{4}\mu_{k,j} + \frac{1}{4}\mu_{j,k}) \\ +(D_p n_p)(n_i n_k p_i + n_i n_j \tau_{ijk}^{(1)} + n_i n_j n_l n_k \tau_{ijl}^{(1)} + \frac{1}{2}n_i n_j e_{lik} m_{lj}^s + \frac{1}{4}n_i n_k \mu_i - \frac{1}{4}\mu_k) \\ -D_j(\delta_{jk}n_i p_i + n_i\tau_{ijk}^{(1)} + n_i n_l n_k \tau_{ilj}^{(1)} + \frac{1}{2}n_i e_{lik}m_{lj}^s + \frac{1}{2}n_i e_{lij}m_{lk}^s + \frac{1}{2}e_{lij}n_p n_i n_k m_{lp}^s \\ +\frac{1}{2}\delta_{jk}n_i\mu_i - \frac{1}{4}n_j\mu_k - \frac{1}{2}n_k\mu_j + \frac{1}{4}n_j n_i n_k \mu_i) = \overline{t}_k \end{array} \quad \text{or } u_k = \overline{u}_k \tag{21}$$

$$n_j m_{kj}^s - n_j n_k n_i m_{ij}^s + 2n_j n_i n_l e_{kls}\tau_{ijs}^{(1)} + \frac{1}{2}n_l e_{slk}\mu_s = \overline{q}_k \text{ or } (\delta_{kl} - n_k n_l)\delta\theta_l = \overline{\theta}_k \tag{22}$$

$$p_i n_i + n_j n_i n_k \tau_{ijk}^{(1)} = \overline{r} \text{ or } \varepsilon_N = n_i n_j \varepsilon_{ij} = \overline{\varepsilon}_N \tag{23}$$

and along the sharp edge C as:

$$\begin{array}{c} [[k_k n_i p_i + k_j n_i \tau_{ijk}^{(1)} + k_l n_i n_j n_k \tau_{ijl}^{(1)} + \frac{1}{2}k_j e_{lik} n_i m_{lj}^s + \frac{1}{2}k_j e_{lij} n_i m_{lk}^s + \frac{1}{2}k_j e_{lij} n_p n_i n_k m_{lp}^s \\ +\frac{1}{2}k_k n_i \mu_i - \frac{1}{4}k_i n_i \mu_k - \frac{1}{2}k_j n_k \mu_j + \frac{1}{4}k_j n_j n_i n_k \mu_i]] = \overline{f}_k \\ \text{or } u_k = \overline{u}_k \end{array} \tag{24}$$

For linear elastic isotropic materials, the internal energy density in Equation (9) can be re-formulated by substituting Equation (15) into Equation (9), written as:

$$U = \frac{1}{2}k\varepsilon_{ii}\varepsilon_{jj} + \mu\varepsilon'_{ij}\varepsilon'_{ij} + a_1\gamma_i\gamma_i + a_2\eta_{ijk}^{(1)}\eta_{ijk}^{(1)} + a_3\chi_{pi}^s\chi_{pi}^s + a_4\kappa_i\kappa_i - a_5\kappa_i\gamma_i \tag{25}$$

where a_i (i = 1, 2, 3, 4, 5) is a higher-order material constant in another form which is related to g_i by:

$$\begin{array}{l} a_1 = g_1 + g_2 + g_3 + \frac{3}{5}g_4 + \frac{3}{5}g_5, \ a_2 = g_4 + g_5 \\ a_3 = \frac{2}{3}g_4 - \frac{1}{3}g_5, \ a_4 = 4g_3 + \frac{12}{5}g_4 + \frac{2}{5}g_5, \ a_5 = 2g_1 + 4g_3 + \frac{8}{5}g_4 + \frac{8}{5}g_5 \end{array} \tag{26}$$

By re-writing the higher-order material constants as:

$$a_1 = \mu l_0^2, \ a_2 = \mu l_1^2, \ a_3 = \mu l_2^2, \ a_4 = 2\mu l_3^2, \ a_5 = \mu l_4^2 \tag{27}$$

with l_i (i = 0, 1, 2, 3, 4) representing five material length scale parameters, the higher-order constitutive relations can be obtained from Equations (17) and (25) as:

$$p_i = 2\mu l_0^2\gamma_i - \mu l_4^2\kappa_i, \ \tau_{ijk}^{(1)} = 2\mu l_1^2\eta_{ijk}^{(1)}, \ m_{ij}^s = 2\mu l_2^2\chi_{ij}^s, \ \mu_i = 4\mu l_3^2\kappa_i - \mu l_4^2\gamma_i \tag{28}$$

The present strain gradient theory is another expression of Mindlin's strain gradient theory, which is a general theory with five higher-order material constants. When the curvature vector κ_i is excluded (by letting l_3 = l_4 = 0), the present formulation of strain gradient theory will reduce to that of Lam et al.'s [7]. When the material length scale parameters are constrained as:

$$l_0 = \frac{3}{\sqrt{5}}\bar{l}_0,\ l_1 = \bar{l}_1,\ l_2 = \sqrt{2}\bar{l}_2,\ l_3 = 3\sqrt{\frac{2}{5}}\bar{l}_0,\ l_4 = 2\sqrt{\frac{6}{5}}\bar{l}_0 \tag{29}$$

the internal energy density of the present strain gradient theory will reduce to

$$\begin{aligned} U &= \tfrac{1}{2}k\varepsilon_{ii}\varepsilon_{jj} + \mu\varepsilon'_{ij}\varepsilon'_{ij} + \tfrac{9}{5}\mu\bar{l}_0^2\gamma_i\gamma_i + \mu\bar{l}_1^2\eta_{ijk}^{(1)}\eta_{ijk}^{(1)} + 2\mu\bar{l}_2^2\chi_{ij}^s\chi_{ij}^s + \tfrac{36}{5}\mu\bar{l}_0^2\kappa_i\kappa_i - \tfrac{24}{5}\mu\bar{l}_0^2\gamma_i\kappa_i \\ &= \tfrac{1}{2}k\varepsilon_{ii}\varepsilon_{jj} + \mu\varepsilon'_{ij}\varepsilon'_{ij} + \mu\bar{l}_0^2\gamma_i\gamma_i + \mu\bar{l}_1^2\eta_{ijk}^{(1)}\eta_{ijk}^{(1)} + \mu(\bar{l}_2^2 + \tfrac{9}{5}\bar{l}_0^2)\chi'_{ij}\chi'_{ij} + \mu(\bar{l}_2^2 - \tfrac{9}{5}\bar{l}_0^2)\chi'_{ij}\chi'_{ji} \end{aligned} \tag{30}$$

which is the internal energy density of Zhou et al. with $\chi'_{ij} = e_{ilk}\varepsilon'_{jk,l}$ denoting the deviatoric rotation gradient [14].

2.3. Couple Stress Theory

In couple stress theory, the rotation gradient rather than the strain gradient is included in the internal energy density. That is, the strain gradient theory will reduce to the couple stress theory when the dilatation gradient γ_i and deviatoric stretch gradient $\eta_{ijk}^{(1)}$ are excluded. Thus, when the higher-order stress components p_i and $\tau_{ijk}^{(1)}$ are excluded, the equilibrium equation and boundary conditions of the strain gradient theory in Equations (20)–(24) can reduce to those of the couple stress theory. The equilibrium equation is:

$$\sigma_{ik,i} - \frac{1}{2}e_{lik}m_{lj,ij}^s - \frac{1}{4}\mu_{i,ik} + \frac{1}{4}\mu_{k,ii} + \bar{b}_k = 0 \tag{31}$$

and the boundary conditions on S are:

$$\begin{array}{c} n_j(\sigma_{jk} - \tfrac{1}{2}e_{lik}m_{lj,i}^s - \tfrac{1}{2}e_{lij}m_{lk,i}^s - \tfrac{1}{2}\delta_{jk}\mu_{i,i} + \tfrac{1}{4}\mu_{k,j} + \tfrac{1}{4}\mu_{j,k}) \\ +(D_p n_p)(\tfrac{1}{2}n_i n_j e_{lik}m_{lj}^s + \tfrac{1}{4}n_i n_k \mu_i - \tfrac{1}{4}\mu_k) \\ -D_j(\tfrac{1}{2}n_i e_{lik}m_{lj}^s + \tfrac{1}{2}n_i e_{lij}m_{lk}^s + \tfrac{1}{2}e_{lij}n_p n_i n_k m_{lp}^s \\ +\tfrac{1}{2}\delta_{jk}n_i\mu_i - \tfrac{1}{4}n_j\mu_k - \tfrac{1}{2}n_k\mu_j + \tfrac{1}{4}n_j n_i n_k \mu_i) = \bar{t}_k \end{array} \quad \text{or } u_k = \bar{u}_k \tag{32}$$

$$n_j m_{kj}^s - n_j n_k n_i m_{ij}^s + \frac{1}{2}n_l e_{slk}\mu_s = \bar{q}_k \text{ or } (\delta_{kl} - n_k n_l)\delta\theta_l = \bar{\theta}_k \tag{33}$$

and along the sharp edge C is:

$$\begin{array}{c} [[\tfrac{1}{2}k_j e_{lik}n_i m_{lj}^s + \tfrac{1}{2}k_j e_{lij}n_i m_{lk}^s + \tfrac{1}{2}k_j e_{lij}n_p n_i n_k m_{lp}^s \\ +\tfrac{1}{2}k_k n_i\mu_i - \tfrac{1}{4}k_i n_i\mu_k - \tfrac{1}{2}k_j n_k\mu_j + \tfrac{1}{4}k_j n_j n_i n_k \mu_i]] = \bar{f}_k \end{array} \quad \text{or} u_k = \bar{u}_k \tag{34}$$

In addition, the anti-symmetric couple stress component m_{ij}^a, which is work-conjugated with the anti-symmetric rotation gradient component χ_{ij}^a, is commonly used in many articles rather than the present higher-order stress component μ_i. In fact, according to the virtual work density of couple stress theory

$$\begin{aligned} \delta U &= \sigma_{ij}\delta\varepsilon_{ij} + m_{ij}^s\delta\chi_{ij}^s + \mu_i\delta\kappa_i = \sigma_{ij}\delta\varepsilon_{ij} + m_{ij}^s\delta\chi_{ij}^s + \tfrac{1}{2}e_{ijk}\mu_i\delta\chi_{kj}^a \\ &= \sigma_{ij}\delta\varepsilon_{ij} + m_{ij}^s\delta\chi_{ij}^s + m_{ij}^a\delta\chi_{ij}^a \end{aligned} \tag{35}$$

The anti-symmetric couple stress component m_{ij}^a is associated with the higher-order stress component μ_i by $m_{ij}^a = \frac{1}{2}e_{kji}\mu_k$. Additionally, in turn, the higher-order stress component μ_i is related to the anti-symmetric couple stress component m_{ij}^a through $\mu_i = e_{ijk}m_{kj}^a$. Then, from Equations (31)–(34), the equilibrium equation and boundary conditions of couple stress theory can be re-formulated in the form of couple stress components m_{ij}^s and m_{ij}^a,which are shown in Appendix B in detail.

For linear elastic isotropic materials, the internal energy density of the couple stress theory can be reduced from Equation (25), written as:

$$\begin{aligned} U &= \tfrac{1}{2}k\varepsilon_{ii}\varepsilon_{jj} + \mu\varepsilon'_{ij}\varepsilon'_{ij} + a_3\chi^s_{ij}\chi^s_{ij} + a_4\kappa_i\kappa_i \\ &= \tfrac{1}{2}k\varepsilon_{ii}\varepsilon_{jj} + \mu\varepsilon'_{ij}\varepsilon'_{ij} + a_3\chi^s_{ij}\chi^s_{ij} + \tfrac{1}{2}a_4\chi^a_{ij}\chi^a_{ij} \end{aligned} \tag{36}$$

Consider the material length scale parameters in Equation (27), the couple stress components can be given as:

$$m^s_{ij} = \frac{\partial U}{\partial \chi^s_{ij}} = 2\mu l_2^2 \chi^s_{ij},\ \mu_i = \frac{\partial U}{\partial \kappa_i} = 4\mu l_3^2 \kappa_i \text{ or } m^a_{ij} = \frac{\partial U}{\partial \chi^a_{ij}} = 2\mu l_3^2 \chi^a_{ij} \tag{37}$$

3. Bending Theory for Plane-Strain Beams

Consider the same plane-strain beam problem as Lam et al. [7]. The length of a beam is L and the thickness is h. The thickness of a beam is much smaller than its length. The Cartesian coordinate system is adopted, and the X-axis coincides with the center line of the beam along the length direction, and the Z-axis coincides with the thickness direction. By ignoring the body forces and only considering the normal tractions $\overline{q}_{\pm h/2}$ in units of N/m^2 applied on the top or bottom surfaces of the beam, the governing equations along the length and thickness directions can be obtained from Equation (20), given by:

$$\left(\sigma_{11} - p_{1,1} - \tau^{(1)}_{111,1}\right)_{,1} + \left(\sigma_{13} - p_{3,1} - 2\tau^{(1)}_{113,1} - \tau^{(1)}_{133,3} - \frac{1}{2}m^s_{12,1} - \frac{1}{2}m^s_{23,3} - \frac{1}{4}\mu_{3,1} + \frac{1}{4}\mu_{1,3}\right)_{,3} = 0 \tag{38}$$

$$\left(\sigma_{33} - p_{1,1} - p_{3,3} - 2\tau^{(1)}_{133,1} - \tau^{(1)}_{333,3} + \frac{1}{2}m^s_{23,1} - \frac{1}{4}\mu_{1,1}\right)_{,3} + \left(\sigma_{13} - \tau^{(1)}_{113,1} + \frac{1}{2}m^s_{21,1} + \frac{1}{4}\mu_{3,1}\right)_{,1} = 0 \tag{39}$$

The boundary conditions on the top and bottom surfaces of the beam, $z = \pm h/2$, from Equations (21)–(23) are:

$$\sigma_{33} - p_{1,1} - p_{3,3} - 3\tau^{(1)}_{133,1} - \tau^{(1)}_{333,3} = \overline{q}_{\pm h/2} \tag{40}$$

$$\sigma_{31} - p_{3,1} - 2\tau^{(1)}_{113,1} - \tau^{(1)}_{133,3} - \frac{1}{2}m^s_{21,1} - \frac{1}{2}m^s_{23,3} - \frac{1}{4}\mu_{3,1} + \frac{1}{4}\mu_{1,3} = 0 \tag{41}$$

$$m^s_{23} + 2\tau^{(1)}_{133} - \frac{1}{2}\mu_1 = 0 \tag{42}$$

$$p_3 + \tau^{(1)}_{333} = 0 \tag{43}$$

On the surfaces normal to the X-axis, $x = 0$ or L, the boundary conditions obtained from Equations (21)–(23) are:

$$\overline{t}_1 = \sigma_{11} - \left(p_1 + \tau^{(1)}_{111}\right)_{,1} - \left(p_3 + 3\tau^{(1)}_{113}\right)_{,3} \tag{44}$$

$$\overline{t}_3 = \sigma_{13} + \frac{1}{2}\left(m^s_{21} + \frac{1}{2}\mu_3 - 2\tau^{(1)}_{113}\right)_{,1} + \frac{1}{2}\left(m^s_{23} - \frac{1}{2}\mu_1 + 2\tau^{(1)}_{133}\right)_{,3} - \left(p_1 + 3\tau^{(1)}_{133}\right)_{,3} \tag{45}$$

$$\overline{q}_2 = m^s_{21} - 2\tau^{(1)}_{113} + \frac{1}{2}\mu_3 \tag{46}$$

$$\overline{r} = p_1 + \tau^{(1)}_{111} \tag{47}$$

The boundary conditions at the edges of the top and bottom surfaces of the beam from Equation (24) are:

$$\overline{f}_1 = \pm\left[p_3 + 3\tau^{(1)}_{113}\right],\ \overline{f}_3 = \pm\left[p_1 + 3\tau^{(1)}_{133}\right],\ z = \pm\frac{h}{2} \tag{48}$$

The stress resultants can be re-defined due to the presence of higher-order stress components as:

$$\begin{aligned}
&N = \int_{-h/2}^{h/2} \sigma_{11} \mathrm{d}z \;\; Q = \int_{-h/2}^{h/2} (\sigma_{13} - \tau_{113,1}^{(1)} + \tfrac{1}{2} m_{21,1}^{s} + \tfrac{1}{4} \mu_{3,1}) \mathrm{d}z \\
&M = \int_{-h/2}^{h/2} (z\sigma_{11} + \tau_{113}^{(1)} + p_3 + m_{21}^{s} + \tfrac{1}{2}\mu_3) \mathrm{d}z \\
&N^h = \int_{-h/2}^{h/2} (p_1 + \tau_{111}^{(1)}) \mathrm{d}z \;\; M^h = \int_{-h/2}^{h/2} z(p_1 + \tau_{111}^{(1)}) \mathrm{d}z
\end{aligned} \tag{49}$$

where N, Q, M, N^h and M^h denote the axial stress resultant, shear stress resultant, moment, higher-order stress resultant and higher-order moment per unit width in the beam, respectively. According to the re-defined stress resultants in Equation (49) and the governing equations and boundary conditions in Equations (38)–(48), the same formulations from that of Lam et al. [7] can be obtained as:

$$\frac{dN}{dx} - \frac{d^2 N^h}{dx^2} = 0 \tag{50}$$

where

$$\frac{dQ}{dx} + \overline{q} = 0 \tag{51}$$

$$\frac{dM}{dx} - \frac{d^2 M^h}{dx^2} - Q = 0 \tag{52}$$

with $\overline{q} = \overline{q}_{h/2} + \overline{q}_{-h/2}$. Substituting Equation (52) into (51) yields:

$$\frac{d^2 M}{dx^2} - \frac{d^3 M^h}{dx^3} + \overline{q} = 0 \tag{53}$$

The stress resultants at the boundary are:

$$N - \frac{dN^h}{dx} = \overline{N} = \int_{-h/2}^{h/2} \bar{t}_1 dz + \overline{f}_1|_{z=h/2} + \overline{f}_1|_{z=-h/2} \tag{54}$$

$$\frac{dM}{dx} - \frac{d^2 M^h}{dx^2} = Q = \overline{Q} = \int_{-h/2}^{h/2} \bar{t}_3 dz + \overline{f}_3|_{z=h/2} + \overline{f}_3|_{z=-h/2} \tag{55}$$

$$M - \frac{dM^h}{dx} = \overline{M} = \int_{-h/2}^{h/2} (z\bar{t}_1 + \overline{q}_2) dz + \frac{h}{2}\overline{f}_1|_{x=h/2} - \frac{h}{2}\overline{f}_1|_{x=-h/2} \tag{56}$$

$$N^h = \overline{N}^h = \int_{-h/2}^{h/2} \bar{r} dz \tag{57}$$

$$M^h = \overline{M}^h = \int_{-h/2}^{h/2} z\bar{r} dz \tag{58}$$

where $\overline{N}$, $\overline{Q}$, $\overline{M}$, $\overline{N}^h$ and $\overline{M}^h$ represent the prescribed axial force, shear force, moment, higher-order axial force, higher-order moment per unit width in the beam, respectively.

4. Semi-Inverse Solution for Pure Bending Beam

Consider a pure bending beam subjected to a moment M_0 acting on its two ends. The governing equations and boundary conditions are listed as Equations (38)–(48) with normal tractions $\overline{q}_{\pm h/2}$ being zero. The solution for the displacement field is suggested in the following form [29]:

$$\begin{aligned}
u_1 &= C_1 xz - C_2 z + u_0 \\
u_3 &= -\tfrac{1}{2} C_1 x^2 + C_2 x + w(z) + v_0
\end{aligned} \tag{59}$$

in which w is an unknown function with respect to coordinate z. C_1, C_2, u_0 and v_0 are four undetermined constants. According to the assumption of displacement, the non-zero strain components are:

$$\varepsilon_{11} = C_1 z,\ \varepsilon_{33} = w_{,3} \tag{60}$$

The non-vanishing components of strain gradient are calculated as:

$$\begin{array}{l} \gamma_3 = C_1 + w_{,33}\ \chi^s_{21} = \kappa_3 = \frac{1}{2}C_1 \\ \eta^{(1)}_{311} = \frac{4}{15}C_1 - \frac{1}{5}w_{,33}\ \eta^{(1)}_{333} = \frac{2}{5}w_{,33} - \frac{1}{5}C_1 \end{array} \tag{61}$$

According to the constitutive relations for plane-strain problems, the non-zero Cauchy stress is given by:

$$\begin{array}{l} \sigma_{11} = \frac{E}{(1+v)(1-2v)}[(1-v)C_1 z + v w_{,3}] \\ \sigma_{33} = \frac{E}{(1+v)(1-2v)}[(1-v)w_{,3} + vC_1 z] \end{array} \tag{62}$$

in which E is the Young's modulus and ν is the Poisson's ratio. The work-conjugated higher-order stress components can be obtained from Equation (28), given as:

$$\begin{array}{l} p_3 = (2\mu l_0^2 - \frac{1}{2}\mu l_4^2)C_1 + 2\mu l_0^2 w_{,33}\ m^s_{21} = \mu l_2^2 C_1\ \mu_3 = (2\mu l_3^2 - \mu l_4^2)C_1 - \mu l_4^2 w_{,33} \\ \tau^{(1)}_{311} = 2\mu l_1^2(\frac{4}{15}C_1 - \frac{1}{5}w_{,33})\ \tau^{(1)}_{333} = \frac{2}{5}\mu l_1^2(2w_{,33} - C_1) \end{array} \tag{63}$$

According to the present bending theory of plane-strain beams, the governing equations and boundary conditions of the pure bending beam subjected to a moment M_0 acting on its two ends can be specified by substituting the stress components from Equation (62) and higher-order stress components from Equation (63) into Equations (38)–(48) along the length direction of Equation (38) and the boundary conditions of Equations (40), (42), (45) and (47) can be satisfied automatically. The current pure bending solution depends on the governing equations, which are Equation (39) and boundary conditions Equations (41), (43), (44), (46) and (48).

Substituting the stress components from Equation (62) and higher-order stress components from Equation (63) into Equation (69) yields the governing equation of the current pure bending beam, that is:

$$\frac{\mathrm{d}^4 w}{\mathrm{d}z^4} - \frac{E(1-v)}{d_1(1+v)(1-2v)}\frac{\mathrm{d}^2 w}{\mathrm{d}z^2} - \frac{Ev}{d_1(1+v)(1-2v)}C_1 = 0 \tag{64}$$

with the coefficient d_1 defined as $d_1 = 2\mu l_0^2 + \frac{4}{5}\mu l_1^2$. The solution of Equation (64) is given by:

$$w(z) = C_3\cosh(\frac{z}{\lambda}) - \frac{v}{2(1-v)}C_1 z^2 \tag{65}$$

where C_3 is an undetermined coefficient and the parameter λ is defined as:

$$\lambda = \sqrt{\frac{1-2v}{1-v}(l_0^2 + \frac{2}{5}l_1^2)} \tag{66}$$

It should be noted here that the constant term is not included in Equation (65) because it has been included in v_0 in the displacement solution of Equation (59).

Moreover, the assumption of displacement in Equation (65) satisfies the boundary condition in Equation (41) automatically. The coefficients C_1 and C_3 in Equation (65) can be determined from the boundary conditions Equations (43), (44), (46) and (48). Based on the boundary condition Equation (43), it can be obtained that

$$C_3 = (\frac{v}{1-v} - \frac{d_2}{d_1})\frac{\lambda^2}{\cosh(\frac{h}{2\lambda})}C_1 \tag{67}$$

with the coefficient d_2 representing $d_2 = 2\mu l_0^2 - \frac{2}{5}\mu l_1^2 - \frac{1}{2}\mu l_4^2$. According to the stress resultants at boundary Equation (56), actually, the applied moment M_0 at the two ends of beam equals

$$M_0 = \int_{-h/2}^{h/2} (z\bar{t}_1 + \bar{q}_2)dz + \frac{h}{2}\bar{f}_1|_{x=h/2} - \frac{h}{2}\bar{f}_1|_{x=-h/2} \tag{68}$$

Then, combining Equations (44), (46), (48) and (68), the coefficient C_1 can be solved as:

$$C_1 = \frac{M_0}{\frac{Eh^3}{12(1-v^2)} + \left(d_3 - \frac{v}{1-v}d_2\right)h + d_4\lambda} \tag{69}$$

with the coefficients d_3 and d_4 denoting

$$\begin{aligned} d_3 &= 2\mu l_0^2 + \tfrac{8}{15}\mu l_1^2 + \mu l_2^2 + \mu l_3^2 - \mu l_4^2 \\ d_4 &= \tfrac{Ehv\lambda}{(1+v)(1-2v)}(\tfrac{v}{1-v} - \tfrac{d_2}{d_1}) + 2(d_2 - \tfrac{Ev\lambda^2}{(1+v)(1-2v)})(\tfrac{v}{1-v} - \tfrac{d_2}{d_1})\tanh(\tfrac{h}{2\lambda}) \end{aligned} \tag{70}$$

Furthermore, the coefficients C_2, u_0 and v_0 can be obtained according to the displacement boundary conditions. For a simply supported beam, the displacement boundary conditions are:

$$u_1|_{\substack{x=0\\z=0}} = u_3|_{\substack{x=0\\z=0}} = 0,\ u_3|_{\substack{x=L\\z=0}} = 0 \tag{71}$$

Substituting Equations (59) and (65) into (71) yields

$$u_0 = 0,\ v_0 = -(\frac{v}{1-v} - \frac{d_2}{d_1})\frac{\lambda^2}{\cosh(\frac{h}{2\lambda})}C_1,\ C_2 = \frac{1}{2}C_1 L \tag{72}$$

Thus, the displacement solution is finally given by:

$$\begin{aligned} u_1 &= C_1(x - \tfrac{L}{2})z \\ u_3 &= C_1[-\tfrac{1}{2}x^2 + \tfrac{L}{2}x + (\tfrac{v}{1-v} - \tfrac{d_2}{d_1})\tfrac{\lambda^2}{\cosh(\frac{h}{2\lambda})}(\cosh(\tfrac{z}{l}) - 1) - \tfrac{v}{2(1-v)}z^2] \end{aligned} \tag{73}$$

in which the coefficient C_1 is given as Equation (69). Especially, for the axis of the beam (z = 0), its displacement solution is:

$$u_3|_{z=0} = C_1(-\frac{1}{2}x^2 + \frac{L}{2}x) \tag{74}$$

which is similar to that of traditional theory except for the bending rigidity. From Equation (69), it can be seen that the bending rigidity of the pure bending beam based on the strain gradient theory includes the classical bending rigidity $\frac{Eh^3}{12(1-v^2)}$ and the higher-order bending rigidity $\left(d_3 - \frac{v}{1-v}d_2\right)h + d_4\lambda$. By using the classical bending rigidity to normalize the total bending rigidity of the strain gradient theory (the denominator in Equation (69)), the dimensionless bending rigidity K can be obtained as:

$$K = 1 + 6(1-v)(\frac{l}{h})^2[1 - \frac{v}{1-v}\frac{d_2}{d_3} + (\frac{v}{1-v} - \frac{d_2}{d_1})[\frac{2v\lambda^2}{(1-2v)l^2} + \frac{2\lambda}{h}(\frac{d_2}{d_3} - \frac{2v\lambda^2}{(1-2v)l^2})\tanh(\frac{h}{2\lambda})]] \tag{75}$$

with the equivalent material length scale parameter l denoted as:

$$l = \sqrt{2l_0^2 + \frac{8}{15}l_1^2 + l_2^2 + l_3^2 - l_4^2} \tag{76}$$

When the Poisson's effect is ignored by $\nu = 0$, the dimensionless bending rigidity K reduces to

$$\widetilde{K} = 1 + 6\left(\frac{l}{h}\right)^2 \left[1 - \frac{2\widetilde{\lambda}}{h}\frac{d_2^2}{d_1 d_3}\tanh\left(\frac{h}{2\widetilde{\lambda}}\right)\right] \tag{77}$$

in which the parameter $\widetilde{\lambda}$ is reduced from Equation (66) by letting $v = 0$.

$$\widetilde{\lambda} = \lambda_{v=0} = \sqrt{l_0^2 + \frac{2}{5}l_1^2} \tag{78}$$

Similarly, for a couple stress plane-strain beam subjected to a moment M_0 acting on its two ends, the displacement solution based on the couple stress theory can be obtained as:

$$\begin{aligned} u_1^c &= C_1^c\left(x - \tfrac{L}{2}\right)z \\ u_3^c &= C_1^c\left(-\tfrac{1}{2}x^2 + \tfrac{L}{2}x - \tfrac{v}{2(1-v)}z^2\right) \end{aligned} \tag{79}$$

where the coefficient is:

$$C_1^c = \frac{M_0}{\frac{Eh^3}{12(1-v^2)} + \mu(l_2^2 + l_3^2)h} \tag{80}$$

Then, the dimensionless bending rigidity for the couple stress theory is given as:

$$K^c = 1 + 6(1-v)\left(\frac{l^c}{h}\right)^2 \tag{81}$$

with the equivalent couple stress length scale parameter l^c denoted as $l^c = \sqrt{l_2^2 + l_3^2}$. When the Poisson's effect is ignored, the dimensionless bending rigidity K^c reduces to

$$\widetilde{K}^c = 1 + 6\left(\frac{l^c}{h}\right)^2 \tag{82}$$

In order to illustrate the solution of the present plane-strain beam, a polyvinylidene difluoride (PVDF) beam with a unit thickness is considered here, in which the Young's modulus E is equal to 3.7 GPa, the material length scale parameters are assumed to be the same, the length of the beam is 20 times its thickness ($L = 20\,h$), and the applied moment M_0 equals 10 μN·μm.

Based on Equations (75) and (81), the dimensionless bending rigidity is shown in Figure 1. It can be seen from Figure 1 that the dimensionless bending rigidity shows an obvious size effect. The dimensionless bending rigidity of beams decreases with an increase in thickness, and the bending rigidities based on the strain gradient theory, couple stress theory and classical theory tend to be consistent as the thickness increases. The effect of the strain gradient is a kind of stiffening effect. The bending rigidity based on the couple stress theory is larger than that of classical theory due to the consideration of a rotation gradient. Additionally, the bending rigidity based on the strain gradient theory is larger than that of the couple stress theory, since the dilatation gradient and deviatoric stretch gradient are also considered in addition to the rotation gradient. In addition, the dimensionless bending rigidity of a plane-strain beam based on higher-order theories increases with the decrease of the Poisson's ratio.

Figure 2 shows the displacement u_3 of the axis (Equation (74)) along the length of the beam. It can be found that the material length scale parameter l_0, which characterizes the dilatation gradient, exhibits a dominant stiffening effect, while the material length scale parameters l_1, l_2 and l_3 characterize the deviatoric stretch gradient, symmetric rotation gradient and curvature, respectively, exhibiting a secondary and decreasing stiffening effect. In particular, the material length scale parameter l_4 exhibits a softening effect. It should be noted here that the overall effect of the strain gradient is a stiffening effect, and the influence of l_4 is weak.

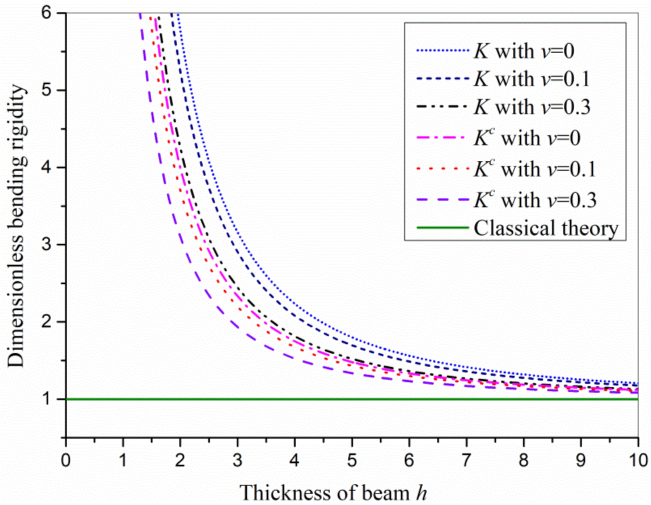

Figure 1. Size effect of plane-strain beams.

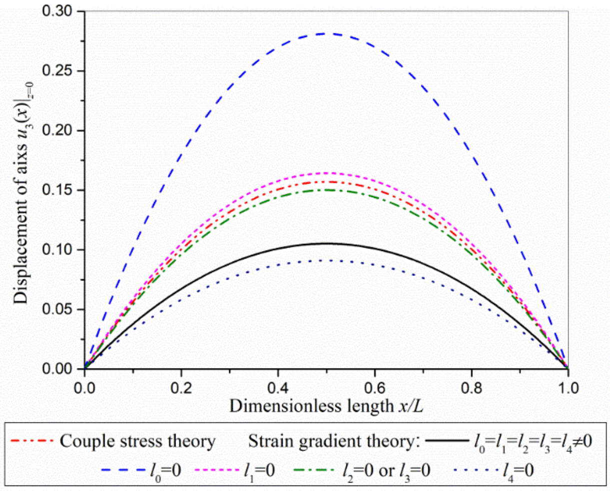

Figure 2. The displacement u_3 of the axis along the length direction of the beam.

Moreover, in order to reveal the deformation of a plane-strain beam along the thickness direction, the strain ε_{33} can be obtained by combining Equations (2) and (73) from the strain gradient theory, which is given by:

$$\varepsilon_{33} = C_1[(\frac{v}{1-v} - \frac{d_2}{d_1})\frac{\lambda^2}{\cosh(\frac{h}{2\lambda})}\frac{1}{l}\sinh(\frac{z}{l}) - \frac{v}{1-v}z] \tag{83}$$

While for couple stress theory, the strain ε_{33} is obtained by:

$$\varepsilon_{33}^c = -C_1^c\frac{v}{1-v}z \tag{84}$$

By defining the normalized strain ε_{33}/C_1 for the strain gradient theory and ε_{33}^c/C_1^c for the couple stress theory, the normalized strain of a plane-strain beam along its thickness direction is shown in Figure 3. Figure 3 reveals that the gradient of a strain ε_{33} along the thickness direction decreases as the Poisson's ratio decreases. When the Poisson's effect is neglected, the strain ε_{33} is equal to zero for the couple stress theory and non-zero for the strain gradient theory. Equation (83) demonstrates that the strain ε_{33} of a plane-strain beam based on the strain gradient theory includes the linear term and the non-linear term. The non-linear term is related to the parameter λ, which characterizes the dilatation gradient and the deviatoric stretch gradient along the thickness direction. When the dilatation gradient and the deviatoric stretch gradient along the thickness direction are neglected by letting λ = 0, the non-linear term will disappear.

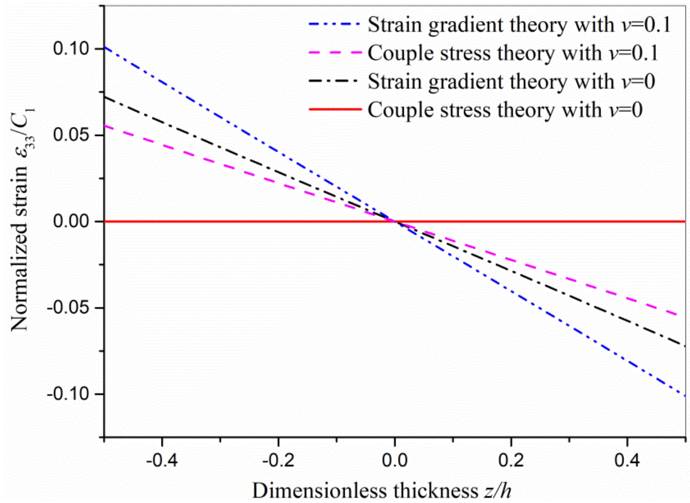

Figure 3. Normalized strain of a plane-strain beam along the thickness direction.

5. Strain Gradient Bernoulli–Euler Beam

Consider a Bernoulli–Euler beam with a unit thickness, the displacement components are set as:

$$u_1 = -z\frac{\partial \overline{w}}{\partial x} \quad u_2 = 0 \quad u_3 = \overline{w}(x) \tag{85}$$

According to the definitions of strain and strain gradient in Equation (2), the non-zero components are:

$$\varepsilon_{11} = -z\frac{\partial^2 \overline{w}}{\partial x^2},\ \eta_{111} = -z\frac{\partial^3 \overline{w}}{\partial x^3},\ \eta_{311} = -\frac{\partial^2 \overline{w}}{\partial x^2} \tag{86}$$

Hence, the non-vanishing strain gradient components are:

$$\begin{aligned}
&\gamma_1 = -z\tfrac{\partial^3 \overline{w}}{\partial x^3}\ \gamma_3 = -\tfrac{\partial^2 \overline{w}}{\partial x^2}\ \chi^s_{21} = \chi^s_{12} = -\tfrac{1}{2}\tfrac{\partial^2 \overline{w}}{\partial x^2}\ \kappa_3 = -\tfrac{1}{2}\tfrac{\partial^2 \overline{w}}{\partial x^2}\\
&\eta^{(1)}_{111} = -\tfrac{2}{5}z\tfrac{\partial^3 \overline{w}}{\partial x^3}\ \eta^{(1)}_{333} = \tfrac{1}{5}\tfrac{\partial^2 \overline{w}}{\partial x^2}\ \eta^{(1)}_{113} = \eta^{(1)}_{131} = \eta^{(1)}_{311} = -\tfrac{4}{15}\tfrac{\partial^2 \overline{w}}{\partial x^2}\\
&\eta^{(1)}_{122} = \eta^{(1)}_{212} = \eta^{(1)}_{221} = \eta^{(1)}_{313} = \eta^{(1)}_{331} = \eta^{(1)}_{133} = \tfrac{1}{5}z\tfrac{\partial^3 \overline{w}}{\partial x^3}\ \eta^{(1)}_{223} = \eta^{(1)}_{232} = \eta^{(1)}_{322} = \tfrac{1}{15}\tfrac{\partial^2 \overline{w}}{\partial x^2}
\end{aligned} \tag{87}$$

Substituting these non-zero components from Equation (87) into the constitutive equations, Equations (10) and (28), the corresponding Cauchy stress and higher-order stress components are:

$$\begin{aligned}
&\sigma_{11} = -Ez\tfrac{\partial^2 \overline{w}}{\partial x^2}\ p_1 = -2\mu l_0^2 z\tfrac{\partial^3 \overline{w}}{\partial x^3}\ p_3 = -2\mu l_0^2\tfrac{\partial^2 \overline{w}}{\partial x^2} + \tfrac{1}{2}\mu l_4^2\tfrac{\partial^2 \overline{w}}{\partial x^2}\\
&m^s_{21} = -\mu l_2^2\tfrac{\partial^2 \overline{w}}{\partial x^2}\ \mu_1 = \mu l_4^2 z\tfrac{\partial^3 \overline{w}}{\partial x^3}\ \mu_3 = -2\mu l_3^2\tfrac{\partial^2 \overline{w}}{\partial x^2} + \mu l_4^2\tfrac{\partial^2 \overline{w}}{\partial x^2}\\
&\tau^{(1)}_{111} = -\tfrac{4}{5}\mu l_1^2 z\tfrac{\partial^3 \overline{w}}{\partial x^3}\ \tau^{(1)}_{333} = \tfrac{2}{5}\mu l_1^2\tfrac{\partial^2 \overline{w}}{\partial x^2}\ \tau^{(1)}_{113} = \tau^{(1)}_{131} = \tau^{(1)}_{311} = -\tfrac{8}{15}\mu l_1^2\tfrac{\partial^2 \overline{w}}{\partial x^2}\\
&\tau^{(1)}_{122} = \tau^{(1)}_{212} = \tau^{(1)}_{221} = \tau^{(1)}_{313} = \tau^{(1)}_{331} = \tau^{(1)}_{133} = \tfrac{2}{5}\mu l_1^2 z\tfrac{\partial^3 \overline{w}}{\partial x^3}\ \tau^{(1)}_{223} = \tau^{(1)}_{232} = \tau^{(1)}_{322} = \tfrac{2}{15}\mu l_1^2\tfrac{\partial^2 \overline{w}}{\partial x^2}
\end{aligned} \tag{88}$$

From Equation (49), the defined bending moment and higher-order moment are given as

$$M = -(\frac{Eh^3}{12} + d_3 h)\frac{\partial^2 \overline{w}}{\partial x^2}\ M^h = -d_1 \frac{h^3}{12}\frac{\partial^3 \overline{w}}{\partial x^3} \tag{89}$$

where the coefficients d_1 and d_3 have been defined in Section 4. The bending governing equation of the beam is given as Equation (53) and the boundary conditions of stress resultants are listed as Equations (55), (56) and (58).

(1) Simply supported beam

For a simply supported beam subjected to a moment M_0 acting on the two ends of beam, the governing equation is:

$$\frac{\mathrm{d}^2 M}{\mathrm{d}x^2} - \frac{\mathrm{d}^3 M^h}{\mathrm{d}x^3} = 0 \tag{90}$$

and the boundary conditions on the two ends of beam are:

$$M - \frac{dM^h}{dx} = M_0,\ M^h = 0,\ \ w = 0 \text{ at } x = 0,\ L \tag{91}$$

Combining Equations (89)–(91), the deflection of pure bending beam is solved as:

$$\overline{w} = C_B(-\frac{1}{2}x^2 + \frac{L}{2}x) \tag{92}$$

where the coefficient is given by:

$$C_B = \frac{M_0}{\frac{Eh^3}{12} + d_3 h} \tag{93}$$

By using the classical bending rigidity $Eh^3/12$ to normalize the bending rigidity based on the strain gradient theory (the denominator in Equation (93)), the dimensionless bending rigidity K_B can be obtained as:

$$K_B = 1 + 6(\frac{l}{h})^2 \tag{94}$$

where the equivalent material length scale parameter l is defined as Equation (76). In addition, when the dilatation gradient γ_i and deviatoric stretch gradient $\eta_{ijk}^{(1)}$ are excluded, the strain gradient pure bending beam model will reduce to that of the couple stress theory. Additionally, the dimensionless bending rigidity will be the same as Equation (82).

The displacement distribution of the pure bending beam along its axis is shown in Figure 4. Figure 4 illustrates once again that the bending rigidity predicted by the strain gradient theory is greater than that predicted by the couple stress theory, and the bending rigidity decreases with the increase of the Poisson's ratio. Moreover, for the couple stress theory, the displacement of the Bernoulli–Euler beam is consistent with that of the plane-strain beam when the Poisson's effect is ignored. While for the strain gradient theory, the bending rigidity of the plane-strain beam without the Poisson's effect is smaller than that of the Bernoulli–Euler beam due to the influence of the dilatation gradient and the deviatoric stretch gradient along the thickness direction, which can also be explained by Equations (77) and (94).

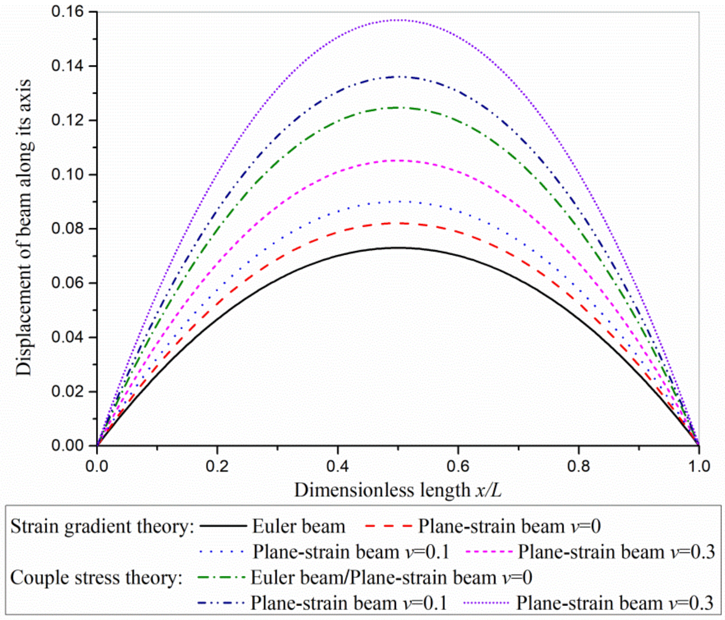

Figure 4. The displacement of beam along its axis.

(2) Cantilever beam

For a cantilever beam subjected to a concentrated force F_0 acting on its free end, the governing equation is the same as Equation (90) and the boundary conditions on the two ends of beam are given by:

$$\overline{w} = \overline{w}_{,1} = 0,\ M^h = 0 \text{ at } x = 0 \tag{95}$$

$$\frac{dM}{dx} - \frac{d^2M^h}{dx^2} = F_0,\ M - \frac{dM^h}{dx} = 0,\ M^h = 0 \text{ at } x = L \tag{96}$$

Combining Equations (90), (95) and (96), the deflection is solved as:

$$\overline{w} = B_1 + B_2x + B_3x^2 + B_4x^3 + B_5e^{\frac{\sqrt{K_B}}{\widetilde{\lambda}}x} + B_6e^{-\frac{\sqrt{K_B}}{\widetilde{\lambda}}x} \tag{97}$$

where $\widetilde{\lambda}$ and K_B are defined as Equations (78) and (94), respectively, and the coefficients B_i(i = 1,2,3,4,5) are:

$$\begin{gathered} B_1 = \frac{12F_0\widetilde{\lambda}^3(e^{\frac{\sqrt{K_B}}{\widetilde{\lambda}}L}+e^{-\frac{\sqrt{K_B}}{\widetilde{\lambda}}L}-2)}{Eh^3K_B^{5/2}(e^{\frac{\sqrt{K_B}}{\widetilde{\lambda}}L}-e^{-\frac{\sqrt{K_B}}{\widetilde{\lambda}}L})}\ B_2 = -\frac{12F_0\widetilde{\lambda}^2}{Eh^3K_B^2}\ B_3 = \frac{6F_0L}{Eh^3K_B}\ B_4 = -\frac{2F_0}{Eh^3K_B} \\ B_5 = -\frac{12F_0\widetilde{\lambda}^3(e^{-\frac{\sqrt{K_B}}{\widetilde{\lambda}}L}-1)}{Eh^3K_B^{5/2}(e^{\frac{\sqrt{K_B}}{\widetilde{\lambda}}L}-e^{-\frac{\sqrt{K_B}}{\widetilde{\lambda}}L})}\ B_6 = -\frac{12F_0\widetilde{\lambda}^3}{Eh^3K_B^{5/2}(1+e^{-\frac{\sqrt{K_B}}{\widetilde{\lambda}}L})} \end{gathered} \tag{98}$$

In addition, many articles only consider the gradient of the axial strain along the thickness direction since the strain gradient along the length direction can be neglected compared with that along the thickness direction for the Euler beam. For a cantilever beam subjected to a concentrated force at its free end, when the strain gradient along the length direction is neglected, the deflection solution of Equation (97) will reduce to

$$\overline{w} = B_3x^2 + B_4x^3 \tag{99}$$

From Equations (97) and (99), the deflection of the cantilever beam is shown in Figure 5. It can be seen that the influence of the strain gradient along the length direction η_{111} on the bending rigidity is negligible. The main stiffening effect comes from the strain gradient along the thickness direction. In addition, compared with the couple stress model, the contribution of the dilatation gradient and deviatoric stretch gradient is non-negligible.

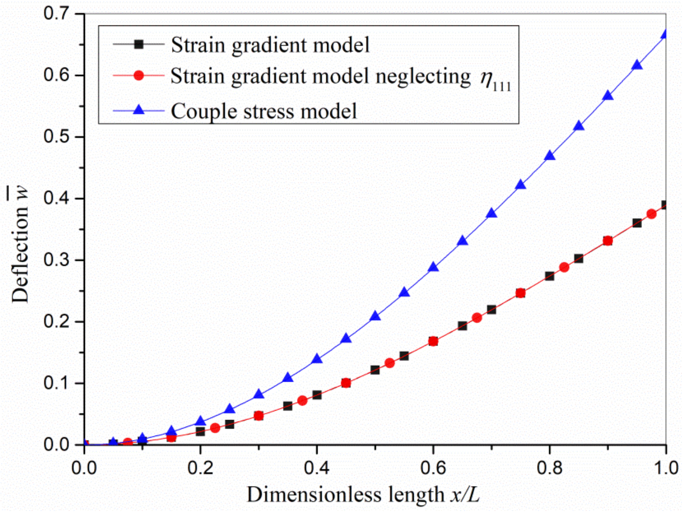

Figure 5. The deflection of cantilever beam.

6. Conclusions

In this paper, a new set of higher-order deformation metrics including dilatation gradient, deviatoric stretch gradient, symmetric rotation gradient and curvature is introduced to re-formulate the strain gradient theory for the sake of investigating the effect of each strain gradient components conveniently. All the constitutive equations, equilibrium equations and boundary conditions in the form of components are obtained. The present strain gradient theory with five higher-order constants is another form of Mindlin's strain gradient theory, which is a general theory. The present theory can be directly simplified to the couple stress theory by eliminating the dilatation gradient and deviatoric stretch gradient.

Based on the present strain gradient theory, the bending theory of plane-strain beam is proposed, in which the stress resultants are re-defined due to the presence of higher-order stress and the corresponding governing equations and boundary conditions of stress resultants are developed. The semi-inverse solution of a pure bending beam subjected to moments at its two ends is obtained. The results demonstrate that the material length scale parameter l_0, which characterizes the dilatation gradient, exhibits a dominant stiffening effect, while the material length scale parameters l_1, l_2 and l_3 characterizing the deviatoric stretch gradient, symmetric rotation gradient and curvature, respectively, exhibit a secondary and decreasing stiffening effect. The dimensionless bending rigidity increases with the decrease in Poisson's ratio.

The Bernoulli–Euler beam model is presented based on the present strain gradient theory and couple stress theory. For the couple stress theory, the displacement of the Bernoulli–Euler beam is consistent with that of a plane-strain beam without the Poisson's effect. While for the strain gradient theory, the bending rigidity of a plane-strain beam without considering the Poisson's effect is smaller than that of a Bernoulli–Euler beam, which is due to the influence of the dilatation gradient and the deviatoric stretch gradient along the thickness direction. In addition, it can be concluded that the influence of the strain gradient along the length direction on bending rigidity is negligible.

Author Contributions: A.L.: Methodology and Conceptualization. Q.W.: Writing—Original Draft. M.S.: Writing—Review and Editing. J.C.: Formal Analysis. W.S.: Editing. S.Z.: Data Curation. L.W.: Validation. All authors have read and agreed to the published version of the manuscript.

Funding: The work reported here is funded by the Pilot Program for the Integration of Science, Education and Industry of Qilu University of Technology (Shandong Academy of Sciences) (2022PX032), the

National Natural Science Foundation of China (NSFC) (52105554) and the Nature Science Foundation of Shandong Province, China (ZR2020QE187).

Institutional Review Board Statement: Not applicable.

Informed Consent Statement: Not applicable.

Data Availability Statement: Not applicable.

Conflicts of Interest: The authors declare no conflict of interest.

Appendix A

According to the definition of stain and strain gradient, the variation of internal energy is written as:

$$\int_V (\sigma_{ij}\delta\varepsilon_{ij} + \tau_{ijk}\delta\eta_{ijk})\mathrm{d}V = \int_V [-(\sigma_{ki,i} - \tau_{ijk,ij})\delta u_k + (\sigma_{ki}\delta u_k - \tau_{jik,j}\delta u_k)_{,i} + (\tau_{jik}\delta u_{k,i})_{,j}]\mathrm{d}V \tag{A1}$$

Applying the divergence theorem yields:

$$\int_V (\sigma_{ij}\delta\varepsilon_{ij} + \tau_{ijk}\delta\eta_{ijk})\mathrm{d}V = -\int_V (\sigma_{ki,i} - \tau_{ijk,ij})\delta u_k \mathrm{d}V + \int_S n_i(\sigma_{ki} - \tau_{jik,j})\delta u_k \mathrm{d}S + \int_S \tau_{jik} n_j \delta u_{k,i} \mathrm{d}S \tag{A2}$$

It should be noted that the variation $\delta u_{k,I}$ in Equation (A2) is not independent of δu_k on the surface boundary S, and only its normal component is independent [36]. Thus, the variation $\delta u_{k,i}$ on the surface S is separated into normal component and tangential component.

$$\delta u_{k,i} = D_i \delta u_k + n_i D \delta u_k \tag{A3}$$

where the normal gradient operator D and the surface gradient operator D_i are given as:

$$D = n_i \partial_i \; D_i = (\delta_{ik} - n_i n_k)\partial_k \tag{A4}$$

Substituting Equation (A3) into Equation (A2), the last integral can be rewritten as:

$$\int_S \tau_{jik} n_j \delta u_{k,i} \mathrm{d}S = \int_S n_j \tau_{jik} D_i \delta u_k \mathrm{d}S + \int_S n_i n_j \tau_{jik} D \delta u_k \mathrm{d}S \tag{A5}$$

Note that the integrand of the first integral in Equation (A5) can be further derived as [37]:

$$\begin{aligned} n_j \tau_{jik} D_i \delta u_k &= D_i(n_j \tau_{jik} \delta u_k) - D_i(n_j \tau_{jik})\delta u_k \\ &= (D_p n_p) n_i n_j \tau_{jik} \delta u_k + n_q e_{qpm} e_{mli} (n_l n_j \tau_{jik} \delta u_k)_{,p} - D_i(n_j \tau_{jik})\delta u_k \end{aligned} \tag{A6}$$

with e_{qpm} denoting the alternating tensor. According to the Stokes' theorem, we have

$$\int_S n_q e_{qpm} e_{mli} (n_l n_j \tau_{jik} \delta u_k)_{,p} \mathrm{d}S = \oint_C [[k_i n_j \tau_{jik} \delta u_k]] \mathrm{d}C \tag{A7}$$

in which $k_i = e_{ijk} s_j n_k$ is the outer co-normal vector with the unit vector s_j tangent to the edge C and the square brackets represent the difference between the values of the enclosed quantity on the two sides of the edge.

Finally, Substituting Equation (A5) into Equation (A2) and combining Equations (A6) and (A7), the variation of internal energy is given by:

$$\begin{aligned} \textstyle\int_V (\sigma_{ij}\delta\varepsilon_{ij} + \tau_{ijk}\delta\eta_{ijk})\mathrm{d}V &= -\textstyle\int_V (\sigma_{ki,i} - \tau_{ijk,ij})\delta u_k \mathrm{d}V \\ &\quad + \textstyle\int_S [n_i(\sigma_{ki} - \tau_{jik,j}) + (D_p n_p) n_i n_j \tau_{jik} - D_i(n_j \tau_{jik})]\delta u_k \mathrm{d}S \\ &\quad + \textstyle\int_S n_i n_j \tau_{jik} D \delta u_k \mathrm{d}S + \oint_C [[k_i n_j \tau_{jik} \delta u_k]] \mathrm{d}C \end{aligned} \tag{A8}$$

Appendix B

For the couple stress theory, the equilibrium equation is:

$$\sigma_{ik,i} - \frac{1}{2}e_{lik}\left(m^s_{lj} + m^a_{lj}\right)_{,ij} + \overline{b}_k = 0 \tag{A9}$$

The boundary conditions on S are:

$$\begin{gathered} n_j[\sigma_{jk} - \tfrac{1}{2}e_{lik}(m^s_{lj} + m^a_{lj})_{,i} - \tfrac{1}{2}e_{lij}(m^s_{lk} + m^a_{lk})_{,i} + \tfrac{1}{2}(D_p n_p)n_i n_j e_{lik}(m^s_{lj} + m^a_{lj} \\ -\tfrac{1}{2}D_j[n_i e_{lik}(m^s_{lj} + m^a_{lj} + n_i e_{lij}(m^s_{lk} + m^a_{lk} + e_{lij}n_p n_i n_k(m^s_{lp} + m^a_{lp})] = \overline{t}_k \\ \text{or } u_k = \overline{u}_k \end{gathered} \tag{A10}$$

$$n_j(m^s_{kj} + m^a_{kj}) - n_j n_k n_i(m^s_{ij} + m^a_{ij}) = \overline{q}_k \text{ or } (\delta_{kl} - n_k n_l)\delta\theta_l = \overline{\theta}_k \tag{A11}$$

and along the sharp edge C is:

$$\frac{1}{2}[[k_j e_{lik} n_i(m^s_{lj} + m^a_{lj}) + k_j e_{lij} n_i(m^s_{lk} + m^a_{lk}) + k_j e_{lij} n_p n_i n_k(m^s_{lp} + m^a_{lp})]] = \overline{f}_k \text{ or } u_k = \overline{u}_k \tag{A12}$$

References

1. Roudbari, M.A.; Jorshari, T.D.; Lü, C.; Ansari, R.; Kouzani, A.Z.; Amabili, M. A review of size-dependent continuum mechanics models for micro- and nano-structures. *Thin-Walled Struct.* **2022**, *170*, 108562. [CrossRef]
2. Kong, S. A review on the size-dependent models of micro-beam and micro-plate based on the modified couple stress theory. *Arch. Comput. Methods Eng.* **2021**, *29*, 1–31. [CrossRef]
3. Thai, H.; Vo, T.P.; Nguyen, T.; Kim, S. A review of continuum mechanics models for size-dependent analysis of beams and plates. *Compos. Struct.* **2017**, *177*, 196–219. [CrossRef]
4. Fu, G.; Zhou, S.; Qi, L. On the strain gradient elasticity theory for isotropic materials. *Int. J. Eng. Sci.* **2020**, *154*, 103348. [CrossRef]
5. Rouhi, H.; Ebrahimi, F.; Ansari, R.; Torabi, J. Nonlinear free and forced vibration analysis of Timoshenko nanobeams based on Mindlin's second strain gradient theory. *Eur. J. Mech. A-Solid* **2019**, *73*, 268–281. [CrossRef]
6. Wang, B.; Zhao, J.; Zhou, S. A micro scale Timoshenko beam model based on strain gradient elasticity theory. *Eur. J. Mech. A-Solid* **2010**, *29*, 591–599. [CrossRef]
7. Lam, D.C.C.; Yang, F.; Chong, A.C.M.; Wang, J.; Tong, P. Experiments and theory in strain gradient elasticity. *J. Mech. Phys. Solids* **2003**, *51*, 1477–1508. [CrossRef]
8. Liu, D.; He, Y.; Tang, X.; Ding, H.; Hu, P.; Cao, P. Size effects in the torsion of microscale copper wires: Experiment and analysis. *Scripta Mater.* **2012**, *66*, 406–409. [CrossRef]
9. McFarland, A.W.; Colton, J.S. Role of material microstructure in plate stiffness with relevance to microcantilever sensors. *J. Micromech. Microeng.* **2005**, *15*, 1060–1067. [CrossRef]
10. Tang, C.; Alici, G. Evaluation of length-scale effects for mechanical behaviour of micro- and nanocantilevers: I. experimental determination of length-scale factors. *J. Phys. D Appl. Phys.* **2011**, *44*, 335501. [CrossRef]
11. Toupin, R.A. Theories of elasticity with couple-stress. *Arch. Ration. Mech. Anal.* **1964**, *17*, 85–112. [CrossRef]
12. Li, A.Q.; Wang, B.L.; Yang, S.Y. On some basic aspects of flexoelectricity in the mechanics of materials. *Int. J. Eng. Sci.* **2021**, *166*, 103499. [CrossRef]
13. Mindlin, R.D.; Eshel, N.N. On first strain-gradient theories in linear elasticity. *Int. J. Solids Struct.* **1968**, *4*, 109–124. [CrossRef]
14. Zhou, S.; Li, A.; Wang, B. A reformulation of constitutive relations in the strain gradient elasticity theory for isotropic materials. *Int. J. Solids Struct.* **2016**, *80*, 28–37. [CrossRef]
15. Aifantis, E.C. On the role of gradients in the localization of deformation and fracture. *Int. J. Eng. Sci.* **1992**, *30*, 1297–1299. [CrossRef]
16. Yang, F.; Chong, A.C.M.; Lam, D.C.C.; Tong, P. Couple stress based strain gradient theory for elasticity. *Int. J. Solids Struct.* **2002**, *39*, 2731–2743. [CrossRef]
17. Hadjesfandiari, A.R.; Dargush, G.F. Couple stress theory for solids. *Int. J. Solids Struct.* **2011**, *48*, 2496–2510. [CrossRef]
18. Tang, Y.; Qing, H. Elastic buckling and free vibration analysis of functionally graded Timoshenko beam with nonlocal strain gradient integral model. *Appl. Math. Model.* **2021**, *96*, 657–677. [CrossRef]
19. Zhang, B.; Li, H.; Kong, L.; Shen, H.; Zhang, X. Coupling effects of surface energy, strain gradient, and inertia gradient on the vibration behavior of small-scale beams. *Int. J. Mech. Sci.* **2020**, *184*, 105834. [CrossRef]
20. Barretta, R.; Faghidian, S.A.; de Sciarra, F.M.; Penna, R.; Pinnola, F.P. On torsion of nonlocal Lam strain gradient FG elastic beams. *Comp. Struct.* **2020**, *233*, 111550. [CrossRef]
21. Zhang, N.; Zhao, X.; Zheng, S.J.; Chen, D. Size-dependent static bending and free vibration analysis of porous functionally graded piezoelectric nanobeams. *Smart Mater. Struct.* **2020**, *29*, 045025.

22. Zhao, X.; Zheng, S.; Li, Z. Size-dependent nonlinear bending and vibration of flexoelectric nanobeam based on strain gradient theory. *Smart Mater. Struct.* **2019**, *28*, 075027. [CrossRef]
23. Barretta, R.; de Sciarra, F.M. Variational nonlocal gradient elasticity for nano-beams. *Int. J. Eng. Sci.* **2019**, *143*, 73–91. [CrossRef]
24. Niiranen, J.; Balobanov, V.; Kiendl, J.; Hosseini, S.B. Variational formulations, model comparisons and numerical methods for Euler-Bernoulli micro- and nano-beam models. *Math. Mech. Solids* **2019**, *24*, 312–335. [CrossRef]
25. Tran, L.V.; Niiranen, J. A geometrically nonlinear Euler-Bernoulli beam model within strain gradient elasticity with isogeometric analysis and lattice structure applications. *Math. Mech. Complex Syst.* **2020**, *8*, 345–371. [CrossRef]
26. Vo, D.; Suttakul, P.; Rungamornrat, J.; Nanakorn, P. Static analysis of planar arbitrarily curved microbeams with the modified couple stress theory and Euler-Bernoulli beam model. *Appl. Math. Model.* **2022**, *112*, 358–390. [CrossRef]
27. Vo, D.; Zhou, K.; Rungamornrat, J.; Bui, T.Q. Spatial arbitrarily curved microbeams with the modified couple stress theory: Formulation of equations of motion. *Eur. J. Mech. A-Solid* **2022**, *92*, 104475. [CrossRef]
28. Li, C.Y.; Zheng, S.J.; Chen, D.J. Size-dependent isogeometric analysis of bi-directional functionally graded microbeams reinforced by graphene nanoplatelets. *Mech. Based Des. Struct.* **2020**. [CrossRef]
29. Lurie, S.; Solyaev, Y. Revisiting bending theories of elastic gradient beams. *Int. J. Eng. Sci.* **2018**, *126*, 1–21. [CrossRef]
30. Li, A.; Ji, X.; Zhou, S.; Wang, L.; Chen, J.; Liu, P. Nonlinear axisymmetric bending analysis of strain gradient thin circular plate. *Appl. Math. Model.* **2021**, *89*, 363–380. [CrossRef]
31. Kong, S.L.; Zhou, S.J.; Nie, Z.F.; Wang, K. Static and dynamic analysis of micro beams based on strain gradient elasticity theory. *Int. J. Eng. Sci.* **2009**, *47*, 487–498. [CrossRef]
32. Lazopoulos, K.A. Post-buckling problems for long elastic beams. *Acta Mech.* **2003**, *164*, 189–198. [CrossRef]
33. Li, X.F.; Wang, B.L.; Lee, K.Y. Size effects of the bending stiffness of nanowires. *J. Appl. Phys.* **2009**, *105*, 074306. [CrossRef]
34. Polizzotto, C. A hierarchy of simplified constitutive models within isotropic strain gradient elasticity. *Eur. J. Mech. A-Solid* **2017**, *61*, 92–109. [CrossRef]
35. Yan, Z.; Jiang, L.Y. Flexoelectric effect on the electroelastic responses of bending piezoelectric nanobeams. *J. Appl. Phys.* **2013**, . [CrossRef]
36. Mindlin, R.D. Micro-structure in linear elasticity. *Arch. Ration. Mech. Anal.* **1964**, *16*, 51–78. [CrossRef]
37. Gao, X.L.; Park, S.K. Variational formulation of a simplified strain gradient elasticity theory and its application to a pressurized thick-walled cylinder problem. *Int. J. Solids Struct.* **2007**, *44*, 7486–7499. [CrossRef]

coatings

Article

Influence of Volume-to-Surface Area Ratio on the Creep Behavior of Steel Fiber Ceramsite Concrete Beams

Xiu Li [1], Hongbing Zhu [2,*], Zhenghao Fu [2], Peng Liu [3,4,*] and Changhuang Xia [2]

[1] School of Transportation Engineering, Wuhan Technical College of Communications, Wuhan 430065, China; hubeilixiu@163.com
[2] School of Urban Construction, Wuhan University of Science and Technology, Wuhan 430065, China; whfzh1998@163.com (Z.F.); 13628659252@163.com (C.X.)
[3] School of Civil Engineering, Central South University, 22 Shaoshan Road, Changsha 410075, China
[4] National Engineering Laboratory for High Speed Railway Construction, Central South University, Changsha 410075, China
* Correspondence: zhuhongbing@wust.edu.cn (H.Z.); lop868@163.com (P.L.)

Abstract: To explore the influence of the volume-to-surface area ratio (V/S) on the creep of ceramsite concrete beams, the creep performance of ceramsite concrete beams with different V/S was studied through a long-term deformation observation test, theoretical derivation analysis and finite element modeling. First, by observing the creep deflection of ceramsite concrete beams with five different V/Ss for 180 days, the relationship between creep deflection and loading time as well as the influence of V/S on creep deflection were obtained. Then, referring to the ACI209 and ACI435 creep coefficient calculation formula, the creep theory of ceramsite concrete beams involving V/S was established. Finally, the numerical model was built according to the test parameters. The results showed that the growth rate of the creep of ceramsite concrete beams increased rapidly in the early stage, but gradually slowed down with the passage of time and tended to be stable after 120 days of loading. The V/S had a significant impact on the creep of ceramsite concrete beams. In the first 7 days, the creep growth rate of each beam was approximately the same. Thereafter, the higher the V/S was, the lower the creep became. After 28 days, the creep of ceramsite concrete beams with varied V/Ss showed sharp differences. After the V/S exceeded 30, the increasing V/S could effectively reduce the creep value and the creep growth rate under a long-term load. The calculated results were in good agreement with the measured values, which fully reflected its creep variation. The finite element simulation further verified the influence of V/S on the creep of ceramsite concrete beams and the reliability of the creep calculation formula.

Keywords: ceramsite concrete beam; volume-to-surface area ratio (V/S); creep; experiment; calculation formula; numerical analysis

Citation: Li, X.; Zhu, H.; Fu, Z.; Liu, P.; Xia, C. Influence of Volume-to-Surface Area Ratio on the Creep Behavior of Steel Fiber Ceramsite Concrete Beams. *Coatings* **2022**, *12*, 977. https://doi.org/10.3390/coatings12070977

Academic Editor: Paolo Castaldo

Received: 13 June 2022
Accepted: 8 July 2022
Published: 10 July 2022

1. Introduction

Ceramsite concrete has the advantages of high strength, heat resistance, fire resistance, heat preservation, moisture retention and earthquake resistance. It not only can decrease the self-weight of the structure to improve the structural load-bearing capacity or increase the span of the structure, but also reduce the problems of arable land loss and forest destruction caused by natural aggregate mining [1,2]. Moreover, the strength and toughness of ceramsite concrete can be improved by adding steel fibers [3]. Recently, ceramsite concrete, which has been used in high-rise buildings, bridges and other structural projects, has good application prospects [4,5].

Creep is a long-term deformation property of concrete [6]. Concrete creep may cause creep deformation or stress relaxation phenomena in structural members, which leads to changes in the structural stress state, deformation patterns and mechanical properties [7]. Therefore, concrete creep patterns are of great theoretical and practical importance to structural analysis and design [8]. Moreover, the existing studies conclude that the creep characteristics of ceramsite concrete should be given sufficient attention [9] because the creep value of ceramsite concrete is larger than that of ordinary concrete and brings about a smaller creep coefficient.

Factors that affect the creep of concrete are usually the loading age [6,10,11] and body surface ratio [12,13] of structural members, the slump [14] and sand content [15] of concrete, the relative humidity [16] and air content [17] of the working environment where concrete members reside, etc. Existing studies showed: (i) The tensile creep of high-absorbent ceramsite concrete was lower than that of low-absorbent ceramsite concrete and ordinary ceramsite concrete [18,19]. (ii) High temperatures increased the creep of concrete specimens. The creep of specimens in dry an environment was higher than that of normal temperature conditions, for which temperature and humidity coefficients were added [20,21]. (iii) The creep of concrete changed significantly with the variation of reinforcement rate in the early stage, which is similar to the creep of plain concrete in the later stage [22]. Jiang [23] found that the early shrinkage creep of lightweight aggregate concrete was low. Its creep coefficient was half that of ordinary concrete in the same period, while the creep strain was 1.3 times that of early-age concrete. Wang [24] studied the effect of polyvinyl alcohol (PVA) fiber content on the creep of high-performance concrete and concluded that the maximum and minimum dry shrinkage creep could be obtained at 0.75% and 0.25% of PVA fiber content, respectively.

The size of the V/S (mm) affects the speed of temperature change inside the concrete and the rate and volume of internal moisture loss. Moreover, existing studies [25] demonstrated specimens with a small V/S, which feature fast-changing internal temperature, rapid water loss and high-water flow. It not only affected the strength and other properties of the concrete after forming, but also influenced the size of concrete. At present, the effect of the V/S of ceramsite concrete beams with a small amount of steel fibers on their creep properties has been not clear. This needs to be studied thoroughly by means of experimental and theoretical analysis.

This study explored the following three aspects. (i) Five steel fiber ceramsite concrete beams with different V/S were poured. Then, after the natural maintenance of sprinkling for 28 days and simple support for 212 days, the loading of 30% flexural ultimate bearing capacity was carried out. Next, the creep performance parameters were tested after 180 days under loading conditions, and the creep variation law influenced by the V/S was summarized. (ii) Based on the creep coefficient of concrete in the ACI209 model and the formula of shrinkage deformation in the ACI435 model, the formula of creep deformation of steel fiber ceramsite concrete beams was established by considering the effect of shrinkage deformation on the creep of steel fiber ceramsite concrete beams. Furthermore, the theoretical calculated values were compared with the experimental test values to verify the applicability of the modified creep calculation equation and the numerical simulation. (iii) ABAQUS finite element software was used to establish the long-term deformation model of steel fiber ceramsite concrete beams subjected to loads. On this basis, the calculation results were compared with the experimental results to analyze the applicability of the simulated model. The purpose of this study is to reveal the influence of the V/S on the creep characteristics of steel fiber ceramsite concrete beams. The research results can provide a reference for the design and analysis of steel fiber ceramsite concrete beam projects.

2. Mixed Proportion and Mechanical Properties of Steel Fiber Ceramsite Concrete

2.1. Materials

(1) Coarse aggregate crushed stone shale ceramsite of 900 grades (from Yichang Guangda, Yichang, China) was used. Its physical properties are shown as Table 1. It was pre-wetted for 4 h and dried for 10 h; then, the concrete was prepared in the end.

Table 1. Physical properties of shale ceramsite.

Particle Size /mm	Volume Density /(kg·m^{-3})	Apparent Density /(kg·m^{-3})	Compressive Strength of Concrete Cylinder/MPa	Water Absorption in 1 h/%
5~20	814	1517	6.8	2.42

(2) The fine aggregate was ordinary river sand (through 4.75 mm square hole sieve), and its physical properties are shown as Table 2.

Table 2. Physical properties of sand.

Apparent Density/(kg·m^{-3})	Volume Density/(kg·m^{-3})	Mud Ration/%	Fineness Number
2650	1570	≤2	2.7

(3) The cement was P.O.42.5 ordinary silicate cement with a density of 3150 kg/m^3 that was produced by Hubei Huaxin Co (from Wuhan, China). Its basic physical index is shown as Table 3.

Table 3. Basic physical index of cement.

Density/(g·cm^{-3})	Mineral Composition of Clinker				Fineness (Sieve Allowance by 80 μm Square Hole)/%
	C_3S	C_2S	C_3A	C_3AF	
3.15	45	25	12	8	6.5

(4) The steel fibers were SHWITCOM (from Wuhan, China) end-hooked steel fibers, and its physical properties are shown as Table 4.

Table 4. Physical properties of steel fiber.

Length/mm	Ratio of Length-Diameter	Density/(g·cm^{-3})	Tensile Strength/MPa	Material
30	60	7.8	≥1100	low carbon steel

(5) The water-reducing agent was high-performance polycarboxylic acid water-reducing agent produced by Qingdao Hongxia (from Qingdao, China). Its technical index is shown as Table 5.

Table 5. Technical index of water-reducing agent.

Color	PH	Relative Density	Solid Content/%	Water-Reducing Rate/%
Pale yellow	6~8	1.08 ± 0.02	40	25–35

(6) The water was Wuhan tap water.

2.2. Mix Proportion Design

Referring to The Technical Specification for Light Aggregate Concrete Structures (JGT 12–2006) in China, C40 was used as the target of the trial formulation. To increase the toughness of ceramsite concrete, steel fibers with a volume rate of 0.5% were incorporated with reference to The Technical Specification for the Application of Fiber Reinforced Concrete (JGJ/T 221-2010) in China. The test mix proportion is shown in Table 6. The measured concrete slump corresponded to 75.0 mm.

Table 6. Mixed proportion of ceramsite concrete beam specimens (Unit: kg/m^3).

Cement	Ceramsite	Sand	Water-Reducing Agent	Water	Ratio of Fiber Content
540	554	730	7.02	152	39 (0.5%)

2.3. Mechanical Property of Ceramsite Concrete

The test block was made according to the mix proportion listed in Table 6. Moreover, a 28 d cubic compressive strength test and flexural test were conducted. The results are shown in Table 7. It should be emphasized that the test blocks were poured in the same batch as the creep test beams and maintained under the same environment with water sprinkling.

Table 7. The mechanical parameters of ceramsite concrete at 28 d.

Mechanical Parameters	Strength			
	Specimen No. 1	Specimen No. 2	Specimen No. 3	Test Results
Compressive strength/MPa	43.82	42.57	43.12	43.17
Flexural strength/MPa	7.71	7.63	7.84	7.73
Elasticity modulus/GPa	2.46	2.40	2.42	2.43

3. Creep Test of Ceramsite Concrete Beams

3.1. Beam Specimens of Ceramsite Concrete

Creep observation tests of ceramsite concrete beams with five different body surface ratios were carried out under long-term loading conditions.

The ceramsite concrete beam specimens were 1500 mm long with protective layer of 20 mm thick. The main parameters are shown in Table 8. There were two HRB400 rebars of 8 mm diameter in both the upper and the bottom of the test beams. The stirrups were HPB235 steel bars of 6 mm diameter, as shown in Figure 1.

Table 8. Main parameters of test beam.

Specimens	Length/mm	Width/mm	Height/mm	V/S /mm	Loading Force/kN
TBB1	1500	100	120	26.316	3.25067
TBB2	1500	100	150	28.846	4.45055
TBB3	1500	100	180	30.823	5.65043
TBB4	1500	120	180	34.351	5.70859
TBB5	1500	150	180	38.793	5.76675

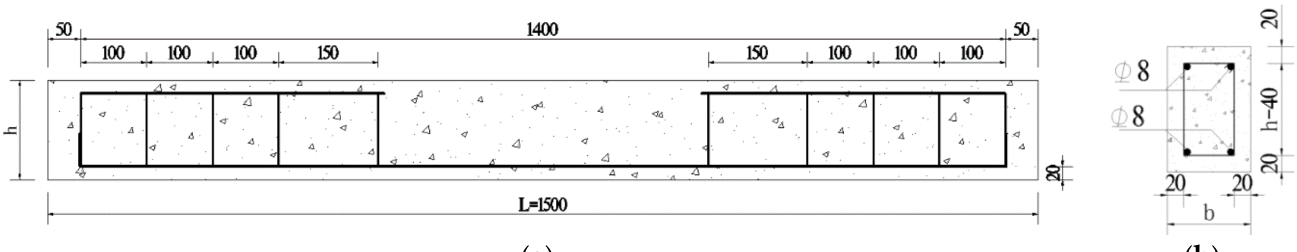

(**a**) (**b**)

Figure 1. Structure of ceramsite concrete beam (Unit: mm). (**a**) Elevation. (**b**) Cross section.

Creep observation tests were conducted on five ceramsite concrete beams with different V/Ss under long-term loading conditions.

3.2. Loading and Testing Methods

The creep performance on beams TBB1~TBB5 were tested in a sealed environment of the interior. The temperature and the relative humidity were 20 °C and 60%, respectively. The measured temperature and humidity fluctuated slightly around the control values. The specimen beams were loaded after being maintained for 240 days. In general, concrete beams need to be kept in the stockyard for some time after being pouring. Moreover, before being officially used, they need to be kept for a period after being installed. Therefore, in practice, concrete beams are subjected to a long maintenance period before being subjected to load. To make the test close to the actual engineering situation, the test piece beams were maintained as follows. First, after being poured, the beams were sprinkled and maintained for 28 days. Then, in the case of simple support (the beam was subject to self-weight), the beams were naturally maintained for 212 days.

During the test, heavy loads were stacked by using the four-point loading method (See Figures 2 and 3). To ensure the safety of the test, two test beams were arranged side by side and parallel to each other. However, as can be seen from Table 8, the loading forces required at each specimen beam loading point were varied. In this case, combining the loading method in Figure 3 with the loading forces listed in Table 8, the following approach was taken. (i) First, the individual stacked test blocks were weighed and pre-stacked. Jacks were placed at the bottom of the loading points of the distribution beams. Then, adjusting the position of each loaded test block and distribution beam, the position of the loading point of the test beams making the reaction force provided by each jack was exactly the same as the loading force listed in Table 8. (ii) Second, position of each loaded concrete block, the distribution beam and the jacking action were marked in detail. (iii) Third, the supports and test beams were placed in order according to the positions that have been marked. Then, the concrete blocks were stacked on top of the specimen beams at the locations pre-marked in (ii) to achieve accurate loading of each specimen beam. For the loading force, referring to existing studies [10,14,16], its size was about 30% of the predicted ultimate load capacity of the ceramsite concrete beam. Dial indicators were used to measure the deflection of the specimen beams.

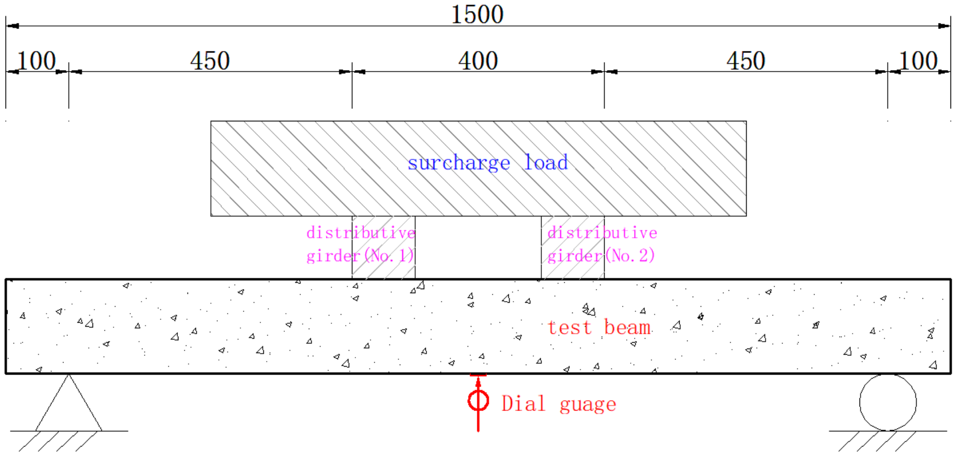

Figure 2. Loading diagram (Unit: mm).

Before loading, the loading points on the ceramsite concrete beam specimen were marked. After that, the upper surface of each contact surface was treated with sanding to ensure that the load can be transferred uniformly downward through the contact surface. To ensure the level of the loading surface, level measurement was performed, following the placement of the test beams. Then, the dial gauges were placed (a thin steel sheet was attached to the bottom contact area of the beam) and read. By doing all the procedures above, the weights of the heavy loads and their locations were measured by the weighting calculation to decrease the loading errors. Finally, the values of the dial indicators were read again, and the initial deflection was calculated.

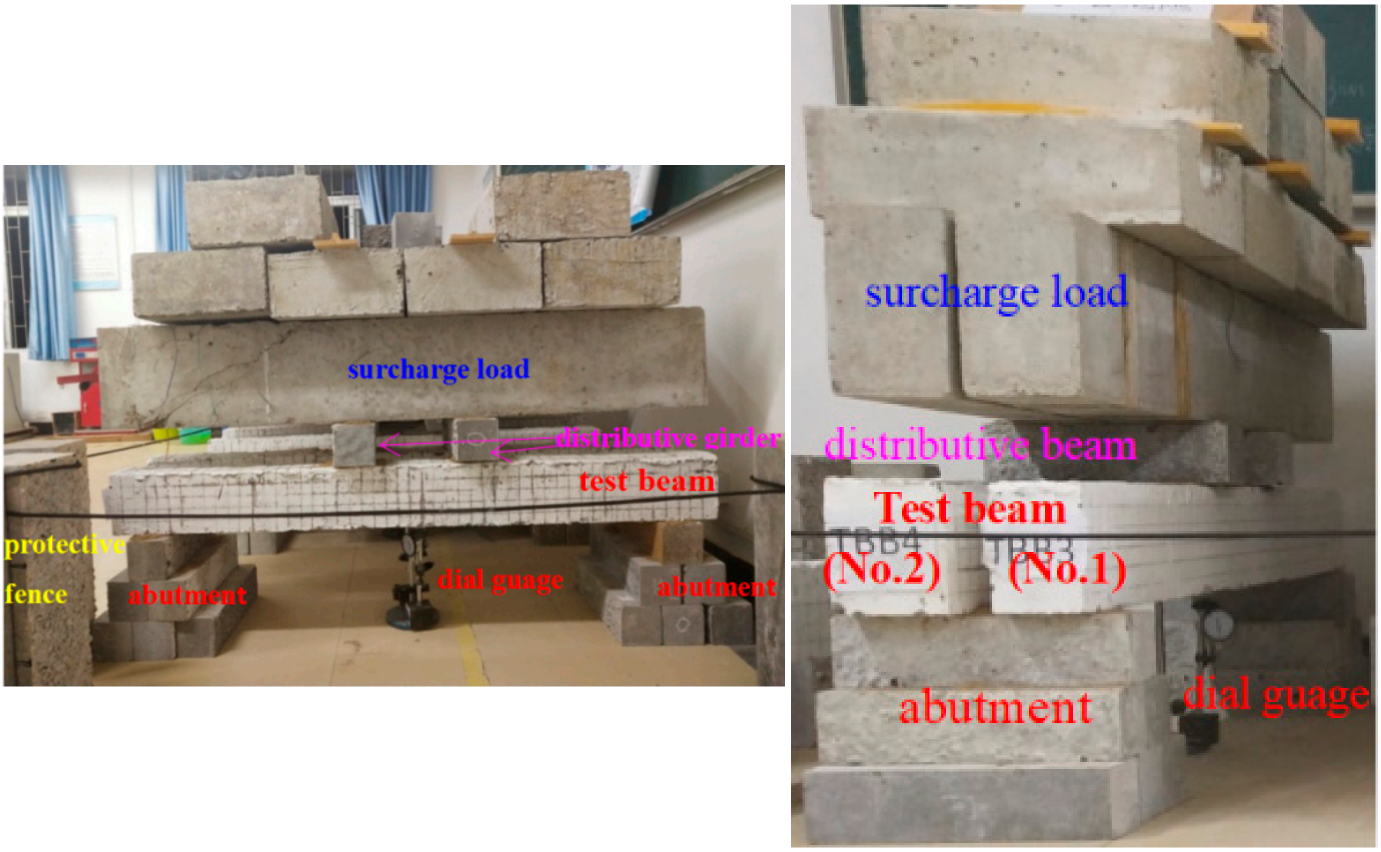

(**a**) (**b**)

Figure 3. Snapshots of loading. (**a**) Front view. (**b**) Side view.

3.3. Analysis of Test Results

The initial deflection (the deformation difference before and after initial loading), with a total deflection of 180 days, creep deflection and residual deflection after the unloading of each specimen beam are shown in Table 9. Figure 4 shows the development process of creep deflection with time growth. In addition, Figure 5 shows the influence of V/S on creep deflection at different loading times.

Table 9. Initial deflection, 180 d total deflection, creep deflection and residual deflection of the beams.

Specimens	V/S /mm	Initial Deflection f_0/mm	180 d Total Deflection f_{180}/mm	Creep Deflection f/mm	Residual Deflection f_r/mm
TBB1	26.316	1.3503	1.8426	0.5513	1.0233
TBB2	28.846	1.2064	1.6845	0.5331	0.9562
TBB3	30.823	1.1031	1.5673	0.5202	0.8765
TBB4	34.351	0.9452	1.3238	0.4106	0.6585
TBB5	38.793	0.8761	1.1645	0.2994	0.5544

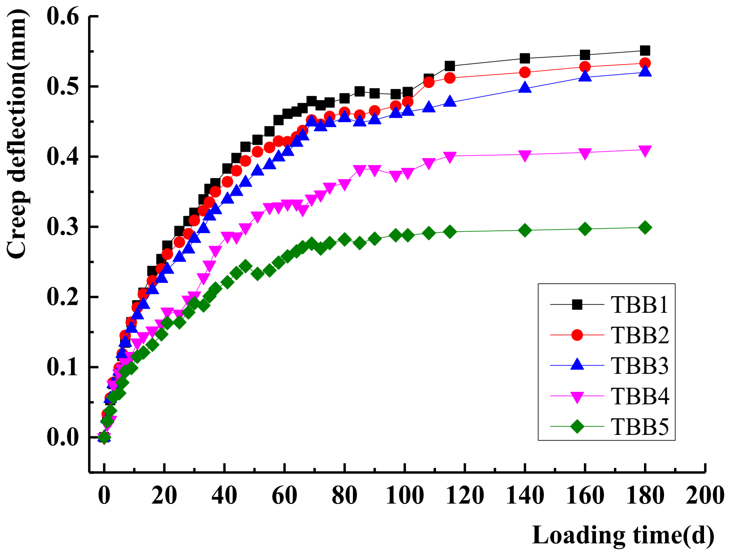

Figure 4. Curves of creep deflection–loading time of test beams with different V/Ss.

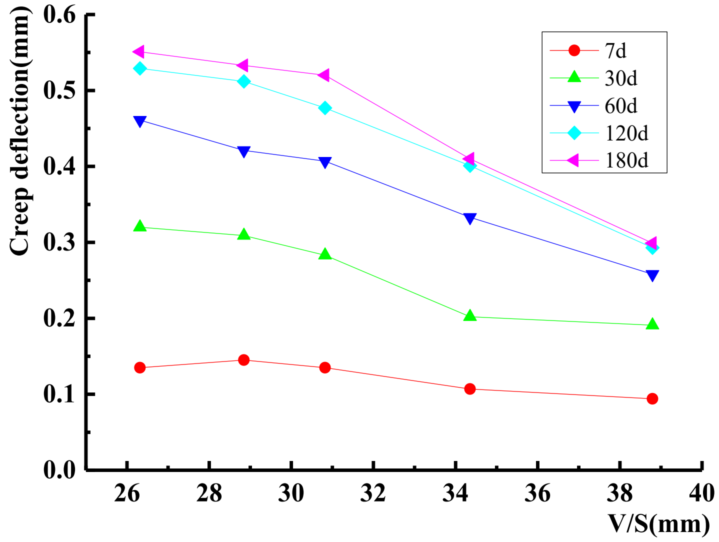

Figure 5. Influence of V/S on creep deflection.

It can be seen from Table 9 that there were differences in the initial deflection, total deflection within 180 days, creep deflection and residual deflection of each beam. In particular, the creep deflection decreased from 0.5513 to 0.2994 mm with an increasing V/S, which decreased by approximately 46%. This demonstrated the significant effect of V/S on the creep deflection of ceramsite concrete beams and proved the value of this paper's research.

Figure 4 shows that the growth rate of creep deflection of each beam was roughly the same in the first 7 days, but it became lower and lower with the rise of V/S after then. By day 28, the creep of ceramsite concrete beams differed significantly from each V/S. On the overall trend, the creep deflections of the TBB1, TBB2 and TBB3 beams had a small difference, but there was a great difference between the TBB4 and TBB5 beam. These indicated that when the V/S exceeded 30 mm, the increasing V/S could effectively decrease the creep under long-term loads.

Figure 5 shows that the creep deflection of the test beams decreased slightly with the increase of V/S at the 7th day. If the V/S was less than 35, the creep deflection of the test beams would decrease with the increase of the V/S at the 30th day. The V/S had little influence on the change of creep when it was lower than 35. However, from the 60th to the

180th day, the V/S had a great influence on the creep deflection, and the creep deflection decreased rapidly with the increase of the V/S. Therefore, the V/S had little influence on the creep of ceramsite concrete in the early stage of loading, but it had great influence on the creep of ceramsite concrete when the loading time exceeded 60 days.

4. Calculation of Creep of Steel Fiber Ceramsite Concrete Beams

The ACI209 model and ACI435 method are widely used in the study of concrete creep. They have been adopted in many countries' regulations. This model considered factors including the loading time, surrounding environment, length-to-height ratio of components, proportion and composition of coarse and fine aggregate, as well as the influence of concrete slump [20,21].

4.1. Calculation of Creep Coefficient

In this paper, the creep coefficient was calculated by the formula of the ACI209 model. The calculation results can be verified with experimental data and the conclusion of the model simulation to verify the applicability of the ACI209 model formula for ceramsite concrete.

The creep coefficient of concrete recommended by ACI 209 is expressed as follows:

$$\varphi(t,\tau) = \frac{(t-\tau)^{0.6}}{10+(t-\tau)^{0.6}}\varphi_u \tag{1}$$

where τ is loading age (d); t is calculated age (d); φ_u is the ultimate creep coefficient, $\varphi_u = 2.35\gamma_{cr}$; γ_{cr} is the product of various influence coefficients, $\gamma_{cr} = \gamma_\tau \cdot \gamma_{RH} \cdot \gamma_{VS} \cdot \gamma_s \cdot \gamma_\varphi \cdot \gamma_\alpha$; γ_τ is the influence coefficient of loading age, $\gamma_\tau = 1.25\tau^{-0.118}$ (when using wet maintenance.); γ_{RH} is the influence coefficient of relative humidity, and RH is the relative humidity of environment, $\gamma_{RH} = 1.27 - 0.67 \cdot RH$ (when RH > 40%); γ_{VS} is the influence coefficient of volume-to-surface area ratio, and *V/S* is the volume-to-surface area ratio (mm), $\gamma_{VS} = \frac{2}{3}[1 + 1.13e^{-0.0213V/S}]$; γ_s is the slump influence coefficient, and s is concrete slump (mm), $\gamma_s = 0.82 + 0.00264 \cdot s$; γ_ϕ is the influence coefficient of sand content, and ϕ is the sand rate (%), $\gamma_\phi = 0.88 + 0.0024 \cdot \phi$; and γ_α is the influence coefficient of air content, and α is the air content (%), $\gamma_\alpha = 0.46 + 0.09\alpha > 1$.

Based on the pouring of this test specimen beams and their actual condition of maintenance and loading, the values of each influence coefficient were calculated. Accordingly, the creep coefficient values of each test beams at different loading times can be further calculated, as shown in Table 10.

Table 10. Value of influence coefficient of creep coefficient.

Specimens	Loading Age (240 d) Influence Factor γ_τ	Relative Humidity Influence Factor γ_{RH}	V/S Influence Factor γ_{VS}	Slump Influence Factor γ_s	Influence Factor of Sand Content γ_ϕ	Influence Coefficient of Air Content γ_α	Ultimate Creep Coefficient φ_u
TBB1	0.6547	0.868	1.0967	1.0180	0.8832	1.009	1.3287
TBB2			1.0742			1.045	1.3478
TBB3			1.0574			1.090	1.3839
TBB4			1.0291			1.144	1.4136
TBB5			0.9964			1.171	1.4010

4.2. Calculation of Shrinkage Deformation

Assuming that concrete did not produce a downward-bending deformation under symmetric reinforcement, for simply supported beams, the calculation formula for shrinkage deformation in the beam span can be deduced as follows [21]:

$$\delta_{sh} = 0.125\varphi_{sh}l^2 = 0.125(\alpha_{sh}\frac{\varepsilon_{sh}}{h})l^2 \tag{2}$$

where l is beam span; ε_{sh} is the shrinkage strain of concrete, $\varepsilon_{sh} = 0.0004$; and α_{sh} is the comprehensive influence coefficient considering the reinforcement constraint, calculated according to Formula (3). In addition, Formula (3) is as follows:

$$\alpha_{sh} = \begin{cases} 0.7(100\rho - 100\rho')^{1/3}\left(\frac{\rho-\rho'}{\rho}\right)^{1/2} & (\rho - \rho' \le 3.0\%) \\ 0.7(100\rho)^{1/3} & (\rho' = 0) \\ 1 & (\rho - \rho' > 3.0\%) \end{cases} \tag{3}$$

where ρ is the reinforcement ratio (%) of tensile reinforcement, and ρ' is the reinforcement ratio (%) of compressed reinforcement.

4.3. Calculation of Creep Deformation

The ACI435 method divides the long-term deformation of concrete into two parts: shrinkage deformation and creep deformation. The deflection increment caused by creep is calculated by plane assumption. Considering the influence of shrinkage deformation on the creep of ceramsite concrete beam, the increase coefficient of creep deformation is [11,21]:

$$\lambda_c = \frac{0.77\xi\varphi(t,\tau)}{1 + 6.3n\rho\prime} \tag{4}$$

Then, the additional deflection increase coefficient is:

$$\lambda = \lambda_c + \frac{\delta_{sh}}{\delta_d} \tag{5}$$

According to "the Standard for Test Methods of Physical and Mechanical Properties of Concrete (GB/T 50081-2019)" in China, the calculation formula of creep deformation is as follows:

$$\delta_{cr} = \lambda\delta_d = \lambda_{\mathrm{c}}\delta_{\mathrm{d}} + \delta_{\mathrm{sh}} \tag{6}$$

where δ_{cr} is the creep deflection of component (mm) and δ_d is the instantaneous deflection of the component (mm).

Taking the elastic modulus of HRB400 reinforcement as 2.0×10^5 MPa, the creep deflection of the test beam can be calculated (Figures 6–10).

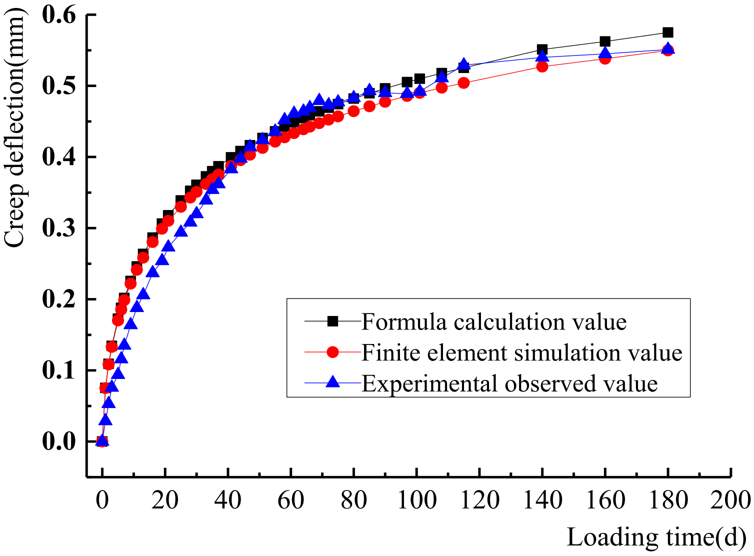

Figure 6. Creep-time curve of specimen TBB1.

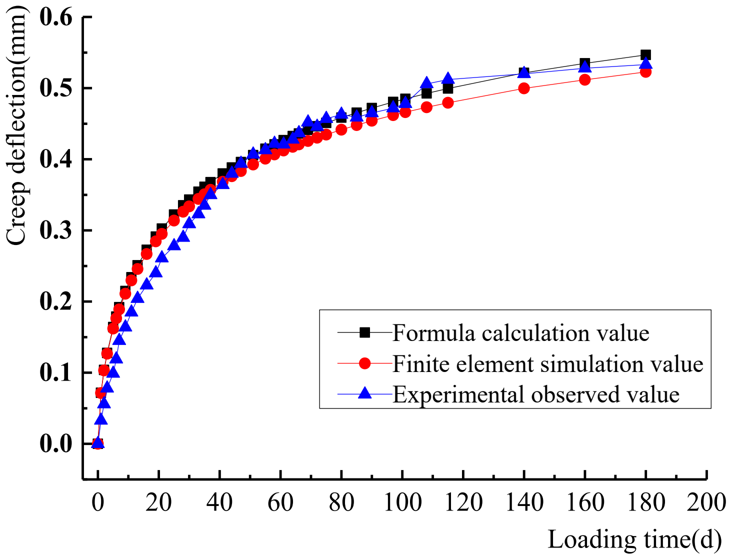

Figure 7. Creep-time curve of specimen TBB2.

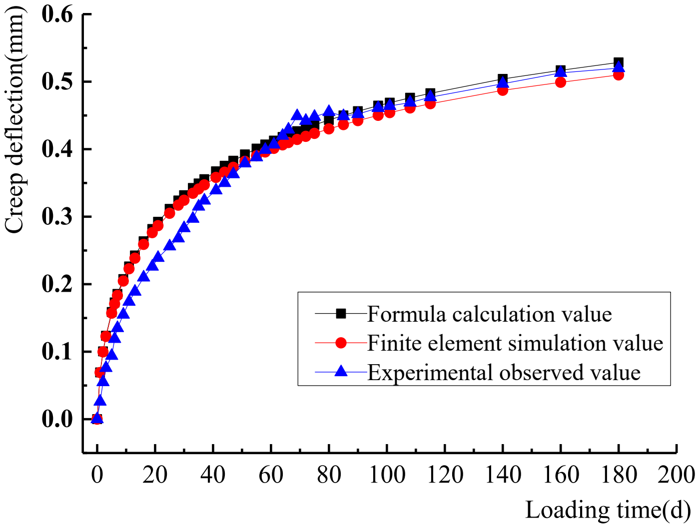

Figure 8. Creep-time curve of specimen TBB3.

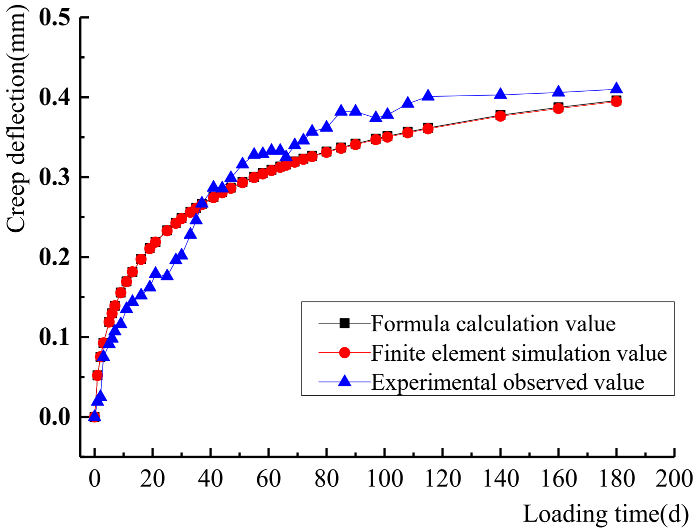

Figure 9. Creep-time curve of specimen TBB4.

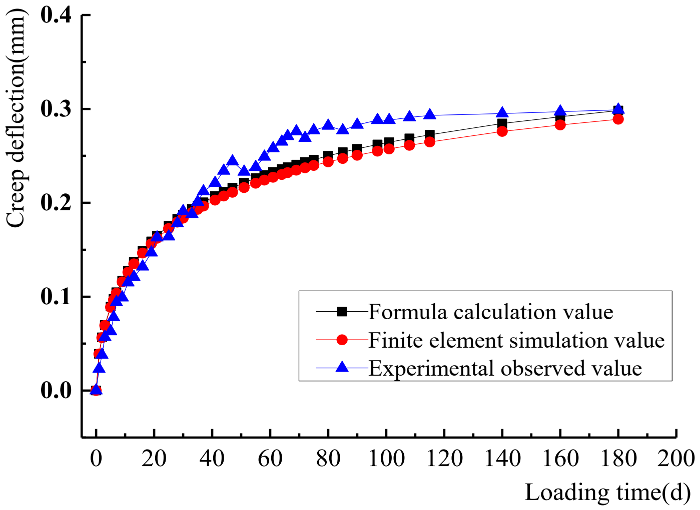

Figure 10. Creep-time curve of specimen TBB5.

From Figures 6–10, it demonstrated that the creep calculated based on the calculation formulas of ACI209 and ACI435 were in good agreement with the experimental and numerical simulated data. This suggested that it could better represent the creep variation rules of steel fiber ceramsite concrete beams. Therefore, it can be used as a formula for calculating the creep of ceramsite concrete beams in practical engineering.

5. Numerical Analysis of Long-Term Deformation of Ceramsite Concrete Beam

5.1. Constitutive Relation of Ceramsite Concrete

ABAQUS software was used to model and analyze the long-term deformation of ceramsite concrete beams under load. First, the plastic damage model provided by ABAQUS was used because it can accurately simulate the creep of ceramsite concrete beams [26]. Then, the stress–strain curve calculation model of concrete under a unidirectional load was used to describe the compression stress–strain curve of the plastic damage model, referring to the "Code for Design of Concrete Structures (GB50010-2019)" in China. The formulas are as follows:

$$\sigma = f(\varepsilon) = \begin{cases} nxf_{c,r}/(n-1+x^n) & (0 \le x \le 1) \\ xf_{c,r}/[\alpha_c(x-1)^b + x] & (x>1) \end{cases} \tag{7}$$

where $n = E_c\varepsilon_{c,r}/(E_c\varepsilon_{c,T} - f_{c,r})$ $x = \varepsilon/\varepsilon_{c,r}$; σ and ε are the stress and strain corresponding to a random point on the curve; $f_{c,r}$ and $\varepsilon_{c,r}$ are the stress and strain at the vertex of the curve; E_c is the elastic modulus of concrete; and α_c and b are the coefficients representing the shape of the curve in the descending part of the curve, which are 3.14 and 1.86, respectively, as referred to in reference [27].

5.2. Definition of Concrete Damage

Under the effect of the unidirectional compressive load, the compressive damage will occur when the deformation of concrete exceeds the elastic deformation. The calculation formula of the compressive inelastic strain ($\tilde{\varepsilon}_c^{in}$) was defined as this: the total compressive strain minus the elastic compressive strain of the material. After the compression damage data was input into ABAQUS, it can be converted into the plastic strain value ($\tilde{\varepsilon}_c^{pl}$) according to Equation (8). d_c is calculated by Equation (9).

$$\tilde{\varepsilon}_c^{pl} = \tilde{\varepsilon}_c^{in} - \frac{d_c}{(1-d_c)}\frac{\sigma}{E_0} \tag{8}$$

$$d_c = \left[\frac{1}{2}E_0\varepsilon^2 - \int f(\varepsilon)d\varepsilon\right] / \left(\frac{1}{2}E_0\varepsilon^2\right) \tag{9}$$

where E_0 is the initial tangent modulus of concrete, which corresponds to $f(\varepsilon)$.

If the plastic strain value $\tilde{\varepsilon}_c^{pl}$ output by the program is less than 0 or the inelastic strain $\tilde{\varepsilon}_c^{in}$ decreases, ABAQUS will display an error and stop the operation. When $\tilde{\varepsilon}_c^{pl} = \tilde{\varepsilon}_c^{in}$, compression damage will not occur.

The treatment of tensile damage to concrete is similar to that of compressive damage.

5.3. Finite Element Model

The finite element models for each of the five beams were built according to the parameters in Table 8 and Figure 1. The concrete was simulated using the 3D eight-node reduced-integration element (C3D8R). The rebar cage was simulated using the 3D two-node truss element (T3D2). The rebar cage was placed inside the concrete slab. Moreover, EMBED bond contacts were applied between the rebar and the surrounding concrete. The constitutive relation and plastic damage of concrete were expressed according to Equations (7)–(9). Poisson's ratio was taken as 0.2. The concrete creep coefficient was calculated using Equation (1) and imported into the ABAQUS model. The modeling and meshing are shown in Figure 11.

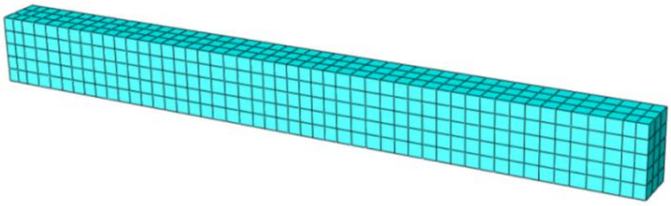

Figure 11. Finite element model and meshing of ceramsite concrete beam.

5.4. Long-Term Loading

Based on the program that comes with ABAQUS, the loading application program for ceramsite concrete beams was simulated using Python. User-defined field variables, state variables and custom expansion options were added to the concrete intrinsic structure definition. Additionally, the fitted creep procedure was written into the modeling file for the subroutine. After each output displacement of the ceramsite concrete beam, the loading state was maintained, the size was unchanged and the next cycle was continued. The variation of the elasticity modulus of ceramsite concrete with time was calculated in real time by using the field and state variables of the material in ABAQUS.

5.5. Finite Element Analysis Results

The parameters of the specimen beams were input into the model. The variation rule of the creep deflection of each model beam with the increase of time was obtained after loading.

To analyze and compare conveniently, the calculated creep, test results and fitting data of ceramsite concrete specimen beams are included in Figures 6–10.

5.6. Comparative Analysis of Simulatd, Experimental and Theoretical Value

The creep coefficient was calculated according to the proposed formula of ACI209. Then, the creep value of the beam was calculated by ACI435. From Figures 6–10, it shows that these values were in good agreement with the experimental and numerical results. In addition, it greatly reflected the creep changes in ceramsite concrete beam.

(1) Comparative analysis of creep at 180 d:

The test results, calculated values and simulated data of each specimen beam at 180 d are shown in Table 11.

Table 11. Comparison of creep value at 180 d.

Number of Test Beam	Test Values	Calculated Values	Error between Calculated and Test Values/%	Finite Element Simulation Values	Error between Simulated and Test Values/%
TBB1	0.5513	0.5749	4.36	0.5497	0.02
TBB2	0.5331	0.5467	2.63	0.5227	1.88
TBB3	0.5202	0.5285	1.54	0.5099	1.92
TBB4	0.4106	0.3960	3.41	0.3946	3.90
TBB5	0.2994	0.2982	0.33	0.2890	3.34

Table 11 and Figures 6–10 indicated that the theoretical and simulated values of creep of ceramsite concrete beams in these 180 days were close to the experimental results (the errors were within 5%). This showed that the finite element simulation can effectively analyze the creep variation patterns of ceramsite concrete beams. Meanwhile, Formulas (1)–(6) based on the method of ACI209 and ACI435 can be used as a predictive model for the creep of vitrified concrete beams. Moreover, they can fully predict the variations of creep values of ceramsite concrete beams over time.

(2) Comparative analysis of creep curve of deflection time:

It can be seen from Figures 6–10 that the creep variation rule of ceramsite concrete beam simulated by the finite element model was in good agreement with the results calculated referring to the ACI209 and ACI435 models. The finite element simulation value was slightly lower than the calculated value. The experimental value was in good agreement with the simulated and the calculated value. It was further shown that Formulas (1)–(6) based on the calculation method of ACI209 and ACI435 can well reflect the creep change in the ceramsite concrete beam, as well as the finite element model.

6. Conclusions

Long-term deformation tests, theoretical analysis and finite element modeling were carried out on five ceramsite concrete beams with different V/Ss. The following conclusions were obtained:

(1) The creep of ceramsite concrete specimens developed rapidly in the early stage of loading, but it gradually slowed down over time and tended to be stable after loading for 120 days.

(2) The V/S had an obvious influence on the creep of ceramsite concrete beams. In the first 7 days, the growth rate of each beam was roughly the same. The higher the V/S was, the lower the creep performance was. After 28 days, the creep of each beam was significantly different. When the volume–surface ratio exceeded 30, the increasing V/S can effectively decrease the creep and creep growth rate under long-term loading. In practical engineering, the V/S of the beam can be increased by controlling the beam length and increasing the beam width or height as appropriate to reduce the creep of the beam.

(3) The creep calculation Formulas (1)–(6) of ceramsite concrete beam were established according to the method of ACI209 and ACI435. The calculated results were in good agreement with the measured values, which can well reflect the creep variation rule of ceramsite concrete beams. This formula can be used for the calculation of creep in the design of ceramsite concrete beams.

(4) After adding 0.5% steel fiber, the creep law of ceramsite concrete beams can still be expressed by the modified formulas of ACI209 and ACI435.

(5) The finite element simulation can fully verify the calculation formula of creep and the influence of V/S on the creep of ceramsite concrete beams.

(6) The experiments, theory and numerical simulation in this paper initially revealed the findings that the creep of steel fiber ceramsite concrete beam was influenced by the V/S of the specimen. However, the quantities of specimens were small. As a result, the further experimental studies were planned to be carried out subsequently.

In the future, it will be planned to pour more steel fiber ceramsite concrete beams to expand the study scope of V/S. A combination of experiments and numerical simulations will be used to investigate the effect of V/S on the 180 d creep value of the beams. Furthermore, it can establish equations and reasonably predict the optimum V/S. The results are hoped to provide a scientific reference for engineering design. Moreover, the amount of steel fibers and the relative humidity of the environment may affect the creep of steel fiber ceramsite concrete beams, which will be viewed as the subsequent research directions.

Author Contributions: Conceptualization, X.L. and H.Z.; Methodology, X.L. and H.Z.; Software, P.L.; Validation, Z.F. and C.X.; Formal Analysis, X.L.; Investigation, C.X.; Resources, C.X. and X.L.; Data Curation, C.X., X.L. and H.Z.; Writing—Original Draft Preparation, X.L.; Writing—Review and Editing, X.L. and H.Z.; Visualization, C.X.; Supervision, X.L.; Project Administration, H.Z.; Funding Acquisition, H.Z. All authors have read and agreed to the published version of the manuscript.

Funding: This study was funded by the National Natural Science Foundation of China (grant numbers 51778630, 52178182 and U1934217), China Railway Science and technology research and development plan project (grant numbers 2020-Major project-02, 2021-Major project-02, 2021-Key projects-11) and Hubei Provincial Education Science Planning Project (2019GB201).

Institutional Review Board Statement: Not applicable.

Informed Consent Statement: Not applicable.

Data Availability Statement: The data presented in this study are available on request from the corresponding author.

Conflicts of Interest: The authors declare no conflict of interest.

References

1. Bu, C.; Zhu, D.; Liu, L.; Lu, X.; Sun, Y.; Yan, Z.; Yu, L.; Wei, Q. A study on the mechanical properties and microcosmic mechanism of basalt fiber modified rubber ceramsite concrete. *Buildings* **2022**, *12*, 103. [CrossRef]
2. Liu, X.; Meng, K.; Zhang, A.; Zhu, T.; Yu, C. Bearing capacity of H-section beam wrapped with ceramsite concrete. *Steel Compos. Struct.* **2021**, *40*, 679–696. [CrossRef]
3. Xie, Y.; Long, G.; Zhou, Q.; Chaktrimongkol, P.; Shi, Y.; Umar, H. Experimental investigation on mechanical property and microstructure of ultra-high-performance concrete with ceramsite sand. *Struct. Concr.* **2021**, *11*, 156. [CrossRef]
4. Bu, C.; Yang, H.; Liu, L.; Zhu, D.; Sun, Y.; Yu, L.; Ouyang, Y.; Cao, X.; Wei, Q. Quantification of ceramsite granules in lightweight concrete panels through an image analysis technique. *Materials* **2022**, *15*, 1063. [CrossRef]
5. Zhu, H.; Fu, Z.; Liu, P.; Li, Y.; Zhao, B. Shear behavior of stud-PBL composite shear connector for steel–ceramsite concrete composite structure. *Coatings* **2022**, *12*, 583. [CrossRef]
6. Mohebbi, A.; Graybeal, B.; Haber, Z. Time-dependent properties of ultrahigh-performance concrete: Compressive creep and shrinkage. *J. Mater. Civ. Eng.* **2022**, *34*, 04022096. [CrossRef]
7. Mei, S.Q.; Wang, Y.F.; Zhang, J.C. Creep of concrete-filled steel tube considering creep-recovery of the concrete core. *Adv. Struct. Eng.* **2020**, *23*, 997–1009. [CrossRef]
8. Liang, S.M.; Wei, Y. Methodology of obtaining intrinsic creep property of concrete by flexural deflection test. *Cem. Concr. Compos.* **2019**, *97*, 288–299. [CrossRef]
9. Wang, S.R.; Wu, X.G.; Yang, J.H.; Zhu, S. Acoustic emission characteristics and dynamic damage constitutive relation of shale-ceramsite concrete subjected to loading Tests. *J. Mater. Civ. Eng.* **2020**, *32*, 76. [CrossRef]
10. Hwang, E.; Kim, G.; Koo, K.; Moon, H.; Choe, G.; Suh, D.; Nam, J. Compressive creep and shrinkage of high-strength concrete based on limestone coarse aggregate applied to high-rise buildings. *Materials* **2021**, *14*, 5026. [CrossRef]
11. Ye, L.; Sun, H.L.; Lu, X.Z. *High Strength Lightweight Aggregate Concrete Structures: Performance, Analysis and Calculation*; Science Press: Beijing, China, 2009.
12. Chen, P.; Zheng, W.Z.; Zhou, X.Y. Creep of reinforced high-strength concrete-containing industrial by-products silica fume and slag. *Struct. Concr.* **2020**, *2*, 201900435. [CrossRef]
13. Zou, D.J.; Liu, T.J.; Teng, J.; Du, C.C.; Li, B. Influence of creep and drying shrinkage of reinforced concrete shear walls on the axial shortening of high-rise buildings. *Constr. Build. Mater.* **2014**, *55*, 46–56. [CrossRef]
14. Li, K.F.; Yang, C.Q.; Huang, W.; Zhao, Y.B.; Wang, Y.; Pan, Y.; Xu, F. Effects of hybrid fibers on workability, mechanical, and time-dependent properties of high strength fiber-reinforced self-consolidating concrete. *Constr. Build. Mater.* **2021**, *277*, 122325. [CrossRef]
15. Cai, X.; Jiang, M.M.; Guo, X.W.; Chen, J.J.; Zhao, Q. Experimental study on the creep behaviour of cemented sand and gravel (CSG) and temperature stress prediction of CSG dam under seasonal temperature change. *Adv. Civ. Eng.* **2020**, *1*, 8289520. [CrossRef]

16. Zheng, Z.H.; Hu, D.; Liu, P.; Sha, F.; Liu, L.; Yu, Z.W. Considering the effect of the randomness of concrete strength and relative humidity on concrete creep. *Struct. Concr.* **2020**, *10*, 201900435. [CrossRef]
17. Zhang, R.; Ma, L.; Wang, Q.; Li, J.; Wang, Y.; Chen, H.; Samosvat, V. Experimental studies on the effect of properties and micro-structure on the creep of concrete-filled steel tubes. *Materials* **2019**, *12*, 1046. [CrossRef]
18. Zhuang, Y.Z.; Chen, C.Y.; Ji, T. Effect of shale ceramsite type on the tensile creep of lightweight aggregate concrete. *Constr. Build. Mater.* **2013**, *46*, 13–18. [CrossRef]
19. Ji, T.; Chen, C.Y.; Chen, Y.B. Effect of ceramsite prewetting degree on tensile creep characteristics of lightweight aggregate concrete. *J. Build. Mater.* **2012**, *15*, 690–696.
20. James, A. *Prediction of Creep, Shrinkage and Temperature Effects in Concrete Structures*; ACI Committee 209: Farmington Hills, MI, USA, 1992.
21. Grouni, H.N. *Control of Deflection in Concrete Structures*; ACI Committee 435: Detroit, MI, USA, 1995.
22. Sun, G.J.; Xue, S.D. Experimental investigation of creep and shrinkage of reinforced concrete with influence of reinforcement ratio. *Adv. Concr. Constr.* **2019**, *7*, 211–218.
23. Jiang, W.; Yang, Z.H. Compressive creep of lightweight aggregate concrete at early age. *J. Build. Mater.* **2016**, *19*, 40–44.
24. Wang, W.L.; Li, J.T.; Peng, W.J. Effects of water-to-cement ratio, curing method and fiber on the autogenous shrinkage of early-age concrete. *J. Ceram. Process. Res.* **2019**, *20*, 77–85. [CrossRef]
25. Gedam, B.A.; Bhandari, N.M.; Upadhyay, A. An APT material model for drying shrinkage and specific creep of HPC using artificial neural network. *Struct. Eng. Mech.* **2014**, *1*, 97–113. [CrossRef]
26. Nie, J.G.; Wang, Y.H. Comparison study of constitutive model of concrete in ABAQUS for static analysis structures. *Eng. Mech.* **2013**, *30*, 59–67.
27. Zhao, S.B.; Zhao, M.S.; Zhang, X.Y. Study on complete stress curves of steel fiber reinforced lightweight aggregate concrete under uniaxial compression. *J. Build. Struct.* **2019**, *40*, 181–190.

coatings

MDPI

Article

Dynamic Strain Response of Hot-Recycled Asphalt Pavement under Dual-Axle Accelerated Loading Conditions

Jin Li [1,*], Yingyong Li [2], Chongsheng Xin [3], Haoyu Zuo [1], Ping An [4], Shen Zuo [1,*] and Peng Liu [5]

[1] School of Transportation Civil Engineering, Shandong Jiaotong University, Jinan 250357, China; 21107008@stu.sdjtu.edu.cn
[2] Highway Service Department of Shandong Provincial Transportation Service Center, Jinan 250002, China; 21107006@stu.sdjtu.edu.cn
[3] Jinan Kingyue Highway Engineering Company Ltd., Jinan 250409, China; 19011059@stu.sdjtu.edu.cn
[4] Rizhao Transportation Development Group Co., Ltd., Rizhao 276800, China; 20107044@stu.sdjtu.edu.cn
[5] School of Civil Engineering, Central South University, Changsha 410083, China; liupeng868@csu.edu.cn
* Correspondence: 204026@sdjtu.edu.cn (J.L.); 204096@sdjtu.edu.cn (S.Z.); Tel.: +86-5-(31)-8068-7989 or +86-13-67-882-4225 (J.L.)

Citation: Li, J.; Li, Y.; Xin, C.; Zuo, H.; An, P.; Zuo, S.; Liu, P. Dynamic Strain Response of Hot-Recycled Asphalt Pavement under Dual-Axle Accelerated Loading Conditions. *Coatings* **2022**, *12*, 843. https://doi.org/10.3390/coatings12060843

Academic Editor: Andrea Simone

Received: 8 May 2022
Accepted: 10 June 2022
Published: 16 June 2022

Abstract: Accelerated pavement testing (APT) is an effective method to study the long-term performance of pavement. Therefore, the dynamic strain behavior analysis of asphalt pavement has important guiding significance in the study of pavement failure modes. To explore the dynamic response of a high-content plant-mixed hot-reclaimed asphalt mixture under a dynamic load of vehicles, a full-scale test road was paved, and ALT biaxial accelerated loading test equipment was used to simulate the dynamic loads of vehicles. Based on parameters such as axle load, temperature, speed, and loading times, the development law for the bottom strain of the three pavement structures was analyzed. The test results show that the most unfavorable position of the asphalt pavement load is located just below the centerline of the wheel track on one side, and the damage effect of a single double-axle wheel load is far greater than that of two single-axle wheel loads. Then, the longitudinal tensile strain of the pavement bottom always maintains the alternating state of compression-tension and compression. The longitudinal tensile strain of the pavement bottom is larger than the transverse tensile strain, and transverse fatigue cracks appear first. Under normal temperature conditions, the bottom tensile strains of the three composite pavement structures under different axial loads are close, and the pavement performance of the hot-recycled asphalt pavement of structure A and structure B can meet the specification requirements. The relationship between the bottom strain and axle load is nonlinear and is directly related to the tire ground pressure, and the difference in the tensile and compressive strain values of the bottom of the three composite pavement structures is small. Under high temperature conditions, the bottom layer temperature of structure A and structure B is lower than that of structure C, and the thermal heat transfer efficiency of hot-recycled asphalt pavement is lower than that of ordinary asphalt pavement. Additionally, the longitudinal tensile strain is about 1–1.5 times that of the transverse tensile strain. Based on the Boltzmann function, the accumulative tensile strain prediction model was established to reflect the relationship between the cumulative strain at the bottom and the number of loads.

Keywords: road engineering; hot-recycled asphalt pavement; dual-axle accelerated loading; dynamic response of strain

1. Introduction

The vehicle dynamic load is one of the key factors that cause road damage and affect road life and service capacity [1,2]. This factor is closely related to the structure, load, speed, and other factors of the vehicle [3,4]. Dynamic strain is a direct reflection of vehicle's dynamic load on the pavement structure and also an important mechanical index to characterize the service performance of asphalt pavement. The value of strain in

China's highway asphalt pavement design code is still based on the theory of a static elastic layered system. Although the fatigue cracking test used for the asphalt mixture layer adopts dynamic compression modulus correction at 20 °C, this test cannot truly reflect the dynamic characteristics of the pavement structure under loads and environmental conditions. Thus, it is necessary to systematically study the dynamic strain behavior characteristics of the asphalt pavement structural layer under the action of vehicle dynamic loads [5–7].

Accelerated pavement testing (APT) can quickly accumulate loads on test pavements to evaluate long-term pavement performance in a short period of time [8] and analyze the pavement's failure mechanism. Through sensitivity analysis [9], an APT project can promote the use of innovative building materials and methods, improve pavement design and analysis procedures, promote aging-pavement survey work, and accelerate loading tests, which are all considered to be effective means of studying dynamic strain characteristics caused by the dynamic loads and service performance of asphalt pavements [10–13]. Dong Zhonghong [14] used ALF (accelerated loading facility) to analyze the effects of lateral distribution, axle weight, and temperature on the dynamic response of asphalt pavement structures under the action of a single-shaft and double wheels. Guan Zhiguang [15] introduced the two factors of vehicle driving speed and tire pressure into a study on the dynamic responses of road surface structures and established a speed–axle weight regression model. Ye Yali [16] preliminarily studied the dynamic strain evolution law of flexible base asphalt pavement structures through an APT test road. Chen Jingyun [17] studied the mechanical response law of a typical asphalt pavement structural layer under a positive load and partial load of traffic based on MLS66. Wu Jinting [18] used a seismic wave modulus measuring instrument to analyze the instantaneous dynamic response of the bottom of the pavement structure layer under the experimental conditions of overweight and high frequency and analyzed the relationship between the number of loads and the cumulative strain of the asphalt surface layer.

Ozer [19] obtained the pavement structural layer response under two different loading states of pure shear and compression shear through indoor testing and analyzed the influence of vehicle load (load and tire inflation pressure) and maneuvering (braking, acceleration, and cornering) on the strain behavior of the pavement structural layer. Saleh [20] established a model between roughness and load repetition, axial load, and asphalt layer thickness, establishing a theoretical basis for studying the influence of vehicle power size on the dynamic characteristics of flexible pavement. Liu Dawei [21] established a three-dimensional finite element analysis model of semi-rigid pavement, which analyzed the effect of changes in vehicle driving speed on the dynamic damage of semi-rigid asphalt pavement. Navarrina [22] studied the changes to power-axle weight applied by heavy vehicles on the road surface over time by extending the quarter-car model and established a comprehensive model of flexible road fatigue analysis considering the impact of vehicle dynamic loads. Lu Zheng [23] and Chen Jingyun [24] established a dynamic analysis model of vehicle-uneven pavement-subgrade structure coupling, which was used to analyze the influence of multiple parameter coupling on road dynamic responses such as the driving speed, road surface unevenness, road thickness, tire stiffness, and base modulus. Huang Zhiyi [24] used the 3D-MOVE Analysis finite-layer software to analyze the dynamic strain characteristics of the structural layer of regenerated asphalt pavement under the action of moving a non-uniform distribution load. M.S.H. Al-Furjan has derived and solved the governing equations of structures using the differential quadrature method (DQM). Afterward, a parametric study is conducted to present the effects of SMA fiber. Due to the difference between the parameter material constitutive relationship and the content gradation and the actual asphalt mixture, it is difficult to accurately describe the fatigue performance by the finite element method and the differential quadrature method, and there are large errors. Since accelerated loading is the most advanced technical means to study the fatigue properties of asphalt, it can provide a more reasonable explanation for the complexity of the material properties of asphalt mixtures. Although domestic and foreign scholars have conducted a number of studies on the dynamic strain behavior of asphalt pavement under the action of driving loads, foreign research has largely focused on flexible pavement. Consequently, the large differences in the pavement structure system decrease the applicability of foreign experimental research results. Moreover, due to the limitations of domestic accelerated loading equipment, funds, and technology, few scholars have conducted a complete study on the evolution of pavement strain behavior.

Plant-mixed hot recycling is one of the main means of producing reclaimed asphalt pavement, but RAP content, pavement structural stability, and durability have always restricted this type of pavement's wide application in China. Most scholars have only studied the strain behavior, dynamic characteristics, and long-term service performance of recycled asphalt pavement through theoretical analysis, material property testing, and numerical calculation methods, but no scholars have conducted a field-accelerated loading test on the omnidirectional strain response of the semi-rigid-base plant-mixed hot-recycled asphalt pavement structural system.

Based on these factors, we carried out an ALT acceleration loading test on an APT test road of the S222 West Lake Section of Rizhao City, Shandong Province, relying on the Applied Basic Research Project of the Ministry of Transport and the Transportation Science and Technology Project of Shandong Province. The bottom strain of the pavement structure in three different combinations was used as the experimental research object. We analyzed the evolution of the bottom-strain behavior of the plant-mixed hot-recycled asphalt pavement under the action of a high axle load, which provided a reference for studying the disease evolution mechanisms and long-term road performance of plant-mixed hot-recycled asphalt pavement.

2. Accelerated Loading Test Based on ALT

2.1. Test Equipment

The mobile road acceleration loading system, ALT, is shown in Figure 1. The equipment used was 26.342 m long, 4.220 m wide, and 7934 cm high. The hydraulic loading stepless adjustment system can apply single-sided single-axle or single-sided double-sided coupling loads. The double-sided wheelbase is 1.4 m, the effective load travel length is 10 m, the one-sided axle load range is 100–200 kN, and the one-way set wheel load can be applied 400–500 times per hour. The lateral offset load can be set, and the main and driven wheel double-axle double-wheel pack loading method is consistent with the actual road vehicle movement load state.

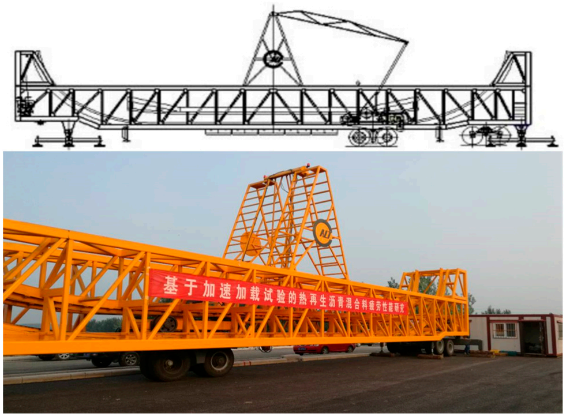

Figure 1. Mobile accelerated pavement loading equipment.

2.2. Road Surface Structure

A full-scale test road was paved at the S222 West Lake section of Rizhao City, Shandong Province, with a total length of 1200 m and a width of 10.5 m. This road is equipped with 3 kinds of pavement combination structures, where the surface layer is a typical 4 + 6 pavement structure, the base layer is cement-stabilized macadam, the thickness is 36 cm, and the bottom base layer is 18 cm low-dose cement-stabilized macadam. The rap dosage in the SMA-13 plant-mixed hot-reclaimed asphalt mixture is 20%, and the RAP dosage in the AC-20 plant-mixed hot-reclaimed asphalt mixture is 40%. To conduct a comparative test, three of the combined forms of pavement (where the width of the test road is 3, 3, 3, and 3 m, the total length is 9 m, and the length is 3.75 m) was selected to accelerate loading under the same test environment. The specific road structure form is shown in Table 1.

Table 1. Types of road surface structures.

Structure A	Structure B	Structure C
4 cm AC-20 Hot-recycled asphalt concrete	4 cm SMA-13 Plain asphalt concrete	4 cm SMA-13 Plain asphalt concrete
6 cm AC-20 Hot-recycled asphalt concrete	6 cm AC-20 Hot-recycled asphalt concrete	6 cm AC-20 Plain asphalt concrete
18 cm Cement-Stabilized Macadam	18 cm Cement-Stabilized Macadam	18 cm Cement-Stabilized Macadam
18 cm Cement-Stabilized Macadam	18 cm Cement-Stabilized Macadam	18 cm Cement-Stabilized Macadam
18 cm Cement-Stabilized Macadam	18 cm Cement-Stabilized Macadam	18 cm Cement-Stabilized Macadam

2.3. Sensor Placement

To analyze the transverse and longitudinal strain behavior at the bottoms of the three different combinations of pavement layers during the accelerated loading process, a sensor was embedded at the bottom of the lower layer. The km-100 HAS-type buried strain sensor (TML Corporation, Tokyo, Japan) is equivalent to the modulus of the asphalt mixture using the intermediate axial rod and the asphalt mixture modulus of Japan. To prevent interference, the horizontal spacing of the sensor was set to 0.400 m, and the vertical spacing was 0.500 m. To truly record the vertical change law for the temperature field of the asphalt pavement structure, the vertical position of the test pavement was 0 cm. Thermocouple temperature sensors with an accuracy of up to 0.002 °C were buried at 4 and 10 cm. The specific temperature and strain transducer layout is shown in Figure 2.

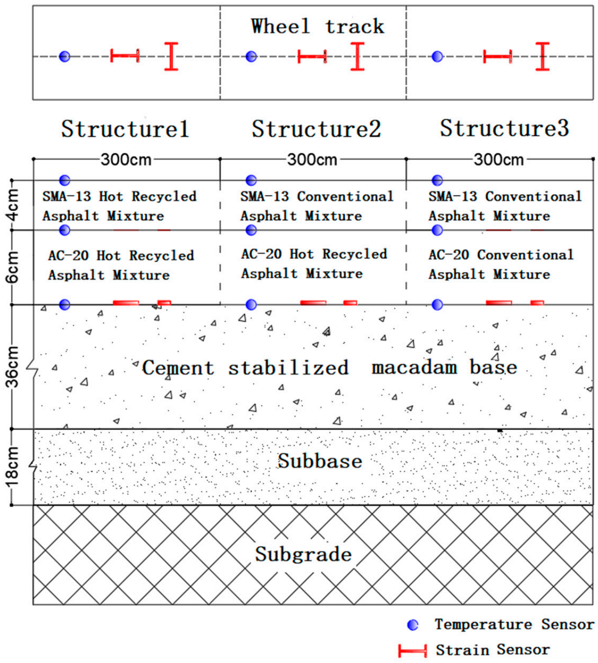

Figure 2. Schematic diagram of the test road sensor burial.

2.4. Implementation Program

This experimental study was carried out using a master–slave dual-axis accelerated loading system. The specific implementation setup for the accelerated loading test was as follows:

(1) Considering the difference in strain behavior under different axle weights, three axle weight classes were set up for comparison tests: 100, 130, and 150 kN.
(2) Considering the difference in strain behavior under different travel speeds, four speed classes were set: 12, 18, 22, and 24 km·h^{-1}.
(3) To test the long-term road performance of the plant-mixed hot-recycled asphalt pavement, the long-term loading test was set to 1.5 times the standard axle load, i.e., 150 kN, without considering the lateral offset moving load. The test environment was an open-air natural environment.
(4) Loading was performed 20 h/day for 60 days for a total of 400,000 times. The asphalt surface bottom layer tensile strain and asphalt surface layer permanent deformation were used as the test index and converted to a cumulative 5.5 million standard axle load.
(5) The base strain and pavement temperature gradient were continuously collected in real time, where the layer substrate strain acquisition frequency was 100 Hz, and the temperature gradient acquisition frequency was 10 Hz.

3. Analysis of Test Results

3.1. Determination of the Most Unfavorable Location for the Load

The dynamic load generated by driving a vehicle will act on the road surface, thereby affecting the road. It is beneficial to determine the most unfavorable position of the load to better study the pavement failure mode and improve road surface design. Therefore, we carried out a strain test under the center and side tracks of the gear train on a previous indoor full-scale test road. The sensor data from the two cases were then compared and analyzed, as shown in Table 2.

Table 2. The longitudinal strain at different position of the wheel bottom.

Sensor Number	Location	Longitudinal Tensile Strain /× 10^{-6}	Longitudinal Compressive Strain/× 10^{-6}	Total Amplitude /× 10^{-6}
11# sensor (Early foundation)	Under the center of the wheel gap	47.8	−3.4	51.2
	Under unilateral wheel tracks	96.3	−12.2	108.5
31# sensor (Early foundation)	Under the center of the wheel gap	44.2	−22.4	66.6
	Under unilateral wheel tracks	47.4	−49.0	96.4

As can be seen from Table 2, the amplitude of longitudinal tensile strain, compressive strain, and total strain under a single-wheel track in the case of two axles and two wheels are all greater than the values under the center of the wheel gap, so the degree of failure under a single-wheel track is much greater than that under the center of the wheel train. Therefore, the loading position of the embedded strain sensor is directly below the center of the single-wheel track.

3.2. Influence of Number of Axles

The acceleration loading equipment used at home and abroad is mainly of the single-axle double-wheel type. We adopted double-axle double-wheel-type acceleration loading equipment and analyzed the transverse and longitudinal bottom-strain test data of structure 3 at 13:00 on 21 August, as shown in Figure 3.

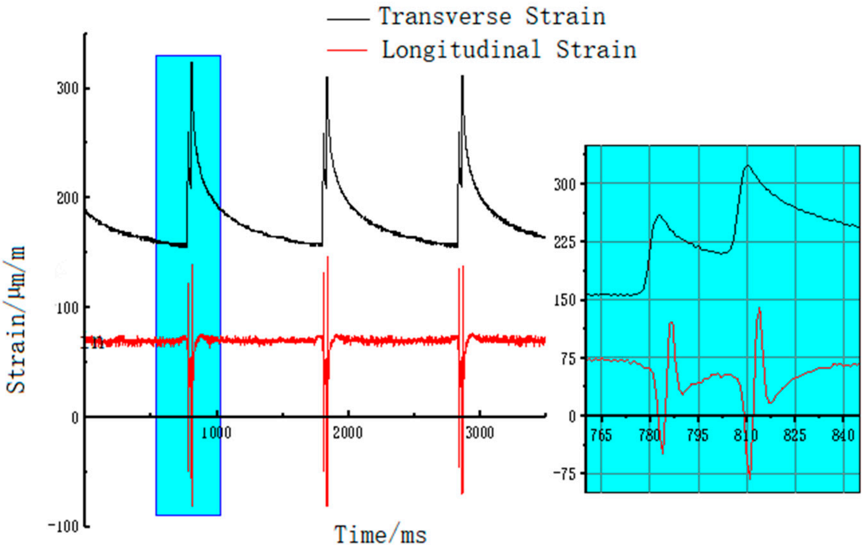

Figure 3. Transverse longitudinal strain at the base of the layer under biaxial action.

Figure 3 demonstrates the following:

(1) The transverse tensile strain value of the pavement is always positive, and the longitudinal tensile strain is alternately positive and negative. This phenomenon occurs mainly because the transverse strain gauge always experiences tension under the vertical action of the wheel load, the longitudinal strain gauge is subjected to horizontal and vertical combined loads, and the strain value alternates between positive and negative. When the tire is close to the strain timing, the horizontal and lateral components of the wheel load act on the longitudinal strain gauge, and the strain is negative. When the wheel load acts directly above the longitudinal strain gauge, the strain gauge is completely subjected to a vertical load, and the strain is positive.

(2) There are two peaks and troughs in the transverse and longitudinal strain data. Taking the transverse strain as the calculation object, the difference between the second peak and the first peak is 60~70 μm/m. Taking the longitudinal strain as the calculation object, the difference between the first wave crest and the second wave crest is 15~20 μm/m, and the difference between the second wave trough and the first wave trough is 40~45 μm/m. Asphalt mixture is a viscoelastic body, which will show elastic properties under the action of instantaneous load. Due to the deformation hysteresis effect caused by its viscoelastic characteristics, the strain generated by the first axle cannot be fully released, and the second axle produces strain superposition. Therefore, the dynamic effect of a biaxial load on pavement is much larger than that of a uniaxial load. Existing design codes still use the static load of a single-axle double-wheel set for the load, which is quite different from the actual multi-axle dynamic load of existing vehicles, which needs further study.

(3) The longitudinal strain reflects the complex stress state of the road surface under the action of the wheel load. The longitudinal compressive strain of the bottom layer is not significantly different from the lateral tensile strain, and the longitudinal tensile strain of the bottom layer is greater than the lateral tensile strain. The actual longitudinal stress on the bottom of the pavement is a variable strain state of alternating compression–tension–compression. Therefore, when designing asphalt pavement, the tensile and compressive strain and strain amplitude of the bottom layer should be considered.

3.3. Influence of Axle Weight

To analyze the effect of axle weight on the dynamic response of the pavement structure, the test data of longitudinal tensile strain and transverse tensile strain at the bottom of the three pavement layers at 08:00 on 21 August were selected for analysis, as shown in Table 3.

Table 3. Dynamic responses of layer substrates under different loads.

Pavement Structure	Longitudinal Tensile Strain/× 10^{-6}			Longitudinal Compressive Strain/× 10^{-6}			Transverse Tensile Strain/× 10^{-6}		
	100 kN	**130 kN**	**150 kN**	**100 kN**	**130 kN**	**150 kN**	**100 kN**	**130 kN**	**150 kN**
Structure 1	76.9	82.6	87.2	−90.5	−99.0	−105.4	132.1	142.3	150.0
Structure 2	76.1	82.0	86.8	−87.5	−97.0	−103.3	132.4	141.6	149.3
Structure 3	78.3	84.3	89.7	−90.1	−100.3	−107.8	133.5	143.2	151.8

The following can be seen in Table 3:

(1) When the axle load increases by 30% and 50%, the longitudinal tensile strain of structure 1 increases by 7.41% and 13.39%, the longitudinal compressive strain increases by 9.39% and 16.46%, and the lateral tensile strain increases by 7.72% and 13.55%, respectively. The longitudinal tensile strain of structure 2 increases by 7.75% and 14.06%, the longitudinal compressive strain increases by 10.86% and 18.06%, and the transverse tensile strain increases by 6.95% and 12.76%, respectively. Finally, the longitudinal tensile strain of structure 3 increases by 7.66% and 14.56%, the longitudinal compressive strain increases by 11.32% and 19.64%, and the lateral tensile strain increases by 7.27% and 13.71%, respectively. The growth of underlayer strain is much less than that of the axial load, and the relationship between the underlayer strain and axial load is nonlinear.

(2) Under the same environment and different axle loads, the three kinds of pavement structures have small differences in their bottom strain, indicating that the pavement performance of the high-volume recycled asphalt pavement studied in this paper can basically achieve the new asphalt pavement standards.

During the test, to deeply study the nonlinear relationship between the axle load and bottom strain, the tire contact area under different axle loads (100, 130, and 150 kN) was tested on the spot using blue paint and white coordinate grid paper. We also measured and calculated the ground pressure (see Table 4 and Figure 4 for details).

Table 4. Wheel ground area under different ground areas.

Axial Load/kN	Single Wheel Ground Area/cm^2	Grounding Pressure/Mpa
100	304.87	0.82
130	318.63	1.02
150	353.77	1.06

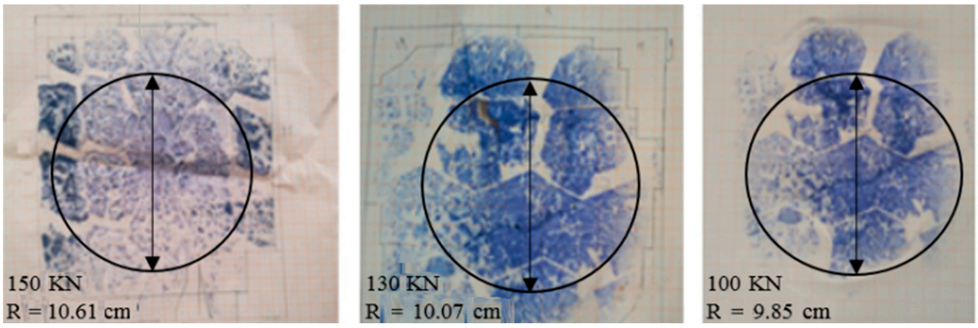

Figure 4. Diagram of wheel ground area.

It can be seen from Table 4 and Figure 4 that with an increase in the axle load of the vehicle, the contact area of the tire increases nonlinearly, and the contact pressure also increases nonlinearly. Therefore, the ground contact pressure can be used as an evaluation index to analyze the influence of overloaded vehicles on the road surface.

3.4. Influence of Temperature

To investigate the effect of temperature on the bottom strain of recycled asphalt pavement, accelerated loading tests were carried out at multiple temperature levels, and the laws of transverse maximum tensile strain and longitudinal maximum tensile strain for the bottom layer under different temperature conditions were analyzed. The driving speed of the vehicle was 24 km·h^{-1}, the axle load was set to 150 kN, and the tire pressure was 1.02 Mpa.

3.4.1. Analysis of Temperature Heat Transfer in Asphalt Pavements

In this paper, test data of Rizhao area in Shandong Province, taken during the high-temperature period from July to November, were used as an example to conduct the study. To intuitively observe the road temperature gradient and environmental temperature distribution, the temperatures during a representative high-temperature period (from 1 September to 22 September) were selected.

Figure 5 shows the temperature and ambient temperature distributions at different depths of asphalt pavement in structure 3. The variation rule of road surface temperature and ambient temperature is basically the same. With an increase in measuring-point depth, the road surface temperature experiences a certain lag with ambient temperature. The deeper the depth is, the more obvious the lag becomes, indicating that the road surface temperature and ambient temperature have obvious nonlinear characteristics.

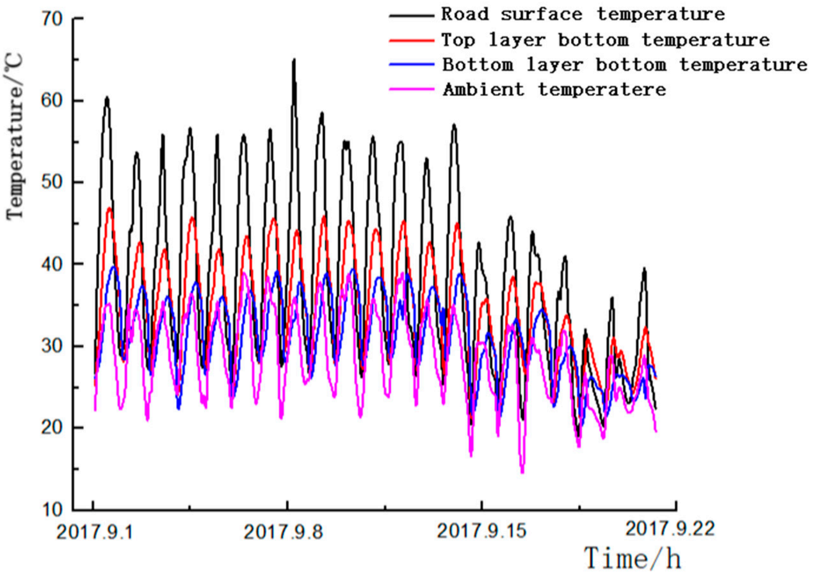

Figure 5. Measured ambient and pavement temperature data.

In this study, we used the temperature gradient calculation formula:

$$G = \frac{T_1 - T_2}{|y_1 - y_2|} \times 1000 \quad (1)$$

where G is the temperature gradient, °C/m; T_i is the temperature in the vertical direction y_i, °C; and y_i is the vertical distance of the i-th test point, mm.

Using to Formula (1), we carried out temperature gradient calculations on the temperature monitoring data from the three kinds of pavement structures. The maximum positive temperature gradient refers to the maximum positive temperature difference formed by the road surface temperature and the bottom layer temperature. The maximum positive temperature gradients of the three pavement structures were 359, 325, and 314 °C/m. The maximum positive temperature gradient occurred at 13:00 on 9 September when the weather was clear and the cloudiness was low. The ambient temperature was 36.3 °C; the surface temperature of the road surface was as high as 69.3 ± 1 °C under the action of strong infrared rays; the temperature of the upper bottom layer was 41.4, 41.5, and 41.8 °C; the bottom layer temperature was 34.4, 34.5, and 35.0 °C. Structure 2 and structure 3 had the same top layer material, and the temperature of the top bottom layer was basically the same. Structure 1 was 0.6 °C lower than the bottom layer temperature of structure 3. The test results show that the pavement used in structure 1 has poor heat transfer. This phenomenon is due to the presence of significant amounts of colloid, asphaltene, and other materials in the recycled asphalt mixture, which together reduce the heat transfer efficiency of the pavement.

3.4.2. Effect of Temperature on the Strain Behavior of the Layer Substrate

On September 18, the weather in Rizhao City was sunny and windy. The bottom temperatures and road surface temperatures of the three kinds of pavement structures, collected from 7:00 to 21:00, were compared and analyzed with the horizontal and vertical maximum strain data of the bottom layer. Specific data are shown in Figures 6–8.

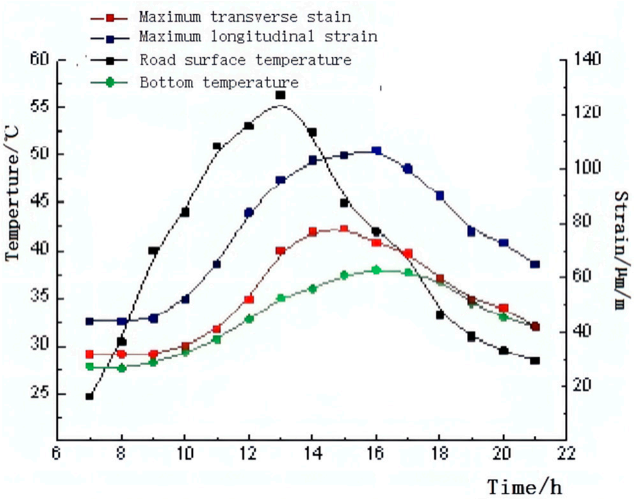

Figure 6. Structure A temperature versus maximum tensile strain in the transverse and longitudinal direction at the base of the layer.

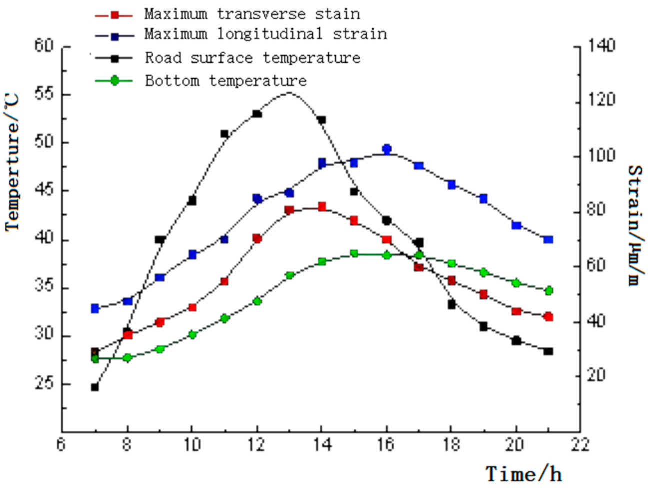

Figure 7. Structure B temperature versus maximum transverse and longitudinal tensile strain at the base of the layer.

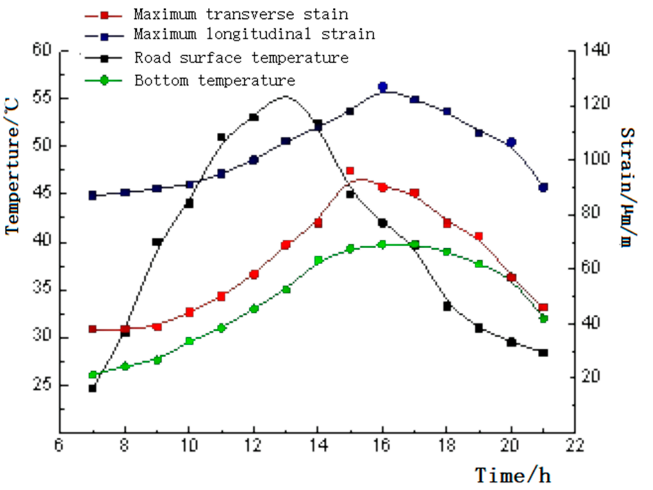

Figure 8. Structure C temperature versus transverse and longitudinal tensile strain at the base of the layer.

The following can be seen in Figures 6–8:

(1) The longitudinal and transverse tensile strains of the three pavement structures are basically consistent with the variation of the temperature at the bottom of the pavement. When the temperature at the bottom increases, the strain increases, and when the temperature decreases, the strain decreases. In Figure 6, we see that the layer bottom temperature, the maximum transverse strain, and the maximum longitudinal should reach a maximum value for structure A about an hour later than the road surface temperature; in Figure 7, in the time range 12–14, the road surface temperature is the highest, and the maximum transverse strain is more sensitive to the change in temperature, while the changes in the bottom temperature and the maximum longitudinal strain with temperature are slightly delayed, and the strain reaches the maximum value around 16 o'clock; the change in Figure 8 is closer to that in Figure 6.

(2) Under the same temperature conditions, the longitudinal tensile strain at the bottom of the three pavement structures is greater than the transverse tensile strain; under high temperature conditions, the longitudinal tensile strain is about 1.0–1.5 times the transverse tensile strain, so transverse fatigue cracking of the pavement bottom layer is the first to appear.

(3) At high temperatures, the bottom strain of structure C is obviously larger than that of structure A and B, with little difference between the bottom strain of structure A and B. Structure C belongs to new asphalt pavement, which has good heat transfer, good viscoelasticity of pavement materials, and a large bottom response. The reclaimed pavement has better high-temperature performance than the new pavement. At room temperature, the bottom temperatures of the three pavement structures are close to each other, but there is little difference in the bottom strain values.

(4) Under the action of repeated axial loads on the road surface, the cracks at the bottom of the layer cannot be directly reflected on the road surface. With the help of the highly consistent relationship between the temperature of the bottom of the layer and the longitudinal tensile strain, the cracks at the bottom of the layer can be analyzed. This analysis is used for road performance inspections and disease control. Assessment provides a new approach.

3.5. Effect of Vehicle Speed

First, we analyzed the relationship between the vehicle speed and the bottom strain of the asphalt pavement at 14:00 on 21 August, when the driving equipment was accelerated and loaded at 12, 18, 22, and 24 km·h^{-1}. Three kinds of lateral and longitudinal strains were collected from the pavement bottom layer during driving for comparative analysis. In this paper, the lateral and longitudinal tensile strains of the pavement bottom layer of structure A under four driving speeds were taken as an example, as shown in Figures 9 and 10.

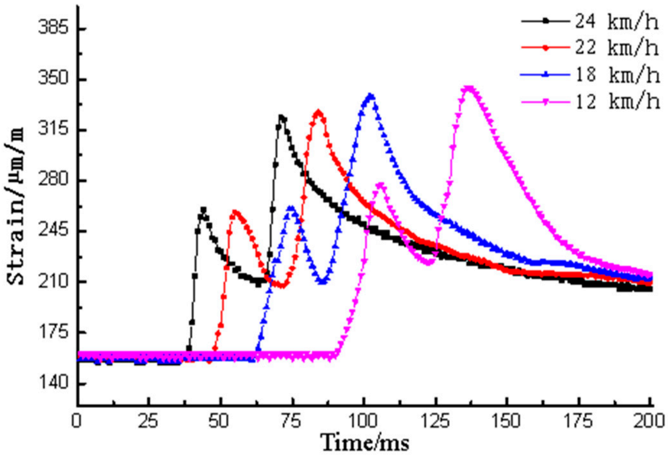

Figure 9. Relationship between vehicle speed and maximum transverse tensile strain at the base of the layer.

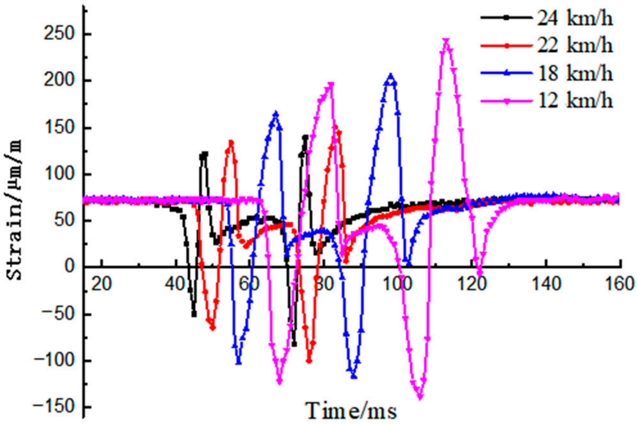

Figure 10. Relationship between vehicle speed and maximum longitudinal tensile strain at the base of the layer.

It can be seen from Figures 9 and 10 that the driving speed of the driving equipment directly affects the wheel load action time and the strain pulse time. As the viscoelastic material of asphalt mixture increases, so too does the vehicle travel speed (relative to the load action frequency). Moreover, the greater the modulus, the lower the strain value at the bottom of the layer.

According to the test data of structures B and C, there is little difference in the bottom strain value between the recycled asphalt pavement and the new asphalt pavement under the same driving speed conditions. The bottom strain values of the three pavement structures all decrease with an increase in the driving speed of the driving equipment, and this trend is consistent. It can be demonstrated that the initial material modulus of the recycled asphalt pavement is close to the modulus of the new asphalt pavement. This conclusion was also confirmed in the previous laboratory tests.

With an increase in vehicle driving degree, the maximum lateral and longitudinal strains of the bottom layer gradually decrease, and the trend of strain reduction does not decelerate. If the driving speed of the driving equipment continues to increase, the bottom layer strain value will reach a relatively stable value. According to the test results, a calculation model for the maximum strain value of structure A (12 km/h $\leq$ v $\leq$ 24 km/h) can be established:

$$\varepsilon = 368.5\mathrm{e}^{-0.05\mathrm{v}} \tag{2}$$

According to the measured data of the Jinan South Ring Expressway field test road (same road structure) paved by the research team, when the heavy-duty vehicle travelled at a speed of 80~120 km/h, the maximum strain value of the bottom layer was 239.3×10^{-6}~206.2×10^{-6}, and the error between the measured value and the calculated value was within 5.0%. The calculation models for different pavement structures and axle loads were established through accelerated loading test data corresponding to the test parameters.

3.6. Influence of the Number of Load Actions

The relationship between the number of loads and the cumulative bottom strain was also analyzed. As an example, we compared and analyzed the lateral and longitudinal cumulative tensile strains of pavement structure A and the number of loads. The relationship between the cumulative tensile strain and the number of loads is shown in Figure 11.

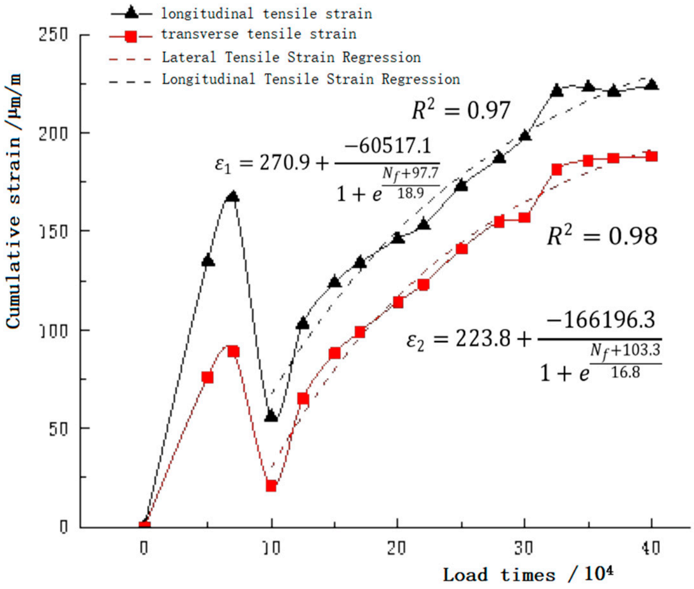

Figure 11. Cumulative strain versus number of load actions.

It can be seen from Figure 11 that in the initial stage of loading, the lateral and longitudinal cumulative strains at the bottom of each layer rise sharply, and the initial cumulative strain is about 75.0% of the total cumulative strain. With an increase in the number of loadings, the increasing trend of the strain decelerates. The cumulative longitudinal and transverse tensile strains tended to be stable when loaded 310,000 times, and the thermally recycled asphalt mixture entered the compaction stage. The average rut at this time was 1.30 cm, and the average rut at the end of the test was 1.55 cm.

According to the comparative analysis of Figures 9–11, the instantaneous strain is sometimes greater than the cumulative strain, indicating that hot-recycled asphalt pavement had self-healing abilities during the test process and in the intermittent stage. Thus, the number of loads here is not directly related to the instantaneous strain but directly related to the cumulative strain. The cumulative strain prediction model based on the Boltzmann function can better reflect the relationship between the cumulative strain at the bottom of the layer and the number of load actions, as shown in Equations (3) and (4):

$$\varepsilon_1 = 270.9 + \frac{-60517.1}{1+\mathrm{e}^{\frac{\mathrm{N_f}+97.7}{18.9}}} \tag{3}$$

$$\varepsilon_2 = 223.8 + \frac{-166196.3}{1 + e^{\frac{N_f + 103.3}{16.8}}} \tag{4}$$

The reason for the sharp decline stage shown in Figure 11 is that the bottom deformation was recovered after the test was interrupted for 6 days due to weather reasons and equipment failure. The test data indicate that the longitudinal accumulated strain recovered by 66.5%, and the lateral accumulated strain recovered by 76.4%, indicating that the thermal regenerative asphalt pavement had a strong ability to recover initial deformation.

4. Concluding Remarks

(1) In the case of dual axles and two wheels, the strain amplitude of the asphalt pavement under the center of the wheel track on one side was larger than that under the center of the wheel gap, and the load on the asphalt pavement under the center of the wheel track on one side was higher than that under the center of the wheel gap.

(2) The damage effect of a single dual-axle wheel load was far greater than that of the two single-axle wheel loads. The longitudinal strain at the bottom of the pavement layer always maintained an alternating state of compression–tension–compression, and the longitudinal tensile strain at the bottom of the pavement layer was always greater than the lateral tensile strain. Moreover, transverse fatigue cracks appeared first. Under high temperature conditions, the longitudinal tensile strain was about 1–1.5 times the transverse tensile strain.

(3) When the axle load increased by 30% and 50%, the longitudinal tensile strain increased by 7.41–14.56%, respectively; the longitudinal compressive strain increased by 9.39–19.64%; and the transverse tensile strain increased by 7.72–13.71%. The bottom strain of asphalt pavement had a nonlinear relationship with the axle load and a linear relationship with the ground pressure.

(4) The maximum positive temperature gradient of structure A was 12.50% higher than that of structure B and 9.50% higher than that of structure C. The heat transfer efficiency of the thermally recycled pavement was lower than that of the new asphalt pavement, and the temperature had a greater impact on the bottom strain of the asphalt pavement.

(5) The driving speed directly affects the load action time and pulse time of the response. The higher the vehicle speed was, the smaller the bottom layer strain value became. Based on the accelerated loading test data, a prediction model for the maximum bottom layer strain was established. The error rate in the calculations of the maximum strain value of the pavement bottom layer was controlled within 5%.

(6) No direct relationship was observed between the loading times and instantaneous strain, and the relationship between the loading times and accumulative bottom could be represented using the Boltzmann function. After 310,000 loads, the hot-recycled asphalt pavement entered the dense stage, and plastic deformation was basically completed. Under a load of 400,000 times, there was no obvious difference in rut performance between the recycled asphalt pavement and the new asphalt pavement.

(7) Certain limitations remain in evaluating the performance of hot-recycled asphalt pavement based on the bottom-strain behavior of asphalt pavement. The mechanical response of high-volume thermally recycled pavement can basically fulfill the new pavement standards, but the uniformity and migration law of thermally recycled materials cannot be determined in the strain behavior clearly and must be further verified in combination with the properties of thermally recycled materials.

(8) Based on the above conclusions, this paper accelerates road damage through the fast loading method of controllable axle load, and provides a real data model for analyzing the influence of various factors such as road load on the strain. Considering the actual operating conditions on the road, the poor accuracy, authenticity, practicability and real-time performance of the experimental data, and the resulting errors in the analysis results, the accelerated loading test is a cost-effective method. In addition, the dynamic strain behavior analysis of asphalt pavement also plays a very important

role in the study of pavement failure modes. Therefore, the popularization and application of the pavement accelerated loading test system is of great practical significance to study the long-term performance of the pavement. In this paper, the ALT biaxial accelerated loading test equipment is used to simulate the dynamic load of the vehicle, and the parameters such as axle load, temperature, speed, and loading times are synthesized, and the development law of the bottom strain of the three kinds of pavement structures is analyzed, which will also provide information for the advancement of related research.

Author Contributions: Conceptualization, J.L.; methodology, J.L. and Y.L.; software, J.L. and Y.L.; validation, H.Z.; formal analysis, H.Z.; investigation, H.Z.; resources, J.L. and S.Z.; data curation, J.L. and H.Z.; writing—original draft preparation, J.L. and H.Z.; writing—review and editing, J.L. and H.Z.; supervision, J.L. and P.L.; project administration, J.L., C.X. and P.A.; funding acquisition, J.L. and C.X. All authors have read and agreed to the published version of the manuscript.

Funding: Shandong Transportation Science and Technology Project: Preparation and road performance of REOB/SBS composite modified asphalt (2021B11).

Institutional Review Board Statement: Not applicable.

Informed Consent Statement: Not applicable.

Data Availability Statement: The experimental data in this paper are from the pavement material laboratory of Shandong Jiaotong University, which is the provincial key laboratory.

Conflicts of Interest: The authors declare that they have no conflict of interest regarding the publication of this paper.

References

1. Pan, T.C.; Li, J. Dynamic vehicle element method for transient response of coupled vehicle-structure systems. *J. Struct. Eng.* **2002**, *128*, 214–223. [CrossRef]
2. Watts, G.R.; Krylov, V.V. Ground-borne vibration generated by vehicles crossing road humps and speed control cushions. *Appl. Acoust.* **2000**, *59*, 221–236. [CrossRef]
3. Bilodeau, J.P.; Gagnon, L.; Doré, G. Assessment of the relationship between the international roughness index and dynamic loading of heavy vehicles. *Int. J. Pavement Eng.* **2017**, *18*, 693–701. [CrossRef]
4. Navarrina, F.; Ramírez, L.; París, J.; Nogueira, X.; Colominas, I.; Casteleiro, M.; Fernández-de-Mesa, J.R. Comprehensive model for fatigue analysis of flexible pavements considering effects of dynamic axle loads. *Transp. Res. Rec.* **2015**, *2524*, 110–118. [CrossRef]
5. Zhuang, C.Y.; Ye, Y.; Zhang, N. Analysis of dynamic response of semi-rigid base asphalt pavement based on APT test. *J. Shandong Transp. Inst.* **2014**, *22*, 55–61.
6. Lv, S.; Chen, J. Study on the decay law of asphalt mixture stiffness based on accelerated loading test. *J. Highw. Transp. Res. Dev.* **2016**, *33*, 1–6.
7. Hu, P.; Liu, Z.J. Analysis of fatigue damage of asphalt pavement under accelerated loading conditions. *J. Shandong Traffic Coll.* **2010**, *18*, 74–77.
8. Embacher, R.A.; Snyder, M.B.; Odden, T.D. *Using the Minnesota Accelerated Loading Facility to Test Retrofit Dowel Load Transfer Systems*; Transportation Research Record No. 1769; National Academy Press: Washington, DC, USA, 2001; Volume 1769, pp. 134–141.
9. Plessis, D.; Nokes, L.; Mahdavi, W.A.; Burmas, N.; Holland, J.; Lee, E.B. *Economic Benefits Assessment of Accelerated Pavement Testing Research in California: Case Study*; Transportation Research Record No. 2225; Research Board of the National Academies: Washington, DC, USA, 2011; Volume 2225, pp. 137–146.
10. Xu, Q. Accelerated loading test study of semi-rigid base and flexible base asphalt pavement. *Highw. Traffic Technol.* **2011**, *7*, 115–119.
11. Meng, S. Accelerated loading test study on the performance of semi-rigid base asphalt pavement. *Highw. Traffic Technol.* **1997**, 61–66.
12. Jiang, H.; Bian, X.; Chen, Y. Full-scale accelerated loading test for high-speed railway track-roadbed train moving load simulation. *J. Civ. Eng.* **2015**, *48*, 85–95.
13. Ran, W.; Ling, J.; Zhao, H. Accelerated loading dynamic response of epoxy asphalt pavement at high temperature and footage. *J. Tongji Univ.* **2015**, *43*, 1823–1828.
14. Dong, Z.H.; Xu, Q.L.; Lv, P.M. Dynamic response of semi-rigid base asphalt pavement based on accelerated loading test. *Chin. J. Highw.* **2011**, *24*, 1–5.
15. Guan, Z.-G.; Zhuang, C.-Y.; Lin, X.-X. Accelerated loading dynamic response of footprint asphalt concrete pavement. *J. Transp. Eng.* **2012**, *12*, 24–31.
16. Ye, Y.; Zhuang, C.; Wang, L.; Song, X.J. Dynamic response of flexible base asphalt concrete pavement based on accelerated loading test. *Highways* **2013**, *58*, 1–7.